

**π^0 Production at High Transverse Momenta
from π^- Collisions at 520 GeV/c on
Be and Cu Targets**

by

Nikos Varelas

Submitted in Partial Fulfillment
of the
Requirements for the Degree
Doctor of Philosophy

Supervised by
Professor Paul Slattery

Department of Physics and Astronomy
College of Arts and Science

University of Rochester
Rochester, New York

1994

Οψις αδηλων τα φαινομενα

Αναξαγορας

Phenomena concede views of the invisible

Anaxagoras

To my son

Αντωνιος

ACKNOWLEDGMENTS

First and foremost, I wish to thank my wife Maria, and my parents Antonios and Ioanna Varelas for their continuous love, sacrifice, support, and encouragement throughout the years. Without them, I would have never been able to accomplish this thesis. Thanks Mom and Dad for not pressuring me to find a job so I could have time to pursue my studies. Thanks Maria for your patience and understanding through these difficult years when the end seemed so far away. Also, thanks Maria for following me to Fermilab even though you had to interrupt your graduate studies at Rochester. My son Antonios receives the dedication of this thesis for brightening up the last six, most stressful, months of this work. Thanks son for giving me a better excuse this time for continuing to watch Bugs Bunny cartoons. My heartfelt thanks also go to my brother Dimitrios for his love and support over the years.

To successfully accomplish the goals of an experiment as large as E706 requires the combined efforts and sometimes personal sacrifices of a large number of people. I feel very privileged to have been a part of such an enjoyable group of people and I would like to take this opportunity to express my sincere appreciation to all of them. Although it is very difficult to thank everyone individually, there are some people who deserve special mention for helping me, in one way or another, to complete this work.

I would like to express my heartfelt thanks to George Ginther for his guidance and advice over the years, and his detailed comments on my thesis. Thanks George for showing me the way to become an experimental physicist. My sincere appreciation to Marek Zielinski for his help and thoughtful guidance with my thesis analysis. Thanks Marek for always being there (one desk away...) to be interrupted with my questions. Special thanks go also to Phil Gutierrez for teaching me all about

data acquisition systems and readout electronics. Thanks Phil for the many rides you gave me home when my wife had the car.

To my thesis advisor, Paul Slattery, I would like to express my sincere gratitude for his continuous support and guidance throughout my graduate years. Thanks Paul for your suggestions and comments on my thesis. And also, thanks for being at MWEST almost every Friday for our weekly meeting, and sorry if sometimes I unintentionally upset your stomach with some “disturbing looking” plots.

Many thanks to Fred Lobkowicz and Tom Ferbel for all their guidance and advice while I was at Rochester and at Fermilab. Thanks Fred and Tom for your continuous feedback on my work and for being at MWEST often enough to have time to answer my questions. I wish also to thank Gene Engels for the many cheerful discussions we have had, and his good choice of cigars which gave a pleasant aroma to the MWEST air! In addition, thanks go to Carl Bromberg, Joey Huston, Pat Lukens, Sudhindra Mani, and Takahiro Yasuda for always being willing to help and share their experience with me.

George and Penelope Fanourakis deserve special mention for their continuous friendship, advice, support, and help in many different ways over the years. Thanks George and Penelope for the numerous cook-outs filled with the sounds of George’s guitar. Many thanks also go to Ioanis Kourbanis and Alecos Sinanidis for their friendship. Thanks Alecos for the first course in ZEBRA.

I would like to express a hearty thank you to John and Sarah Mansour for their warm friendship and support over the years at Fermilab. Thanks John for always being there for me and helping me every step of the way. Many heartfelt thanks also to Chris Lirakis, Dane Skow, Jim Dunlea, Jan Ftacnik, Casey Hartman, Eric Prebys, Vijay Kapoor, Carlos Yosef, and Bill DeSoi for their help and friendship. Thanks

Chris for teaching me all these computer “tricks” with UNIX that made my life a little bit easier. Thanks Dane for your help with the “crate 15” battle during the run.

I would like to thank all my fellow graduate students for their superb work in this experiment. My sincere thanks and appreciation to my “buddy” Rob Roser for lighting up those “gloomy” tiring days and for the years of warm friendship and partnership. Thanks Rob for always being there for me, and for the long days and nights working together during the data taking and data analysis. Special thanks go to my friend Wiesiek Dlugosz (or “Speedy”) for his help over the years and for the “Taco Bell” lunches that we had together. Many thanks to George and Richelle Osborne for their continuous help and friendship. Thanks Richelle for taking care of Antonios when both Maria and I were very busy. Thank you Lenny Apanasevich for processing the data used in this thesis over the Christmas holidays, and for being a good partner during the data taking shifts. Many thanks to Lucyna de Barbaro, Paoti Chang, Lee Sorrell, and Steve Blusk for their help and friendship. Thanks Steve for explaining to me how the tracking code works.

My sincere thanks to Dan Ruggiero for always being there to help. Thanks Dan for the numerous “emergency” rides and for your help and friendship over all these years. And also, thanks for taking good care of the LAC readout electronics during the run.

I would like to thank Ruth Pordes, Carmenita Moore, and Terry Dorris of the Fermilab computing department for their help and advice in developing the FASTBUS data acquisition system. Also, many thanks to Zonghan Shi for his help in debugging the ICBM modules.

Many thanks to Betty Cook, Judy Mack, Connie Jones, Sue Brightman, and Barbara Warren of the University of Rochester for their support and help in

overcoming numerous bureaucratic obstacles while I was at Rochester and at Fermilab.

Finally, I would like to thank all my teachers from primary to graduate school who influenced my future directly or indirectly. I will always be especially thankful to Manolis Dris for believing in me and inspiring me to become involved in experimental high energy physics.

This research was supported by the United States Department of Energy, the National Science Foundation, and the UGC of India.

ABSTRACT

The inclusive π^0 cross section in 520 GeV/c π^- Be and π^- Cu interactions has been measured as a function of transverse momentum and rapidity, using the E706 spectrometer at FNAL. The production of π^0 s was studied using ≈ 5.2 events/pb of π^- Be data and ≈ 0.84 events/pb of π^- Cu data collected during the 1990 run of the E706 experiment. This data sample represents an order of magnitude increase in statistics over the data recorded during the initial run of the experiment in 1988. The π^0 decay photons were detected by a finely segmented liquid argon electromagnetic calorimeter.

The π^0 cross section was measured for transverse momenta between 3.5 and 10 GeV/c and rapidities between -0.75 and 0.75 . From the data on Be and Cu, we have extracted the nuclear dependence of π^0 production. The measurements are compared with earlier results, as well as with recent next-to-leading-log calculations from Quantum Chromodynamics (QCD).

TABLE OF CONTENTS

CURRICULUM VITAE	iii
ACKNOWLEDGMENTS	iv
ABSTRACT	viii
TABLE OF CONTENTS	ix
LIST OF FIGURES	xi
LIST OF TABLES	xix
1. THEORETICAL MOTIVATION	1
1.1 PARTON MODEL AND QCD	1
1.2 DIRECT-PHOTON PRODUCTION	9
1.3 π^0 PRODUCTION	16
1.4 NUCLEAR DEPENDENCE	17
1.5 OTHER EXPERIMENTS ON π^0 PRODUCTION	18
2. THE MWEST SPECTROMETER	21
2.1 THE MWEST BEAMLINE AND TARGET	21
2.2 THE TRACKING SYSTEM	25
2.3 LIQUID ARGON CALORIMETER	29
2.4 FORWARD CALORIMETER	49
3. DATA ACQUISITION	52
3.1 1987-88 DA OVERVIEW	52
3.2 MOTIVATIONS FOR THE DA UPGRADE	53
3.3 1990-92 DA OVERVIEW	54
3.4 DESCRIPTION OF THE HARDWARE	56
3.5 LAC CALIBRATION AND BETWEEN SPILL TASKS	66
3.6 THE LAC EVENT READOUT PROCESS	75
3.7 THE LAC DA PERFORMANCE	80
3.8 TRIGGER	82
4. EVENT RECONSTRUCTION	88
4.1 OVERVIEW	88
4.2 TRACKING RECONSTRUCTION	90
4.3 EMLAC SHOWER RECONSTRUCTION	95
4.4 THE LAC PEDESTAL CORRECTIONS	105

5. EMLAC ENERGY SCALE.....	114
5.1 OVERVIEW	114
5.2 ELECTRONS.....	115
5.3 PHOTONS	127
5.4 MONTE CARLO SIMULATION.....	133
5.5 ENERGY CORRECTIONS FOR PHOTONS	136
5.6 ENERGY CORRECTIONS FOR ELECTRONS	150
5.7 RESULTS AND SYSTEMATIC UNCERTAINTY	154
6. DATA ANALYSIS.....	166
6.1 DATA SELECTION.....	166
6.2 π^0 SIGNAL DEFINITION.....	181
6.3 COMPARISON OF DATA AND MONTE CARLO.....	184
6.4 π^0 CROSS SECTION CALCULATION	189
7. RESULTS AND CONCLUSIONS.....	203
7.1 CROSS SECTIONS.....	203
7.2 SUMMARY OF SYSTEMATIC UNCERTAINTIES	210
7.3 NUCLEAR DEPENDENCE OF CROSS SECTIONS.....	214
7.4 COMPARISON TO OTHER EXPERIMENTS	216
7.5 CONCLUSIONS.....	221
REFERENCES.....	222
APPENDIX A	229
APPENDIX B	233

LIST OF FIGURES

1.1	Schematic illustration of high a p_T hadronic interaction.	7
1.2	Leading order diagrams for direct-photon production.	11
1.3	Selection of Feynman diagrams for direct-photon production that contribute to the $O(\alpha\alpha_s^2)$ calculation.	14
2.1	Layout of the MWEST spectrometer.	22
2.2	Schematic of the Target/SSD region a) for the 1990 run and b) for the 1991 run.	26
2.3	Cut view of the LAC gantry.	30
2.4	Exploded view of the EMLAC.	33
2.5	Geometry for the a) Radial and b) Azimuthal anode boards.	34
2.6	Example of EMLAC readout boards.	36
2.7	Exploded view of a HALAC cell, or cookie.	37
2.8	HALAC pad configuration.	39
2.9	HV excitation curves taken using 50 GeV/c electrons in the EMLAC. a) HV curve taken at the beginning of the 1990 run. b) Comparison of three HV curves corresponding to the three data runs of the experiment. The vertical scale is normalized arbitrarily to the highest data point.	43
2.10	a) Reconstructed π^0 and η masses relative to their nominal values as a function of "beam days" for the 1990 run. The reference day is 31- May-1990. The curve represents a fit to the π^0 data points. b) Reconstructed π^0 and η masses relative to their nominal values as a function of "real days." The vertical lines indicate a 7-day shutdown period during the 1990 run.	44
2.11	The ratio of the energy reconstructed in the HALAC over the momentum reconstructed using the tracking system for hadrons, as a function of "beam days" for the 1990 run. The dashed line represents a fit to the data points in Fig. 2.10a.	46

2.12	a) Reconstructed π^0 mass relative to its nominal value as a function of “beam days” for the 1991 run. The reference day is 1-Aug-1991. The curve represents a fit to the data points. b) Reconstructed π^0 mass relative to its nominal value as a function of “real days”. The vertical lines indicate shutdown periods for the 1991 run.	47
2.13	Reconstructed π^0 mass relative to its nominal value as a function of “beam days” for the 1990 and 1991 running periods (dark circles). The reference day is 31-May-1990. The open triangles represent the energy ratio detected by the EMLAC for 50 GeV/c incident electron beam data recorded prior to each running period.	48
2.14	The forward calorimeter.....	50
3.1	Block diagram of the data acquisition system.	55
3.2	Flowchart of LAC data acquisition system.....	57
4.1	Difference of the E_{front}/E_{tot} ratios between the r and ϕ view GAMMAS as a function of the total reconstructed energy for Monte Carlo photons.	102
4.2	Difference between two corrected pedestal sets a) for EMLAC channels and b) for HALAC channels.	108
4.3	Difference between the calibration and the corrected EMLAC pedestals as a function of the run average beam intensity per spill.	110
4.4	Difference between the calibration and the corrected EMLAC pedestals versus the time between RESET and EVENT signals for data taken using a high rate PULSER trigger.	111
4.5	Distribution of the RMS of pedestal distributions for LAC channels measured in ADC counts.	113
5.1	ΔR^2 distribution for track-shower matching. ΔR^2 for a) all track-shower matches and b) ZMP tracks.	117
5.2	ΔS_Y distributions. The effect for various cuts on the ΔS_Y distribution: a) all oppositely charged tracks; b) $188 < ZXI < 208$ cm; c) at least one ZMP track matched with shower with $E_{front}/E_{tot} > 0.5$; d) both ZMP tracks matched with showers. Each plot has the cuts of the previous plot.	119

5.3	<i>ZXI</i> distributions. The effect for various cuts on the <i>ZXI</i> distribution: a) all oppositely charged tracks; b) $ \Delta S_Y < 3$ mrad; c) at least one ZMP track matched with shower with $E_{front}/E_{tot} > 0.5$; d) both ZMP tracks matched with showers. Each plot has the cuts of the previous plot.	120
5.4	Momentum spectrum of ZMP tracks.	121
5.5	Position of ZMP electrons at EMLAC with a) $P < 10$ GeV/c and b) $P > 20$ GeV/c.	122
5.6	E_{front}/E_{tot} distribution a) for all EMLAC showers that matched with tracks and b) for ZMP electrons.	124
5.7	E_{front}/E_{tot} distribution for ZMP electrons in different energy ranges. In this sample both ZMP tracks matched with showers.	125
5.8	E/P distribution a) for all EMLAC showers that matched with tracks and b) for ZMP electrons for which both tracks matched with showers.	126
5.9	e^+e^- invariant mass distribution for double matched ZMP electrons after the cleaning cuts described in the text. Only tracking information was used to calculate the four momenta of these electrons.	128
5.10	E/P distributions in several energy ranges for a high quality sample of ZMP electrons as described in the text.	129
5.11	a) $\pi^+\pi^-$ invariant mass in the K_S^0 mass region for secondary vertices upstream of the analysis magnet; b) $\mu^+\mu^-$ invariant mass in the J/ψ region.	130
5.12	Two-photon invariant mass spectrum with $p_T > 3.5$ GeV/c. The π^0 and η peaks are clearly visible. The lower, dashed, line represents $\gamma\gamma$ pairs with energy asymmetry less than 0.5.	132
5.13	γe^+e^- invariant mass spectrum with $p_T > 3$ GeV/c. The π^0 and η peaks are clearly visible.	134
5.14	The ratio of the reconstructed π^0 mass to its accepted value as a function of octant number.	137
5.15	Radial dependence of the reconstructed π^0 mass relative to its accepted value using as photon energy a) twice the r view GAMMA energy or b) twice the ϕ view GAMMA energy. The dotted lines represent ± 5 cm from the inner/outer ϕ boundary.	139

5.16	Average energy lost for photons (solid line) and electrons (dashed line) as a function of their reconstructed energy.	140
5.17	Radial dependence of the reconstructed π^0 and η masses relative to their accepted values. The π^0 events have $p_T > 2$ GeV/c whereas the η events have $p_T > 3.5$ GeV/c.	141
5.18	Radial dependence of the E/P ratio for ZMP electrons of momentum $P \approx 20$ GeV/c.	142
5.19	Radial dependence of the reconstructed π^0 mass with $p_T > 2$ GeV/c relative to its accepted value for octants 1 to 4.	144
5.20	Radial dependence of the reconstructed π^0 mass with $p_T > 2$ GeV/c relative to its accepted value for octants 5 to 8.	145
5.21	Radial dependence of the reconstructed π^0 mass relative to its accepted value for runs for which the BEFORE-AFTER gate was ≈ 400 ns, half of the standard value. The π^0 events have $p_T > 2$ GeV/c.	147
5.22	a) The ratio of the π^0 mass in the $\gamma e^+ e^-$ mode to its accepted value as a function of the photon energy. The $\gamma e^+ e^-$ events have $p_T > 0.8$ GeV/c. b) $\gamma e^+ e^-$ invariant mass distribution with $p_T > 3$ GeV/c in the π^0 mass region. c) $\gamma e^+ e^-$ invariant mass distribution with $p_T > 3$ GeV/c in the η mass region. For the above plots all energies are based on the final energy scale.	148
5.23	a) Monte Carlo two-photon invariant mass distribution with $p_T > 4$ GeV/c and $A < 0.5$ in the π^0 mass region. The π^0 events have radii greater than 50 cm. b) Monte Carlo $\gamma e^+ e^-$ invariant mass distribution with $p_T > 3$ GeV/c in the π^0 mass region.	149
5.24	The ratio of the π^0 mass in the $\gamma e^+ e^-$ mode to its accepted value as a function of the Z position of the reconstructed vertex. All energies are based on the final energy scale.	151
5.25	$e^+ e^- e^+ e^-$ invariant mass distribution for events with reconstructed primary vertices in the Be target. The π^0 peak is clearly visible. Only tracking information was used to calculate the four momenta of these electrons.	152
5.26	E/P ratio for ZMP electrons as a function of electron energy for data (dark circles) and Monte Carlo (open circles).	153

5.27	Two-photon invariant mass distribution with $p_T > 4$ GeV/c and $A < 0.5$ in the π^0 mass region after all energy scale corrections a) overall and b) for events with π^0 radius greater than 50 cm.	155
5.28	Two-photon invariant mass distribution with $p_T > 4$ GeV/c and $A < 0.5$ in the η mass region after all energy scale corrections.	156
5.29	$\pi^0\gamma$ invariant mass in the ω mass range, with $p_T > 3.5$ GeV/c. All energies are based on the final energy scale.	158
5.30	The ratio of the π^0 and η masses relative to their accepted values a) as a function of octant number and b) as a function of p_T . All energies are based on the final energy scale.	159
5.31	The ratio of the η mass to its accepted value as a function of energy asymmetry for $p_T > 3.5$ GeV/c. All energies are based on the final energy scale.	160
5.32	a) Radial dependence of the π^0 mass relative to its accepted value for data (dark circles) and Monte Carlo (open circles). b) Radial dependence of the η mass relative to its accepted value for events with $p_T > 3.5$ GeV/c (dark circles) and for events with $p_T > 5$ GeV/c (open circles). All energies are based on the final energy scale.	162
5.33	The ratio of the π^0 mass to its accepted value as a function of run number after all energy scale corrections.	163
5.34	a) Radial dependence of the E/P ratio for ZMP electrons with $E > 15$ GeV. b) E/P ratio as a function of electron energy. All energies are based on the final energy scale.	164
5.35	E/P distribution for ZMP electrons with $E > 10$ GeV and after all energy scale corrections.	165
6.1	Distribution of reconstructed primary vertices for high p_T π^0 events. The two Be and Cu targets as well as the SSD planes nearest to the target are clearly visible.	168
6.2	X and Y positions of reconstructed vertices for high p_T π^0 events which interacted a) in the two Be targets or b) in the two Cu targets. The square corresponds to the sensitive area of the beam hodoscope, the circle (a) shows the physical location of the Be targets, and the truncated circle (b) shows the shape of the Cu targets.	169

6.3	Two-photon mass distribution in the π^0 mass region with $7 < p_T < 10$ GeV/c a) for $0 < y_{cm} < 0.8$ and b) for $-0.8 < y_{cm} < 0$. For this sample, only the E_{front}/E_{tot} cut was applied to both showers.....	172
6.4	Two-photon mass distribution in the π^0 mass region with $7 < p_T < 10$ GeV/c after the veto wall cut.	174
6.5	Illustration of the concept of photon directionality. Showers generated by particles from the target have directionalities close to zero. Showers produced by particles incident parallel to the beamline have large positive directionalities.	175
6.6	Directionality distribution for the higher energy photon of the $\gamma\gamma$ pair with $5.5 < p_T < 10$ GeV/c and mass in the π^0 region for events when the VWS signal indicated a potential muon candidate; a) for $0.3 < y_{cm} < 0.8$, b) $-0.4 < y_{cm} < 0.3$, and c) $-0.8 < y_{cm} < -0.4$	176
6.7	Directionality distribution for the higher energy photon of the $\gamma\gamma$ pair with $5.5 < p_T < 10$ GeV/c and mass in the π^0 region after the veto wall cut; a) for $0.3 < y_{cm} < 0.8$, b) $-0.4 < y_{cm} < 0.3$, and c) $-0.8 < y_{cm} < -0.4$	178
6.8	Ratio of the total away side p_T to the p_T of the π^0 candidate with $5.5 < p_T < 10$ GeV/c for events when the VWS signal indicated a potential muon candidate; a) for $0 < y_{cm} < 0.8$, b) $-0.4 < y_{cm} < 0$, and c) $-0.8 < y_{cm} < -0.4$	179
6.9	Ratio of the total away side p_T to the p_T of the π^0 candidate with $5.5 < p_T < 10$ GeV/c after the veto wall cut; a) for $0 < y_{cm} < 0.8$, b) $-0.4 < y_{cm} < 0$, and c) $-0.8 < y_{cm} < -0.4$	180
6.10	Two-photon mass distribution in the π^0 mass region for some selected p_T intervals after the muon rejection cuts.	182
6.11	Two-photon mass distribution in the π^0 mass region for $p_T > 3.5$ GeV/c and $A < 0.75$	183
6.12	Two-photon energy asymmetry distribution for the π^0 mass region, half sideband regions, and sideband subtracted for $p_T > 4$ GeV/c.	185

6.13	a) The sideband subtracted two-photon energy asymmetry distribution for photon pairs in the π^0 mass range for $p_T > 4$ GeV/c. The Monte Carlo distribution is shown as the histogram and the data with the circles. b) Two-photon mass distribution in the π^0 mass region with $p_T > 4$ GeV/c for data (circles) and Monte Carlo (histogram).	187
6.14	E_{front}/E_{tot} distribution for data (points) and Monte Carlo (histogram) in different photon energy ranges.	188
6.15	π^0 geometric acceptance as a function of y_{cm} for selected p_T intervals.	191
6.16	π^0 reconstruction efficiency as a function of p_T and y_{cm}	193
6.17	Efficiency distribution for four sections of an octant for <i>SINGLE LOCAL HI</i> triggers as a function of trigger p_T	196
6.18	Efficiency distribution for four sections of an octant for <i>SINGLE LOCAL LOW</i> triggers as a function of trigger p_T	197
6.19	PRETRIGGER efficiency distribution as a function of trigger p_T a) for the inner region and b) for the outer region.	198
6.20	PRETRIGGER efficiency distribution as a function of π^0 p_T a) for the inner region and b) for the outer region.	199
7.1	Inclusive invariant cross sections per nucleon for π^0 production in 520 GeV/c π^- Be interactions, as a function of p_T averaged over the rapidity intervals: $-0.75 < y_{cm} < -0.5$, $-0.5 < y_{cm} < -0.3$, and $-0.3 < y_{cm} < -0.1$	204
7.2	Inclusive invariant cross sections per nucleon for π^0 production in 520 GeV/c π^- Be interactions, as a function of p_T averaged over the rapidity intervals: $-0.1 < y_{cm} < 0.1$ and $0.1 < y_{cm} < 0.3$	205
7.3	Inclusive invariant cross sections per nucleon for π^0 production in 520 GeV/c π^- Be interactions, as a function of p_T averaged over the rapidity intervals: $0.3 < y_{cm} < 0.5$ and $0.5 < y_{cm} < 0.75$	206
7.4	Inclusive invariant cross sections per nucleon for π^0 production in 520 GeV/c π^- Be interactions, as a function of rapidity averaged over different p_T intervals.	207

7.5	Inclusive invariant cross section per nucleon for π^0 production in 520 GeV/c π^- Be interactions, as a function of p_T averaged over the full rapidity range, $-0.75 < y_{cm} < 0.75$. The curves represent QCD calculations as described in the text.	208
7.6	Inclusive invariant cross section per nucleon for π^0 production in 520 GeV/c π^- Cu interactions, as a function of p_T averaged over the full rapidity range, $-0.75 < y_{cm} < 0.75$. The curves represent QCD calculations as described in the text.	209
7.7	Inclusive invariant cross section per nucleon for π^0 production in 520 GeV/c π^- Be interactions, as a function of p_T averaged over the full rapidity range, $-0.75 < y_{cm} < 0.75$. The curve represents a fit of Eq. (7.1) to the data points.	212
7.8	The value of α as a function of p_T (dark circles), as determined from the ratio of π^0 cross sections from 520 GeV/c π^- interactions on Cu and Be targets. The measurements of the value of α by experiment E258 for similar regions of p_T are also shown (open circles).	215
7.9	The value of α as a function of rapidity for three p_T regions, as determined from the ratio of π^0 cross sections from 520 GeV/c π^- interactions on Cu and Be targets.	217
7.10	π^0 cross sections per nucleon in π^- induced collisions as a function of p_T , from several experiments. For experiments E706 and NA3 we have scaled the cross sections by the A-dependence factor using our average measurement of α	218
7.11	Inclusive invariant cross section per nucleon for π^0 production in 520 GeV/c π^- Be interactions, as a function of p_T averaged over the rapidity range $-0.7 < y_{cm} < 0.7$ (dark circles). The π^0 cross section in 500 GeV/c π^- Be interactions reported by E706 based upon the 1988 data sample is shown with the open circles.	119
7.12	The ratio between the π^0 cross sections based on measurements using the 1990 and 1988 data samples, as a function p_T averaged over the rapidity range $-0.7 < y_{cm} < 0.7$. The dashed line represents the theoretical calculation for the cross section ratio for the increase of the π^- beam momentum from 500 to 520 GeV/c between the two runs.	220

LIST OF TABLES

1.1	Selected experiments on π^0 production using π^- beam.	20
3.1	Trigger characteristics for the end of the 1990 run.	87
6.1	Data sets from 1990 running period.	166
6.2	Listing of average values of corrections applied to the data.	202
B.1	Invariant differential cross section per nucleon in units $\text{pb}/(\text{GeV}/c)^2$ for the inclusive π^0 production in 520 GeV/c π^- Be interactions. The cross sections are averaged over the specified p_T and y_{cm} intervals.	233
B.2	Invariant differential cross section per nucleon in units $\text{pb}/(\text{GeV}/c)^2$ for the inclusive π^0 production in 520 GeV/c π^- Be interactions. The cross sections are averaged over the full rapidity range, $-0.75 < y_{cm} < 0.75$	236
B.3	Invariant differential cross section per nucleon in units $\text{pb}/(\text{GeV}/c)^2$ for the inclusive π^0 production in 520 GeV/c π^- Cu interactions. The cross sections are averaged over the full rapidity range, $-0.75 < y_{cm} < 0.75$	238
B.4	Values of α averaged over the full rapidity range $-0.75 < y_{cm} < 0.75$ for π^- induced collisions. The parameter α was determined assuming an A^α dependence for the cross sections on Be and Cu.	239

1. THEORETICAL MOTIVATION

The goal of this thesis is to study large transverse momentum (p_T) π^0 production in π^- interactions on Beryllium (Be) and Copper (Cu) targets. The results presented are from data accumulated during the 1990 run of experiment E706 carried out at the Fermi National Accelerator Laboratory (FNAL or Fermilab). Experiment E706 is a fixed-target experiment designed to measure direct-photon production and the underlying event structure. One of the challenges in measuring the direct-photon cross section is understanding the substantial backgrounds coming from π^0 and η production and subsequent electromagnetic decays. Although the measurement of π^0 production is essential to direct-photon physics, the study of inclusive particle production at high momenta has proved to be a valuable probe of hadronic matter at the constituent level. This thesis reports on a measurement of the π^0 inclusive cross section, and provides comparisons with next-to-leading-log perturbative QCD expectations.

The following sections will briefly discuss the theoretical motivation for this work. A comparison to other experiments in the field will also be provided.

1.1 PARTON MODEL AND QCD

Around 1964, Gell-Man^[1] and Zweig^[2] proposed the idea that nucleons and other strongly interacting particles were not fundamental in structure but were

[1] M. Gell-Man, *Phys. Lett.* 8 (1964), 214.

[2] G. Zweig, CERN report 8182/Th. 401 (1964).

composed from more basic entities, named *quarks*[‡]. At that time, the word “quark” was more a synonym for the successful symmetry scheme of SU(3) than a name for real physical particles. In 1964, all strongly interacting particles fit into the SU(3) symmetry scheme of which three quarks (u , d , and s) form the fundamental representation. Around 1968, experiments at SLAC[†] on deep inelastic electron-nucleon scattering gave the first clear evidence that “pointlike” particles, called *partons*^f, existed inside nucleons.^[3] These experiments revealed that the energy and angular distributions of the scattered electrons exhibit a correlation known as *scaling* which suggests that the partons were structureless spin $\frac{1}{2}$ Dirac particles.^[4, 5] This result, combined with data from inelastic neutrino-nucleon scattering, indicated that partons had the same quantum numbers as quarks.

According to the present theoretical view (called the Standard Model), nature has selected two families of particles, *leptons* and quarks, as the fundamental constituents. Each family contains six spin $\frac{1}{2}$ particles grouped into three distinct doublets, or generations:

$$\text{Leptons: } \begin{pmatrix} \nu_e \\ e \end{pmatrix}, \begin{pmatrix} \nu_\mu \\ \mu \end{pmatrix}, \begin{pmatrix} \nu_\tau \\ \tau \end{pmatrix}$$

[‡] The word “quark” was adopted by Gell-Man from a rather obscure passage of James Joyce's *Finnegan's Wake*:

Three quarks for Muster Mark!
Sure he hasn't got much of a bark
And sure any he has it's all beside the mark.

[†] Stanford Linear Accelerator Laboratory, Palo Alto, California, USA.

^f The word “parton” was introduced by R. P. Feynman.

[3] For a broader historical perspective, see: R. N. Cahn and G. Goldhaber, *The Experimental Foundations of Particle Physics*, Cambridge Univ. Press, 1989.

[4] J. D. Bjorken and E. A. Paschos, *Phys. Rev.* 185 (1969), 1975.

[5] R. P. Feynman, *Phys. Rev. Lett.* 23 (1969), 1415.

$$\text{Quarks:} \quad \begin{pmatrix} u \\ d \end{pmatrix}, \begin{pmatrix} c \\ s \end{pmatrix}, \begin{pmatrix} t \\ b \end{pmatrix}$$

The lepton family consists of the electron, muon, and tau leptons, with electric charge of $-e$, and their associated neutrinos, with zero electric charge. Quarks appear in six varieties or *flavors*, labeled as u (up), d (down), c (charm), s (strange), t (top)[◇], and b (bottom), and they carry fractional electric charges, of $+\frac{2}{3}e$ (u , c , and t quarks) or $-\frac{1}{3}e$ (d , s , and b quarks). Neutrinos participate exclusively in weak interactions, whereas the remaining particles also experience electromagnetic and gravitational interactions; only quarks experience the strong interaction.

So far, only two kinds of quark bound states are confirmed, and they are designated by the common name of *hadrons*. The half-integral spin *baryons* (of which the proton and neutron are examples) are bound states consisted of three quarks (qqq states), and the integral spin *mesons* (of which the pions and kaons are examples) are bound states formed by a quark-antiquark pair ($q\bar{q}$ states). In order to preserve the Pauli exclusion principle in the formation of baryons from quarks (for example uuu in Δ^{++}), a new quantum number was introduced, named *color*,^[6] which facilitated the anti-symmetrization of the baryon wave function. Quarks come in three primary colors. It is assumed that only colorless states (or color singlets under color symmetry) are physically realizable and hence that quarks cannot be observed in isolated states (quark confinement).

The quantum field theory of quark interactions is called quantum chromodynamics (QCD)^[7, 8] in analogy with quantum electrodynamics (QED). QCD

◇ The top quark required by the lepton-quark symmetry has not yet been directly observed.

[6] M. Gell-Mann, *Acta Phys. Austriaca Suppl.* 9 (1972), 733.

[7] M. R. Pennington, *Rep. Prog. Phys.* 46 (1983), 393.

[8] T. Muta, *Foundations of Quantum Chromodynamics*, World Scientific Publishing Co. 1987.

is a non-Abelian[†] gauge field theory identified with the SU(3) color symmetry.^[9] In analogy with QED, where the photon is an Abelian gauge field mediating electromagnetic interactions between charged particles, in QCD there are eight non-Abelian gauge fields of spin 1 which mediate color interactions between quarks. These non-Abelian gauge fields are called *gluons*. While photons have no electric charge, gluons carry color charges and can interact directly with other gluons. This property of gluons is mainly responsible for the differences between QCD and QED. In the literature, quarks and gluons are often referred to collectively as partons, even though the term originally referred only to the spin $\frac{1}{2}$ particles.

Two important properties of quark dynamics are accommodated in QCD: quark and gluon confinement (mentioned above), and asymptotic freedom.^[10, 11] The property of asymptotic freedom describes the weakening of the effective quark-gluon coupling at short-distances (or large momentum transfers), while the confinement of quarks follows from its strength at long distances. The feature of asymptotic freedom allows the perturbative treatment of strong interactions in obtaining predictions for processes that are dominated by short-distance interactions.^[12, 13]

[†] The term non-Abelian refers to the non-commutative generators of the SU(3) symmetry group.

[9] H. Fritzsch et al., *Phys. Lett.* 47B (1973), 365.

[10] D. J. Gross and F. Wilczek, *Phys. Rev. Lett.* 30 (1973), 1343.

[11] H. D. Politzer, *Phys. Rev. Lett.* 30 (1973), 1346.

[12] CTEQ Collaboration, Handbook of Perturbative QCD, Version 1.0 (1993), FERMILAB-PUB-93/094.

[13] R. D. Field, Applications of Perturbative QCD, Addison-Wesley Publishing Co. 1989.

QCD Running Coupling Constant^{*}

In QCD, the coupling constant for strong interactions can be expressed, to leading-log[◇] in Q^2 by the form^[14]

$$\alpha_s(Q^2) = \frac{12\pi}{(11N_c - 2n_f)\log(Q^2/\Lambda^2)} \quad (1.1)$$

where n_f is the number of quark flavors and N_c is the number of colors. The momentum scale Λ (often referred to as the QCD scale parameter) is the only adjustable parameter in QCD, except for the quark masses. The magnitude of Λ is not predicted by the theory and is defined as

$$\Lambda^2 = \mu^2 \exp \left[\frac{-12\pi}{(11N_c - 2n_f)\alpha_s(\mu^2)} \right] \quad (1.2)$$

where μ is an arbitrary scale introduced to regulate divergences in the perturbative calculation of α_s . This technique of replacing divergent integrals by finite expressions in a systematic fashion is called *renormalization*.^[15] All physical quantities (or theoretical predictions calculated to all orders in perturbation theory) must be independent of the particular choice that is made for the scale μ . Since μ is completely arbitrary, and may differ from integral to integral, it is necessary in a finite order calculation to specify a set of rules to determine its value. Such a set of rules define the different renormalization schemes (e.g. momentum subtraction scheme,

* The term “running coupling constant” is used in the literature to indicate that the coupling constant is a function of Q^2 .

◇ The term “leading-log” is used to indicate an all-orders calculation in which only the leading logarithm terms are retained.

[14] A. J. Buras, *Rev. Mod. Phys.* 52 (1980), 199.

[15] G. Sterman, *An Introduction to Quantum Field Theory*, Cambridge University Press 1993.

modified minimal subtraction scheme, or $\overline{\text{MS}}$ scheme). After choosing a convenient renormalization scheme, the coupling constant and scale Λ are defined within that scheme. The magnitude of the parameter Λ defined in a given renormalization scheme should be determined by comparing experimental data to QCD predictions expressed in that scheme.

Eq. (1.1) shows that the strong coupling constant tends to zero (assuming that the number of flavors is less than 17) as $Q^2 \rightarrow \infty$, and that quarks and gluons become asymptotically free. Thus QCD perturbation theory can be justified in the large momentum transverse regime. When Q^2 is of the order of Λ^2 , expression (1.1) is no longer valid since $\alpha_s(Q^2)$ becomes large and the perturbation expansion breaks down. In this limit, quarks and gluons arrange themselves into strongly bound clusters, namely, hadrons.

High p_T Hadronic Interactions

In QCD, at high energies and large momentum transfers, hadron-hadron interactions appear to be due to the hard scattering of the hadron constituents (i.e., the quarks and gluons). Large p_T processes are interpreted as large-angle scattering resulting from parton hard scattering.^[16, 17] Let us assume the inclusive hadronic interaction of $A + B \rightarrow C + \text{anything}$, where the detected particle C (a π^0 , for example) has large momentum transverse (see Fig. 1.1). To obtain a cross section for this inclusive reaction, as described by only the lowest-order subprocesses, we must convolute the cross section for the elementary process (i.e., two-body scattering $ab \rightarrow cd$) with the gluon or quark contents of the initial hadrons (A, B), as well as

[16] R. D. Field and R. P. Feynman, *Phys. Rev. D* 15 (1977), 2590.

[17] S. D. Ellis and M. B. Kislinger, *Phys. Rev. D* 9 (1974), 2027.

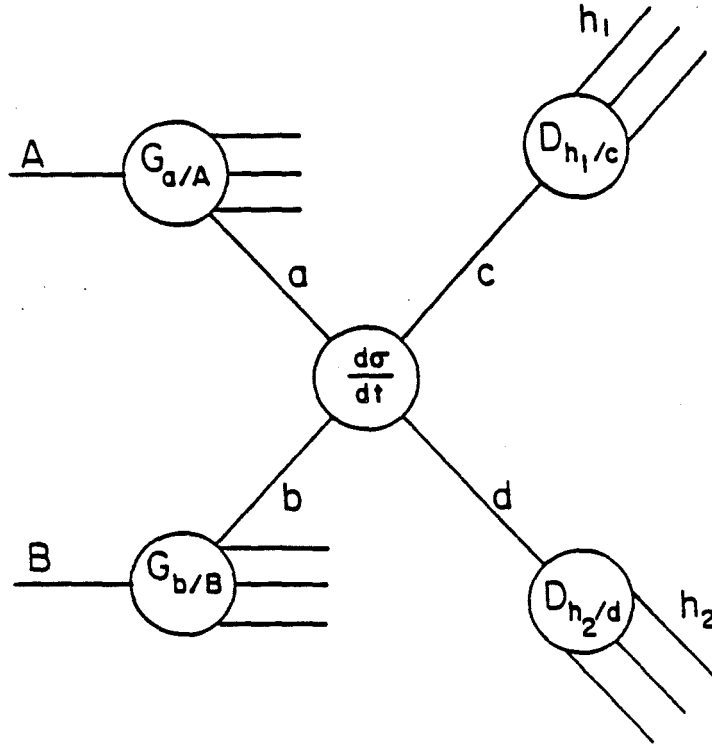


Figure 1.1 Schematic illustration of a high p_T hadronic interaction.

with the probability of obtaining the final state hadron (C) from the outgoing parton. Assuming that the initial and final partons are collinear with the corresponding initial and final hadrons, the corresponding expression for the invariant cross section is:^[18, 19]

$$E_C \frac{d^3\sigma}{dp_C^3}(AB \rightarrow C + X) = \sum_{abcd} \int dx_a dx_b dz_c G_{a/A}(x_a, Q^2) G_{b/B}(x_b, Q^2) D_{C/c}(z_c, Q^2) \frac{\hat{s}}{z_c^2 \pi} \frac{d\sigma}{d\hat{t}}(ab \rightarrow cd) \delta(\hat{s} + \hat{t} + \hat{u}) \quad (1.3)$$

[18] R. Cutler and D. Sivers, *Phys. Rev. D* 17 (1978), 196.

[19] J. F. Owens, *Rev. Mod. Phys.* 59 (1987), 465.

where \hat{s} , \hat{t} , and \hat{u} are the Mandelstam variables corresponding to the interacting partons, defined as $\hat{s} = (p_a + p_b)^2$, $\hat{t} = (p_a - p_c)^2$, and $\hat{u} = (p_a - p_d)^2$; p representing the four momenta of the partons (or hadrons), $G_{i/H}(x)$ is the parton distribution function, giving the probability of finding a parton i in a hadron H with a momentum fraction between x and $x+dx$. The probability of obtaining a hadron C with a momentum fraction between z and $z+dz$ from a parton c is denoted by the fragmentation function $D_{C/c}(z)$. $d\sigma/d\hat{t}$ is the cross section for the underlying subprocess, and the summation is over all possible constituent interactions. For the two-to-two scattering there are eight elementary processes that must be considered:^[20] $gg \rightarrow gg$, $gq \rightarrow gq$, $qq \rightarrow qq$, $q\bar{q} \rightarrow q\bar{q}$, $qq' \rightarrow qq'$, $q\bar{q} \rightarrow gg$, $q\bar{q} \rightarrow q'\bar{q}'$, $gg \rightarrow q\bar{q}$.

When effects due to gluon bremsstrahlung and quark-antiquark pair production are taken into account, a characteristic Q^2 dependence is predicted for the parton distribution and fragmentation functions, referred to as scaling violations. These parton distribution and fragmentation functions cannot be calculated within the framework of perturbative QCD, and must be extracted by fitting some parametrization to the data at a scale Q_0^2 . The evolution of the distribution^[21] and fragmentation^[22] functions from Q_0^2 to any other scale Q^2 is calculable by the perturbative QCD.

Early calculations (Ref. [17]) predicted that the inclusive single particle cross section should behave as:

[20] B. L. Combridge, et al., *Phys. Lett.* 70B (1977), 234.

[21] G. Altarelli and G. Parisi, *Nucl. Phys.* B126 (1977), 298.

[22] J. F. Owens, *Phys. Rev. Lett.* B76 (1978), 85.

$$E \frac{d^3\sigma}{dp^3} \xrightarrow{s \rightarrow \infty} \frac{f(x_T, \theta)}{s^2} \quad (1.4)$$

where $f(x_T, \theta)$ is a dimensionless function, θ is the scattering angle measured relative to the beam direction, and $x_T = 2p_T/\sqrt{s}$. The form (1.4) results from the assumption of scattering by vector gluon exchange between spin $\frac{1}{2}$ particles, and that the distribution and fragmentation functions are scale-invariant. At fixed x_T , s^2 is proportional to p_T^4 , hence for a given x_T and θ one expects $E d\sigma/d^3p \approx p_T^{-n}$, where $n = 4$. However, experimentally this is not observed; in fact, data for high p_T meson production suggest $n \approx 9$. The deviation between the naive expectation and the data is attributed to the many theoretical corrections that must be applied. The Q^2 dependence of the strong coupling constant and the Q^2 variation of both distribution and fragmentation functions can accommodate larger value of n . Furthermore, higher order corrections produce similar effects.

1.2 DIRECT-PHOTON PRODUCTION

The study of the production of hadrons at large p_T has played an important role in testing QCD. However, these processes are rather complicated at the level of the constituent quarks and gluons, since many subprocesses contribute. Furthermore, the out-going quarks and gluons distribute their momentum over a collimated collection of hadrons that form a *jet* along the direction of the outgoing parton. In this view, the production of large p_T hadrons is due to the fragmentation of partons, and is thus an indirect product of the elementary parton-parton interaction processes. In the study of jets, the definition of a jet in the theoretical calculations is unambiguous, whereas experimentally the low-momentum component of a jet is often mixed with spectator fragments and the jet definition therefore becomes algorithm dependent. An alternate

way to study the interactions of constituent partons is to investigate the production of direct photons at large p_T .

Direct photons are photons that originate from the hard scattering interaction, and not from the electromagnetic decays of produced hadrons. In lowest order, such photons represent the “full jet,” therefore no (non-perturbative) fragmentation function enters the theoretical prediction. The several advantages of direct-photon production as a source of information on the hard scattering dynamics of quarks and gluons have been pointed out in the literature^[23, 24, 25] (see also Ref. [19]).

To first order, direct photons are produced through gluon Compton scattering and quark-antiquark annihilation (Fig. 1.2). Gluons appear in the diagrams for both processes, in the initial and final states, respectively. By isolating the Compton subprocess contribution to direct-photon production, one can extract information about the gluon distribution function of the colliding hadrons, whereas the annihilation subprocess can provide information about the gluon fragmentation function.^[26] This direct sensitivity to the gluon distribution function through the Compton subprocess is one of the prime motivations for studying direct-photon production. Deep inelastic lepton-nucleon scattering (DIS) has provided accurate information on the quark distribution functions in nucleons[†]; however the gluon distribution contributes to the process only indirectly, through scaling violations. In addition, the DIS data are most sensitive to the gluon distribution in the region of

[23] T. Ferbel and W. R. Molzon, *Rev. Mod. Phys.* 56 (1984), 181.

[24] L. Camilleri, CERN-EP/88-125 (1988).

[25] A. P. Contogouris et al., *Phys. Rev.* D32 (1985), 1134.

[26] L. Cornell and J. F. Owens, *Phys. Rev.* D22 (1980), 1609.

[†] For another measurement of the antiquark content of hadrons, the Drell-Yan process is commonly used. In this process a quark of one hadron annihilates with an antiquark of another hadron to a “time-like” massive virtual photon, which then materializes into a lepton-antilepton pair.

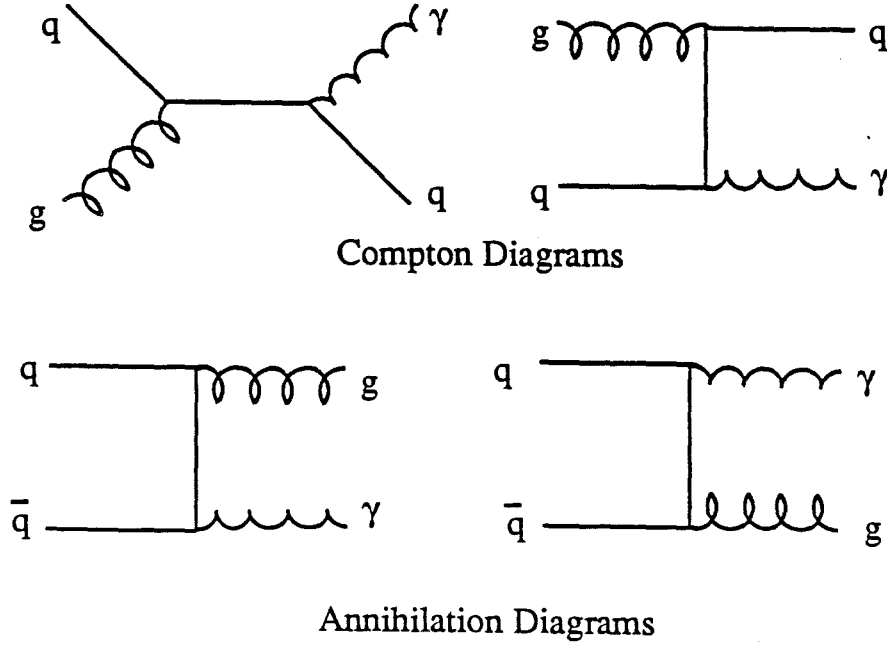


Figure 1.2 Leading order diagrams for direct-photon production.

relatively small values of x , whereas direct-photon data are also sensitive to the gluon distribution at larger values of x , providing complementary input information to global fits of different data sets in determining the gluon content of hadrons.

The invariant inclusive cross section in leading order of perturbative QCD for direct-photon production in the interaction $AB \rightarrow \gamma + X$ can be written as follows:

$$E_\gamma \frac{d^3\sigma}{dp_\gamma^3}(AB \rightarrow \gamma + X) = \sum_{abd} \int dx_a dx_b G_{a/A}(x_a, Q^2) G_{b/B}(x_b, Q^2) \frac{\hat{s}}{\pi} \frac{d\sigma}{d\hat{t}}(ab \rightarrow \gamma d) \delta(\hat{s} + \hat{t} + \hat{u}) \quad (1.5)$$

The cross section expressions for the two subprocesses shown in Fig. 1.2, after performing color sums and spin averages are:^[27, 28]

$$\frac{d\sigma}{d\hat{t}}(qg \rightarrow \gamma q) = -\frac{\pi\alpha\alpha_s}{3\hat{s}^2} e_q^2 \frac{\hat{u}^2 + \hat{s}^2}{\hat{s}\hat{u}} \quad (1.6)$$

$$\frac{d\sigma}{d\hat{t}}(q\bar{q} \rightarrow \gamma g) = \frac{8\pi\alpha\alpha_s}{9\hat{s}^2} e_q^2 \frac{\hat{u}^2 + \hat{t}^2}{\hat{t}\hat{u}} \quad (1.7)$$

where, e_q is the fractional charge of the quark q , and α is the electromagnetic coupling constant.

Next-to-Leading-Order Calculations

Although the leading order theoretical prediction for the direct-photon cross section is in reasonable agreement with data, there are several ambiguities in the calculation which affect the absolute normalizations of those calculations. In order to achieve a higher level of theoretical precision, it is necessary to go beyond the leading order approximation by including higher order terms. The sensitivity to the choice of the momentum scale Q^2 in estimating of the scaling violations of the parton distribution functions and the strong coupling constant in Eq. (1.5) is one of the main weaknesses of the leading order calculation. Different choices of Q^2 (i.e., p_T^2 , $p_T^2/4$) may result in significant changes in the predicted cross section. This sensitivity of the cross section with respect to the definition of Q^2 is reduced when higher order terms are included in the calculation.

[27] F. Halzen and D. M. Scott, *Phys. Rev. D*18 (1978), 3378.

[28] R. Ruckl et al., *Phys. Rev. D*18 (1978), 2469.

Another ambiguity arises from the fact that the colliding partons might have some initial transverse momentum k_T with respect to the incoming hadrons, coming from quark and gluon interactions.^[29, 30] The existence of such “intrinsic k_T ” among the interacting partons can lead to an increase in the cross section in the p_T region below about 5 GeV/c. In the leading order calculation, the initial and final partons have been assumed to be collinear with the corresponding initial and final hadrons, and therefore the k_T smearing becomes important ($\langle k_T \rangle \approx 0.4 - 1$ GeV/c). However, if one increases the amount of QCD dynamics included in the calculation by including next to leading order subprocesses, then the size of the requisite k_T term is decreased.

When higher order subprocesses (see Fig. 1.3) to the direct-photon cross section are evaluated, one encounters divergences that arise from collinear gluon emission from the incoming and outgoing partons. These divergent perturbative contributions to the process can be summed, factored off, and absorbed into the uncalculated portions of the parton distribution and fragmentation functions (factorization theorem). Divergences coming from soft gluon emission (tree diagrams such as Fig. 1.3c) will cancel with the infrared divergences coming from loop diagrams (Fig. 1.3e). Finally ultraviolet divergences associated with loop diagrams can be regulated by some renormalization technique (like $\overline{\text{MS}}$ scheme) and then subtracted. Two calculations of the inclusive direct-photon cross section to the order of $\alpha\alpha_s^2$ have been presented in the literature. In the first,^[31, 32] the calculation was done

[29] R. P. Feynman et al., *Phys. Rev. D*18 (1978), 3320.

[30] A. P. Contogouris et al., *Phys. Rev. D*17 (1978), 2314.

[31] P. Aurenche et al., *Phys. Lett.* 140B (1984), 87.

[32] P. Aurenche et al., *Nucl. Phys.* B297 (1988), 661.

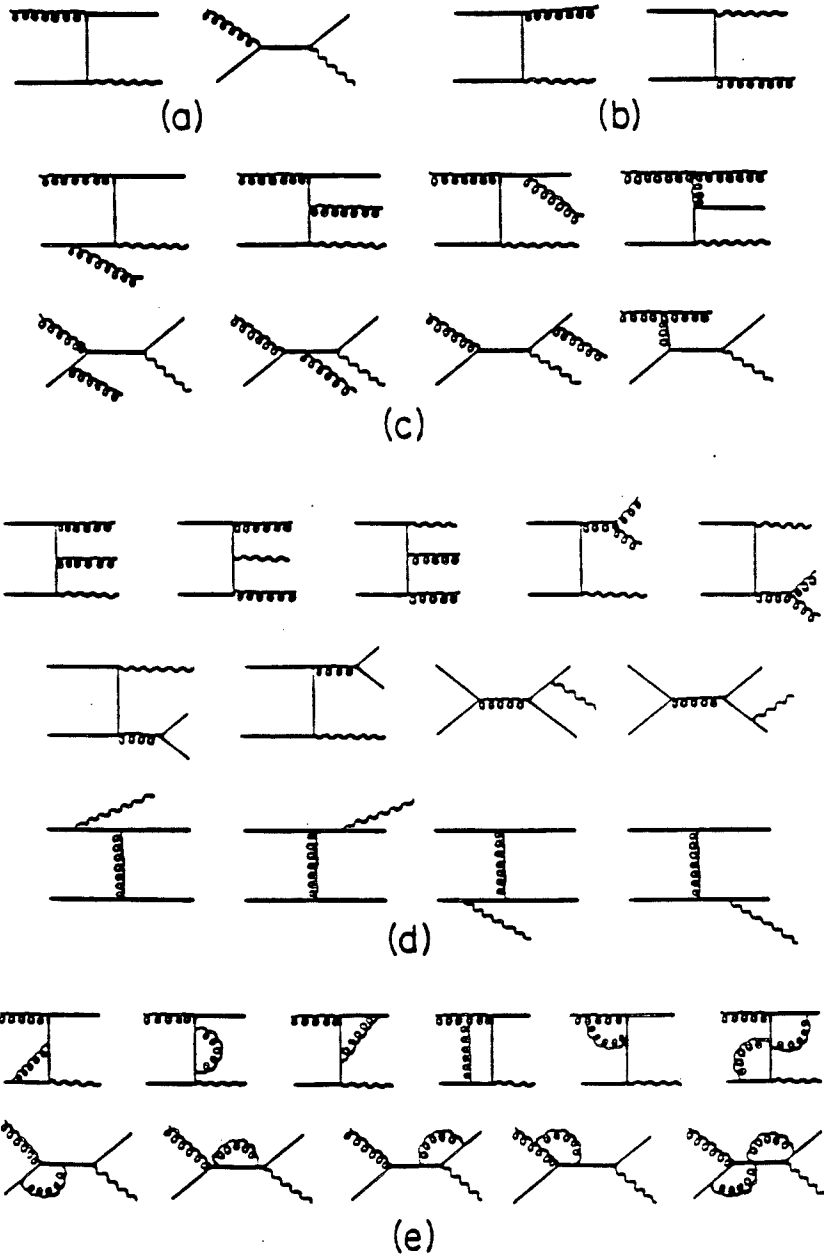


Figure 1.3 Selection of Feynman diagrams for direct-photon production that contribute to the $O(\alpha_s^2)$ calculation.

analytically, whereas in the second^[33] a Monte Carlo algorithm was employed for the required integrations.

Although, in the leading-log approximation, we have seen that there is only one momentum scale, when next-to-leading-log terms are considered one can choose in general three different momentum scales; one for the distribution functions, another for the fragmentation functions, and a third for α_s . The next-to-leading-log theoretical predictions are less sensitive to the variations in the definitions of these scales, and if an exact calculation were performed to all orders in perturbation theory then the result would necessarily be independent of the choices made. This fact has motivated a method for specifying a set of momentum scales, known as the Principle of Minimum Sensitivity (PMS).^[34, 35] The idea is to select the momentum scales for the distribution functions, fragmentation functions, and α_s that minimize the dependence of the calculated cross sections on these parameters. Although, the PMS scales (typically for E706 $\approx 0.1p_T^2$ for the next-to-leading-log prediction for the direct-photon cross section) tend to be somewhat smaller than the “conventional” choices (i.e., p_T^2 , $p_T^2/4$), the PMS technique[†] has been used with notable success in direct-photon theoretical predictions (see Ref. [32]).

[33] H. Baer et al., *Phys. Rev. D* **42** (1990), 61.

[34] P. M. Stevenson, *Phys. Rev. D* **23** (1981), 2916.

[35] H. D. Politzer, *Nucl. Phys. B* **194** (1982), 493.

[†] For the next-to-leading-log direct-photon predictions, the momentum scale for the fragmentation function for obtaining a photon from a massless quark can not be optimized and has been fixed by hand to a given value (Ref. [32]). Choosing another large scale does not make a significant difference because the bremsstrahlung component gives only a small contribution to the direct-photon cross section in the high p_T region.

1.3 π^0 PRODUCTION

Direct-photon production seems ideal to probe certain aspects of QCD, but experimentally it suffers from potentially large backgrounds. The primary source of background[◇] (typically $\geq 80\%$) comes from high transverse momentum π^0 production in which one of the two photons of the π^0 decay is not detected. To account for this background, a detailed study of π^0 production, reconstruction, and simulation by Monte Carlo methods, is essential for the proper identification of the direct-photon signal and for estimating the associated systematic uncertainties.

An important component of the measurement of the direct-photon signal is the γ/π^0 ratio. If this ratio is too small then a measurement will be very difficult. The γ/jet ratio starts out reduced by approximately α_s/α (a factor of ≈ 40 at the p_T values of interest). The relative yield is further reduced due to the large number of contributing diagrams to jet production, and the overall γ/jet ratio thereby becomes of order 10^{-3} . However, the jet rate is suppressed by a factor between $10^2 - 10^3$ if a constraint is imposed that the π^0 carries most of the jet's momentum. Therefore, the γ/π^0 ratio, depending on the kinematic region of interest, might be on the order of few tens of percent, increasing with p_T .

Although the measurement of the π^0 cross section is essential in extracting the direct photon signal, it is also interesting on its own merit, since hadroproduction of high p_T particles provides another mechanism for testing QCD.^[36] The cross section for inclusive π^0 production in the leading-log approximation is given by Eq. (1.3). The prediction involves the convolution of the fragmentation functions $D_{C/c}(z_c, Q^2)$ with the cross-section for the constituent subprocesses. As already mentioned, the

[◇] The background due to η decays is reduced with respect to the π^0 contribution by a production ratio of $\eta/\pi^0 \approx 0.5$ and a branching ratio to $\gamma\gamma$ decays of ≈ 0.4 .

[36] W. M. Geist et al., *Phys. Rep.* 197 (1990), 263.

fragmentation functions and the parton distribution functions must be determined experimentally. Therefore, the measured π^0 cross section provides a means of determining the fragmentation functions, which are known less accurately than the parton distribution functions. A next-to-leading-log QCD calculation has been performed,^[37] including parton-parton subprocesses of order α_s^3 and two loop evolved fragmentation and parton distribution functions. By comparing these next-to-leading-log QCD calculations to data several sets of π^0 fragmentation functions have been determined,^[38] depending on the input data sample used and definition of the momentum scales. These calculations for π^0 production will be presented in Section 7.1.

1.4 NUCLEAR DEPENDENCE

Experiment E706 is the only direct-photon experiment that collected data using a variety of different nuclear targets, including hydrogen, copper and beryllium. In the literature, the form A^α is often used to parametrize the nuclear dependence of the cross section. The power α may be a function of p_T and rapidity, as well as of the nature of the incident particle.

Previous data on inclusive pion production in nuclei have shown that at low p_T values (below ≈ 1 GeV/c) the A -dependence can be approximated by $A^{2/3}$ as expected from geometric shadowing considerations. At higher p_T , the A -dependence increases monotonically from $A^{0.9}$ at $p_T \approx 1$ GeV/c to values exceeding unity for $p_T > 2$ GeV/c.^[39, 40] A possible explanation of this result is that when p_T increases

[37] F. Aversa et al., *Nucl. Phys.* B327 (1989), 105.

[38] P. Chiappetta et al., preprint CPT-92/PE.2841 (1992).

[39] J. W. Cronin et al., *Phys. Rev.* D11 (1975), 3105.

[40] D. Antreasyan et al., *Phys. Rev.* D19 (1979), 764.

the point-like parton-parton interactions start to dominate producing an A -dependence proportional to A^1 . Furthermore, the produced partons can rescatter one or more times inside the nuclear matter (with the probability of each rescattering proportional to the traversed path length, $\approx A^{1/3}$ in the nucleus), leading to a parameter α that can exceed unity.^[41]

Although theoretical models provide some qualitative description of nuclear effects, they still do not provide a comprehensive description of the experimental data. Hopefully, the unique E706 data set at high p_T , with a variety of nuclear targets and particle types, will contribute to the understanding of the properties of high energy hadron-nucleus interactions.

1.5 OTHER EXPERIMENTS ON π^0 PRODUCTION

Over the past twenty years, several fixed target and collider experiments have published results on π^0 production with a variety of beam particles and momenta. This section will briefly describe the most recent fixed target experiments that measured the π^0 cross section using a π^- beam. Some of these measurements will be compared with our data in Section 7.4.

The first measurements of inclusive π^0 production using high energy pion beams were reported by Fermilab experiment E111.^[42] Since then, there have been several other fixed target experiments publishing π^0 cross sections. Experiments E258^[43] (Chicago-Princeton collaboration^f) and E706^[44] were performed at Fermilab.

[41] K. Kastella et al., *Phys. Rev. D* 39 (1989), 2586.

[42] G. Donaldson et al., *Phys. Rev. Lett.* 36 (1976), 1110.

[43] H. J. Frisch et al., *Phys. Rev. D* 27 (1983), 1001.

^f Experiment E258 recorded data for π^+ and π^- production and not directly for π^0 .

[44] G. Alverson et al., *Phys. Rev. D* 48 (1993), 5.

Experiments NA3,^[45] NA24,^[46] and WA70^[47] were performed at the CERN[‡] SPS. Table 1.1 lists the center of mass energy, and the target material used for these experiments. It also gives the center-of-mass rapidity or x_F (where x_F is the Feynman's x variable in the center-of-mass frame $x_F \approx x_T \sinh(y_{cm})$) range, as well as the p_T region of their published data. For E706, the rapidity and p_T ranges[◇] correspond to the data presented in this thesis.

[45] J. Badier et al., *Z. Phys.* C30 (1986), 45.

[46] C. De Marzo et al., *Phys. Rev.* D36 (1987), 16.

[47] M. Bonesini et al., *Z. Phys.* C37 (1987), 39.

[‡] European Center for Nuclear Research, Geneva, Switzerland.

[◇] If one uses different type of triggers, the p_T range of π^0 production at E706 could be extended from 0.5 to 10 GeV/c.

EXP	Target	\sqrt{s} (GeV)	y_{cm} or x_F	p_T (GeV/c)
E706	Be, Cu, H ₂	31.2	$-0.75 < y_{cm} < 0.75$	$3.5 \rightarrow 10$
NA24	H ₂	23.8	$-0.65 < y_{cm} < 0.52$	$1 \rightarrow 7$
WA70	H ₂	22.9	$-0.45 < x_F < 0.6$	$4 \rightarrow 7$
NA3	C	19.4	$-0.4 < y_{cm} < 1.2$	$2.9 \rightarrow 6$
E258	H, Be, Cu, W	19.4, 23.8	$y_{cm} \approx 0$	$1 \rightarrow 6$
E111	H ₂	13.7, 19.4	$y_{cm} \approx 0$	$1 \rightarrow 5$

Table 1.1 Selected experiments on π^0 production using π^- beam.

2. THE MWEST SPECTROMETER

Experiment E706 was located in the Meson West (MWEST) beamline at FNAL. The spectrometer used a finely segmented liquid argon electromagnetic calorimeter to optimize the reconstruction of overlapping photons coming primarily from π^0 decays, the largest source of background to the direct-photon signal. A tracking system was used to identify charged particles, to measure their momentum, and to reconstruct interaction vertices. Fig. 2.1 shows the layout of the various components of the MWEST detector. This spectrometer was used by E706 and experiment E672. Experiment E672 ran simultaneously with E706 using an independent high mass dimuon trigger.

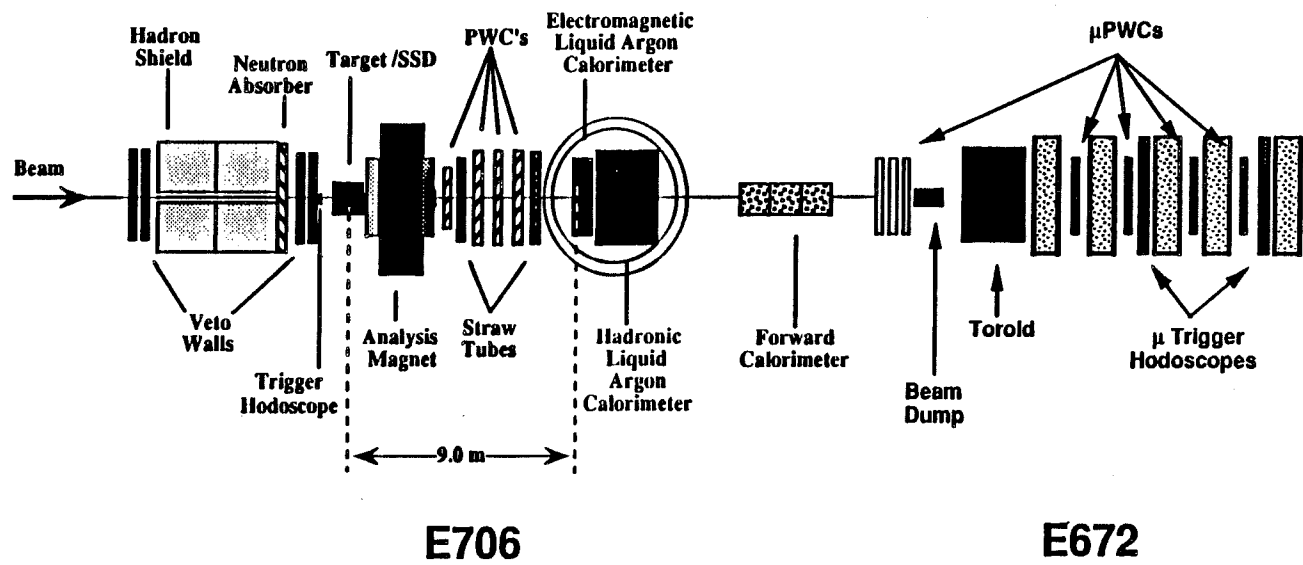
Since the MWEST spectrometer has been described thoroughly elsewhere, only a summary of the major parts of the system will be described in this section, along with the appropriate references.

2.1 THE MWEST BEAMLINE AND TARGET

Beamline

The MWEST secondary beamline was capable of delivering a high intensity mass tagged beam of either positive or negative polarity. The secondary beam delivered to the experiment was produced by an 800 GeV/c proton primary beam. The primary protons, extracted from the Tevatron, interacted with a 1.14 interaction length beryllium target producing the secondary particles. For the 1990 run of the experiment, the secondary beamline transported a ≈ 520 GeV/c beam of negative polarity. The 1991 run was divided into three periods: ≈ 520 GeV/c positive beam, ≈ 520 GeV/c negative beam and 800 GeV/c primary proton beam. The negative secondaries were produced with a yield of $\approx 3 \times 10^7$ per 10^{12} primary protons and

Figure 2.1 Layout of the MWEST spectrometer.



the positives with a yield of $\approx 9 \times 10^7$ per 10^{12} primary protons. The Tevatron operated on a 58 sec cycle, using the first 35 sec to accelerate protons up to 800 GeV/c, followed by a 23 sec extracted *spill*, during which the experiment received $1 - 2 \times 10^8$ secondary beam particles.

The 520 GeV/c negative polarity beam consisted of $\approx 97\%$ π^- and $\approx 3\%$ K^- , while the positive 520 GeV/c beam consisted of $\approx 91\%$ p , $\approx 7\%$ π^+ and $< 2\%$ K^+ .^[1] A 42 m long Cherenkov counter was used to tag the incident particle types. It was located 98 m upstream of the experimental target. The counter used helium gas as a radiator, at a pressure of 4 to 7 psia. Photons were detected by three rings of six phototubes each. The geometry of the rings was such that the three major components of the beam could be simultaneously tagged. The operating pressure of the counter was selected to maximize the tagging efficiency for the minority particles.

To deflect the muons produced by pion decays away from the spectrometer the beamline included five spoiler magnets. At the end of the beamline and upstream of the experimental target was a 5 m long hadron shield, composed of 900 tons of steel. Its function was to absorb hadrons in the beam halo. In order to stop the neutrons produced in the shield a neutron absorber, consisting of a tank filled with water, was installed just downstream of the hadron shield.

Large walls of scintillation counters (veto walls), arranged in quadrants, were positioned one upstream and two downstream of the hadron shield to reject events caused by any remaining beam halo particles. An event was rejected when, within corresponding quadrant, there was a signal in the upstream veto wall in coincidence

[1] I. Kourbanis, The A Dependence of Leading Particle Production by 800 GeV/c Protons, Ph.D. Dissertation, Northeastern University (1989).

with the logical OR of the signals from the two downstream veto walls[†]. This veto eliminated triggers caused by beam halo muons. The veto wall information was also used during the off-line analysis to detect additional fake high p_T photons.

Beam and Interaction Counters

A beam hodoscope^[2] and a scintillation counter were positioned upstream of the experimental target to define incident beam particles. The beam hodoscope consisted of three planes (X, Y, and U) covering a total area of 2×2 cm. Each plane was composed of 12 scintillating paddles ranging in width from 1 to 5 mm. A scintillation counter (BH), with a 1 cm diameter hole in its center, was used in veto with the beam hodoscope to define a useful beam particle. The hodoscope information was read out as a part of the event and used in the off-line analysis to identify multiple beam particles in a single bucket.

An interaction of a beam particle in the experimental target was detected by a set of four scintillation counters (SW1, SW2, SE1, SE2) positioned on either side of the analysis magnet; SE1 and SW1 were 7.6×15.2 cm and placed just upstream of the magnet. SE2 and SW2 were 10.2×20.4 cm and placed just downstream of the magnet. Both sets of counters mated to form holes (1.9 cm diameter between SE1 and SW1 and 3.8 cm diameter between SE2 and SW2) centered on the beam axis.

[†] For the 1991 data run a fourth veto wall was added further upstream from the three veto walls used during the 1990 run. An event was rejected in the trigger when there was a signal from the coincidence of the logical OR of the signals from the two upstream veto walls with the logical OR of the signals from the two downstream veto walls.

[2] C. Bromberg et al., *Nucl. Instr. and Meth.* 200 (1982), 245.

Target

The targets used during the 1990 run were copper (Cu) and beryllium (Be) with a total thickness of $\approx 9\%$ of an interaction length. Specifically, the target area consisted of two Cu pieces 0.08 cm thick each, spaced 0.24 cm apart, followed by two Be pieces 3.708 cm and 1.12 cm thick respectively and spaced 1.02 cm apart. The first Be target was positioned 0.507 cm from the Cu. During the 1991 run, the experimental target included the two upstream Cu pieces, spaced 0.49 cm apart, followed by 15 cm of liquid hydrogen sandwiched between two Be windows 0.25 cm and 0.28 cm thick, respectively. The upstream Be window was positioned 1.2 cm from the downstream Cu piece. Another Be piece, 2.54 cm thick, was located downstream of the Be window. Fig. 2.2 shows the target configuration for both the 1990 and 1991 runs.

2.2 THE TRACKING SYSTEM

The E706 charged particle tracking system, designed to run at a 1 MHz interaction rate, consisted of Silicon Strip Detectors (SSDs), an analysis magnet, a set of Proportional Wire Chambers (PWCs), and a set of Straw Tube Drift Chambers (STRAWs). The following sections will briefly describe the system.

Silicon Strip Detectors

The SSDs provided information for the reconstruction of upstream tracks and interaction vertices.^[3] There were 16 SSD planes constructed of $5 \times 5 \text{ cm}^2$ wafers, and paired into vertical (X) and horizontal (Y) modules with a total 8912 instrumented strips (Fig. 2.2). With the exception of the pair directly downstream of

[3] E. Engels et al., *Nucl. Instr. and Meth.* A279 (1989), 272.

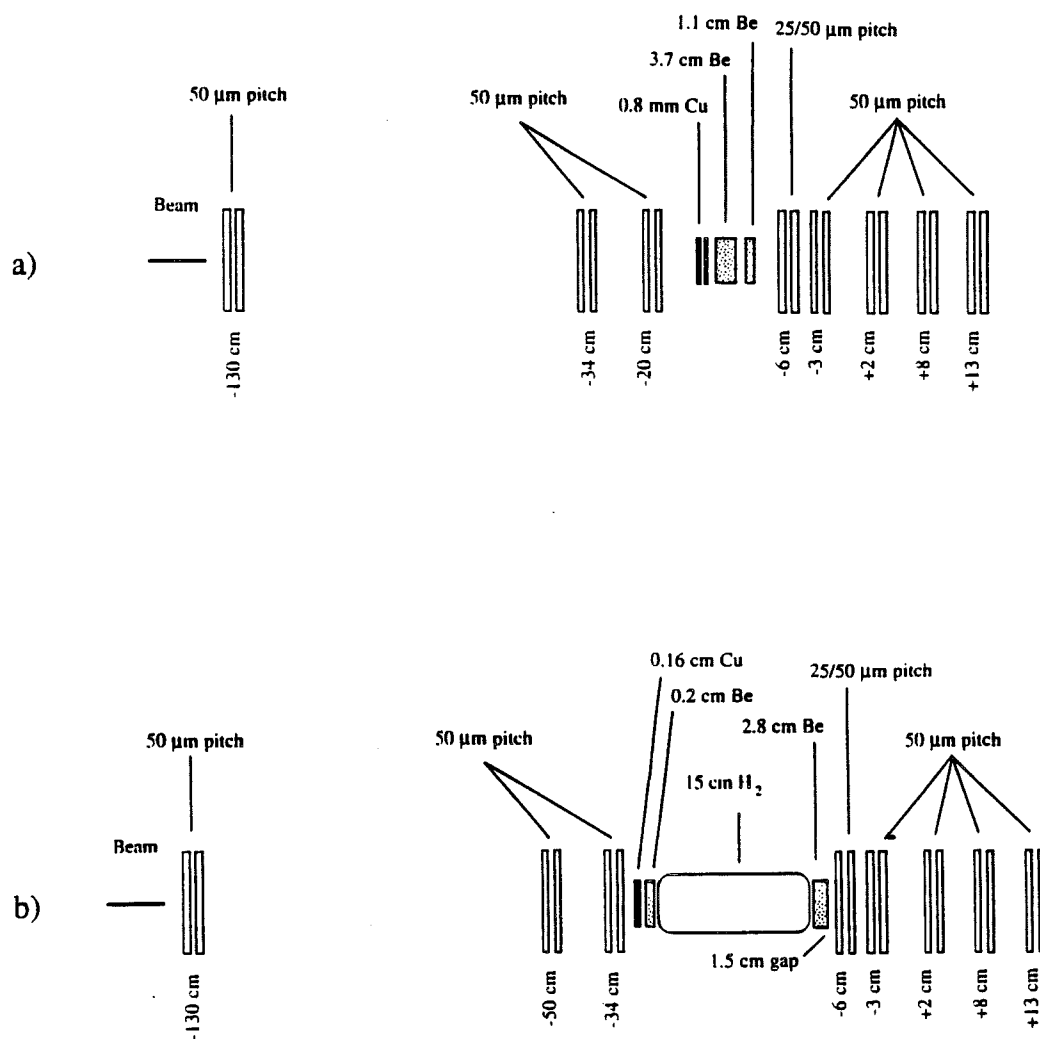


Figure 2.2 Schematic of the Target/SSD region a) for the 1990 run and b) for the 1991 run.

the target, the SSDs all had 50 μm pitch and a thickness of 250–300 μm ; this doublet had a central region with 25 μm pitch. The SSDs, their front-end electronics, and the experimental target were placed in an aluminum box.

Analysis Magnet

The analysis magnet was a vertical dipole centered 2 m downstream of the target. The magnet current was adjusted to generate a 450 MeV/c momentum impulse in the horizontal plane. In order to reduce the fringe field outside the volume of the magnet, mirror plates were installed on the upstream and downstream ends of the magnet. A polyethylene bag filled with helium was installed in the aperture of the magnet to minimize the effects of multiple Coulomb scattering.

Proportional Wire Chambers

The PWCs were configured into 4 separate modules located downstream of the analysis magnet with a total of 13440 channels. Each module was subdivided into 4 planes of wires in an X, Y, U, and V geometry (with U being $+37^\circ$ relative to Y and V being at -53°). The U and V planes were used to match tracks from the X and Y views and to increase the overall tracking efficiency. The four modules had active areas $1.22 \times 1.22 \text{ m}^2$, $2.03 \times 2.03 \text{ m}^2$, $2.03 \times 2.03 \text{ m}^2$ and $2.44 \times 2.44 \text{ m}^2$, respectively. The gold-plated tungsten sense wires were 20 μm in diameter and had a pitch of 0.254 cm. The cathodes were constructed of graphite coated mylar. The graphite coating was segmented into pads, so that the high voltage could be independently set over different sections of the cathode.^[4] This allowed the

[4] K. Hartman, Hadronic Production of π^0 Pairs and Associated Event Structure, Ph.D. Dissertation, Pennsylvania State University (1990).

desensitization of the beam region during high intensity running. The gas mixture in the PWCs was 18% isobutane, 1.1% isopropyl alcohol, 0.1% freon and 79.7% argon. The readout of the SSDs and PWCs was identical after the preamplifiers used for the SSDs. The common readout system was provided by Nanometric System, Inc. The Nanometric modules were housed in CAMAC crates and read out via serial CAMAC highway by a PDP-11 micro-computer (see Chapter 3).

Straw Tube Drift Chambers

The STRAWs were configured into 2 modules, each containing 4X and 4Y planes with a total of 2612 channels. The smaller module was located between PWC1 and PWC2 and the larger module was just downstream of PWC4. The modules were installed between the 1988 and 1990 data runs. The spatial resolution of this system was $\approx 250 \mu\text{m}$ per plane, and it was employed to improve the linking between SSD view tracks (there is no U or V information upstream of the magnet) and downstream space tracks to yield improved vertex and momentum measurements.

Each aluminized mylar tube was 10.4 mm in diameter for the upstream module and 16.3 mm for the downstream module.^[5] The anode was 20 μm diameter gold plated tungsten wires, tensioned with a 50 gm weight and soldered into the tube. A standard gas mixture of 50% Argon and 50% Ethane, bubbled through ethyl alcohol at 0°, was used. The readout amplifier-discriminator cards were mounted on the chambers and the output connected to Time-to-Digital Converters (TDCs). The TDCs were read out through a FASTBUS based system described in Chapter 3. The drift-time corresponded to the distance between the charged particle trajectory and the nearest anode.

[5] C. Bromberg et al., *Nucl. Instr. and Meth.* A307 (1991), 292.

2.3 LIQUID ARGON CALORIMETER

A key element of the spectrometer was the large-acceptance Liquid Argon Calorimeter (LAC) located 9 m downstream of the target. Its purpose was to measure the energies and positions of photons, electrons and hadrons and to select events with high p_T electromagnetic showers. The LAC consisted of two sections: an electromagnetic section (EMLAC) followed by a hadronic section (HALAC), residing in a common cryostat. A comprehensive description of the construction and design criteria of the LAC appears elsewhere,^[6, 7] we give here only a brief description of the device.

The LAC Gantry and Cryostat

Both the EMLAC and HALAC were suspended in a large stainless steel cylindrical cryostat, supported by a steel I-beam frame gantry (Fig. 2.3). The gantry could be moved on rails transverse to the beam direction. This motion was necessary for the construction of the LAC and was also used during calibration. A cooling system attached to the cap of the cryostat supplied and controlled the liquid nitrogen flow to the cooling coils used to keep the argon in a liquid state. To prevent cooling the carbon steel cap below a critical temperature an insulating layer of plastic baffling was placed above the cooling coils.

The cryostat was made of 1.6 cm stainless steel plate and was ≈ 5.5 m in diameter and 9 m high. The outside of the cryostat was covered with ≈ 20 cm of

[6] W. E. DeSoy, Construction and Performance of a Liquid Argon Calorimeter for Use in Experiment E-706 at the Fermi National Accelerator Laboratory, Ph.D. Dissertation, University of Rochester (1990).

[7] F. Lobkowicz et al., *Nucl. Instr. and Meth.* A235 (1985), 332.

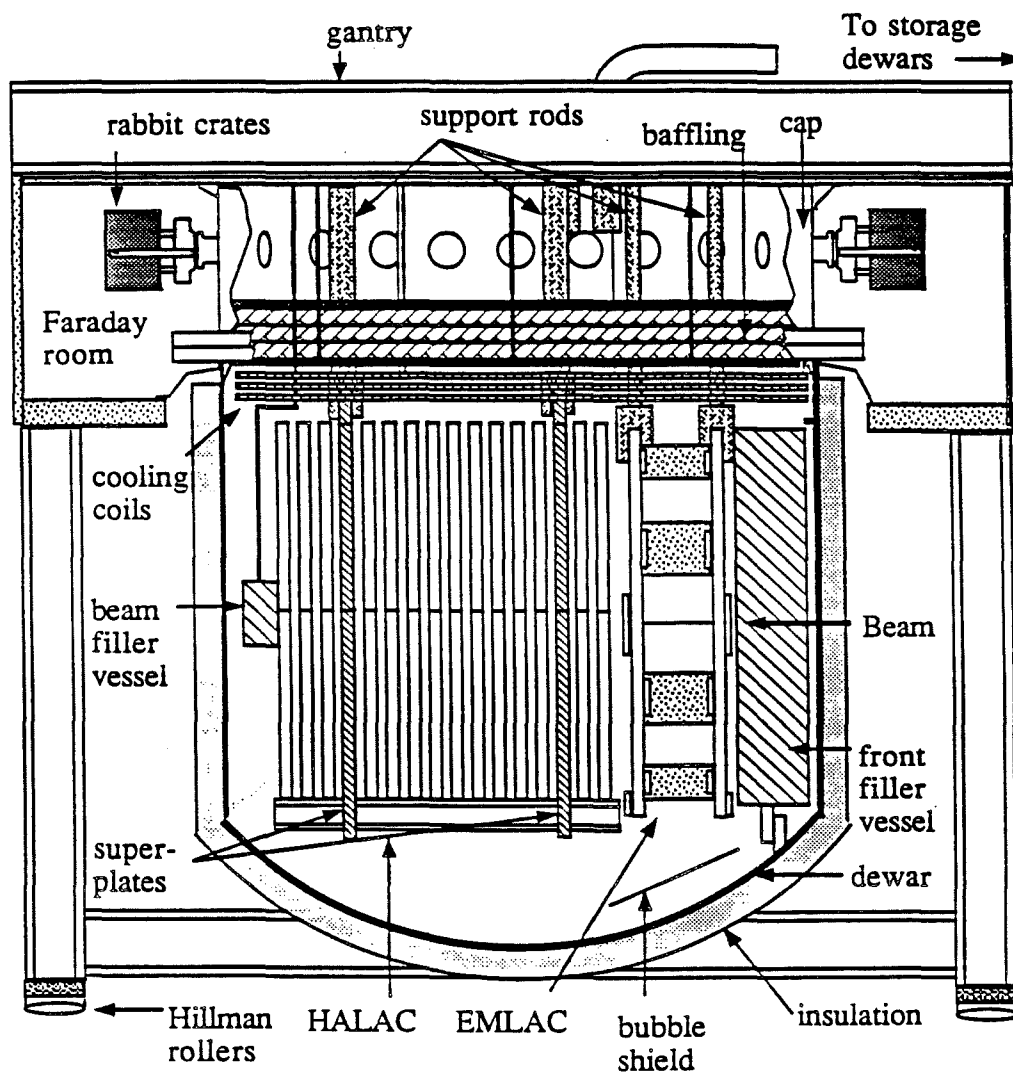


Figure 2.3 Cut view of the LAC gantry.

fiberglass and polyurethane foam insulation. In order to reduce the amount of material in the beam, a 5 cm diameter port made of 1.6 mm thick stainless steel was installed at beam height on the upstream side of the cryostat. To reduce interactions in the uninstrumented regions in the cryostat two argon excluder vessels were installed inside the cryostat. The first was directly upstream of the EMLAC and referred to as the *front filler vessel*. It was made of a closed cell foam (Rohacell) with a density of 0.07 g/cm^3 , enclosed in a 1.6 mm stainless steel skin. The second vessel was a tapered cylindrical volume ($\approx 40 \text{ cm}$ in diameter) inserted into beam holes through the two calorimeters and referred to as the *beam filler vessel*. This vessel was made of 3.2 mm stainless steel and pressurized with helium gas to prevent the liquid argon pressure from crushing it. The front end cap of this vessel was 1.6 mm thick and the rear end cup was 3.2 mm thick.

Cables, $\approx 10 \text{ m}$ long, carried the signals from the calorimeters to charge integration amplifiers, through special vacuum-sealed *feed-through* ports around the sides of the top (cap) of the cryostat. All the electronic crates containing the amplifiers were attached directly to the cryostat cap. In order to reduce the sensitivity of the amplifiers to the effects of external electronic noise, a Faraday room, made of galvanized sheet metal walls, was built into the top of the gantry. Signals into and out of the Faraday room were isolated using optical couplers or transformers. The LAC high voltage supplies along with racks of crates containing modules used in the high-level trigger also resided in the Faraday room.

The Electromagnetic Calorimeter

The EMLAC had a cylindrical geometry, 300 cm in diameter (with a 40 cm diameter central hole) and 71 cm depth. The active area covered a polar angle range of $1.3^\circ < \theta < 10^\circ$ in the laboratory coordinate system. The calorimeter was subdivided into four mechanically independent quadrants as shown in Fig. 2.4. Each quadrant consisted of 66 layers with 22 layers (≈ 10 radiation lengths) in the *front* section and 44 (≈ 20 radiation lengths) in the *back*. A layer was constructed of a 0.2 cm thick lead sheet, 0.25 cm liquid argon gap, a double sided copper-clad G-10 anode board, and another 0.25 cm argon gap. The lead sheets were quadrant sized and served both as absorber material and as high voltage cathodes.

A radial and azimuthal geometry was used for the readout of the EMLAC. The anode boards that measured the shower radial position are referred as r-boards (Fig. 2.5a) and the boards that measured the azimuthal location are referred as ϕ -boards (Fig. 2.5b). The r and ϕ boards were octant sized and had strips on both sides of the board. The r and ϕ boards were alternated, the first board being of the radial type in both the front and back sections.

The r-boards consisted of concentric strips centered on the beam axis. The r-strips were numbered from 0 to 255, where strips 0 and 255 corresponded to the flash left at the inner and outer edges of the board after the strips have been cut into the copper. The flash-strips were capable of producing a signal and they were used in the pattern recognition process. The r-strips were focused in tower-like fashion at the target located 900 cm upstream. As a result of the focusing, the r-strip width increased with depth into the calorimeter as given by the formula

$$w(\text{cm}) = \frac{0.5466}{900} [900 + 1.56 \times (i - 1)] \quad (2.1)$$

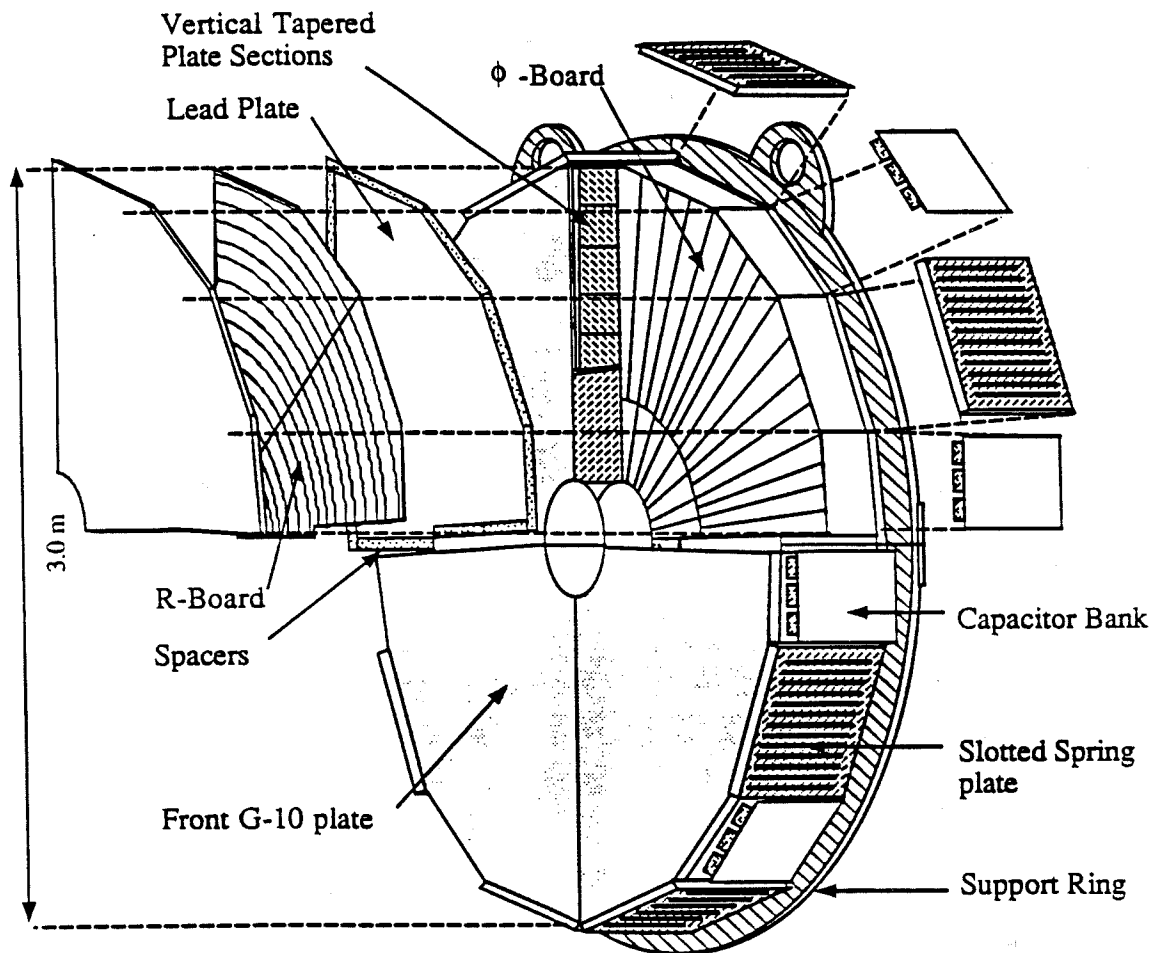


Figure 2.4 Exploded view of the EMLAC.

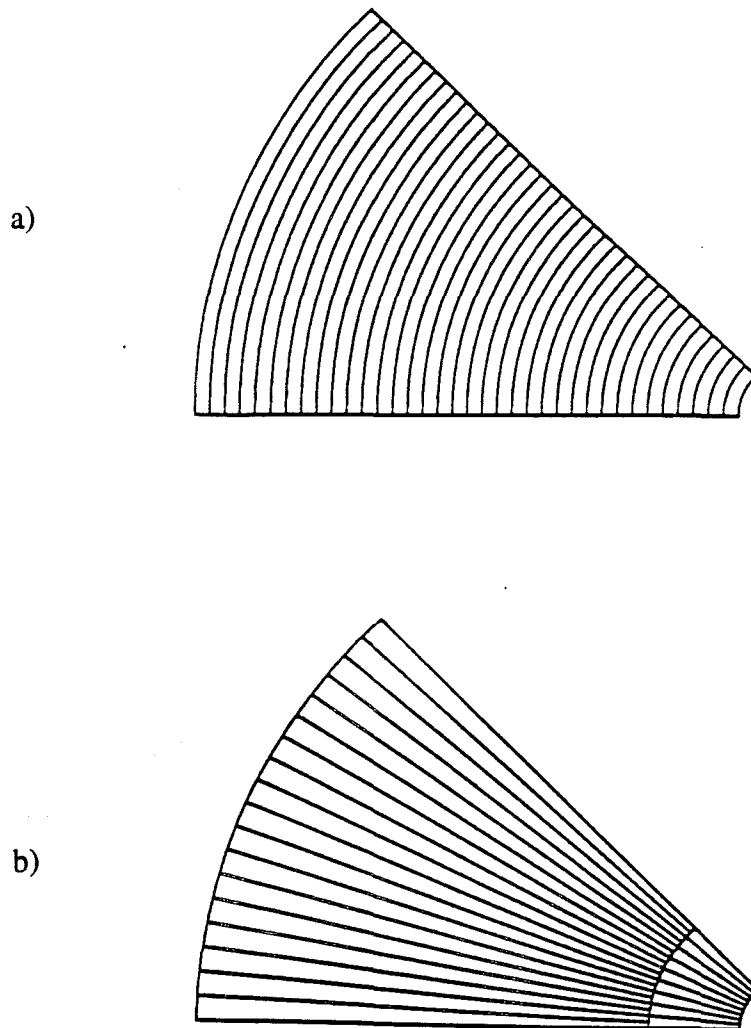


Figure 2.5 Geometry for the a) Radial and b) Azimuthal anode boards.

where i is the i^{th} r-board, 1.56 cm is the distance between two consecutive r-boards and 0.5466 cm is the strip width of the first r-board.

The ϕ -boards were subdivided into independently read out inner and outer regions by a boundary at a radius of 40.2 cm from the LAC centerline. This boundary formed a cone which was focused at the target like the r-strips. The inner section consisted of 96 strips each covering an azimuthal angle of $\pi/192$, and the outer section consisted of 192 strips each subtending an angle of $\pi/384$. The inner/outer ϕ split was intended to improve the position and energy resolution at large radii by subdividing the outer ϕ -strips by a factor of two. This split also reduced r- ϕ correlation ambiguities in the reconstruction caused by multiple showers in the calorimeter. It also introduced some reconstruction challenges for showers that hit close to the boundary since energy from those showers was detected by both inner and outer ϕ -strips.

Each EMLAC octant was read out independently in front and back sections. For each octant, corresponding r-strips in the front section were connected together, along the sides of the r-boards, by wire braid called *connector strings*. The inner ϕ -strips were channeled along the inner edge of the quadrant, and the outer ϕ -strips along the outer edge. The connector strings for the front section were attached to several readout boards (shown in Fig. 2.6) in the front of the EMLAC and the summed signals were carried to the outer edge of the calorimeter, where cables were connected to the amplifiers in the Faraday room. The back section was read out the same way with readout boards at the rear end of the calorimeter. There were a total of 6272 readout channels in the EMLAC.

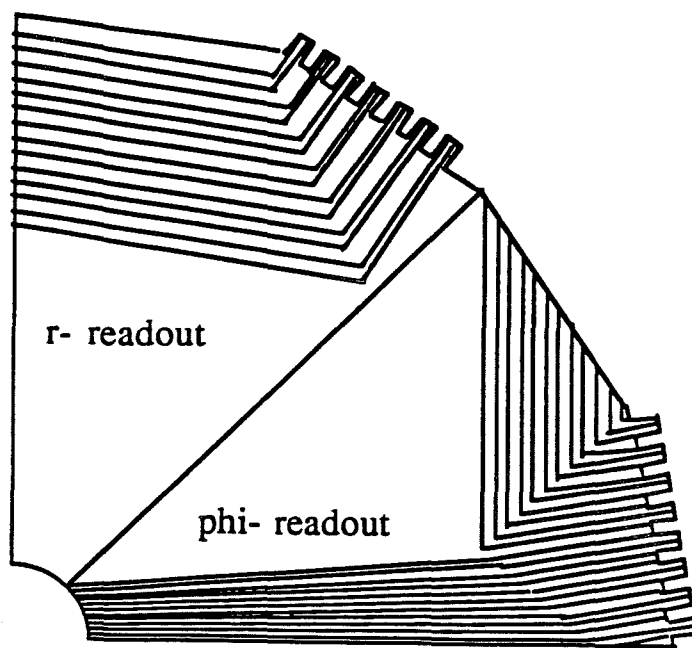


Figure 2.6 Example of EMLAC readout boards.

The Hadronic Calorimeter

The HALAC measured the energy and position of charged and neutral hadrons that did not decay electromagnetically and thus detected in the EMLAC. The HALAC also used liquid argon as the active material, but steel as the absorber. It was ≈ 8 interaction lengths deep (the EMLAC represented an additional 2 interaction lengths).

The HALAC^[8] was constructed of 52 layers, with each layer consisting of a ($\approx 3.7 \text{ m} \times 3.7 \text{ m}$) 2.54 cm thick steel plate, and a 0.32 cm liquid argon gap followed

^[8] C. B. Lirakis, A Study of High Transverse Momentum η Production in 530 GeV/c Hadronic Interactions, Ph.D. Dissertation, Northeastern University (1990).

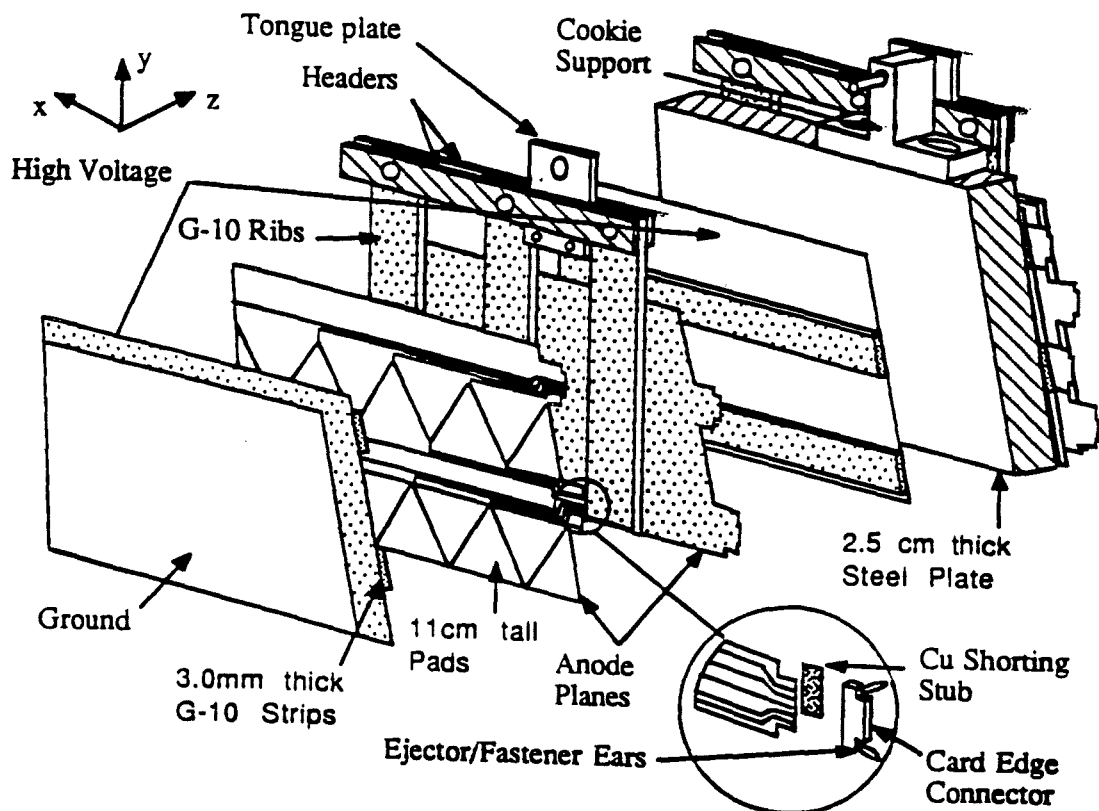


Figure 2.7 Exploded view of a HALAC cell, or cookie.

by a readout module, called *cookie*. An extra readout module was placed in front of the first steel plate to provide a total of 53 cookies. The calorimeter was separated into front and back sections. The front section contained the first 14 cookies and 13 absorber plates. Each cookie was composed out of 7 layers of G-10 glued together, and included 0.8 cm single and double copper-clad G-10 interleaved with strips of 3.2 mm G-10 (Fig. 2.7). The outer two layers were made from double sided copper-clad

G-10 and served as the high voltage planes with the interior side held at high voltage and the outer grounded. The two anode planes were made from single sided G-10 glued together with vertical G-10 ribs between them. They were separated from the high voltage boards by horizontal G-10 strips. The charge collection pads on the anode boards were cut into equilateral triangles (Fig. 2.8). This geometry minimized the X-Y correlation problem during reconstruction. The triangular pad sizes increased longitudinally, providing a geometry focused on the target. The pad sizes were chosen to match the typical spread of hadron showers. The pad height for the first anode board in the front section was 10.9 cm and for the last board of the back section was 13.3 cm. Corresponding pads of the front section were connected together and read out into the same amplifier channel. The back section was similarly read out. The HALAC had a total of 2368 readout channels.

Charge Collection & High Voltage Response

When a charged particle passes through the liquid argon gaps of the calorimeter, it produces electron-ion pairs along its path. Applying a voltage causes the electrons to drift toward the readout boards and the positive ions toward the cathodes. The electron drift velocity (v) dependence on the electric field (E) can be approximated in the range of 1 and 50 kV/cm by^[9, 10]

$$v(\text{cm/s}) = 2.1 \times 10^4 \left[\frac{E}{\text{V/cm}} \right]^{1/3} \quad (2.2)$$

and the total drift time by $T = D/v$, where D is the gap width.

[9] J. Engler et al., *Nucl. Instr. and Meth.* 120 (1974), 157.

[10] L. S. Miller et al., *Phys. Rev.* 166 (1968), 871.

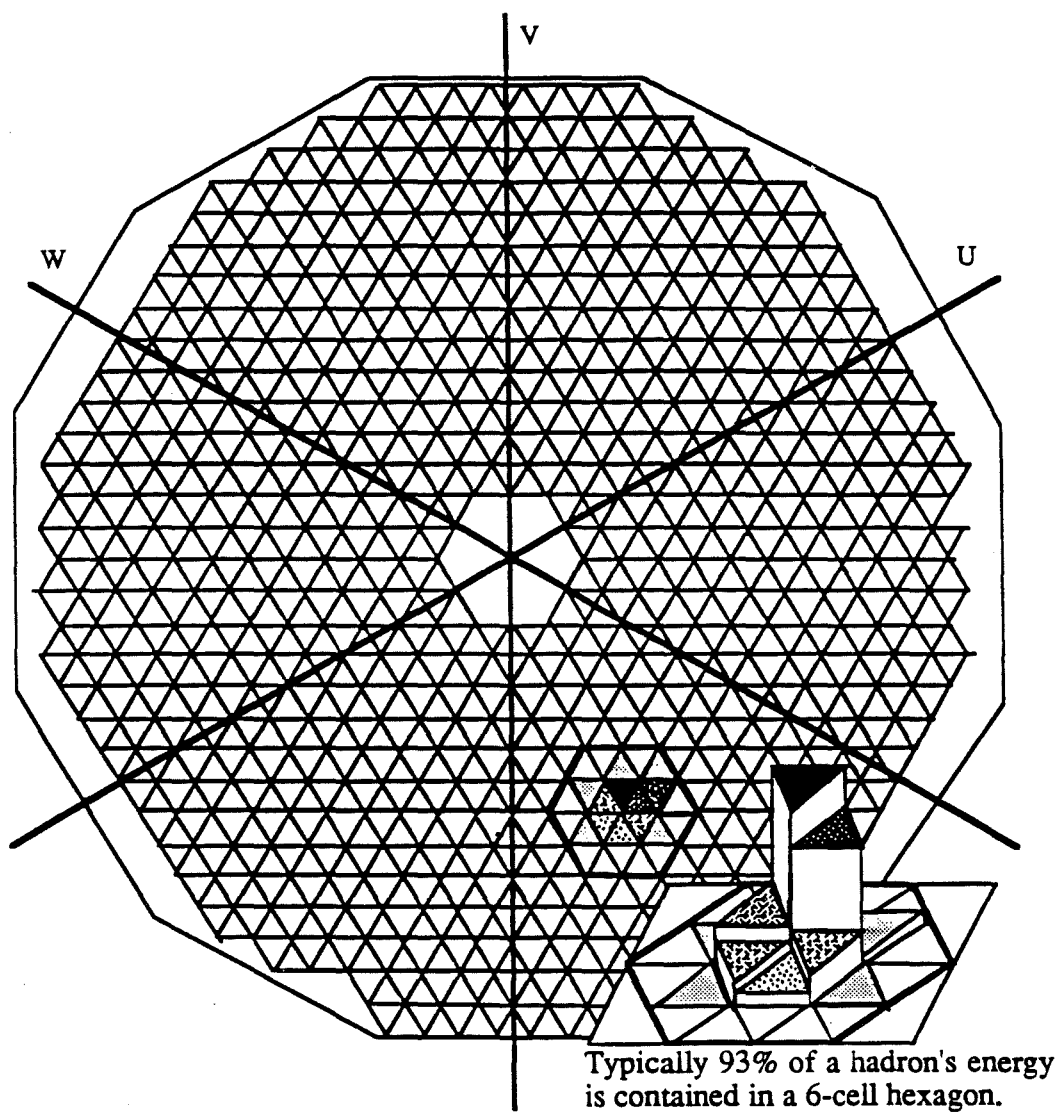


Figure 2.8 HALAC pad configuration.

For the EMLAC, $D = 0.25$ cm and the operating electric field was 10 kV/cm yielding a drift velocity of $v = 4.5 \times 10^5$ cm/s and a drift time of 550 ns. The positive ions move about three orders of magnitude slower than the electrons and for the time of relevance to E706 (0.4 - 1.5 μ s) contributed little to the signal.

If W is the average energy needed to produce an electron-ion pair in liquid argon, the total amount of electronic charge (Q_0) produced by an ionizing track is given by

$$Q_0 = e \frac{dE}{dx} \frac{D}{W} \quad (2.3)$$

where dE/dx is the energy loss per unit length due to ionization, e is the electron charge, and $W = 23.7 \pm 0.7$ eV for liquid argon,^[11] slightly smaller than the value 26.4 eV for gaseous argon. The induced current in the readout boards, assuming a uniform charge distribution for $0 \leq x \leq D$ with no electron-ion recombination and no electronegative impurities, is given by^[12]

$$I(t) = \frac{Q_0}{T} \left(1 - \frac{t}{T} \right) \quad (2.4)$$

which implies that the total collected charge is $Q = \int_0^T I(t) dt = Q_0/2$, as expected due to the low mobility of the positive ions.

A significant factor that can influence the amount of charge collected at the anodes is electronegative impurities. These will capture electrons, changing their mobility to the negligible ion mobility. Oxygen (O_2) is a potentially very dangerous contaminant for the LAC due to its high affinity for electrons and its abundance in the

[11] T. Doke, *Portugal Phys.* 12 (1981), 9, also in *Experimental Techniques in High Energy Physics*, Addison-Wesley Publishing Company 1987, T. Ferbel, ed.

[12] W. J. Willis and V. Radeka, *Nucl. Instr. Meth.* 120 (1974), 221, also in *Experimental Techniques in High Energy Physics*, Addison-Wesley Publishing Company 1987, T. Ferbel, ed.

atmosphere. The net effect of impurities is a charge loss which can be characterized by supplying a damping factor $e^{-t/\tau}$ to the current Eq. (2.4), where τ is the average time before an electron is captured. This is connected to the mean free path length λ ($\lambda = v\tau$) for the absorption of electrons by impurities (concentration p in units of molar parts-per-million or ppm) in liquid argon, where experimentally one finds^[13]

$$\lambda = \alpha \frac{E}{p}, \text{ and } \alpha \approx (0.13 \pm 0.03) \text{ cm}^2 \text{ kV}^{-1} \text{ ppm}. \quad (2.5)$$

The amount of total charge collected is then given by

$$Q = \int_0^T I(t) e^{-t/\tau} dt = Q_0 \frac{\lambda}{D} \left[1 - \frac{\lambda}{D} (1 - e^{-D/\lambda}) \right]. \quad (2.6)$$

For the limiting case where $\lambda \rightarrow \infty$ (when $E \rightarrow \infty$ or $p \rightarrow 0$) then $Q \rightarrow Q_0/2$ as expected from the case of negligible amounts of impurities.

In order to reduce the concentration of impurities to the minimum possible, the 17,000 gallons of liquid argon inside the cryostat were replaced prior to the 1990 run. The purity of the argon was monitored during the filling procedure and during the 1990 and 1991 runs. Before accepting a load of argon, a sample of argon gas was condensed into an ionization test cell. This test cell^[14] had 2.2 mm argon gaps and the ionizing particles were supplied by a 10 μC Ruthenium beta source. By plotting the amount of charge collected with respect to the voltage applied, the contamination of the argon sample by impurities was estimated by fitting Eq. (2.6) to the data. Another estimate of the argon impurity contamination was done using an oxygen

[13] J. Engler et al., *Nucl. Instr. and Meth.* 133 (1976), 521.

[14] E. Prebys and F. Lobkowicz, E706 Internal Note 163 (1988).

analyzer. If the impurity level measured from the test cell was below 0.5 ppm and that from the oxygen analyzer was below 0.3 ppm, the argon was accepted.

After the cryostat was completely filled with liquid argon, a High Voltage (HV) curve was taken using 50 GeV/c electron beam in the EMLAC. The signal integration time (BEFORE-AFTER time as described in Section 3.4) for all voltage settings was set to the maximum of 1.5 μ s. By fitting Eq. (2.6) to the data points, as shown in Fig. 2.9a, an oxygen-equivalent contamination level of 0.78 ppm was measured. Fig. 2.9b compares the shape of the 1990 HV curve to the curve taken prior to the 1991 run as well as during the 1987 run.^[15] All curves have been normalized to each other relative to their highest point. It is clear that the 1991 curve saturates faster than the corresponding 1990 curve, implying that the argon got “cleaner” with time. The 1987 curve indicates the highest oxygen contamination level among the three curves. In addition to the HV curve shape difference between the 1990 and 1991 data runs, the total charge collected was also different. It was measured that the charge collected during the 1991 HV curve was 43% more than the charge collected during the 1990 HV curve. This charge increase cannot be attributed only to a change in the oxygen level since even if the oxygen concentration from 0.78 ppm decreased to zero the charge increase, around the saturation voltage (i.e., 2.5 kV), would have been only 5% (see Eq. (2.6)).

The energy scale observed in the EMLAC shifted as a function of time. The size and rate of that shift can be monitored by plotting the measured π^0 (or η) mass reconstructed with a constant conversion between ADC counts and energy. Fig. 2.10a shows the time dependence of the reconstructed π^0 and η masses relative to

[15] A. Lanaro, π^0 Production with K^- and π^+ Beams at 530 GeV/c, Ph.D. Dissertation, University of Rochester (1989).

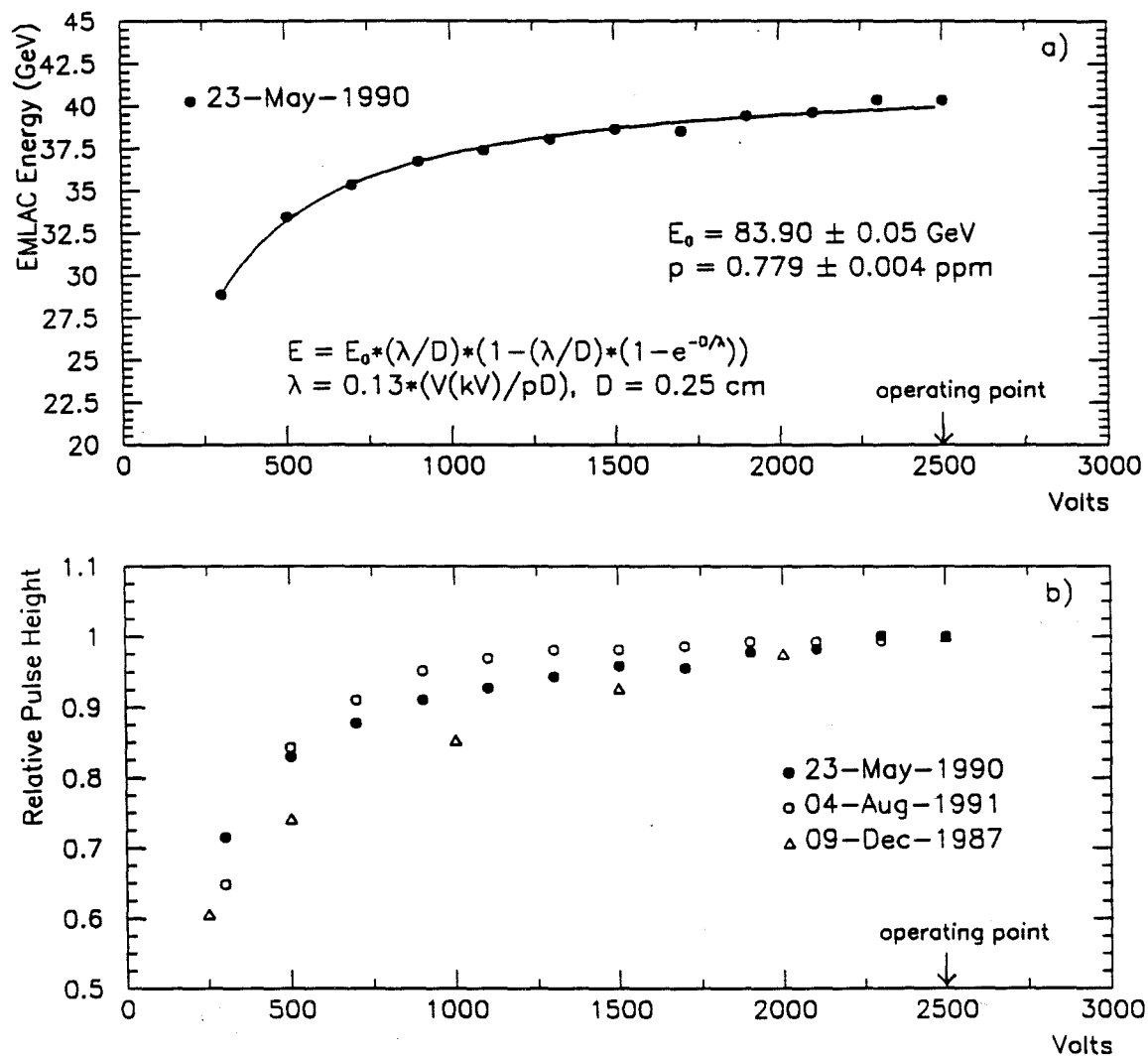


Figure 2.9 HV excitation curves taken using 50 GeV/c electrons in the EMLAC. a) HV curve taken at the beginning of the 1990 run. b) Comparison of three HV curves corresponding to the three data runs of the experiment. The vertical scale is normalized arbitrarily to the highest data point.

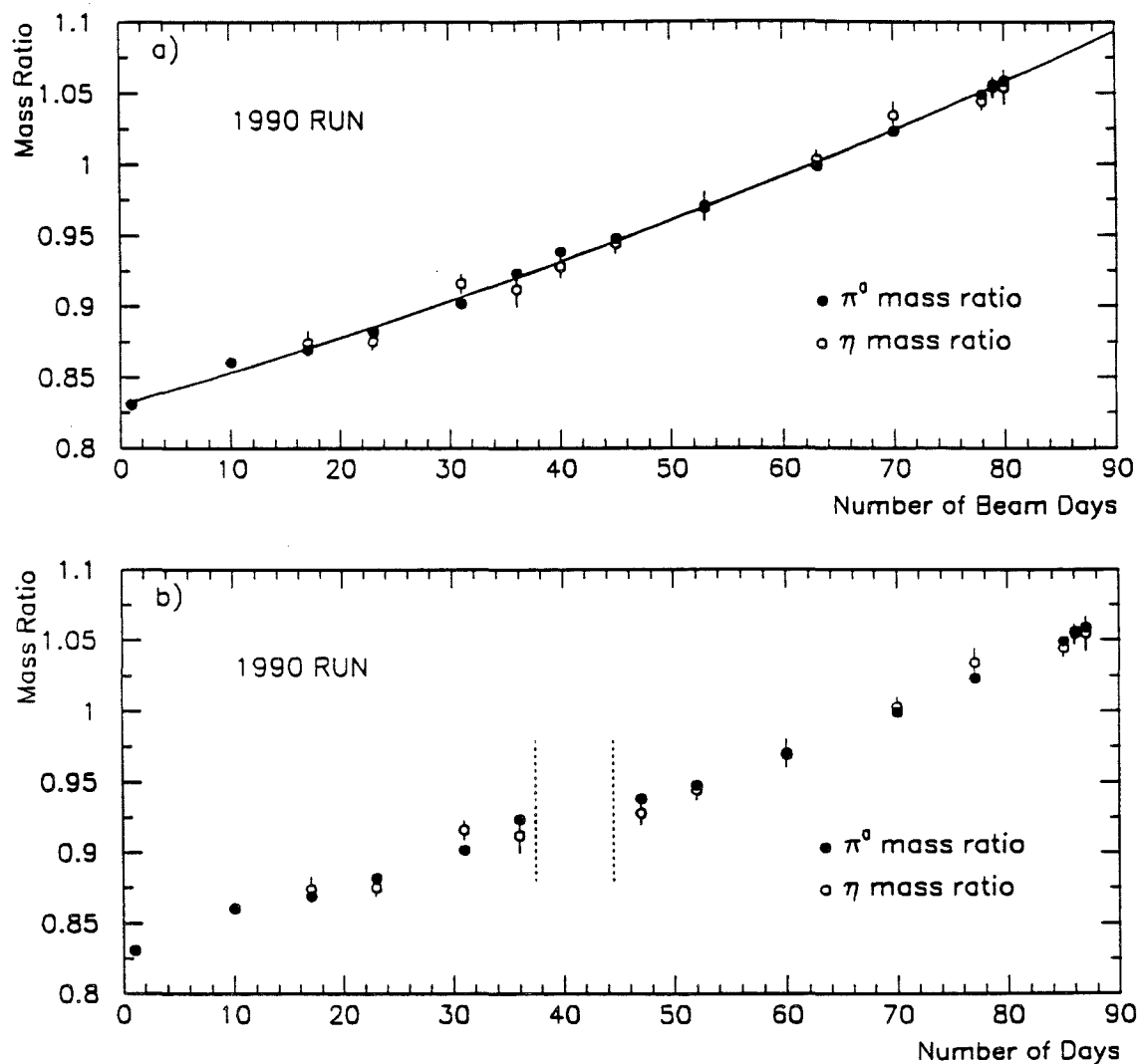


Figure 2.10 a) Reconstructed π^0 and η masses relative to their nominal values as a function of "beam days" for the 1990 run. The reference day is 31-May-1990. The curve represents a fit to the π^0 data points. b) Reconstructed π^0 and η masses relative to their nominal values as a function of "real days." The vertical lines indicate a 7-day shutdown period during the 1990 run.

their nominal values for the 1990 run. The effect is very dramatic. There was a 27% relative increase of the apparent collected charge over a period of 80 days. The number of days that go into the Fig. 2.10a corresponds to “beam days”. It was observed that the measured π^0 mass did not change during beam-off periods. This is illustrated in Fig. 2.10b, where there was a 7-day shutdown during the 1990 run where the collected charge did not increase. This beam-off time was subtracted from the fit (shown in Fig. 2.10a) that was used to correct the energy scale versus time at the reconstruction level. The HALAC showed a similar effect, as illustrated in Fig. 2.11. This plot demonstrates how the reconstructed energy (E) of hadrons with respect to their momentum (P) determined by the tracking system changed with “beam time” for the 1990 run. The size of the effect is similar to that of EMLAC as demonstrated by superimposing the fit curve which corresponds to the EMLAC data points in Fig. 2.10a.

Fig. 2.12a shows the π^0 mass relative to its nominal value as a function of “beam days” for the 1991 run. The relative π^0 mass as a function of “real days” for this run is illustrated in Fig. 2.12b. The vertical lines indicate shutdown periods longer than one day. Again during beam-off periods the energy scale remained approximately constant. From these plots it is clear that the energy scale did not increase indefinitely with time but rather leveled off toward the end of the 1991 run.

In order to illustrate the combined effect for the 1990 and 1991 runs together, we have to remove the one year beam-off period between the two data runs and count approximately “beam days”. Fig. 2.13 shows the π^0 mass relative to its nominal value as a function of “beam days” for the entire running period. The result is a

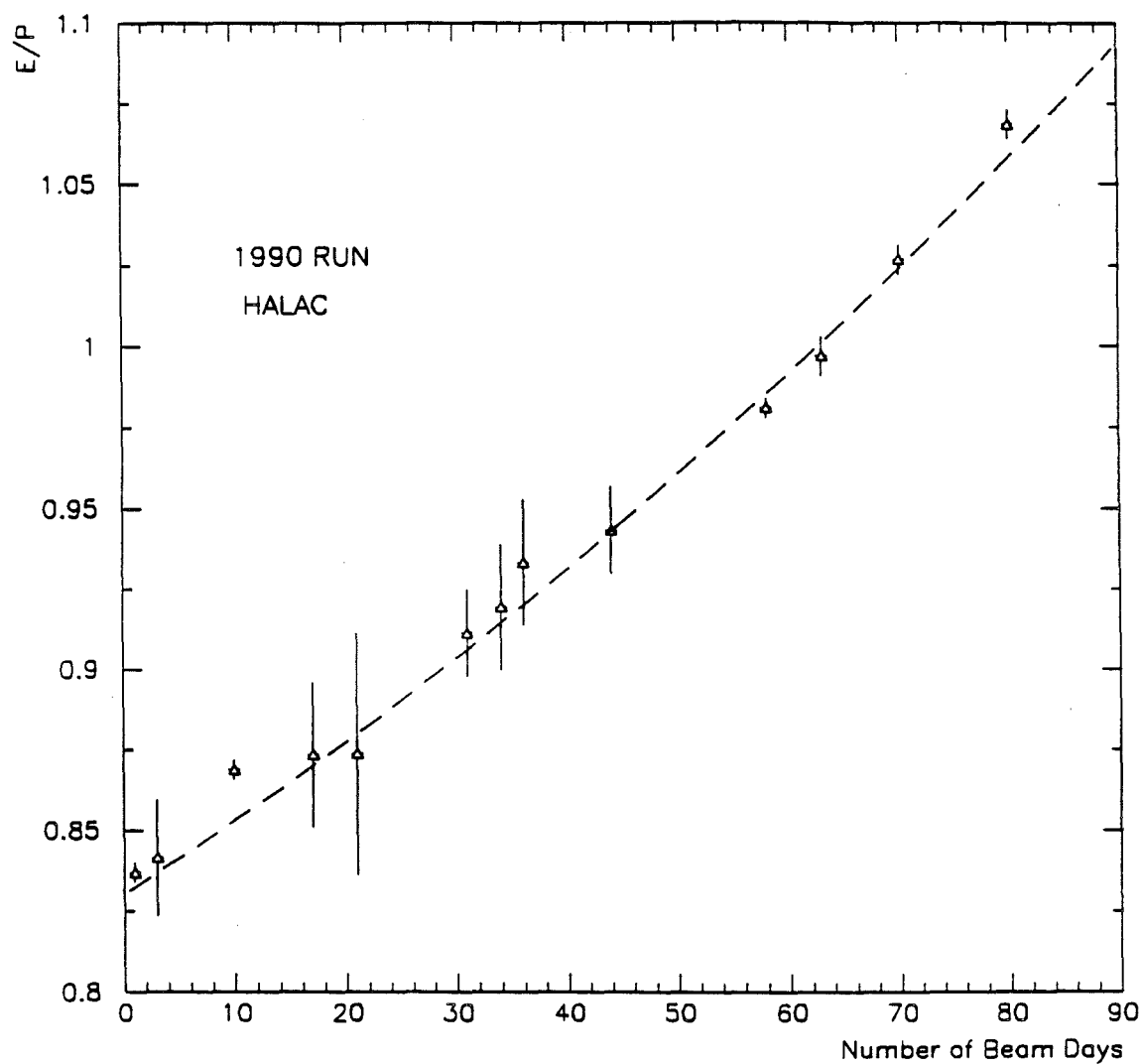


Figure 2.11 The ratio of the energy reconstructed in the HALAC over the momentum reconstructed using the tracking system for hadrons, as a function of “beam days” for the 1990 run. The dashed line represents a fit to the data points in Fig. 2.10a.

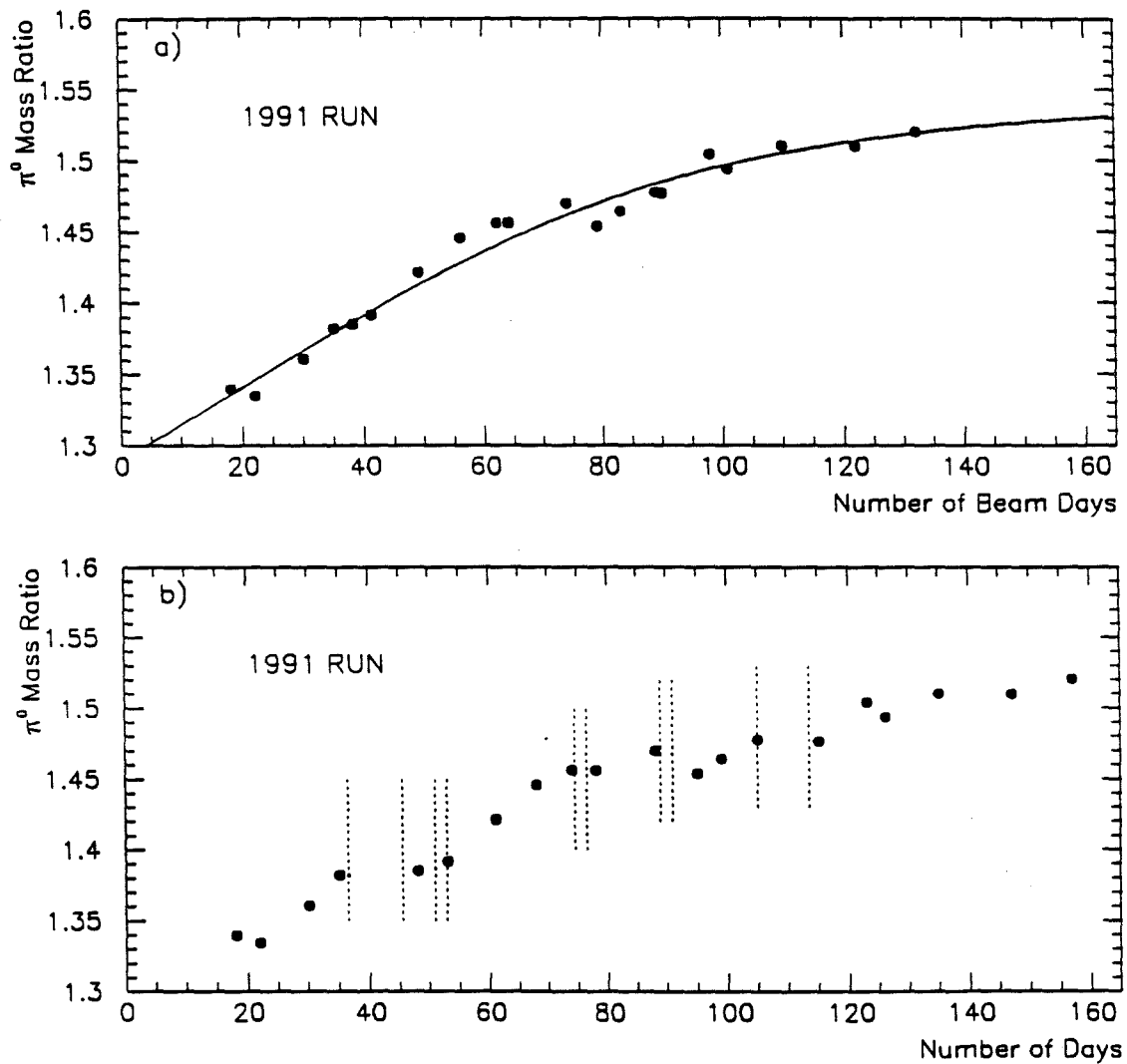


Figure 2.12 a) Reconstructed π^0 mass relative to its nominal value as a function of "beam days" for the 1991 run. The reference day is 1-Aug-1991. The curve represents a fit to the data points. b) Reconstructed π^0 mass relative to its nominal value as a function of "real days". The vertical lines indicate shutdown periods for the 1991 run.

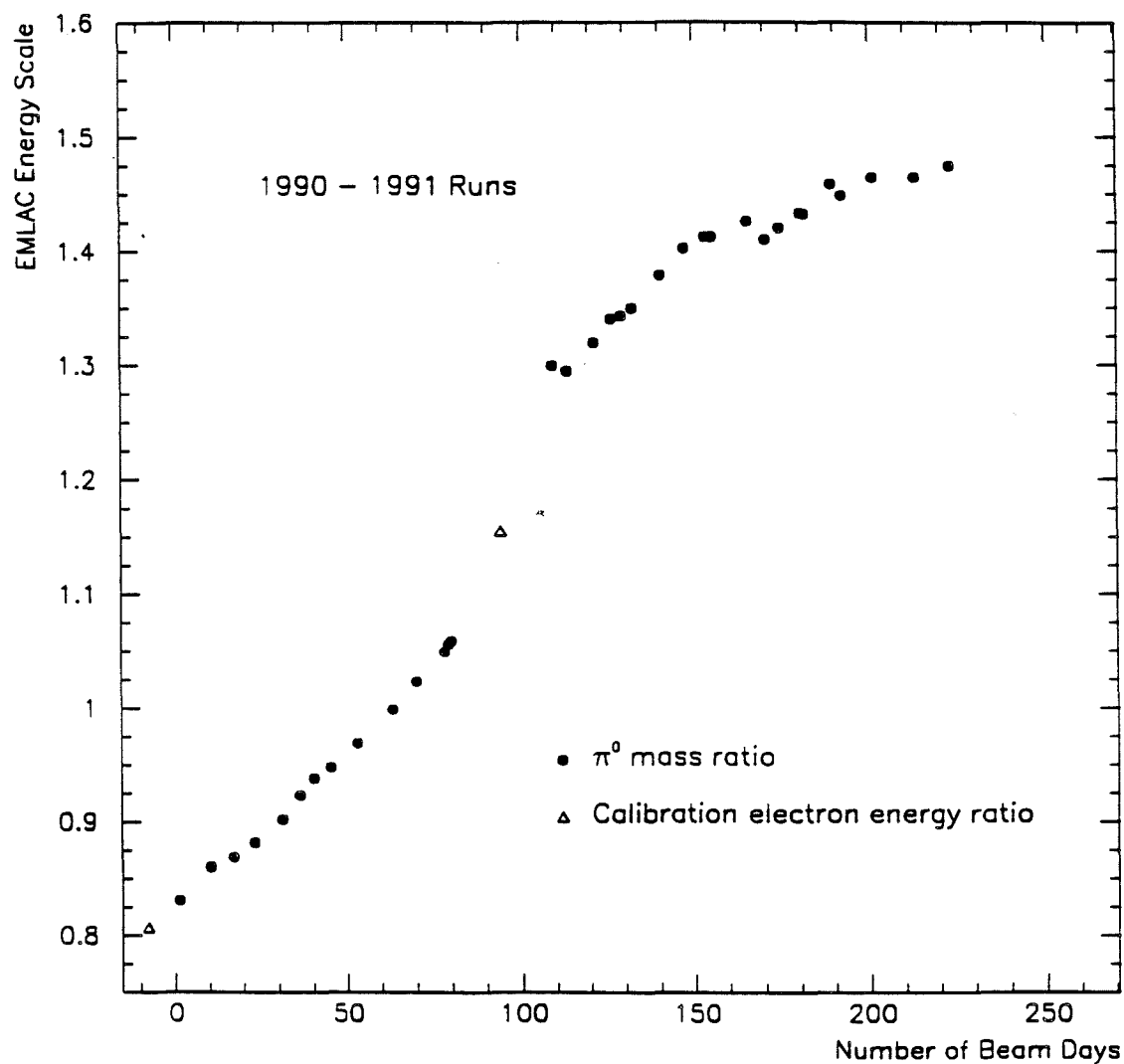


Figure 2.13 Reconstructed π^0 mass relative to its nominal value as a function of “beam days” for the 1990 and 1991 running periods (dark circles). The reference day is 31-May-1990. The open triangles represent the energy ratio detected by the EMLAC for 50 GeV/c incident electron beam data recorded prior to each running period.

reasonably smooth transition between 1990 and 1991 runs[†]. In addition, the data points that correspond to the energy ratio detected by the EMLAC for the 50 GeV/c incident electron beam used for the HV curve prior to each running period, follow the π^0 mass points very well. However, no satisfactory explanation has been found for this curious effect.

2.4 FORWARD CALORIMETER

The Forward Calorimeter (FCAL) was located approximately 15 m downstream of the target and was used to cover the forward jet region not covered by the LAC. This calorimeter measured the total energy and p_T of the forward beam jet which was composed of particles coming from the fragments of the beam spectator partons. No attempt was made to identify individual hadrons.

The FCAL,^[16] capable of operating at 10 MHz rates, was divided into three identical units of alternating layers of steel and scintillator with a 3.2 cm beam hole (Fig. 2.14). Each unit was 3.2 interaction lengths thick and consisted of 32 circular steel absorber plates, spaced 6.9 mm apart, and 32 interleaved acrylic scintillator sheets 4.8 mm thick. Each steel plate was 114 cm in diameter and 1.9 cm thick. The scintillator sheets contained 76 holes of 1.12 cm in diameter on a 11.43 cm grid, through which the 86.4 cm long wavelength-shifter bars (BBQ) were inserted.* The corresponding holes in the steel were 1.27 cm in diameter. Both ends of each wavelength-shifter bar were connected to a photomultiplier tube (except the third unit

[†] Due to changes in the reconstruction program (EMREC) that occurred between the processing of the 1990 and 1991 data sets, the 1991 data points in Fig. 2.13 are scaled down by 3% in order to be compared to the 1990 data points.

[16] R. Benson, Characteristics of Forward Energy Production in Proton-Nucleus and Pion-Nucleus Collisions at $\sqrt{S} = 31.5$ GeV, Ph.D. Dissertation, University of Minnesota (1990).

* During the 1990/91 runs only the inner 60 of the 76 holes were instrumented.

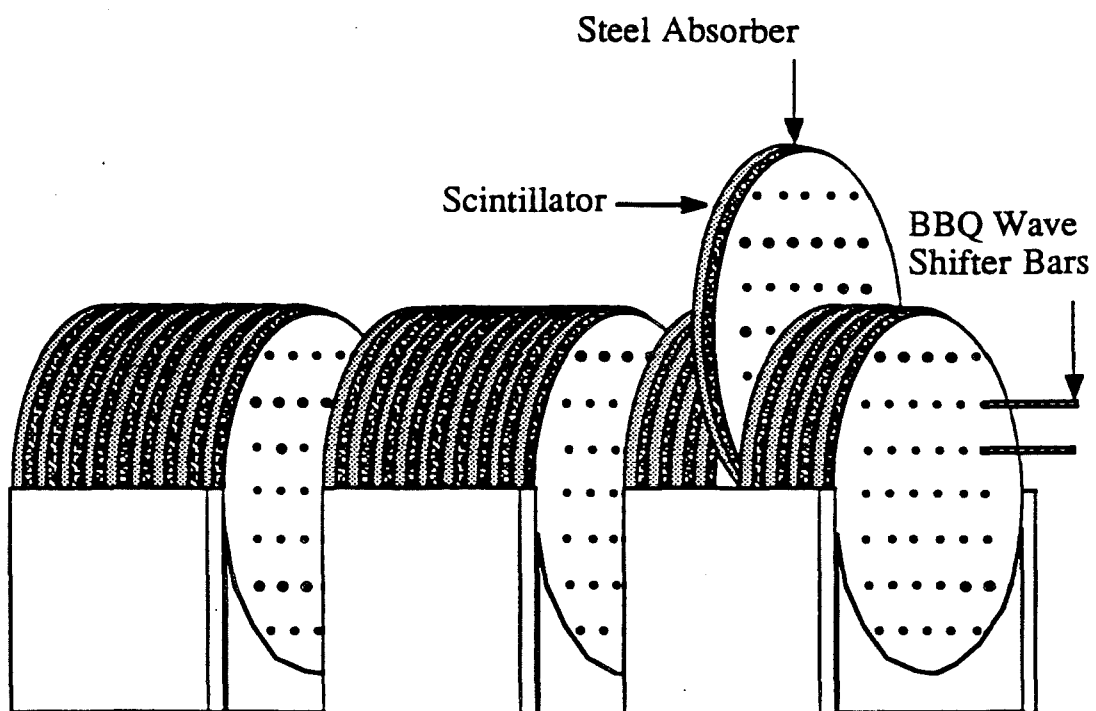


Figure 2.14 The forward calorimeter.

which had phototubes attached to the upstream end only) and read out via a flash ADC. The calorimeter was mounted on a rail system so that the FCAL could be moved transverse to the beam direction for calibration purposes.

3. DATA ACQUISITION

There were many improvements and changes made to the E706 spectrometer after the successful first data run (1987-88) in order to accomplish the physics goals of the experiment. One major improvement was the upgrade of the LAC readout system from a PDP-11 to a FASTBUS based^[1] Data Acquisition (DA) system. Since the author devoted much of his time to developing and installing the new LAC DA system, special attention will be given in this chapter to discuss the motivation, the detailed design, and the performance of the new system.

3.1 1987-88 DA OVERVIEW

A complete description of the 1987-88 LAC readout system as well as the associated electronics is given elsewhere;^[2] here I give only a brief description of that system.

The DA system used for the first data run of the experiment was controlled by a Digital Equipment Corporation (DEC) micro VAX (μ VAX) II computer. This μ VAX was responsible for collecting and concatenating the data from four DEC PDP-11 series micro-computers into events. The PDPs controlled the individual readouts from the different detector subsystems. One controlled the LAC readout. A second controlled the Cherenkov, tracking (SSDs, PWCs) and trigger system. A third, the forward calorimeter, and the fourth was responsible for the E672 readout system.

[1] IEEE Standard FASTBUS Modular High-Speed Data Acquisition and Control System, IEEE 1986, ISBN 471-84472-1.

[2] D.D. Skow, A Study of High Transverse Momentum Eta Meson Production, Ph.D. Dissertation, University of Rochester (1990).

All the PDPs except the LAC PDP^{*} read out the subsystems through serial and parallel CAMAC^[3] crates. The LAC PDP was used to control the MXs[†] which were used to control up to four RABBIT readout crates (see later section for description). During the data taking period, nine MXs were used for the LAC readout with three RABBIT crates per MX, except the MX controlling the back section of HALAC which was connected to four crates. Two additional MXs were employed to control the RABBIT trigger modules.

3.2 MOTIVATIONS FOR THE DA UPGRADE

The 1987-88 LAC DA system had some serious limitations:

1. Zero Suppression: In order to reduce the amount of data read from the LAC which increases the overall DA speed, a hardware threshold was introduced and only channels with voltages above that threshold were read out. This hardware cutoff corresponded to approximately 175 MeV of energy. The implementation of such a cutoff necessarily compromised the reconstruction of low energy showers.

2. Speed and Reliability: Due to their complexity, cost, and the limited number of spares of the MX boards, there were not enough MXs available to increase the parallelism of the readout system by connecting fewer RABBIT crates per MX. The time to read an average E706 event was around 18 ms. This long readout time limited the “live time” of the spectrometer. In addition, the monitoring of the LAC electronics under this system was inadequate.

^{*} The LAC PDP also read out the event scaler through a CAMAC Jorway.

^[3] CAMAC Instrumentation and Interface Standards, IEEE 1982, ISBN 0-471-89737.

[†] The MXs were FNAL (CDF) custom designed intelligent controllers for the RABBIT system.

The DA upgrade was designed to address the above limitations^f and consisted of a FASTBUS based replacement of the PDP-11/MX based LAC readout system.

3.3 1990-92 DA OVERVIEW

A schematic of the DA system employed during the second data run of the experiment is shown in Fig. 3.1. The top level of the system was a DEC VAXstation 3200 computer (host VAX). Below it in the chain were the three existing PDPs and the new FASTBUS system. The FASTBUS system was divided into three subsystems. One subsystem consisted of two FASTBUS crates, and read out the STRAWs, using LeCroy 1879 TDC modules. The second subsystem consisted of one FASTBUS crate (CRATE-11), and was responsible for the LAC readout via E706 custom made modules (ICBM-WOLF) which replaced the old MX system. The third subsystem consisted of one FASTBUS crate (CRATE-20) which concatenated the LAC and STRAW subevents and sent the data to the host VAX.

The VAXONLINE software package^[4] developed by FNAL was used as the master control program and ran on the host VAX. It consisted of five major processes: GLOBAL_MENU, RUN_CONTROL, EVENT_BUILDER, OUTPUT and BUFFER_MANAGER. The GLOBAL_MENU process was the user interface for the other four processes. RUN_CONTROL was the user interface to the DA system, initiating begin run tasks (program loading, calibration tasks, trigger setup, etc.). It communicated directly with the LACSERVER process which controlled and monitored the LAC readout. EVENT_BUILDER received the data from the

^f The DA upgrade also provided a means to incorporate the readout of the two Straw Tube Drift chambers.

[4] VAXONLINE System, FNAL Computer Department publication PN-252.

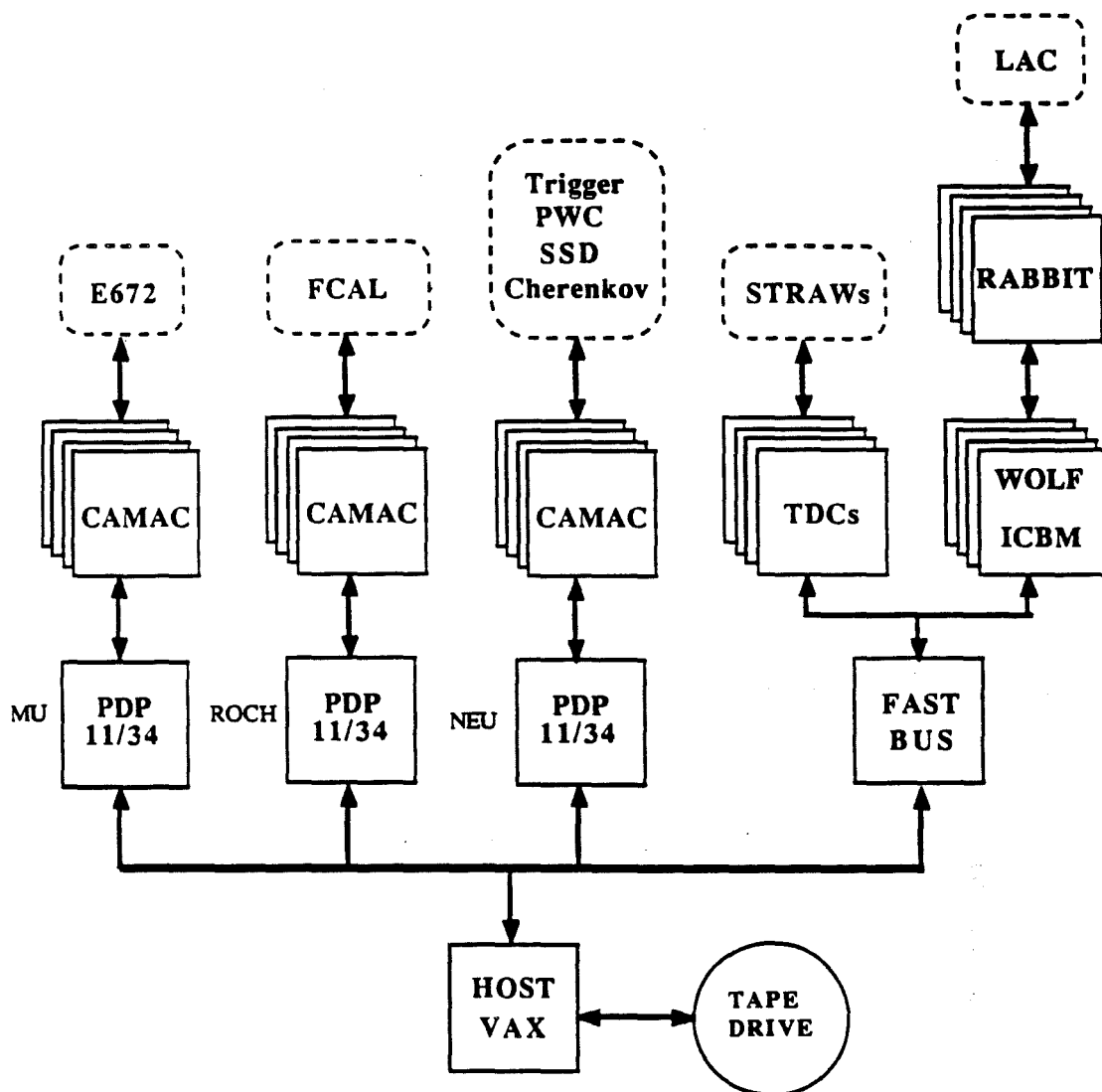


Figure 3.1 Block diagram of the data acquisition system.

subsystems, concatenated these data into individual events, and made the events available to other processes. OUTPUT handled the output of these data and wrote them to either 9 track tape or single/double 8 mm cassette, or to disk. Finally, BUFFER_MANAGER was the process responsible for sending a subset of events to different computers for on-line monitoring purposes. The on-line monitoring of the data was very important for identifying problems or malfunctions of the spectrometer at the time of failure.

3.4 DESCRIPTION OF THE HARDWARE

A schematic of the main components of the LAC FASTBUS DA system is shown in Fig. 3.2. The general structure of the FASTBUS system was designed to allow fast readout of the LAC combined with the ability to monitor the LAC electronics. This section discusses the hardware involved, providing an overview of the functionality of each of the components and how these components interacted with each other.

The RABBIT System

The RABBIT (Redundant Analog Bus Based Information Transfer) system developed by the Particle Instrumentation Group (PIG) at FNAL^[5] was the key component for reading out the signals from the LAC. It had two redundant busses, called Top and Bottom, over which analog and digital information was transported. Each RABBIT crate consisted of up to 22 charge integrating amplifiers (LACAMPs), two crate controllers/digitizers (EWes), and a special purpose module, called BAT

[5] G. Drake, *Nucl. Instr. and Meth.* A269 (1988), 68-81.

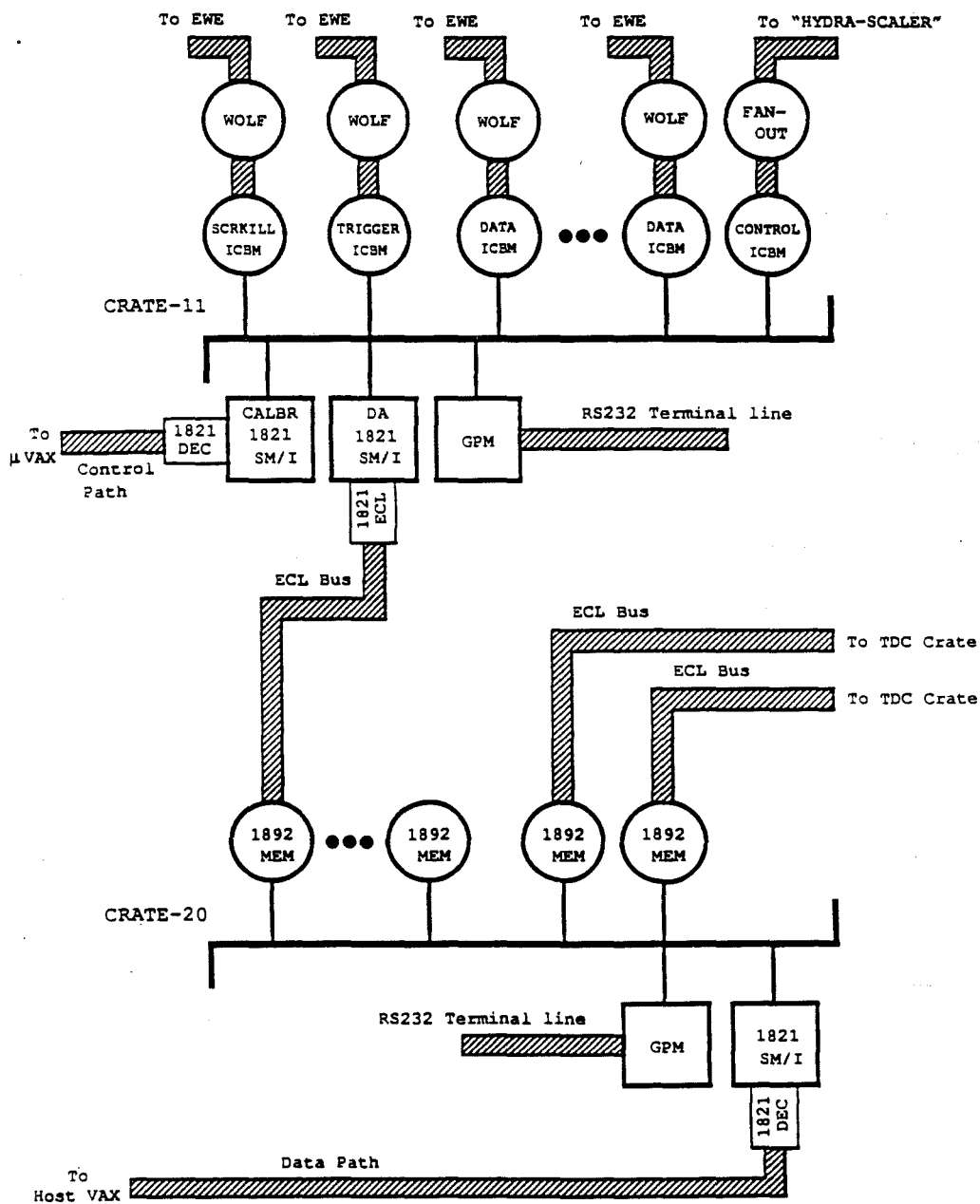


Figure 3.2 Flowchart of LAC data acquisition system.

(Before After Timer), that terminated both busses and generated the required timing signals based on information from the trigger system. The BAT also provided several crate-wide timing and voltage signals for monitoring and calibrating of the crate.

Each LACAMP board (Ref. [2]) contained 16 integrating amplifiers, 8 Time to Voltage Converters (TVCs), and fast trigger outputs. The integrated output signal of each amplifier was sent three separate routes: the fast output, the Sample and Hold circuit, and the TVC. The fast output was used in forming the trigger, while the initiating signal entered an 800 ns delay. This delay allowed enough time for the trigger decision to be made. When the trigger was satisfied, an EVENT signal was sent to the BATs, initiating the BEFORE and AFTER time sequence. In this sequence, the BATs generated two timing signals to all LACAMPs within their crate. The first, called the BEFORE signal, caused the Sample and Hold circuit to open a switch and to hold the output level on an 1 nF capacitor, sampling the voltage level before the event occurred. The AFTER signal opened a switch to a separate 1 nF capacitor, sampling the full integrated signal. The difference between the integrated signal after and before the event occurred was digitized by the EWE when the corresponding channel was selected. The value of the AFTER-BEFORE time was selected to be 790 ns for the 1990 run and 840 ns for the 1991 run. Its setting was programmable through an 8 bit DAC on the BAT. The reason behind the sampling of the amplifier output at two different times was to minimize the effects of low frequency noise as well as the effects of pile-up from signals of previous events.

The differentiated output of four adjacent amplifier channels was summed and fed into the TVC circuit. If a sum was over a crate-wide threshold set by the BAT then the MASTER TVC was triggered. If another signal occurred during the period that the MASTER TVC was busy (1.5 μ s), a second TVC (SLAVE TVC) recorded the timing information. With the arrival of the BEFORE time, the MASTER and/or

SLAVE TVC produced a voltage signal proportional to the time between the charge deposition in the LAC and the trigger.

FASTBUS Crate

The FASTBUS crate was a standard rack-mountable package with 26 slots. The cooling and power supply systems were nonintegral with the crate. The backplane consisted of two parts; the Segment and the Auxiliary Backplane (Ref. [1]). The FASTBUS segment was the digital data bus (32-bit wide) of the system, providing for the control and flow of the data. The Geographical Address Control card (GAC) was used to terminate the FASTBUS signal lines, and located in slot 25 on the rear side of the FASTBUS backplane. It also generated signals for geographical addressing. The Arbitration Timing Control card (ATC) provided the required timing signals for bus arbitration and broadcast addressing, and was located in slot 0 on the rear side of the backplane. The GAC and ATC cards were part of the Ancillary Logic of the crate segments. The Auxiliary connector was not employed for the data transfer. It was used to implement optional features, rear panel inputs, or custom I/O.

WOLF Interface Module

The WOLF board was an interface module^[6] between the ICBM (FASTBUS) and the EWE (RABBIT). It enabled communication via two separate data paths, each consisting of two cable pairs controlling up to four EWEs (2 RABBIT crates). The cables had a maximum length of 255 feet. The connection to the EWEs was electrically isolated at the Faraday room wall by an optical coupling device, used to

[6] C. R. Benson, Next Generation Digital Readout Electronics for the E706 Liquid Argon Calorimeter, M.S. Dissertation, University of Rochester (1989).

minimize noise propagation into the room and to amplify the signals due to the long cables.

The WOLF board's primary function was to execute read or write commands from the ICBM to the EWEs. It had numerous secondary functions such as error checking, proper termination of the cables, and providing interrupt signals to the ICBM based on EWE conditions. The WOLF module was housed in a FASTBUS crate as a passive card using only the power lines and had no FASTBUS logic.

CRATE-11

CRATE-11 was the FASTBUS crate connected to the VAXstation II/RC (μ VAX II) computer. It consisted of two 1821 SM/I modules (one connected to the μ VAX through an 1821/DEC card and the other to the 1892 memory modules through an 1821/ECL card), one GPM and 17 ICBMs. Of the 17 ICBMs, 14 were used for the LAC readout (two RABBIT crates per ICBM), one was responsible for the trigger system^{*}, another for the SCRKILL RABBIT crate[◇], and one used as a control ICBM.

Intelligent Control & Buffer Module (ICBM)

The ICBM was a FASTBUS slave module^[7] developed specifically for E706 and designed around the Motorola DSP 56001 Digital Signal Processor.^[8] This processor

* This ICBM was responsible for initializing the trigger RABBIT modules, setting up the channel trigger weights and various discriminator thresholds. It also monitored various aspects of the trigger system.

◇ The SCRKILL signal detected a 4 KHz spike due to coherent noise on the LAC electronics generated from the 400 Hz power supplies used in the RABBIT crates. For the 1990 run this spike was detected, and a veto was produced, by using a LACAMP as an "antenna". For most of the 1991 run, a separate device was built to detect the signal.

[7] C. Lirakis, E706 Data Acquisition System, in Proceedings of the First Annual Conference on Electronics for Future Colliders, edited by George Blamar, LeCroy Corporation (1991), 37-50.

[8] DSP56000/DSP56001 Digital Signal Processor User's Manual, available as DSP56000UM/AD from Motorola Literature Distribution, P.O. Box 20912, Phoenix, Arizona 85036.

operated at ≈ 10 MIPS[‡], and it was programmable in Assembler and C. The ICBM had a total of 192K×24-bits of random access memory which was accessible both to the DSP and via the FASTBUS segment. Some of the memory addresses were mapped to an internal register space to communicate with the WOLF interface module and miscellaneous logic signals via the FASTBUS auxiliary connector. The onboard memory was divided into three data memory spaces: “P” for program memory, and “X” and “Y” memories for storage of various configuration lists and data[†].

In order to save access time the first 512 memory locations in the “P” memory and the first 256 locations in the “X” and “Y” memories were mapped to the internal memory address space. The remaining memory locations corresponded to the external memory space. Using a 20 MHz external crystal oscillator one internal instruction cycle was approximately 100 ns. The access time to the external memory was adjustable from a minimum of 45 ns to a maximum of 800 ns. The ICBM incorporated an onboard buffer management, allowing up to 4 buffers of arbitrary length and location to be defined within the onboard memory.

In addition to the onboard memory, there were three FASTBUS Control Status Registers (CSRs) which provided all the FASTBUS controls to the module. These CSR registers were:

- CSR0: This register handled most of the FASTBUS controls, such as starting and stopping the DSP processor, and issuing a master reset of the module. In addition to the predefined CSR0 bits, there were also 8 user bits defined according to our DA needs. The state of one of the bits (DONE) corresponded to a logic signal output to the front panel of the module, and another (START

[‡] 1MIP = 1 Million Instructions per Second.

[†] The ICBMs used by E706 had only the lower 32K×24-bits of each memory populated.

SCAN) had the ability to be set by a signal to the FASTBUS auxiliary connector. The other bits were used to specify which of the buffers were to be filled (2 bits) and which buffers were full (4 bits). All FASTBUS writes to CSR0 caused an interrupt to the DSP.

- CSR1: This was a user defined register, used for diagnostics and error handling.
- CSR7: Unlike the other two CSR registers, CSR7 was not accessible to the DSP. The state of this register determined the different classes of case-2 broadcasts to which the module could respond in accordance with the FASTBUS standards.

Struck General Purpose Master (GPM)

The GPM was a high performance general purpose FASTBUS master/slave module^[9] driven by a 68000 - family microprocessor. It operated like a computer with its own operating system. The operating system was required to boot and initialize the GPM and to provide I/O drivers and a set of debugging aids. The pSOS^[10] operating system was used in our GPMs. Access to the GPM was via FASTBUS, or via an RS232 serial line interface. The software for the GPM was written in C language, but some of the low level FASTBUS routines were optimized in Assembler. The programs were loaded through the terminal line. When a frozen version of the programs was available, it was deposited in EPROMs (like the system software) to reduce the download overhead. The GPM had a 32K×32-bit data

[9] GPM Manual, STR500, Dr. B. Struck.

[10] pSOS-68K User's Manual, available as PK68K-MAN V4.1 from Software Components Group Inc., Santa Clara, California.

memory accessible by both FASTBUS and the 68000. It also provided two interrupt and two “live” front panel inputs, and one pulse and one level output.

LeCroy 1821 SM/I

The 1821 SM/I (Segment Manager/Interface) was a programmable FASTBUS module^[11] intended to be used primarily as a crate segment master. It was the fastest FASTBUS segment master available, supporting fast data transfers and intelligent pre-processing, regardless of the slaves used. It provided two sections, the SEQUENCER (where the programs were executed) and the INTERFACE. The SEQUENCER operated under the control of its microcode, executing one instruction every 33 ns. It was programmable in a MICROTEC 2900 Meta Assembler language^[12] or directly in a bit map representation of an 1821 instruction. The decision was made by the author to use the latter approach in programming the 1821 because it was more direct and faster. The SEQUENCER’s instruction word was 64-bit wide and had multiple fields, typically allowing five operations to be performed at once. The SEQUENCER did not allow arithmetic operations on the data. The INTERFACE offered a 8K×10-bit pedestal memory (not used in our system) and a 4K×32-bit data memory.

The 1821 offered 8 Menu Memories. The Menu Memories were 8 optional memory sockets used to locally store SEQUENCER programs, in EPROM, or RAM 2K×8-bit memory chips. The loading of any one of these memories into the SEQUENCER was controlled by the host computer. All our DA 1821 microcodes were stored in EPROM menu memories to minimize download time. Each 1821 had

[11] 1821 SM/I Manual, LeCroy Corporation.

[12] LeCroy 1821 Microcode Tools, FNAL Computer Department publication IN-128.

a LeCroy microcode in Menu Memory 0, which provided subroutines for general FASTBUS operations.

At the front panel, the 1821 provided three differential ECL inputs and outputs under microcode control. Several 1821s could be chained together with at least one 1821 in the chain connected through the auxiliary port to the MDB DRV-11W using the 1821/DEC interface card. Other 1821s might be chained to this primary, either through connections to their front panel or, with a slight modification of the standard 1821/DEC card, through a private 1821/DEC connected to their auxiliary port.

1821/DEC Personality Card

The 1821/DEC was an interface^[13] between a LeCroy 1821 SM/I and the MDB DRV-11W. It was plugged into the auxiliary connector of the FASTBUS crate segment on which the 1821 resided (left hand positioned connector on the 1821 viewed from the front panel). The 1821/DEC could be operated in either burst-request or cycle-stealing modes (depending on the position of jumper P4 on the card). In cycle-stealing mode (used in our system), the MDB DRV-11W shared the Q-Bus[□] with the CPU on alternate cycles. In the burst-request mode, the bus was held for at least two cycles (depending on a switch in the MDB DRV-11W) before letting the CPU back on. Even though the latter was the faster mode, we were not able to use it since it caused problems (VAX crashes during DMAs).

[13] 1821/DEC Manual, LeCroy Corporation.

□ Q-Bus is an open architecture bus standard for DEC VAX computers.

1821/ECL Personality Card

The 1821/ECL^[14] connected the 1821 SM/I into the ECL bus as a data source. It also provided the required connection to the 16-bit bus for setup and control. Connection to ECL bus provided a high speed connection directly to the 32-bit high speed output of the 1821, connecting directly to the output of the SEQUENCER. In our system, we used LeCroy 1892 memory modules which provided a 32-bit ECL port that could receive data from the ECL bus output of the 1821/ECL. The 1821/ECL was plugged into the auxiliary connector at the exact same place as the 1821/DEC card.

MDB DRV-11W Interface

The MDB DRV-11W* direct memory interface module was plugged into the Q-Bus of the host computer, which was a VAXstation 3200 for one FASTBUS crate and a VAXstation II/RC for the other, and it was connected directly to the 1821/DEC card. The cable that connected the MDB DRV-11W with the 1821/DEC card was 50 feet long and had to be shielded in order for the connection to work properly at maximum speed. All of the intelligence involved in handling transfers was located in the MDB DRV-11W interface. Two basic modes were possible. One was program controlled transfers and the other was DMA (Direct Memory Access).

CRATE-20

CRATE-20 was the FASTBUS crate connected to the host VAX. It held six LeCroy 1892 memory modules. Four of the six modules were used to store the LAC

[14] 1821/ECL Manual, LeCroy Corporation.

* The DEC DRV11-W interface was found not to work with a Q-bus connection. This was because the 1821/DEC relied on the GO strobe to initiate its operations, and the DEC DRV11-W did not provide this strobe. However, the MDB Systems DRV11-W interface did work.

data and the other two buffered the data from the STRAW TDCs[◇]. CRATE-20 had one 1821 SM/I and one GPM.

LeCroy 1892 Multiple Record Buffer Module

The 1892 was an intelligent dual-port memory FASTBUS slave module.^[15] It could receive data via a front panel 32-bit ECL port at the same time that data were being read out via FASTBUS. The module could be used as a fast first-in first-out (FIFO) memory in a linear or circular mode for 16 or 32-bit data input. Our 1892 modules had a four megabyte data memory and were daisy-chain connected to look like one long linear buffer. In order to daisy-chain more than two 1892s, a special fanout board was developed for the data and control lines. This board was housed in the same FASTBUS crate as the 1892s, using only the power lines of the crate. The data and control cables connecting the 1821/ECL card of CRATE-11 to the 1892s were 100 feet long and shielded.

3.5 LAC CALIBRATION AND BETWEEN SPILL TASKS

As mentioned previously, during the fixed target mode of accelerator operation, beam was delivered to the experimental areas periodically in specific time periods, called *spills*. For the 1990 run, the spill gate was set to be 23 sec while the *between spill* period was 35 sec. Data collection was segmented into periods, called *runs*, where the experimental conditions could be expected to be reasonably constant. The start and end of a run was controlled by RUN_CONTROL. The operator could select

◇ The readout of the STRAW-TDCs was done via an 1821 SM/I module and the data were transferred to the 1892s through an ECL bus connection. The data and control cables connecting the 1821/ECL card of the TDC FASTBUS crate to the 1892s were shielded and 260 feet long.

[15] 1892 Manual, LeCroy Corporation.

options within RUN_CONTROL to initiate different begin run tasks for the separate subsystems.

Every few runs (around 8 hours) a LAC *cold start* was initiated prior to the start of a run. It included a reset of the LAC FASTBUS system, and recorded to an archival database information about the status of the LAC electronics (e.g., pedestal and gain values of the LACAMPs, temperature and voltage measurements of each crate, and inventory of RABBIT cards). When it was necessary (when the ICBM memories were corrupted or a newer version of the LAC readout program was available), a reload of the ICBM memories with a fresh copy of the LAC readout programs and/or various parameter lists was performed. The results of this download were checked against a copy of the programs or the corresponding lists kept on the VAX to insure accurate transmission, and the programs and lists were written to the database for further reference.

The process responsible for the control of the LAC readout as well as for the calibration and between spills monitoring tasks was LACSERVER. The following sections describe the operations of LACSERVER and the various LAC tasks in more detail.

LAC-ICBM Tasks

The ICBM readout program performed seven separate tasks[†] and each was selected according to a flag set to the CSR1 register, by either the LACSERVER process or the GPM module. All tasks were performed in parallel in all ICBMs. Some of the tasks (LACAMP readout, PROMs readout, PATH check) were initiated in each ICBM separately and others (BATs, Pedestals, ADC, and TVC Gains readout)

[†] There was also another special task performed during beam-off periods that measured the gain values for the trigger p_T system. The results from this task were used in the trigger analysis.

were controlled by the control ICBM. Each ICBM produced a front panel logic signal output (DONE) to notify the rest of the system that its selected task was completed. The logical AND of these ICBM DONE signals was used as the task completion signal[◇]. For the tasks controlled by the control ICBM, the task completion signal was produced by the control ICBM. The ICBM tasks were the following:

1. BATs Readout: During this task, the ICBMs read out the BAT module from each RABBIT crate. This included the readout of various important timing signals (like the BEFORE and AFTER times), all crate voltages, and a temperature measurement for each crate. Variations from the expected values were monitored and when any significant changes occurred, these were frequently correlated with problems found with the crate power supplies or the BAT modules.

2. PROMs Readout: This task was an inventory of all RABBIT modules including the trigger system. Each RABBIT card had an identifying number which was written in a PROM and also attached to the front of the module. Reading out this information gave us the ability to easily record hardware changes that happened in the system. It also provided a cross check on the integrity of some aspects of the path from the FASTBUS to the LACAMPs by monitoring any changes to the PROM values during data taking.

3. Pedestals Readout: The pedestal is the integrated noise detected by an amplifier channel -- it is the output of a channel when no particles deposit energy in the detector. For that reason, the pedestal task was performed during between spill periods. In this task, the control ICBM sent the EVENT signal to the BATs in order

◇ Due to problems we had with spurious DONEs caused by signal "glitches", when the ICBMs set or reset the DONE signal, a more complicated NIM logic was implemented to define the task completion signal, as shown in Appendix A.

to initiate the BEFORE-AFTER time sequence. It then started the pedestal readout program on the ICBMs by issuing a signal to the FASTBUS auxiliary card in order to set the START SCAN bit of CSR0. When all ICBMs were done reading out the LACAMPs a “global DONE” signal was issued back to the control ICBM which then sent a signal to reset the BATs. The control ICBM waited for an SCRKILL spike to occur, and after a vetoing time, it issued another EVENT signal. The above process was repeated up to 128 times in order to reduce the statistical uncertainties in the measurement of the mean pedestals. The resulting pedestal means and RMSs were stored in a database for use in the reconstruction programs. Monitoring the pedestal means and RMSs during data taking helped us to identify noisy and “dead” channels as well as EWE problems.

4. ADC Gains Readout: This task measured the gain of each amplifier channel, and was performed during between spill periods. A known charge pulse was generated and fanned out by the BAT on each channel. The resulting average of 8 readings for 6 different input pulses for each channel was stored in the ICBMs. When the task was done, the data were read from LACSERVER and transferred to UPDATE (see following section) where a linear fit was made to the data points, and the gain value was calculated and stored in the database. The raw data used to calculate the gain for each channel were also stored for further study and subsequent corrections to the gain measurements.

5. TVC Gains Readout: This task measured the timing response of each TVC channel, and was also performed during between spill periods. For this task, the BAT produced two pulses with programmable separation, one for each TVC circuit (MASTER/SLAVE). The position of the BEFORE time relative to these pulses was then varied. An average of 8 readings was taken for each of 6 different time values.

Again a linear fit was done inside UPDATE, and the results of the fit as well as the raw data were stored to the database.

6. LACAMP Readout: The LACAMP readout task was the most crucial ICBM task. It performed the actual readout of the LAC. The readout was performed in parallel for both the TOP and BOTTOM busses. Each ICBM first set up the EWEs under its control to begin a digitization sequence on one channel (i.e., two channels per crate). After checking the status of the EWEs, the ICBM performed the readout. Then the EWEs were directed to start the digitization of the signal from the next channel. When all ADC channels corresponding to that ICBM were read out, the ICBM began the readout of the TVC channels. A TVC channel was read out only when the sum of its corresponding four ADC channels were above a software threshold. The sum of the four ADC channels was calculated after subtracting the pedestal value for each channel. The pedestal values were kept inside the ICBM memory and corresponded to the previous calibration pedestal set. These pedestal values were updated every time that a pedestal calibration task was performed.

7. PATH Check: This task was done to monitor the entire path from the ICBMs to the EWEs. This check included the ICBM, the WOLF, all data cables, the optical couplers, and the EWE. Each ICBM wrote a set of words to all EWE registers testing all available data bits. Then a comparison was made inside the ICBMs, and if the reading values were different from the reference values, an error bit was set (CSR1) and the necessary information (i.e., crate, bus, EWE register that failed) was written to specific memory locations. The status of this error bit was checked by the LACSERVER, and if found to be set, LACSERVER notified the operator.

LACSERVER

The LACSERVER ran on the μ VAX computer connected to the CRATE-11 FASTBUS system. It was the heart of the LAC DA system. It had the ability to communicate directly with CRATE-11 and other DA related processes, like RUN_CONTROL, various monitors, and a process called UPDATE. UPDATE was also run on the same μ VAX as LACSERVER. UPDATE was responsible for sending the ICBM programs and lists to LACSERVER^f, and storing that information as well as the calibration data received from LACSERVER in the archived database. The communication between processes running on separate computers (e.g., LACSERVER and RUN_CONTROL) was done through the Status Manager database^[16] software developed by FNAL. This software provided a method of storing status information and data relevant to the different parts of the experiment (e.g., run number, logging status, etc.), and provided access to these data from all processes on all DECnet nodes.

The connection between the LACSERVER and CRATE-11 was through the VAX -- MDB DRV-11W -- 1821/DEC -- 1821 SM/I hardware path (see Section 3.4). The 1821 SM/I module connected to the μ VAX will be referred as CALiBRation 1821 (CALBR-1821) to distinguish it from the DA-1821 which performed the data readout. The FLPACK software package,^[17] also developed by FNAL, provided to LACSERVER the low level FASTBUS routines to communicate with the 1821 modules. These low level access routines, written in FORTRAN, required several I/O requests to the 1821 device driver for a given FASTBUS operation, and hence were

^f The handshake between UPDATE and LACSERVER was done through VAX event flags, whereas the data transfer employed a mailbox connection.

[16] Guide to Status Manager Database and Routines, FNAL Computer Department publication PN-304.

[17] Low Level Routines for the LeCroy 1821, FNAL Computer Department publication FBN-039.

relatively slow for ICBM memory loading or data readout. For that purpose some of the time consuming FASTBUS operations were written in list environment format by using the FLMENU software package.^[18] The FLMENU was a menu driven interactive program used to generate lists of 1821 operations. These lists could then be executed immediately, and/or saved on a disk file and read in for later execution or list editing. There was also an input interface to FLMENU for reading out ASCII text files containing list element definitions. The environment lists were loaded and executed (using FLPACK routines) inside the μ VAX 1821 device driver, allowing the user to perform a list of 1821 and FASTBUS operations through a single I/O request^{*}. A very useful diagnostic tool,^[19] which provided an interpretive environment for the user to perform 1821 operations and to test functions of the 1821, was developed by FNAL, based on the FLPACK routines. This tool aided in debugging and testing the integrity of our FASTBUS crates and modules.

The CALBR-1821 executed microcode which handled all the FASTBUS operations initiated from the μ VAX, the front panel communications with the other FASTBUS modules in the crate, and part of the trigger busy logic. Appendix A shows a block diagram of the CRATE-11 signals and the associated FASTBUS trigger busy logic.

In order to synchronize the FASTBUS with the PDPs and to insure that the data taking process started at the beginning and not during the spill, LACSERVER was the first DA process receiving the *begin run* signal from RUN_CONTROL. Then LACSERVER initiated the calibration tasks that the operator had selected within

[18] Interactive List Generation Program FLMENU, FNAL Computer Department publication FBN-047.

* The time required for the system to issue an I/O request was on the order of 2 to 4 ms, whereas the overhead per list element was around 160 to 360 μ s, depending on the actual operation being performed.

[19] LeCroy 1821 SM/I Diagnostic Tool (LDT), FNAL Computer Department publication FBN-041.

RUN_CONTROL. Some of the calibration tasks were done asynchronously with the spill gate (ICBM memory loading, BATs and PROMs readout) and some others were done only during between spill periods (pedestals, ADC and TVC gains readout). After the completion of the asynchronous calibration tasks, LACSERVER acknowledged a *global begin run* signal back to RUN_CONTROL, which then initiated the DA process on each PDP. Then the pedestal task was performed at the first between spill period, since a pedestal set was required for the TVC readout during the data taking mode. During the time that LACSERVER was performing the cold start tasks, and until the completion of the pedestal task, a trigger busy was asserted by CRATE-11. After the run started, LACSERVER performed the remaining calibration tasks (ADC and TVC gains) between spills. When all tasks were done the data were sent to UPDATE for further analysis and storage.

The loading of the ICBM memories[‡], performed much less often than the other tasks, was the most time consuming calibration task since the LACSERVER performed the actual loading and verified that the programs were transmitted correctly. In this task LACSERVER also initialized the GPM and loaded into its data memory the slot addresses and data buffer locations of the control and data taking ICBMs. This was necessary in order for the GPM to keep track of which ICBM buffer was read at any time. Thus, if we had to remove an ICBM from the system it was very easy to do so. It required a modification to the ICBM loading list which was included in a control file that was read by LACSERVER. After this loading was completed and verified, the GPM program was started.

The on-line monitoring of the RABBIT electronics was orchestrated by the LACSERVER. The spill gate was connected to one of the inputs of CRATE-11

[‡] There were 4 different ICBM programs. One for the control ICBM, another for the data taking ICBMs, a third for the trigger ICBM and a fourth for the SCRKILL ICBM.

GPM. In data taking mode, the GPM performed the spill synchronization. When the spill was complete, and all ICBM buffers were read out (see next section), the GPM sent a front panel signal to the CALBR-1821. This signal triggered the microcode on the CALBR-1821, which then notified the LACSERVER, by writing a specific word to a register in the 1821 (PDREG) that was readable by the VAX, that the spill was complete. Then LACSERVER started the corresponding between spill task^f. LACSERVER rotated between the five different between spill tasks. The data collected by these between spill tasks were compared against the latest calibration data, and various checks were made to monitor the status of the LAC electronics. This monitoring system helped us detect potential problems in the system within 6 spills of the time of the failure. Most of the ICBM between spill tasks required a few seconds to complete with the exception of the ADC gains task, which normally required 15 seconds. Then LACSERVER had to read the data from the ICBMs and that process required of the order of 14 seconds. Even though there was enough time to complete a given task between spills, a busy signal was asserted and a maximum time was allowed for a given task to complete. After the data were read by the LACSERVER, a front panel signal was issued from the CALBR-1821 to notify the GPM that the task was done and the system was clear to accept a trigger. Then LACSERVER started analyzing the between spill data.

When an *end run* signal was issued from RUN_CONTROL, LACSERVER acknowledged a *global end run* when the first end of spill was detected. Then RUN_CONTROL ended the DA process on each PDP.

^f There were 5 between spill monitoring tasks: Pedestals, ADC gains, BATs, PROMs, and PATH check.

3.6 THE LAC EVENT READOUT PROCESS

The readout of a LAC event was a two step process that occurred in parallel. The first step, done in CRATE-11, was the LACAMP readout and local event buffering, and the second, done in CRATE-20, was the concatenation of the LAC and STRAW subevents, and then data transfer to the host VAX. The next two sections describe these two tasks in detail.

LACAMP Readout

When an interesting event was detected, a trigger was generated (see Section 3.8), and the charge deposited in the LAC was latched by the LACAMPs. The readout of the LACAMPs was controlled by the GPM in CRATE-11. The trigger for the experiment was fanned out to all DA computers (PDPs, LAC and STRAW FASTBUS systems). For the LAC system, the trigger was received as an interrupt sent to the GPM of CRATE-11. When the spill gate opened, the GPM started waiting for a trigger signal. When a trigger arrived, a busy was generated and the GPM performed two FASTBUS broadcast operations to all 15 data taking ICBMs (14 ICBMs responsible for the LAC readout and one control ICBM). The first broadcast, done to CSR1, specified the LACAMP readout task and wrote a diagnostic word which was the same for all ICBMs and incremented by one for every trigger, to be used as an event continuity check. The second broadcast, done to CSR0, specified which ICBM buffer to fill and started the task on all ICBMs by setting the START SCAN bit. Since each LAC readout ICBM was connected to two RABBIT crates, and there were approximately 20 LACAMPs per crate, a total of 640 ADC and some TVC channels had to be readout and locally stored from each ICBM. In order to

decrease the “dead time”, and therefore improve the data taking rate, each ICBM had the ability to buffer up to 4 events.

In data taking mode, the control ICBM was used as an event scaler. The signals from the master event scaler of the experiment, called the “Hydra-Scaler”, were fanned out to all DA subsystems. These signals were latched by the control ICBM and information, including run and event number and absolute time of the trigger, were stored in the corresponding ICBM buffer. When all 15 ICBMs were done, a “global done” signal was generated, causing an interrupt to the GPM, which then sent a signal to reset the LAC trigger busy and start the ICBM readout process. At this point the DA system was ready to accept another trigger.

The readout of the ICBMs, and the data transfer to the 1892 memories of CRATE-20, was done by the DA-1821 which was executing the DA microcode. The GPM looped over the ICBMs to be read out. Then, for a given ICBM the GPM wrote the ICBM slot and the starting buffer address to specific locations of its data memory, and issued a front panel signal to the DA-1821 to perform the actual readout. The DA-1821 read the ICBM slot and buffer address from the GPM and initiated a FASTBUS block read, transferring the ICBM data to the memories of CRATE-20. Since the information from the RABBIT crates was contained in 16-bit data words^{*}, only the low 16 bits of the 32-bit FASTBUS word were transferred to the 1892 memories. Thus, a 32-bit data word in the 1892 memory corresponded to the data from two LAC channels, reducing the actual event size by half. When the data transfer was complete, the DA-1821 responded with a “done” pulse back to the GPM.

^{*} Since we were reading out all channels from both calorimeters, the address for each channel was not necessary due to the fixed length readout process.

After receiving the DA-1821 "done" signal, the GPM checked if a trigger signal were latched during the ICBM readout^f, and if not, it continued the readout process for the next ICBM of the same event. If a trigger had occurred, then the GPM would check whether there was a free ICBM buffer available, and if there was, it would start the LACAMP readout process. When that was done, it would continue with the readout of the following ICBM of the previous event, where the readout was interrupted by the arrival of the trigger. In the case that all ICBM buffers were found to be filled, the GPM would finish the readout of one buffer and then service the trigger. After reading out the last ICBM for a given event, the DA-1821 sent an *End Of Record* signal (EOR) to the 1892, which allowed the record to be marked and its length noted. The EOR signal wrote special header words into the 1892 memory that were used during the 1892 readout.

When the end of spill occurred, the GPM finished the readout of all the remaining ICBM buffers, and notified the DA-1821 to send a special end of event to the 1892 memories in order to notify CRATE-20 that an end of spill occurred. Then the DA-1821 notified the CALBR-1821, which passed the information to LACSERVER in order to start the corresponding between spill task.

VAX Transfer

The readout of the 1892 memories and the data transfer to the host VAX was done in parallel with the readout of the LACAMPs. This process was controlled by

^f All the GPMs that we tested had a hardware "feature" with respect to interrupt handling. If a trigger signal caused an interrupt to one of the inputs of the GPM, while at the same time the DA-1821 "done" signal was causing an interrupt to the other input, then the "done" interrupt that the GPM was waiting for was missed and not serviced. Each interrupt routine set a variable equal to one and that variable was checked in the main program to identify if an interrupt had occurred. To bypass this problem, the trigger interrupt was disabled when the GPM was waiting for the DA-1821 "done". If a trigger occurred while the interrupt was disabled, then it was waiting in the queue, and it was serviced when the trigger interrupt was enabled, after the DA-1821 "done" was received.

the GPM of CRATE-20, and the EVENT_BUILDER program which was running on the host VAX. The EVENT_BUILDER sequentially selected each DA source, and by executing a list of commands, it transferred data from the given source to the VAX. The communication between the EVENT_BUILDER and the FASTBUS crate was through the 1821 SM/I. The FASTBUS list, executed by the EVENT_BUILDER, initiated the data transfer from the 1892s to the VAX. At first it initialized the FASTBUS crate and started the 1821 microcode. Then the 1821 sent a front panel signal to the GPM to start the readout of the 1892s, after which the GPM started reading the data at a specific location in the first LAC 1892, waiting for a bit to be set indicating that data had been transferred from CRATE-11[◇]. When data arrived, the GPM started the readout of the memories. It first read the data from the LAC 1892, and then from the two STRAW 1892s. It then performed various checks to insure data integrity and to verify that the event and run numbers among the three data buffers agreed with each other in order to produce a single record. If any inconsistencies were found, an error message was displayed on the terminal connected through the RS232 serial line to the GPM. This was very useful for monitoring the concatenation process. In the resulting concatenated record, the GPM added a VAXONLINE event header containing information, including the run and event number, the total length of the event, and the length of each of the three subevents.

After reading an integer number of events (typically three) prior to filling its data memory, or until end of spill special event was identified, the GPM issued a front panel signal back to the 1821 in order to start the data transfer to the VAX. The 1821 informed the VAX, through the PDREG register in the 1821, that the GPM was ready

[◇] This bit, called Valid Header Bit, was set with the arrival of the EOR signal.

to be read out. Then the VAX started to read out the GPM by initiating FASTBUS block read operations to the 1821 and performing DMAs from the 1821 to the VAX. The data were transferred in $4K \times 32$ -bit word blocks until the GPM data memory was emptied. After collecting all data from the GPM, another front panel signal was issued from the 1821 to the GPM and the readout process was repeated. In order to insure that the readout of the 1892s was completed before taking data for the next spill, a busy signal was asserted at the end of each spill. A reset signal was sent from the GPM to CRATE-11 busy logic after reading out the end of spill special event.

When data written to an 1892 reached an address equal to “end of memory less offset”, a front panel differential ECL “full warning” output signal was generated. The offset was user programmed, and it was set to at least the maximum event size. The logical AND of the “full warning” and the EOR signals was used to enable the next 1892 to receive data. Since CRATE-11 was sending data to the 1892s at a much faster rate than they were being read out, a “global full warning” busy signal had to be produced for the case when all 4 LAC 1892 memories were full. This signal was sent to the DA-1821 of CRATE-11 causing a hold on the current ICBM readout, and data transfer to the 1892s. When the GPM finished reading out one LAC 1892, the module was initialized and its “full warning” signal was reset. Then the transfer of data from CRATE-11 to CRATE-20 was resumed. With normal trigger rates, there was always a free 1892 available, and therefore the “global full warning” signal was not adding an extra “dead time”. A trigger busy signal was also produced when either one of the STRAW 1892s was full. This situation was very unlikely to happen since the length of the STRAW buffers was relatively small, and one 1892 was enough to buffer the data from one FASTBUS TDC crate for one spill.

3.7 THE LAC DA PERFORMANCE

One of the goals for the LAC FASTBUS readout system was to read out the entire detector with a resulting “dead time” comparable to that of the other components of the DA and the trigger. In order for this goal to be achieved many optimizations had to be made both in hardware and software for maximum performance. Another goal was to be able to calibrate and monitor the LAC electronics, as well as to monitor the data while they were being recorded. This was achieved by our ability to perform calibration and between spill tasks, and with our error handling for the entire FASTBUS DA process. In addition to the between spill monitoring tasks, there were other monitors used to verify the quality of the LAC data by analyzing sample events sent from the BUFFER_MANAGER process.

A crucial component to the LAC DA performance was the readout time of the LACAMPs by the ICBMs. The ICBM program, written in Assembler language, was optimized to read out the channels in a parallel fashion. The majority of the program resided in the ICBM internal memory space to minimize access times. The ICBM readout time for 2 RABBIT crates was 7.4 ms reading no TVC channels, and 9.2 ms including reading out all TVC channels. The average time during data taking was approximately 8 ms. A small “dead time” (250 μ s) was introduced by the CRATE-11 GPM corresponding to the time between the trigger signal was accepted and the ICBM program was started[†]. This time included the service of the trigger interrupt, the two broadcast FASTBUS operations to the ICBMs, and the code to perform these operations, written in C language. To minimize this “dead time”, the GPM standard FASTBUS routines were optimized in the Assembly language, gaining a factor of 2 in speed. Further optimization on this “dead time” was unnecessary since the LAC

[†] The corresponding trigger handling time for the PDP-MX system was around 5 ms.

readout was no longer the slowest source of the DA system. If the trigger was received by the GPM while the DA-1821 was reading out an ICBM buffer, a small "dead time" was introduced to finish reading out the current ICBM.

With an expected data rate of 30 to 50 Hz, and the ability to buffer up to 4 events in the ICBMs, the readout time of the ICBM buffers and the data transfer to the 1892 memories by the DA-1821, was transparent to us. The DA-1821 was able to read out an ICBM at the rate of 390 ns per 32-bit word plus an overhead of 7.54 ns per ICBM[‡]. The GPM had also an overhead of 75 μ s corresponded to the time required to inform the DA-1821 to read out the next ICBM. Hence the time required to transfer one LAC event from the ICBMs to the 1892s, consisting of an average 9000 16-bit words (including the event scaler ICBM), was approximately 4.6 ms.

The readout of the 1892s and the data transfer to the host VAX was done in parallel with the LAC and ICBM readout. Therefore CRATE-20 had the full spill cycle time to complete its task. The VAX readout rate of the LAC and STRAW 1892s was measured to be 330 Kbytes/sec. When events were concatenated and written to double 8 mm cassettes, the average 1892 readout rate was 280 Kbytes/sec. The drop in the rate was due to the tape writing speed.

The improvement of the "live time" of the experiment due to the new DA system was significant. For a typical spill of 600 events, the DA "live time" -- i.e., the fraction of the time that the DA system was ready to service a trigger -- was 75%, about a factor of 1.5 greater than for the 1987-88 run. This increase of the "live time" was significant, especially since we were reading out the entire LAC, improving our ability to reconstruct low energy photons.

[‡] The readout rate for the PDP-MX system was 1.5 μ s per 32-bit word.

3.8 TRIGGER

As already mentioned, the goal of the E706 was to measure the production of high p_T neutral particles (direct photons, π^0 s, η s) in fixed-target hadronic interactions. Due to the steeply falling p_T dependence of the cross section, the fraction of events containing a neutral particle with large p_T is relatively small. For this reason, a trigger system was implemented to select only the “interesting” events.

The E706 trigger was designed to run at 10^6 interactions/sec, selecting events containing high p_T electromagnetic showers. It was built using a combination of NIM modules, CAMAC programmable logic units, and custom-designed summing and weighting p_T cards.^[20] Most of the trigger system was computer controlled through one of the PDPs. The loading of various trigger parameters (e.g., delays, prescaled factors, trigger combinations, etc.) was done through RUN_CONTROL, by initiating the trigger loading process on the corresponding PDP. The trigger decision consisted of three stages:

- Beam and Interaction definition
- Pretrigger definition
- Final event selection

A simplified discussion of the system is presented in the following paragraphs.^[21]

Beam and Interaction

One beam particle was defined by the requirement that there was one and only one cluster of signals, consisting of adjacent paddles, on any two of the three beam

[20] C. M. Yosef, Production of High Transverse Momentum π^0 Mesons in Interactions of 530 GeV/c Proton and π^- Beams on Beryllium and Copper Targets, Ph.D. Dissertation, Northeastern University (1990).

[21] L. Sorrell, private communication.

hodoscope planes. In addition, to define a *triggerable beam particle*, another two signals were used; the *BEAM_GATE* and *RF_CLOCK*. The *BEAM_GATE* indicated the begin and end of the “beam spill”[◇]. The *RF_CLOCK* was a pulser received from the accelerator control, running at a frequency of ≈ 53 MHz, and producing 1 ns wide pulses in phase with the accelerator, simulating the beam structure. Therefore a triggerable beam particle was defined:

$$BEAM1 = (Beam\ Hodoscope) \otimes BEAM_GATE \otimes RF_CLOCK$$

An *interaction* was defined as signals from at least two of the four interaction counters (SE1, SW1, SE2 and SW2) in coincidence with the beam signal. The interaction signal was then sent to a delay unit, producing an output signal corresponding to the status of the interaction definition for that beam bucket time slice. There were 16 such delay units, allowing us to buffer up to 16 beam buckets of time. A *CLEAN* signal was generated when no interactions were present within ± 3 buckets ($\approx \pm 60$ ns) from a given interaction. To define a *live triggerable interaction* (*LIVE_INT*), in addition to the *CLEAN* requirement it was further required that the incident particle was not identified as a beam halo particle, by taking the signal from the BH counter in anticoincidence with the beam hodoscope signal. The computer ready signal (*CMPRDY*) was also required, specifying that the DA system was ready to accept a trigger. Therefore the live triggerable interaction strobe was generated from the coincidence of the following signals:

◇ The *BEAM_GATE* signal was turned on 100 ms after the accelerator “begin spill” signal (used to define the begin spill in the DA system), and remained enabled until the arrival of the “end spill” signal (an 100 ms delayed signal was generated to define the end of spill for the DA system). This delay of the *BEAM_GATE* signal with respect to the “begin spill” was done to allow the computers that controlled the various subsystems of the spectrometer to become ready to start collecting data when the beam arrived.

$$LIVE_INT = BEAM1 \otimes INTERACTION \otimes CLEAN \otimes \overline{BH} \otimes CMPRDY$$

The *LIVE_INT* signal was sent to the Faraday room where it was used in the definition of the pretrigger.

Pretrigger

In order to minimize the “dead time” introduced by the LAC trigger decision process, a pretrigger was introduced for fast rejection of low p_T events. As mentioned earlier, the integrated output signal of each LACAMP channel corresponding to the r view was sent through the fast output to the local p_T summing modules. These modules were designed to operate within the RABBIT standard, and they were controlled by the trigger ICBM at CRATE-11. The p_T in the calorimeter was determined by using the energy (e_i) in each radial strip weighted according to its radial distance (r_i) from the beamline:

$$p_T = 2 \sum_i e_i \sin \vartheta_i, \text{ where } \sin \vartheta_i = \frac{r_i}{Z_f^{LAC}}.$$

The factor of two came from the assumption that half of the total energy was deposited in the r view and half in the ϕ view; the Z_f^{LAC} was the Z position of the front face of the EMLAC relative to the target.

An *octant pretrigger* was defined by the coincidence of the following:

- *LIVE_INT* signal.
- A total p_T deposition within the innermost 128 r-strips or total p_T deposition within the outer r-strips, of at least $\approx 1.7 \text{ GeV} / c$.
- A total p_T depositing in the octant within the preceding 100-200 ns of less than $\approx 1.5 \text{ GeV} / c$.

- No incident muon, as defined by a signal in the upstream veto wall in coincidence with the logical OR of the signals from the two downstream veto walls.
- The absence of a power supply noise spike (SCRKILL).

The final LAC *PRETRIGGER* signal was generated by the logical OR of all octant pretriggers. This signal was sent to the BATs in order to initiate the BEFORE-AFTER time sequence, and as a LOAD to latch the PWC/SSD and FCAL information. After the *PRETRIGGER* was issued, the next step was to evaluate whether conditions were satisfied to select the event.

Final Event Selection

There were three octant signals used in this part of the event selection: a global- p_T , a 1/2 global- p_T , and a local- p_T signal. The global- p_T signal corresponded to the total p_T deposited in one octant. The 1/2 global- p_T signal corresponded to the total p_T deposited in the inner 128 r-strips, or in the outer r-strips in one octant. The local- p_T signal corresponded to the sum of sixteen contiguous r-strips (≈ 8 cm, approximately one photon shower width) in one octant and was used to minimize the generation of global- p_T signals due to low p_T multiphoton events or coherent noise effects.

All p_T signals were discriminated using two different threshold levels, called the high and low thresholds*. Using a combination of these three p_T signals and the two threshold levels, six LAC triggers were implemented:

- $LOCAL\ GLOBAL\ HI = (LOCAL\ LOW) \otimes (GLOBAL\ HI)$

*

During the course of the 1990/91 runs, there were many changes in these trigger thresholds in order to adjust the trigger rate with respect to the beam intensity delivered to the experiment.

- $LOCAL\ GLOBAL\ LOW = (LOCAL\ LOW) \otimes (GLOBAL\ LOW)$
- $SINGLE\ LOCAL\ HI = LOCAL\ HI$
- $SINGLE\ LOCAL\ LOW = LOCAL\ LOW$
- $LOCAL\ 1/2\ GLOBAL\ HI = (LOCAL\ LOW) \otimes (1/2\ GLOBAL\ HI)$
- $TWO\ GAMMA = \sum_{\alpha\beta} (LOCAL\ LOW)_{\alpha} \otimes (LOCAL\ LOW)_{\beta}$, where β is any of the three corresponding away-side octants to octant α .

If one of the above conditions was satisfied, a *trigger interrupt* was sent to the DA subsystems. If no LAC triggers were satisfied, then the electronics was reset and the experiment was ready for another trigger, after allowing a $\approx 20\ \mu s$ of settling time. In addition to the LAC triggers, low bias triggers were recorded with high prescaled factors. These triggers were *BEAM*, *INTERACTION* and *PRETRIGGER*. Besides the E706 triggers mentioned above, there was another trigger generated from the E672 trigger processor to indicate that the event was a DIMUON trigger candidate. All triggers were serviced by the DA system in the same way. Table 3.1 lists the nominal trigger settings along with their rates towards the end of the 1990 running period.

Trigger Type	Prescale Factor	Threshold	Fraction
<i>LOCAL GLOBAL HI</i>	1	3 GeV/c	35%
<i>LOCAL GLOBAL LOW</i>	40	2.5 GeV/c	20%
<i>SINGLE LOCAL HI</i>	1	3.5 GeV/c	40%
<i>SINGLE LOCAL LOW</i>	40	3 GeV/c	18%
<i>TWO GAMMA</i>	1	2.8 GeV/c	20%
<i>LOCAL 1/2 GLOBAL HI</i>	1	3 GeV/c	35%
<i>PRETRIGGER</i>	2925	1.7 GeV/c	7%
<i>BEAM</i>	15^6	none	2%
<i>INTERACTION</i>	15^5	none	3.1%
<i>DIMUON</i>	1	none	20%

Table 3.1 Trigger characteristics for the end of the 1990 run.

4. EVENT RECONSTRUCTION

4.1 OVERVIEW

The off-line reconstruction of the raw data was controlled by a program written specifically for E706 called MAGIC.^[1] MAGIC was written in FORTRAN-77 and maintained by a CERN code-management system called PATCHY.^[2] The ZEBRA memory management system^[3] was employed to provide dynamic memory allocation. ZEBRA allowed, at execution time, the creation and manipulation of dynamic data structures (banks and divisions) of variable sizes, and the ability to write the data banks in a machine independent format.

MAGIC was able to read the input data in a variety of formats; a raw format as provided by the data acquisition system, and an unpacked or reconstructed data format as provided by MAGIC after unpacking or reconstruction. Once an input event was read, MAGIC performed user selected tasks controlled through a set of control cards. These tasks included unpacking of the data (depending upon the input data format -- i.e., raw or unpacked), calling the reconstructor subroutines needed for each detector, and writing the output in a selected format. The control cards were also used to determine the number of runs and events to be processed, the application of certain corrections to the raw or unpacked data, and the error handling during the event processing.

There were six independent reconstructors used in the first pass processing of the data:

[1] G. O. Alverson and E. L. Pothier, E706 Internal Note 139 (1985).

[2] H. J. Klein and J. Zoll, PATCHY reference manual, CERN Computer Center program library (1983).

[3] R. Brun et al., ZEBRA User's Guide, CERN Computer Center program library, DD/EE/85-6, Q100, or FNAL Software note PU-0046.

- DLREC, which reconstructed the trigger and Cherenkov information;
- PLREC, which reconstructed the charged tracks detected in tracking system;
- EMREC, which reconstructed the showers detected in EMLAC;
- HCREC, which reconstructed the showers detected in HALAC;
- FCREC, which reconstructed the energy detected in FCAL;
- MUREC, which reconstructed the charged tracks detected in the E672 tracking system.

MAGIC was able to run on a variety of computers and operating systems. VAX/VMS was used for developing and debugging, whereas the first pass reconstruction of the raw data was performed on Silicon Graphics computers using UNIX as the operating system (UNIX farms). These UNIX farms were developed at Fermilab with the focus on event oriented multiprocessing. In the production environment, a UNIX farm consisted of a single host node and a number (around 10-13) of processing nodes in parallel. The host handled the I/O and distributed events for reconstruction on the processing nodes. When a node finished reconstructing an event, it sent the output to the host in order to be written to either disk or 9 mm tape. Then another event was sent to the processing node for reconstruction. There were two UNIX farms used for the processing of the 1990 data sample. The reconstructed output of all E706 triggers were written out to Data Summary Tapes (DSTs).

A brief description of the tracking and EMLAC data reconstruction is presented below. A complete description of HCREC is given elsewhere.^[4]

[4] A. P. Sinanidis, Particles Produced in Association with High Transverse Momentum Single Photon and π^0 in Hadronic Collisions, Ph.D. Dissertation, Northeastern University (1989).

4.2 TRACKING RECONSTRUCTION

The charged-track reconstruction code constructed tracks upstream of the magnet using the information from the SSD planes, and downstream of the magnet using the data from the PWC and STRAW planes. These tracks were then linked at the center of the magnet and various physics parameters -- e.g., momenta, charge, direction cosines -- were calculated. Upstream track information was then used to calculate the position of the primary vertex and any other secondary vertices arising either from the decay or interaction of the particles produced at the primary vertex. For the purpose of this analysis, the tracking system was used to reconstruct the primary vertex and to calibrate the EMLAC energy response by identifying electrons and calculating their momenta. The following paragraphs describe the main features of PLREC.^[5, 6]

Downstream Tracking

The first step in the downstream tracking reconstruction involved forming three and four-hit tracks in each of the four views (X, Y, U, and V) of the PWCs. These view tracks were formed in two passes. In the first pass, the first and third planes were chosen as seed planes and the second and fourth planes as search planes. A straight line was defined from the hits on the seed planes, and then projected onto the search planes. The search planes were searched for hits within ± 1 wire spacing of the line projection. If both search planes had hits satisfying this criterion then the track was called a four-hit track candidate; if hit was found in only one of the two search planes then a candidate three-hit view track was formed. In the second pass the whole procedure was repeated with the second and fourth planes as seed planes and the first

[5] S. Easo, Structure of Events Containing a Direct Photon or Neutral Pion in Hadronic Interactions, Ph.D. Dissertation, Pennsylvania State University (1989).

[6] S. Blusk, private communication.

and third as search planes. The purpose for this was to pick up three-hit tracks missed during the first pass. Least-squared fits were performed to all view tracks to determine their parameters.

Once all possible view tracks were found, the program proceeded in three stages, with the matching of the view tracks to form three dimensional *space tracks*. The procedure employed to match the view tracks was similar to that described above. Two seed views (e.g., X and Y) were selected to define a space track candidate. The space track was projected to the other two search views (U and V) and a search was performed for hits within ± 1.5 wire spacing of the track projection. This procedure was repeated, this time starting with the U and V views and searching for hits in the X and Y views.

At the first stage, each accepted space track was required to have at least 13 hits and a minimum χ^2/DOF of less than 3 for the 16, 15 and 14-hit tracks, and less than 2 for the 13-hit tracks. If two space tracks shared more than a certain number of hits, the track with the lowest number of hits was dropped. If they had the same number of hits, then the one with the higher χ^2/DOF was rejected.

Having found all high quality space tracks, PLREC continued with the reconstruction of 10-hit tracks that leave the acceptance of the first or the last PWC module and the reconstruction of 11 and 12-hit tracks with a minimum χ^2/DOF of less than 1.5. The hits used to form the high quality space tracks were excluded from this second stage of reconstruction. At the final stage and after removing all hits used in the previous stages, the program continued with the reconstruction of wide-angle tracks that leave the acceptance and hit only the first two PWC modules (8 view planes). The minimum number of hits required was 6 with χ^2/DOF of less than 1.5.

When the PWC tracking was completed, PLREC used the information from the STRAW tubes in order to refine space tracks parameters. Each PWC space track was projected to the two STRAW modules (each module consisted of 4 X and 4 Y view planes) and the closest hit pairs (due to the left/right ambiguity) were stored. Then using the best set of STRAW hits a refit was done with all 32 planes (PWCs and STRAWs) to determine more accurate space tracks parameters. The STRAW information improved the resolution of the downstream tracking system significantly. The combined resolution of the upstream and downstream tracks projected at the center of the magnet was momentum dependent and for high momenta, for PWC (only) tracks it was ≈ 1.25 mm, and when STRAW hits were included it was ≈ 500 μm .

Upstream Tracking and Linking

The upstream tracking utilized the 5 SSD modules, each with a set of orthogonal X and Y planes, located downstream of the target. Using these planes, five and four-hit view tracks were formed in the X and Y views. These SSD view tracks and the previously reconstructed downstream space tracks were projected to the X-Y plane at the center of the magnet. After accounting for the effects of the magnetic field, the spatial difference of each downstream-upstream track pair was compared to find the best match. If this best match satisfied a predetermined momentum[†] dependent window, it was identified as a *linked track*. This matching window was set to be 3.3 times the combined resolution of the upstream and downstream tracks at the center of the magnet. Since the tracks bend primarily in the X-Z plane, an additional requirement was imposed on the Y slope difference between the upstream and

[†] At this stage the momentum was estimated by projecting the downstream space track to the center of the target.

downstream tracks. This cut was also momentum dependent and for high momenta PWC (only) tracks it was ± 1.32 mrad, and when STRAWs were included it was ± 0.58 mrad. Due to fewer constraints of the upstream system (i.e., there were no upstream space tracks formed), up to five upstream view tracks were allowed to link to a downstream space track. After the four and five-hit upstream tracking was completed the reconstructor formed three-hit view tracks from the remaining hits not used to form 4 and 5-hit linked or isolated view tracks. A 3-hit view track was kept only if it linked to a downstream track that was not linked to a 4 or 5-hit track.

Vertex Finding

The primary vertex reconstruction procedure was to first find the X and Y view vertices using SSD view tracks and then match the two view vertices to get the three dimensional position of the vertex. The algorithm required three or more tracks in order to search for a view vertex. At first it looked for three or more 5, 4 or 3-hit view tracks that linked with downstream space tracks. If there were not enough tracks, the algorithm also included unlinked 4 or 5-hit tracks. If there were not sufficient tracks selected, the view vertex fitting was not performed.

Once a set of SSD view tracks was selected, the algorithm determined the vertex position by minimization of χ^2 , defined as

$$\chi^2 = \sum \frac{b_i^2}{\sigma_i^2} \quad (4.1)$$

where b_i was the impact parameter of the i^{th} track and σ_i was the uncertainty in the projection of the i^{th} track. After both view vertices were found, a refitting was done in both views using the tracks in one view and the Z position of the view vertex found in the other view. Then the final matched Z position was determined using a

weighted average of the Z positions of the two view vertices. The resulting vertex resolution was $\approx 400 \mu\text{m}$ along the beam direction and $\approx 10 \mu\text{m}$ transverse to the beam.

Having found one vertex, the program removed the tracks associated with that vertex and searched for another vertex. This was done to reduce the probability for designating a secondary vertex as the primary since secondaries (occurring downstream of primary) have larger acceptance. If a second matched vertex was found, then the one further upstream was declared as the primary vertex of the event.

Relinking

After the location of the primary vertex was established, the tracks were linked again. When two or more SSD tracks were linked to the same downstream track a preference was given to the SSD track projected “closest” to the reconstructed vertex. For a given downstream track, if no SSD track was found within the linking window, the track was assumed to originate at the primary vertex in order to estimate the momentum of the track. After the relinking was done, the physics parameters of all tracks were redetermined.

Beam Tracking

The beam track reconstruction used the 6 SSD planes upstream of the experimental target. The reconstruction was done independently in the two orthogonal views. First all possible 3-hit tracks in a given view were reconstructed by using a least squared fit. Then 2-hit view tracks were formed from the hits not used in the 3-hit tracking. At a later stage of the program, after the vertex position was

determined, the track with the smallest impact parameter to the vertex was considered as the beam track associated with the vertex.

4.3 EMLAC SHOWER RECONSTRUCTION

The positions and energies of showers detected in the EMLAC were reconstructed by EMREC.^[7, 8] EMREC reconstructed each quadrant separately, and each quadrant was divided into four views: left r (1), right r (2) for the two radial views in each quadrant; inner ϕ (3) and outer ϕ (4). The reconstruction was performed in the following steps:

- Conversion of ADC counts to units of energy;
- Group and Peak finding in each view;
- Reconstruction of GAMMAS;
- Correlation of r and ϕ GAMMAS into photons;
- Determination of the time of arrival for each photon from TVCs.

These steps are described in more detail below.

Unpacking

The EMLAC unpacker received the raw data in a crate-amplifier-channel format and transformed them to section-quadrant-view-strip format, converting the ADC pulse height to units of energy, based on the formula:

$$E_i = A_{em} \times B_{em}(t) \times G_i \times (N_i - N_{0i}) \quad (4.2)$$

where

[7] J. P. Mansour, High Transverse Momentum π^0 Production from π^- and p Beams at 530 GeV/c on Be and Cu, Ph.D. Dissertation, University of Rochester (1989).

[8] W. Dlugosz, private communication.

- E_i was the energy assigned to the i^{th} strip;
- A_{em} was an overall conversion constant from ADC counts to energy (3.1 MeV/count);
- $B_{em}(t)$ corrected the time dependent energy scale of the EMLAC based on the π^0 mass dependence as a function of “beam days” as discussed on Section 2.3 - the time for each run was determined based on the day that the run started;
- G_i was the relative amplifier gain correction for the channel;
- N_i was the measured ADC value of the pulse height in the channel;
- N_{0i} was the measured pedestal offset for the channel in ADC counts.

The gains term G_i in Eq. (4.2) represented the channel gain as measured from the corresponding calibration task (see Section 3.5) corrected for effects introduced by the card to card variations of the BAT reference voltage and the LACAMP injection capacitance. After these corrections, the gains were normalized by the average of the gains of all EMLAC channels. The fluctuations of gains was an important factor in the energy resolution of the calorimeter, especially for high energy showers, since they resulted in a resolution term linearly proportional to energy.

The initial estimates of the pedestal values were measured approximately every eight hours during the run as a part of the cold start procedure. These “between spill” pedestals were subsequently adjusted in order to remove hardware and software biases and determine the “on-line” pedestals. A discussion of the pedestal correction method used for the 1990 data is given in Section 4.4. Both corrected pedestals and gains contained information about the status of a given channel. Channels that were flagged as “dead”[†] in either of these tasks were given a large negative offset by the

[†] There were some “dead” channels that corresponded to strips in the calorimeter which were known to have problems, either shorts or bad connections. In addition, amplifier channels occasionally stopped functioning.

unpacker to be recognized by EMREC and “corrected.” The correction for a single “dead” strip was to assign an energy equal to the average of its two adjacent strips. More complicated formulas were used to correct the cases of two adjacent “dead” strips. This was done to prevent “dead” strips from reducing the reconstruction efficiency.

As mentioned previously, the front and back sections of the EMLAC were read out independently. For reconstruction purposes in the unpacking routine, energies above a specific cutoff (-180 MeV) from corresponding strips in the front and back were added together to form a third section, called the *summed section*. The reason for this was to minimize the dependence of the shower shape on the point of origin of the shower in the EMLAC. These summed signals were used by EMREC in the pattern recognition process.

After the unpacker and before EMREC started the pattern recognition process, a routine (FREDPED) was called to correct for event by event overall “pedestal” shifts. These variations were attributed to several causes, such as background energy depositions from event pile-up, trigger rate and readout hardware effects (see Section 4.4). A linear fit was employed in each view (except the inner ϕ view) separately in front and back sections. Information from strips that corresponded to significant energy depositions were excluded from the fit. Due to the smaller number of strips and the corresponding larger probability that any given strip had energy deposited by a particle, the inner ϕ view was not fit. The inner section of the corresponding r view was used to approximately correct the overall offset in the inner ϕ view.

Group and Peak Finding

EMREC searched each view for clusters of energy. A group was defined as a set of consecutive strips that satisfied the following requirements:

- There were at least 3 strips (2 for outer ϕ since the strips became wider at large radii) with energies above 80 MeV (95 MeV for outer ϕ);
- The total group energy was at least 600 MeV;
- The strip with the maximum energy contained at least 300 MeV (350 MeV for outer ϕ).

Once all groups were identified, EMREC proceeded to search for energy peaks within each group.

A peak was identified when the slope of the energy distribution in the group changed from a positive to a negative value. There were two valleys associated with each peak, located to either side of the peak. A valley was defined as the strip with the lowest deposited energy between two peaks or the end strip in a group. Since low energy showers deposit most of their energy in the front section of the calorimeter, after a peak was found in the summed section, a search for peaks in the front section was performed between the two found valleys. When a peak candidate was found (in either the summed or the front section), a quality factor was calculated to determine if the peak was significant or a fluctuation. The sum of strip energies between its front valleys was calculated and stored for all peaks judged to be significant. For peaks found in the radial view, the program calculated the front radius and searched for the corresponding peak in the back to determine the back radial position. The front and back radial positions were used to determine the *directionality* of the particle -- the difference between the back radial position projected to the front section and the front radius. The directionality was used in the off-line analysis to eliminate particles (e.g., muons) that did not originate from the target (see Section 6.1).

GAMMA Reconstruction

Having found all the peaks, EMREC started the reconstruction of the GAMMAS. The GAMMAS differed from the peaks in that they corresponded to fits to shower shape for determining positions and energies. For the case of single peak groups the process was unambiguous. The treatment of those groups which contained multiple peaks was more complicated. A global fit was performed to such group, and the positions and energies of the constituent peaks were then calculated.

The parametrization of the shower shape was determined by fitting energy deposition from single photon showers generated from the GEANT based E706 Monte Carlo program (see Section 5.4). The shape was also compared to isolated photon showers in the data, and it was found to be consistent. The shower parametrization was tuned to match the photon showers which were found to have smaller "tails" compared to the electron showers -- electrons started showering in the material in front of the active region of the EMLAC earlier than photons. There were different parametrizations for the front and back sections of the detector -- the back shower shape had a wider lateral spread. The summed shower shape was determined by a weighted sum of the front and back shower parametrizations ($E(r) = 0.7 \times E_f(r) + 0.3 \times E_b(r)$). The parametrizations were done as a function of the radial distance from the center of the shower, and the integral of the shape was normalized to unity. The normalized shower shape parametrization was found to be energy-independent in the summed section.

The position and the energy (E) of a GAMMA were calculated in an iterative process. First the program assigned the center position of the peak strip as an approximate position for the GAMMA. Then, based on weights determined according to the neighboring strip energies, a shift from the center was found and a new position X was defined. After determining this first approximation to the

position, the energy of the GAMMA was estimated. Then, using this energy approximation, shower shape fits were performed based on locations around X , and the χ^2 values of the fits were used to find the best estimate of the GAMMA position.

After the position of the GAMMA was determined, the energy was recalculated by minimizing the χ^2 of the fit of the energy distribution to the shower shape. The χ^2 was determined based on the formula:

$$\chi^2 = \sum_i \frac{1}{\sigma_i^2} (e_i - Ez_i)^2 \quad (4.3)$$

where e_i was the energy in strip i , z_i was the fraction of energy in strip i as predicted from the shower shape, and σ_i was the estimate of the standard deviation[†] for the energy in strip i . In order to minimize noise fluctuations in the shower tails from influencing the fit, the last strips of the GAMMA were included in the fit only if their energy was more than twice the group threshold. Once the energy, E_{fit} , that minimized the χ^2 was determined, then the amount of energy in the tails of the shower was calculated as

$$E_{tail} = E_{fit} \left(1 - \sum_i z_i \right) \quad (4.4)$$

If the χ^2 was less than five, then the shower shape fit was judged acceptable and the fitted energy stored as the energy of the shower. Otherwise, the energy was re-determined based on the summed energy in the strips between the peak's valleys as follows

$$E_{sum} = \sum_i e_i + E_{tail}$$

[†] The average energy resolution for showers detected by the EMLAC was measured to be $\sigma^2(E) = (0.22)^2 + (0.16)^2 E + (0.01)^2 E^2$, where energy (E) and σ are in GeV.

When a GAMMA hit the inner/outer ϕ transition or the octant boundary, there was energy deposition in both views, and if this sharing was large enough then two separate GAMMAS were reconstructed. When the fraction of energy deposited in one view was not large enough to be properly reconstructed, an energy correction was determined based on the expected energy leakage from one view to the other. This energy was added to the reconstructed GAMMA. This correction was very important when the program tried to correlate this boundary GAMMA (e.g., in the ϕ view) with a GAMMA from the other view (e.g., the r view) by comparing their energies.

GAMMA Correlation and Photon Reconstruction^[9]

After all the GAMMAS were reconstructed, the next step was to correlate them to form the final photons. As mentioned previously, the EMLAC readout boards alternated between r and ϕ boards. Therefore, it was expected that for photon initiated showers the r and ϕ view energies should be nearly equal. In addition to the balance of the two view GAMMA energies, the shower development in each view was also used for matching the view GAMMAS to form a photon. The variable most sensitive to the shower development is the E_{front}/E_{tot} ratio. Monte Carlo results indicated that the E_{front}/E_{tot} of the ϕ view was slightly higher than the E_{front}/E_{tot} of the r view. Fig. 4.1 shows the difference of the E_{front}/E_{tot} ratios between the two views versus the total reconstructed energy for Monte Carlo photons.^[10] The curve represents a fit to the points, which was used as an offset when the reconstructor compared the E_{front}/E_{tot} ratio of the view GAMMAS.

[9] M. Zielinski, private communication.

[10] L. Apanasevich, private communication.

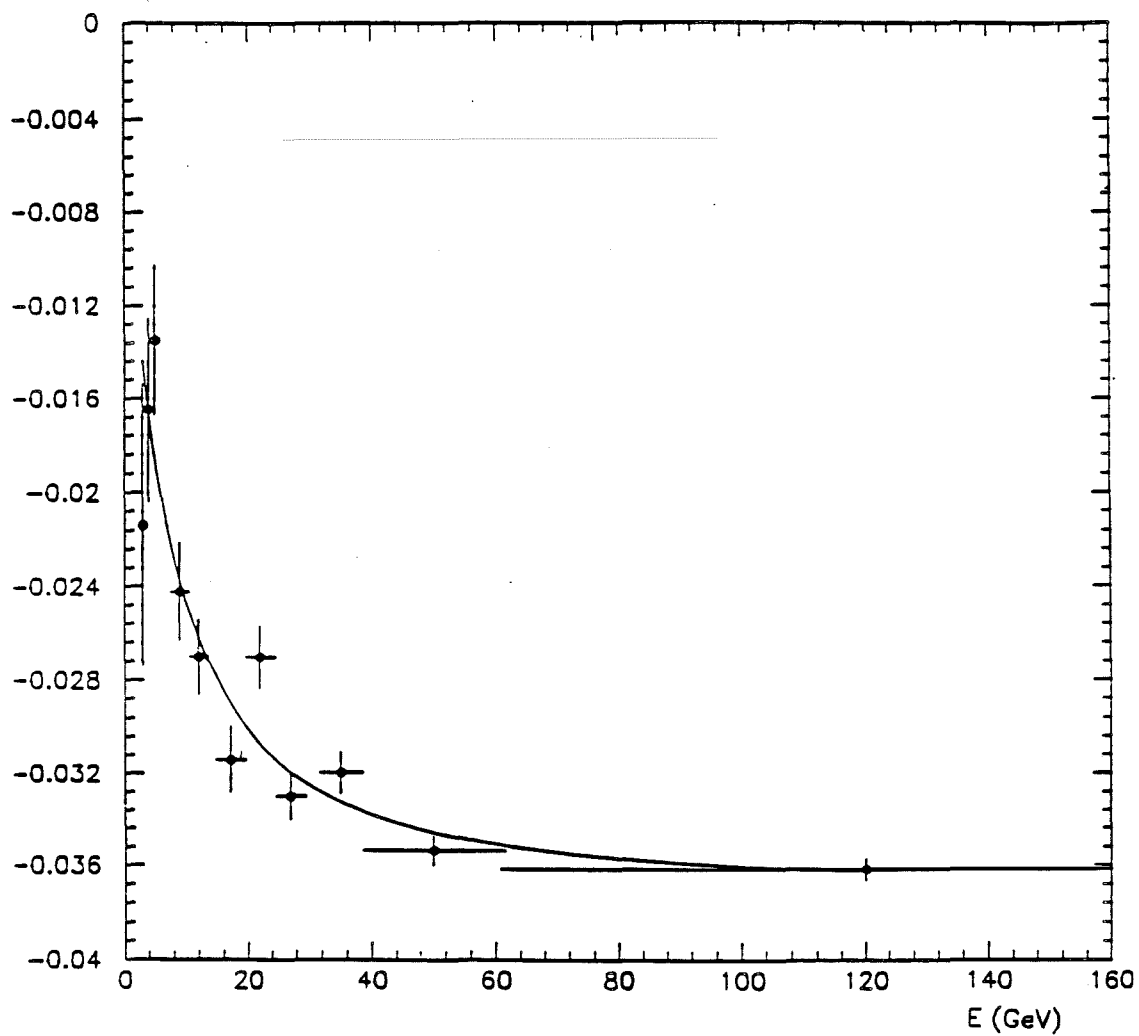


Figure 4.1 Difference of the E_{front}/E_{tot} ratios between the r and ϕ view GAMMAS as a function of the total reconstructed energy for Monte Carlo photons.

Inner ϕ GAMMAS were correlated with r GAMMAS that had a radius less than 40 cm, and outer ϕ GAMMAS were correlated with r GAMMAS with a radius greater than 40 cm. The simplest of correlations (named a 1-1 correlation) was when one r GAMMA correlated with one ϕ GAMMA to form a photon. The next level of complexity was when two photons overlapped in one view (say the r view), producing one GAMMA, and they were separated in the other view (the ϕ view), producing two GAMMAS. In this situation once the correlation was found, the program attempted to split the r view GAMMA into two using the energies of the two ϕ GAMMAS, producing two reconstructed photons. This type of correlation was termed 1-2. The two r to one ϕ correlation was essentially the same and termed a 2-1 correlation. However, there were additional problems when a GAMMA happened to fall near the inner/outer ϕ boundary, the octant boundary, or a combination of these boundaries, resulting in higher order correlations. In some cases, it was not possible for the algorithm to perform the correct correlation, and this resulted in an inefficiency in the reconstruction program. Corrections for this effect will be discussed in Section 6.4.

The correlation of the GAMMAS was done in incremented steps and each step represented a maximum number of allowed standard deviations for the $E_r - E_\phi$ difference. Since there were many types of correlations corresponding to possible geometrical ways that view GAMMAS could form one photon, a priority had to be assigned to each of the correlations. The correlations for boundary GAMMAS were done first. Then the code proceeded with other correlations of GAMMAS away from the boundaries, such as one r GAMMA to one ϕ GAMMA, one r GAMMA to two ϕ GAMMAS, and one ϕ GAMMA to two r GAMMAS. More complicated types of correlations were performed next and corresponded to one ϕ GAMMA to three r

GAMMAS, and one ϕ GAMMA to four r GAMMAS. After every correlation, the difference of the sum of all GAMMA energies between the two views was compared, and if there was a large imbalance the correlation was delayed by one step and the next type of correlation was tried.

After all the GAMMAS were correlated, the ϕ GAMMAS were reconstructed again using the information obtained from correlation. This was done since the shower shape fit depended on the ϕ -strip width which depended on the radial position of the GAMMA. During the ϕ GAMMA reconstruction, an estimate of its radial position was done using the shower width information. After the correlation, a refined radial position was determined and the ϕ GAMMA energies were calculated again. Then the code performed the correlation of GAMMAS once again because of the new ϕ GAMMA energy values.

Photon Timing

A time of arrival was associated with each GAMMA and photon. This was done using information from the timing circuitry (TVCs) within the amplifier modules (see Section 3.4). The pedestals for the TVCs were measured as a part of the cold start procedure, using the TVC calibration task mentioned in Section 3.5. These pedestal values were not reliable enough to be used in the data analysis and so a data driven method was employed to determine a better set of TVC pedestals.^[11] In the data driven method, the average in-time information was determined for each TVC channel by looking at events for which there was a significant energy deposition (above 4 GeV) in its associated 4 strips.

[11] R. Roser, E706 Internal Note 193 (1991).

In order to assign a time to a reconstructed GAMMA, all TVC channels that corresponded to the strips associated with that GAMMA were grouped into sets of TVCs that fell within 3 standard deviations (21 ns) of each other. Only TVCs with an associated energy of more than 4 GeV were considered as candidates. Then the best time was determined from the TVC set that had the greatest number of TVC candidates. In a case of a tie the set with the largest associated energy was chosen to provide the best time. The best time of a TVC set was defined as the energy weighted average of the corresponding TVC times within the set.

The time associated with a photon was determined in a similar way as that described above. All TVCs corresponding to the GAMMAS associated with the photon were grouped into sets of TVCs, and the best time was determined from the set contained the most TVCs.

4.4 THE LAC PEDESTAL CORRECTIONS

While the pedestal fluctuations represented for the most part changes in the offsets for individual channels, they were crucial during reconstruction. Significant differences between r and ϕ pedestals of the EMLAC could affect the reconstruction program during correlation of energies between the two views. The pedestal for each channel as determined by the calibration task was useful as a starting reference, but found to deviate from the pedestal as determined from the actual data. Some of the potential causes of this pedestal discrepancy were the following:

- Different “sampling rate”: During the calibration task the EVENT signal was generated by the control ICBM at an approximately constant rate, while during the data taking the rate was determined by the actual experimental trigger;

- Pile-up effects caused from the background energy in the LAC left from previous interactions.

Therefore, a data driven method was employed in order to determine the corresponding pedestal set for each run.

Data Driven Pedestal Determination

The principle of the data driven method was to collect enough data for each channel without energy deposition in order to determine its “on-line” pedestal. For this purpose, the prescaled beam triggers were used to minimize any shower activity in the LAC. The data sample was defined as follows:

- Use prescaled beam triggers (typically $\approx 2\%$ of the total triggers);
- Eliminate events with an SCRKILL noise spike[‡];
- Eliminate events if 2 or more interaction counters fired in any of the ± 3 buckets around the in-time bucket;
- Eliminate EMLAC channels (in front and back sections) that corresponded to strips which belonged to a reconstructed GAMMA or to strips which were less than 10 strips away from either GAMMA valley;
- Eliminate the EMLAC quadrant if the corresponding section of the upstream veto wall recorded a signal in coincidence with the logical OR of the signals from the two downstream veto walls.

The pedestal offset for each channel was determined by calculating the average offset within a predetermined window. The window was chosen to be ± 150 ADC counts centered around an offset value different for each channel. The window center for a channel was set by calculating an approximate pedestal shift within a fixed range

[‡] The SCRKILL signal was latched as a logic bit and was read out for each event as a part of the trigger system. Only the LAC triggers used the SCRKILL signal as an on-line veto.

of ± 800 counts using the first 50 events of the data sample. The veto wall cut was not applied during this process. The reason for the variable window center was so that the window would cover the entire distribution of channels, including those with relatively large pedestal offsets.

The above method was used for the majority of the 1990 data run. There was, however, a large running period where there was excessive noise in the Faraday room causing big calibration task pedestal offsets (≈ 100 counts) for a large group of channels. The data taking was not affected by this effect. These runs were corrected using a slightly different method than for the “normal” runs. The first 60 events of the data sample were employed to approximately correct for the large offsets by calculating an average pedestal within a 600-counts window. No cut was made for EMLAC strips that belonged to a GAMMA, since the input pedestals were questionable. After the approximate pedestals were determined from the data, a correction to the pedestals was applied, and the final pedestals were determined by the method used for the “normal” runs as described above.

Pedestal Stability and Results

The stability of the corrected pedestals was varied depending on the status of the hardware in the Faraday room. An average time period over which a pedestal correction was considered valid was around 8 hours. When any hardware work was done to the LAC electronics, a new corrected pedestal set was determined. Fig. 4.2a shows the difference between two corrected pedestal sets for all EMLAC channels and Fig 4.2b for all HALAC channels. The two runs were 8 hours apart. The data driven method resulted in an average run to run pedestal variations of less than 2 ADC counts.

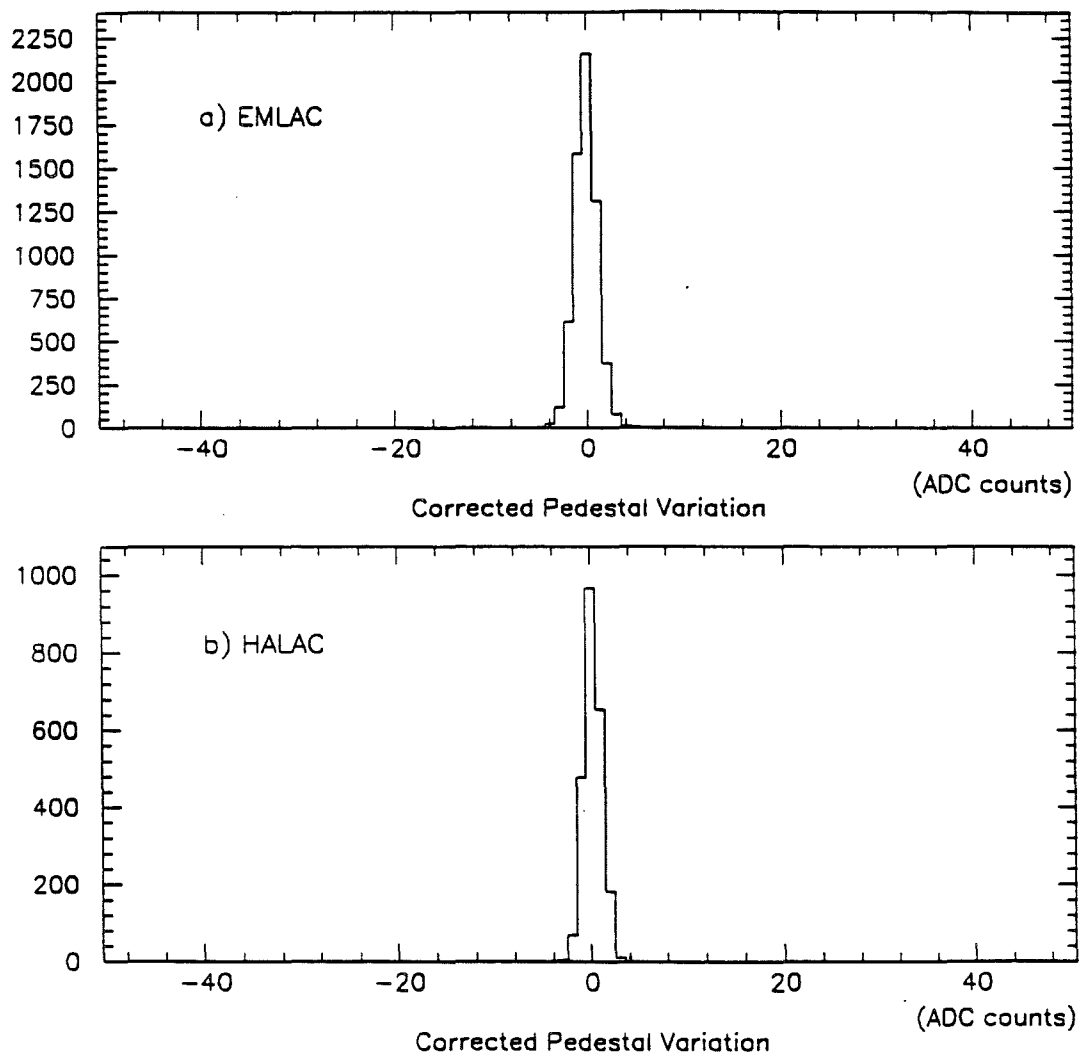


Figure 4.2 Difference between two corrected pedestal sets a) for EMLAC channels and b) for HALAC channels.

The corrected pedestals were normally lower than the calibration pedestals and the size of this difference was correlated with the average beam intensity of the run. Fig. 4.3 shows how the average difference between the calibration and the corrected EMLAC pedestals varied with respect to the average beam intensity per spill for a given run. The effect was not large but it could produce a systematic pedestal shift[†]. During the process of correcting the pedestals, runs were selected so that the intensity effect on the average was negligible. On the other hand, the FREDPED program as mentioned above corrected any residual overall pedestal offsets on an event by event basis.

The intensity dependence of the corrected pedestals was attributed to changes in the time between previous RESET and next EVENT signals caused by intensity variations. In the calibration task, this timing was approximately constant ($\approx 650 \mu\text{s}$), and longer than the average timing during data acquisition. The RESET signal reset the BAT modules and opened the sample-hold capacitors (see Section 3.4). The EVENT signal started the event sequence as described in Section 3.5. The measured pedestals were found to be increasing with respect to the time difference between the RESET and EVENT signals as shown in Fig. 4.4. The data points in this figure correspond to the average difference between the calibration pedestals and the pedestals as measured from data taken using a high rate *PULSER* trigger* with variable delays between the RESET and EVENT signals. This correlation was discovered during the 1991 run, and since then the time between the trigger CLEAR

[†] The effect on the reconstructed energy due to a systematic pedestal shift can be illustrated by the following example. Let us assume that the pedestals for all strips in a GAMMA were shifted by 5 counts. Consider a GAMMA with an energy of 50 GeV that occupied 16 strips in both sections (total of 32 strips). Then the shift to the reconstructed energy due to this pedestal shift will be $\Delta E = 32 \text{ strips} \times 5 \text{ counts/strip} \times 3.1 \text{ MeV/count} \approx 500 \text{ MeV}$ or 1% of the true GAMMA energy.

* The *PULSER* trigger was a periodic trigger generated with a predetermined frequency for testing the trigger and the DA systems.

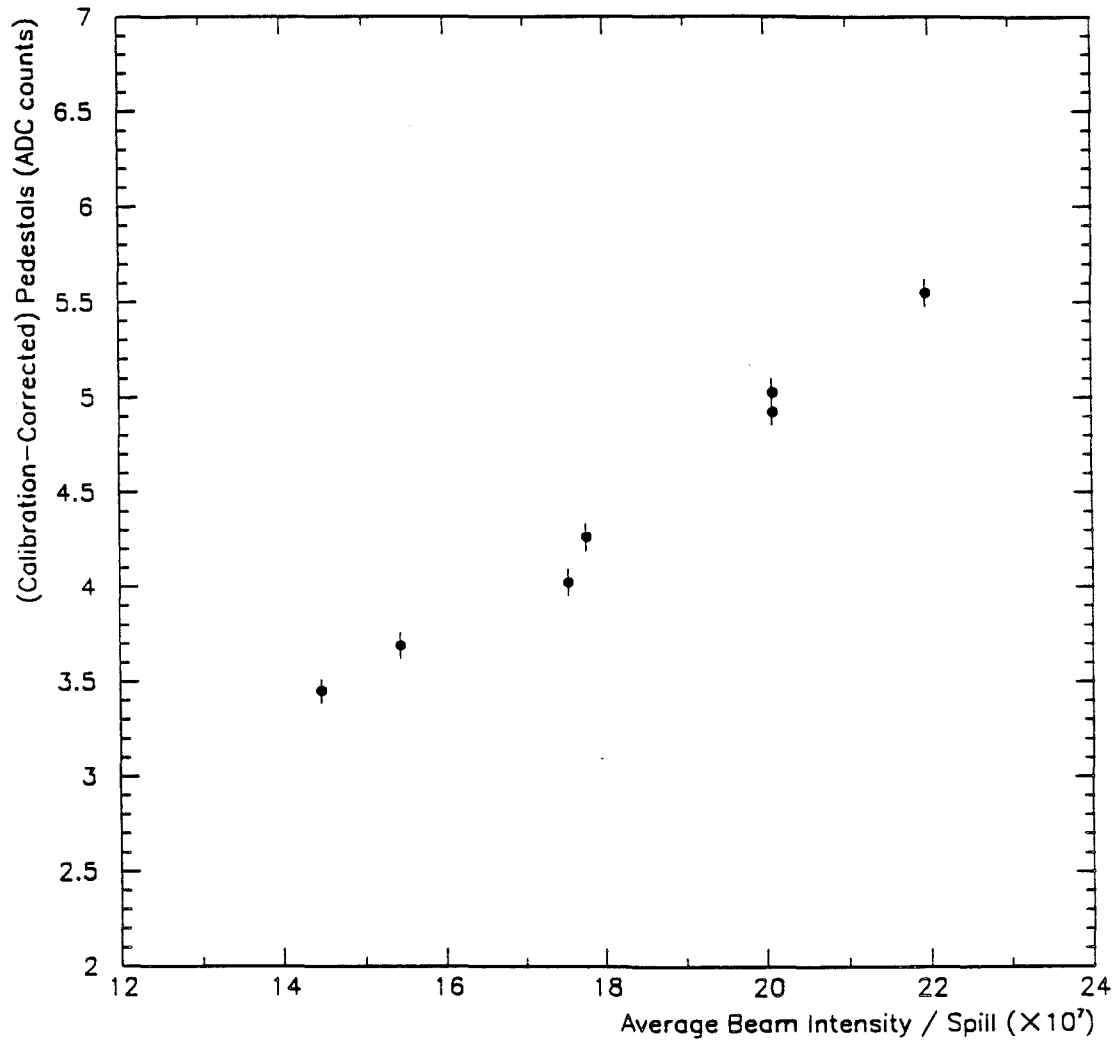


Figure 4.3 Difference between the calibration and the corrected EMLAC pedestals as a function of the run average beam intensity per spill.

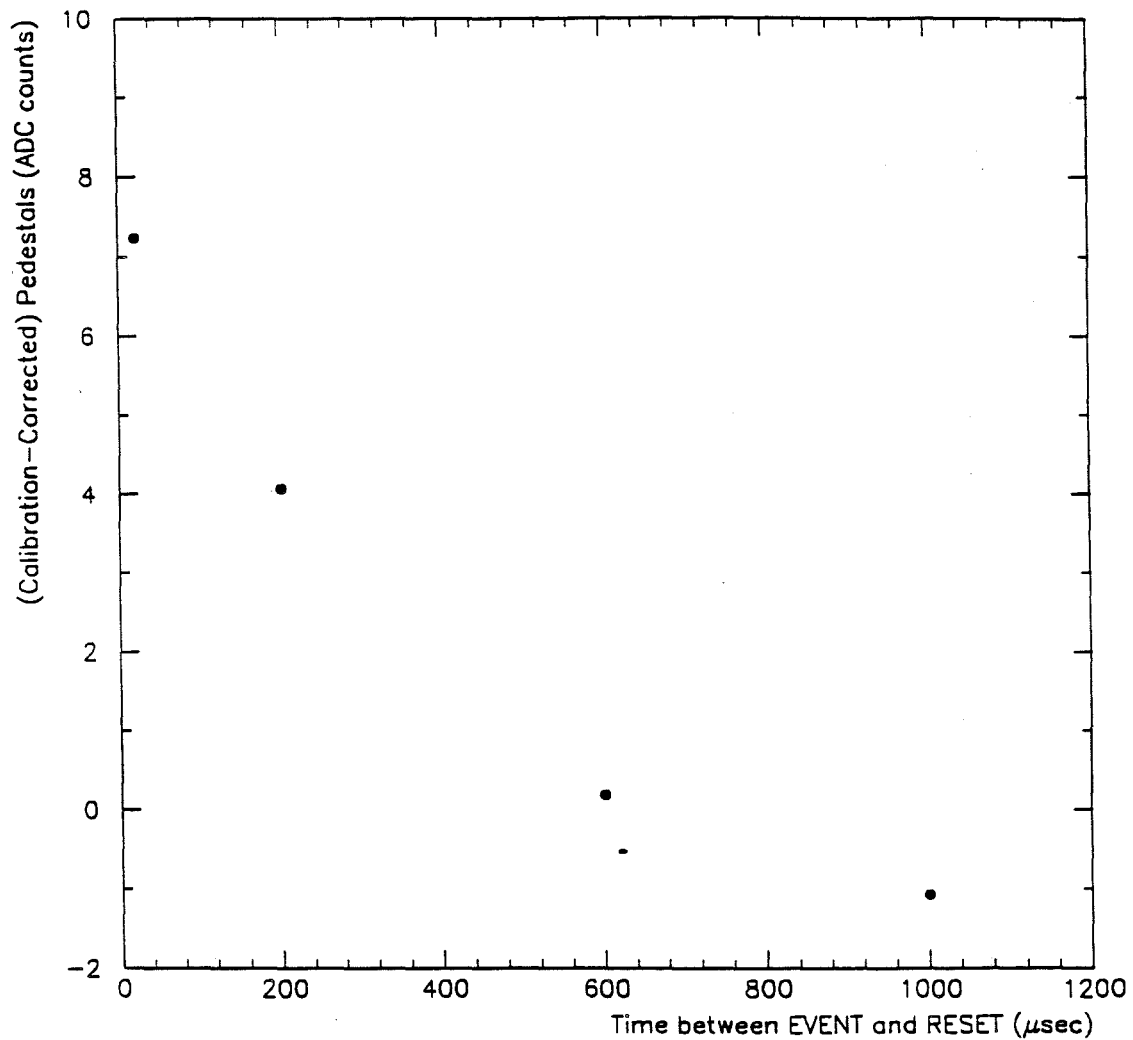


Figure 4.4 Difference between the calibration and the corrected EMLAC pedestals versus the time between RESET and EVENT signals for data taken using a high rate *PULSER* trigger.

signal and the *PRETRIGGER* was stored in the data as a part of the event for further use in the pedestal corrections for this data run.

In addition to the corrected pedestal for each channel, information about the status of the channel was also written out. There were flags indicating if the channel was found to be “dead” or very noisy based on the value of the RMS of its pedestal distribution. Typical EMLAC channel pedestals had a value near 6400 counts, and the RMS of the distributions for the front and back sections were 19 and 22 counts, respectively, as shown in Fig. 4.5. The average RMS for the HALAC pedestal distributions for the front and back sections were found to be 15 and 19 counts, respectively (Fig. 4.5). The low RMS tail (less than 10 counts for EMLAC channels and less than 8 counts for HALAC channels) of these distributions corresponded to channels flagged as “dead.”

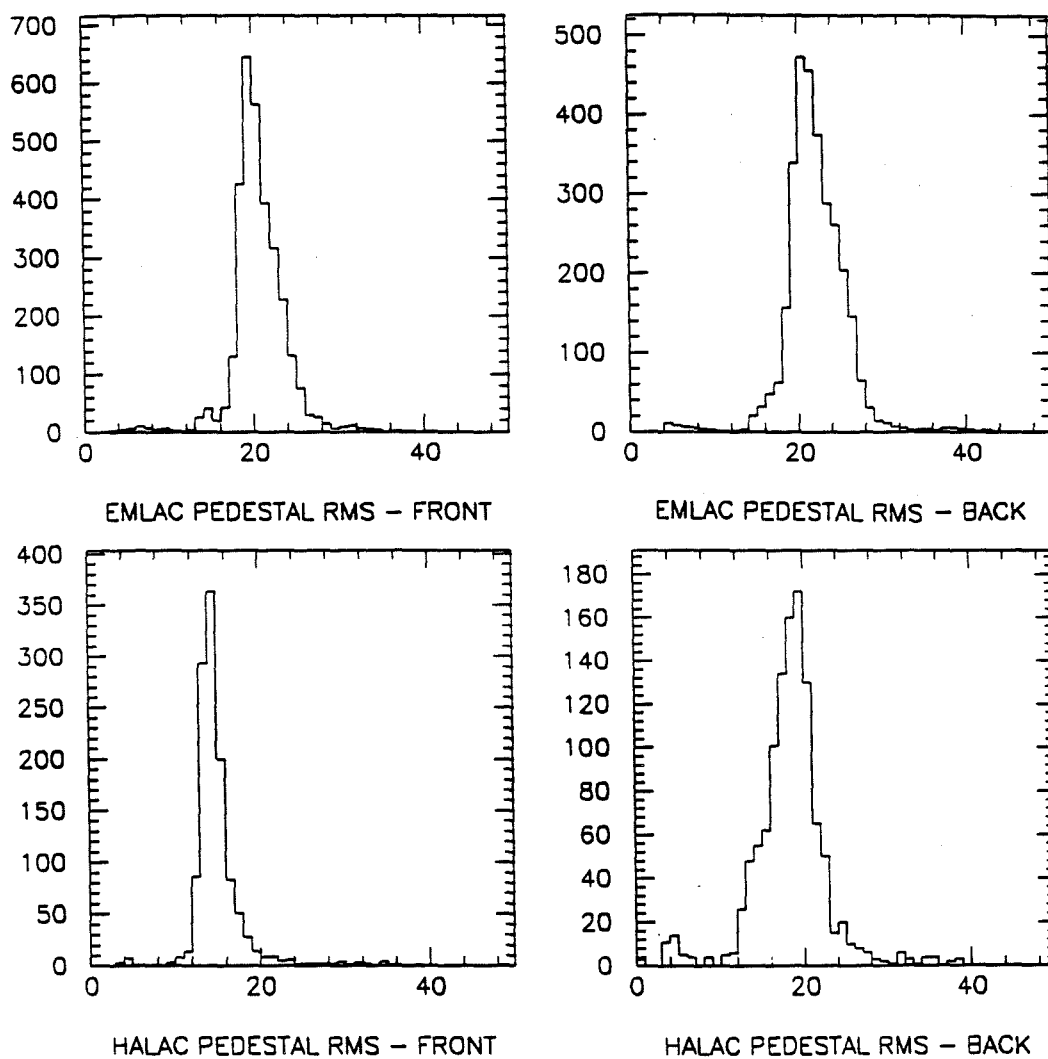


Figure 4.5 Distribution of the RMS of pedestal distributions for LAC channels measured in ADC counts.

5. EMLAC ENERGY SCALE

5.1 OVERVIEW

The determination of a precise EMLAC energy scale is of critical importance since a small shift in the measurement of p_T can produce large changes in the cross sections at a given p_T due to the steep p_T dependence. For example, a relative uncertainty of 1% in the energy scale results in an uncertainty of about 11% in the π^0 inclusive cross section. Because of this extreme sensitivity, special care was taken in determining the energy scale for photons and electrons.

The first step in determining the energy associated with showers detected in the EMLAC involved adjustments applied at the unpacking level for the amplifier pedestals and gains as described in Sections 4.3 and 4.4. In addition, another correction was applied for the observed time dependence of the energy scale as mentioned in Section 2.3.

The next correction accounted for octant-to-octant variations in the overall energy scale, attributed to variations in the construction and operation (e.g., different lead thicknesses, readout electronics, high voltage variations) of each octant.

A correction was also made to account for energy losses at the inner/outer ϕ boundary. The Monte Carlo was used to generate a correction for the energy lost due to showering in the material in front of the active region of the EMLAC (E-loss correction). This correction was found to be different for photon and electron initiated showers.

An additional correction to the shower energy was determined based on the radial dependence of the reconstructed π^0 mass observed in data. This correction was found to be approximately independent of the shower energy and particle type.

Finally, after the above corrections were applied to the photon and electron energies, using events in which one of the photons from a π^0 or η decay converted into an e^+e^- pair upstream of the magnet, a search was performed for any residual energy corrections not accounted by the Monte Carlo E-loss correction.

The following sections describe the details of the method used to set the energy scale for photons and electrons. We will begin with a description of the electron and photon samples used in the study. Then the Monte Carlo simulation will be discussed, followed by the list of all energy scale corrections applied to photons and electrons.

5.2 ELECTRONS

When a photon whose energy is above the two-electron mass threshold passes through matter, it may convert to an electron-positron pair. For photon energies above 1 GeV, the probability (P) for pair creation is approximately constant with energy and given by^[1, 2]

$$P = 1 - e^{-7X/9} \quad (5.1)$$

where X is the thickness of the material in radiation lengths. Since most of the photons in our data originate from π^0 or η decays, these were the primary sources of electron-positron pairs. These photon conversions occurred mainly in the target material and the SSD planes.

The invariant mass of the electron-positron pair is approximately $2m_e$ -- i.e., very nearly zero -- and we will refer to these conversion electrons as ZMPs (Zero Mass

[1] K. Kleinknecht, *Detectors for Particle Radiation*, Cambridge University Press 1986.

[2] J. W. Motz et al., *Rev. Mod. Phys.* 41 (1969), 581.

Pairs). Most of the ZMP electrons were reconstructed as a single track in the SSD system since the opening angle of a ZMP is $\approx 2m_e/E_\gamma \approx 0.1$ mrad for a 10 GeV photon, comparable to the angular resolution of the SSDs. When the electron-positron pair passes through the magnet, the magnetic field causes the two tracks to bend in the X direction, producing two separate tracks in the three views (X, U and V) and one track in the Y view of the downstream tracking system.

Data Selection of ZMPs

The data selection of the ZMP electrons was based in the following geometrical characteristics:

- Oppositely charged tracks;
- Both tracks had same slope in their Z-Y projection plane;
- Both tracks intersected near the center of the magnet in their Z-X projection plane.

During the event reconstruction pass, the candidate ZMP electron tracks were flagged and various bits were set in order to readily identify these events during the data analysis. After selecting a pair of oppositely charged tracks, the following requirements were used to identify ZMPs in the data:

ΔS_Y : Difference between the Z-Y slopes of the two tracks less than 3 mrad;

ZXI : Z-X intersection point between 188 and 208 cm;

ΔR : Distance between the projected track position at the front face of the EMLAC and the closest shower position less than 2 cm, specifically

$$\Delta R = \sqrt{(X_T - X_S)^2 + (Y_T - Y_S)^2} < 2 \text{ cm}, \quad \text{where the } T \text{ subscript corresponds to the track and the } S \text{ to the shower (Fig. 5.1).}$$

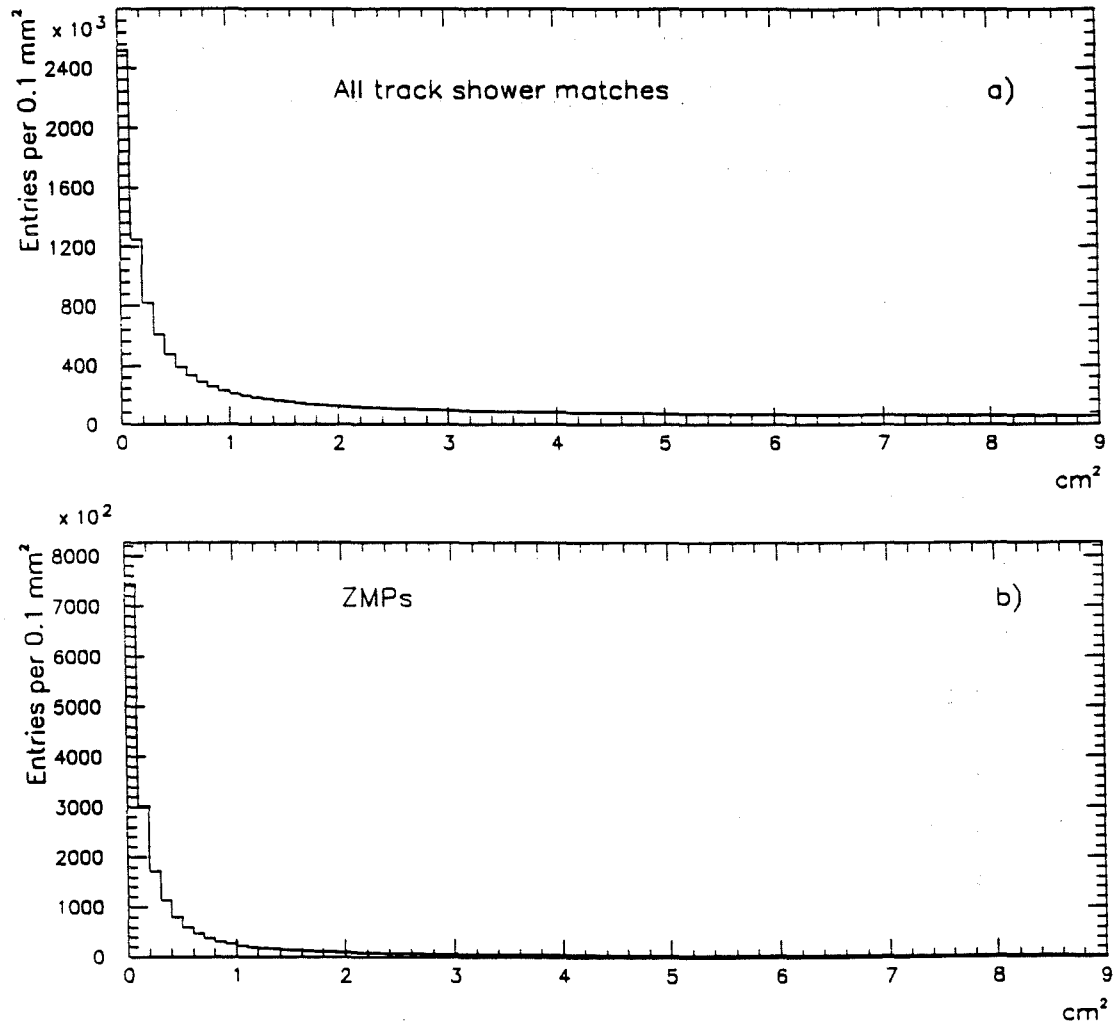


Figure 5.1 ΔR^2 distribution for track-shower matching. ΔR^2 for a) all track-shower matches and b) ZMP tracks.

Fig. 5.2a shows the ΔS_Y distribution for all oppositely charged tracks. When we apply the additional constraint given by the ZXI cut, the ZMP signal is more pronounced as shown in Fig. 5.2b. If we also require that at least one ZMP track matched with an EMLAC shower with $E_{front}/E_{tot} > 0.5$ the signal becomes even cleaner (Fig. 5.2c), and if both tracks match with showers, the background is reduced substantially (Fig. 5.2d). In a similar way, we can illustrate the effects of the various cuts on the ZXI distribution in Fig. 5.3. The cleanest signal is when we apply the ΔS_Y cut to doubly matched oppositely charged tracks as shown in Fig 5.3d.

The analysis of the ZMP electrons was done from the DST output data stream where a further selection was made in order to generate a cleaner sample of ZMPs with tighter cuts; i.e., $|\Delta S_Y| < 2.5$ mrad, $193 < ZXI < 203$ cm and $\Delta R < 1.5$ cm. Subsequently further cuts were applied on either the ZMP tracks or the EMLAC showers depending on the purpose of the study. These cuts will be described as they become relevant.

Characteristics of ZMP Electrons

Having defined the ZMP electron sample, it is instructive first to examine its characteristics. Since the primary sources of ZMP electrons are π^0 and η decay photons, it is expected that the momentum spectrum of these electrons will be heavily weighted towards the low momentum region, as shown in Fig. 5.4. Furthermore, the position distribution of electrons that intersect the sensitive regions of the EMLAC is momentum dependent, mainly due to the impulse of the analyzing magnet's field. At low momenta (Fig 5.5a), the effect of the magnet is more pronounced, and the electrons are primarily distributed horizontally across the face of the EMLAC. At higher momenta, the electron positions become more uniformly distributed (Fig.

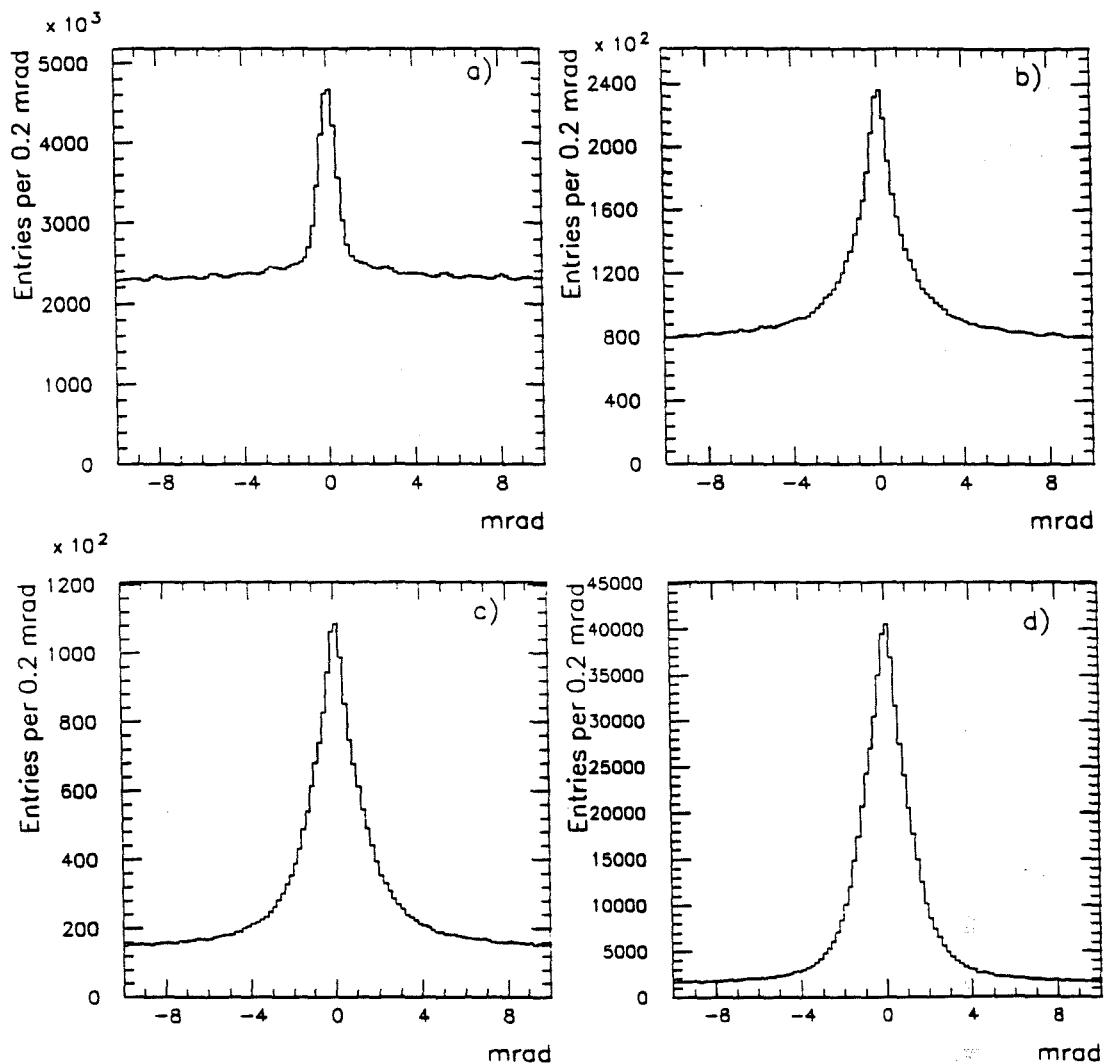


Figure 5.2 ΔS_Y distributions. The effect for various cuts on the ΔS_Y distribution: a) all oppositely charged tracks; b) $188 < ZXI < 208$ cm; c) at least one ZMP track matched with shower with $E_{front}/E_{tot} > 0.5$; d) both ZMP tracks matched with showers. Each plot has the cuts of the previous plot.

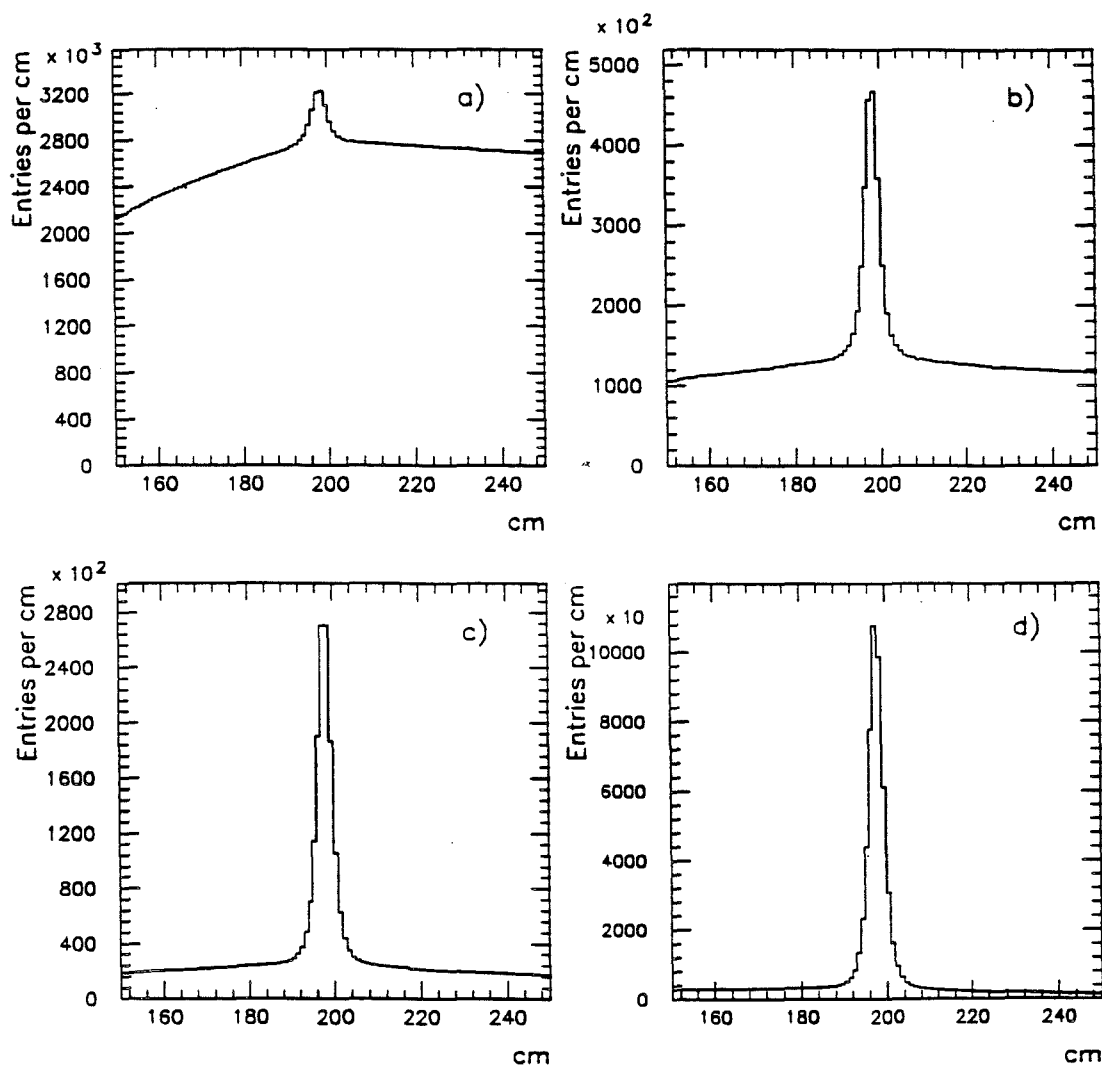


Figure 5.3 *ZXI* distributions. The effect for various cuts on the *ZXI* distribution: a) all oppositely charged tracks; b) $|\Delta S_Y| < 3$ mrad; c) at least one ZMP track matched with shower with $E_{front}/E_{tot} > 0.5$; d) both ZMP tracks matched with showers. Each plot has the cuts of the previous plot.

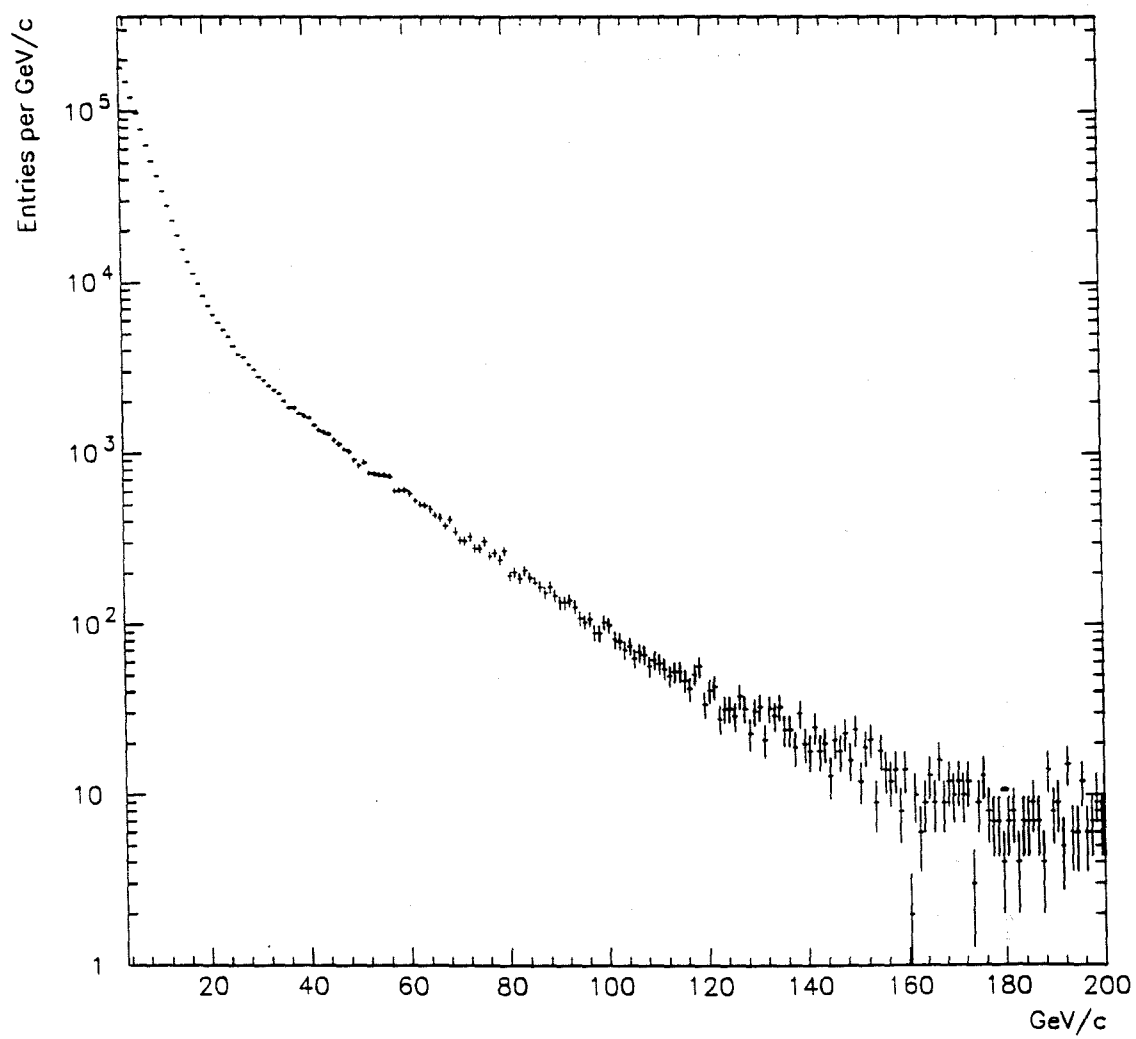


Figure 5.4 Momentum spectrum of ZMP tracks.

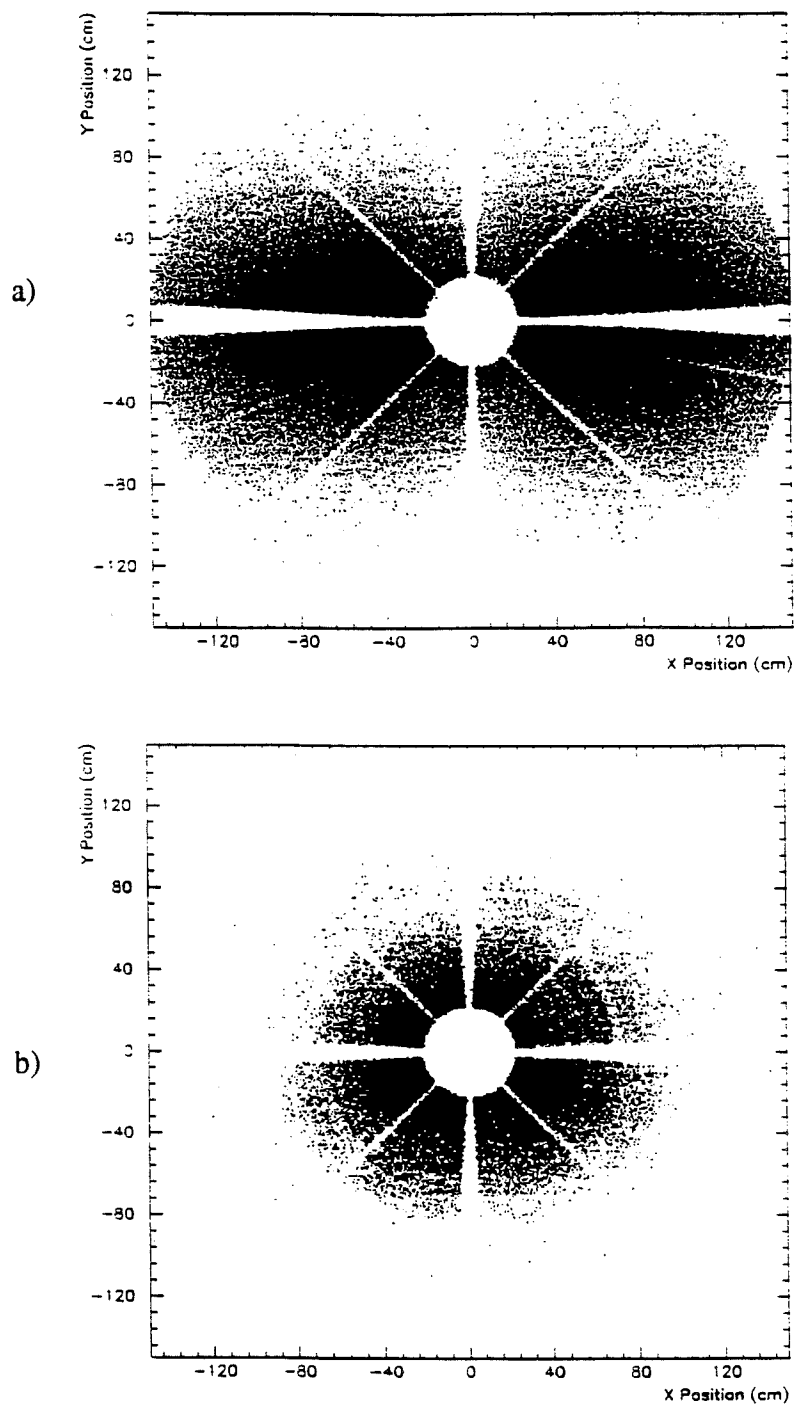


Figure 5.5 Position of ZMP electrons at EMLAC with a) $P < 10$ GeV/c and b) $P > 20$ GeV/c.

5.5b). In these plots, the EMLAC hole, as well as the octant and quadrant boundaries are clearly visible.

A variable sensitive to the differences between hadronic and electromagnetic showers is the E_{front}/E_{tot} ratio. A typical electromagnetic shower tends to deposit most of its energy in the first few radiation lengths of the detector. Fig. 5.6a shows the E_{front}/E_{tot} for all showers that matched with tracks. The peak at low values of E_{front}/E_{tot} is attributed primarily to hadronic showers, whereas the electromagnetic showers tend to populate the high end of the E_{front}/E_{tot} distribution. The E_{front}/E_{tot} distribution for ZMP electrons is shown in Fig. 5.6b. The hadronic bump is very significantly reduced. Fig. 5.7 shows the E_{front}/E_{tot} distribution for selected energy bins with the additional “cleaning” requirement that both ZMP tracks match with showers. A requirement of $E_{front}/E_{tot} > 0.4$ was used to reduce residual hadronic contamination.

Since the momentum of these electrons and positrons was independently determined from the tracking system, these particles provided a constraint upon the energy scale for showers measured in the EMLAC. The ratio between the electron energy (E) determined using the EMLAC and its momentum (P) determined by the tracking system for all tracks that matched with electromagnetic showers is shown in Fig. 5.8a. If we require that the track belong to a ZMP and both tracks match with showers then the additional peak at low ratio values, which comes mainly from the hadronic background, is eliminated (Fig. 5.8b). To further clean the E/P distribution we applied in addition the following cuts:

- Both EMLAC showers were required to have $E_{front}/E_{tot} > 0.4$;
- Both EMLAC showers had χ^2 less than 5;

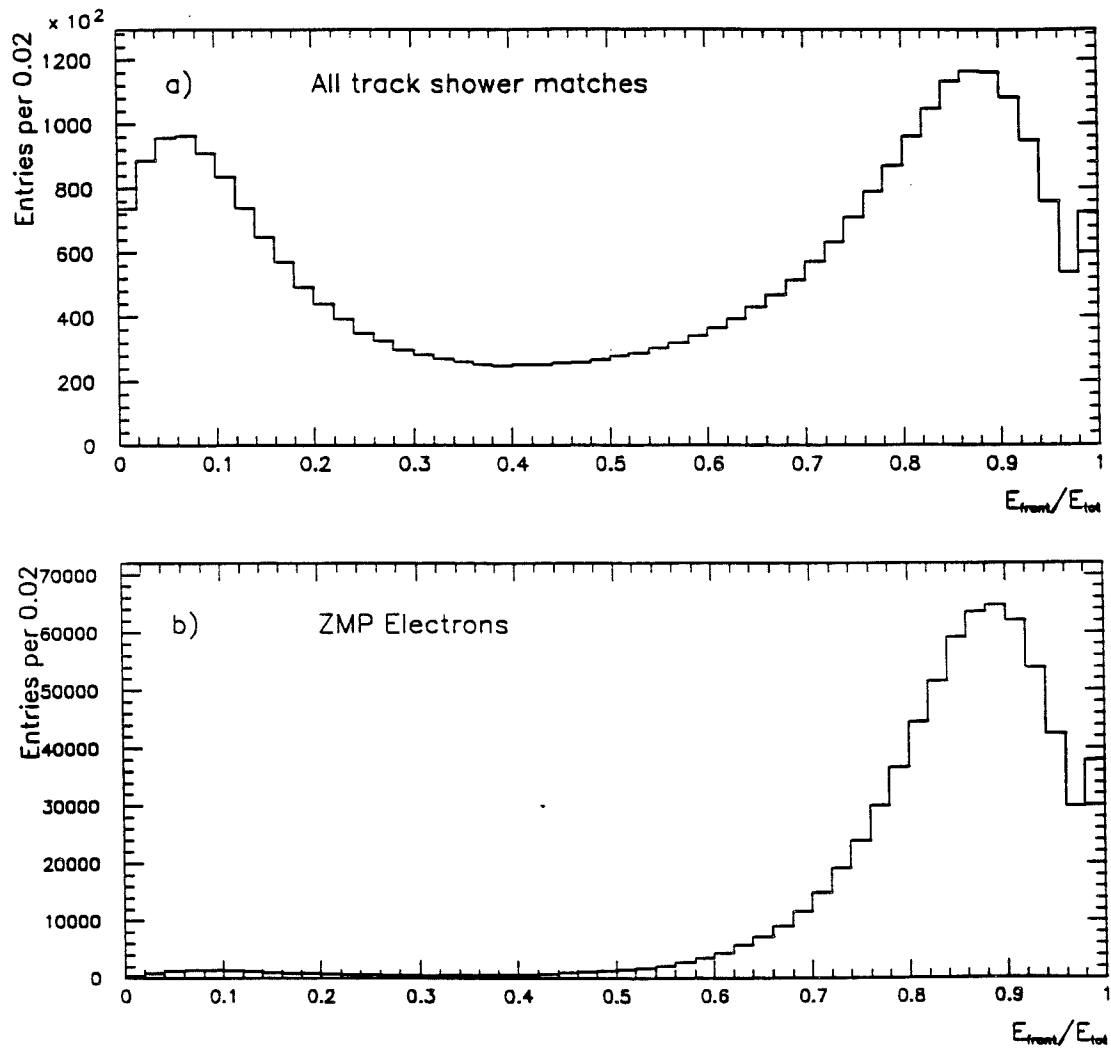


Figure 5.6 E_{front}/E_{tot} distribution a) for all EMLAC showers that matched with tracks and b) for ZMP electrons.

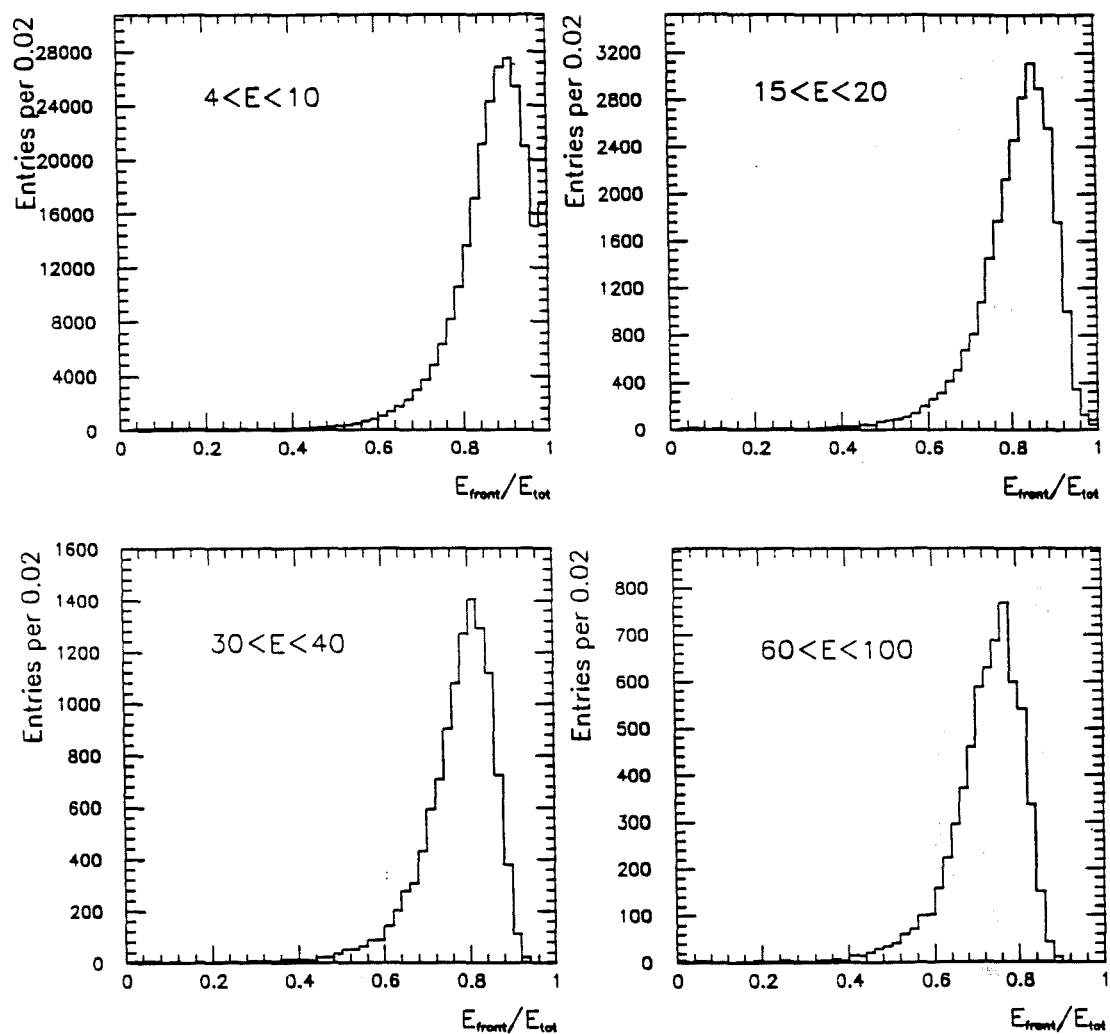


Figure 5.7 $E_{\text{front}}/E_{\text{tot}}$ distribution for ZMP electrons in different energy ranges. In this sample both ZMP tracks matched with showers.

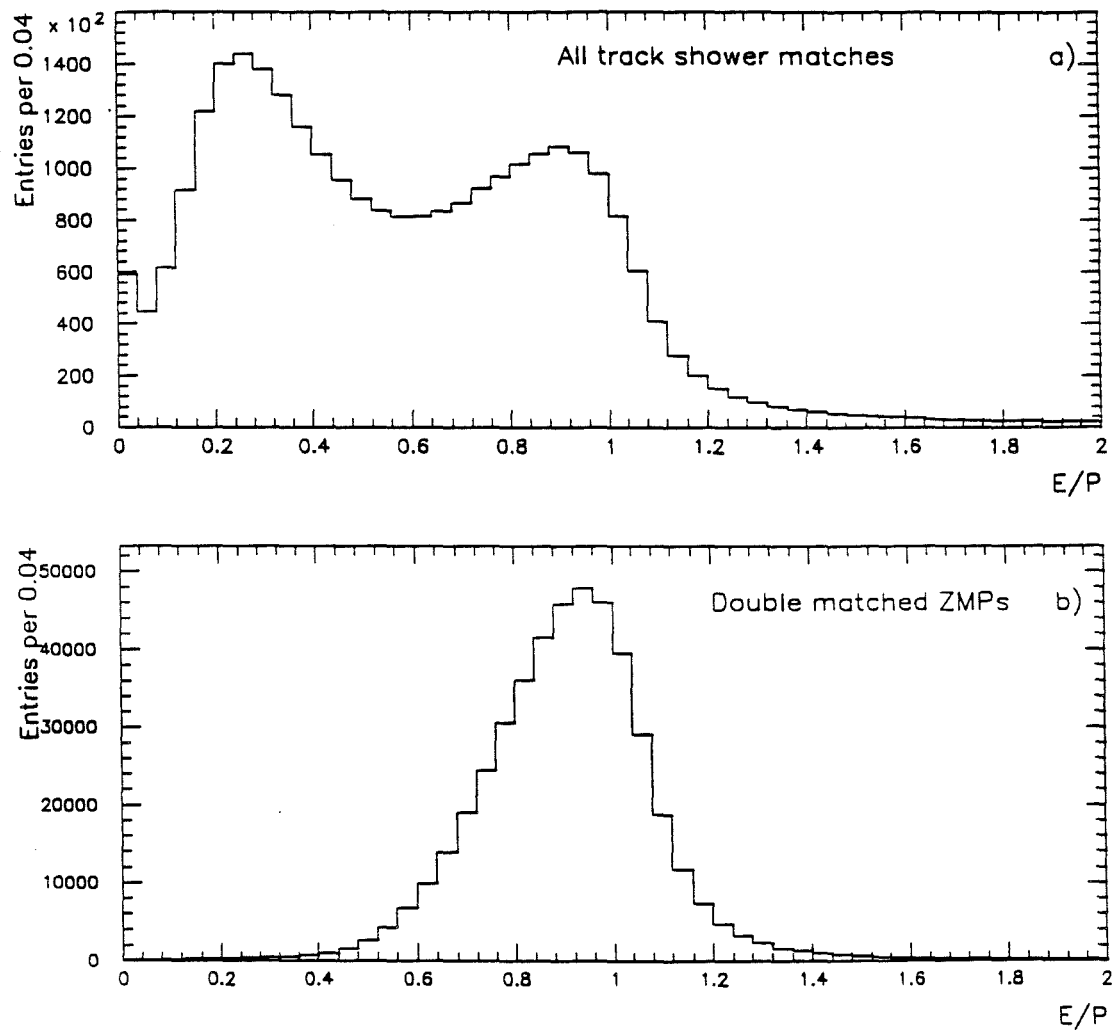


Figure 5.8 E/P distribution a) for all EMLAC showers that matched with tracks and b) for ZMP electrons for which both tracks matched with showers.

- Both ZMP downstream tracks were required to link with SSD tracks in both X and Y views, and point to the reconstructed vertex of the event;
- Both ZMP tracks had at least X view hits recorded in both STRAW tube modules;
- The reconstructed e^+e^- mass was less than $1.5 \text{ MeV}/c^2$ (Fig. 5.9).

After applying all these cuts, the E/P distribution for selected energy bins is shown in Fig. 5.10. This high quality sample of ZMP electrons was used for the energy scale studies.

Momentum Scale

Before describing how we used the electron momentum to investigate the energy scale in the EMLAC, we will describe how the momentum scale of the tracking system was established.

The momentum scale of the tracking system was calibrated by using the decays: $K_S^0 \rightarrow \pi^+\pi^-$ and $J/\psi \rightarrow \mu^+\mu^-$. The K_S^0 sample was constructed from pairs of oppositely charged tracks coming from secondary vertices. The J/ψ events were selected by the E672 dimuon trigger, but reconstructed via the E706 tracking system. Fig 5.11a and b show the K_S^0 and J/ψ mass peaks respectively.^[3] The reconstructed masses are within 0.1% of their accepted values.

5.3 PHOTONS

The photon samples used for the energy scale study originated from π^0 and η decays where both photons were detected by the EMLAC ($\gamma\gamma$ sample), or where one photon converted into an e^+e^- pair (ZMP) upstream of the magnet (γe^+e^- sample).

[3] L. de Barbaro, private communication.

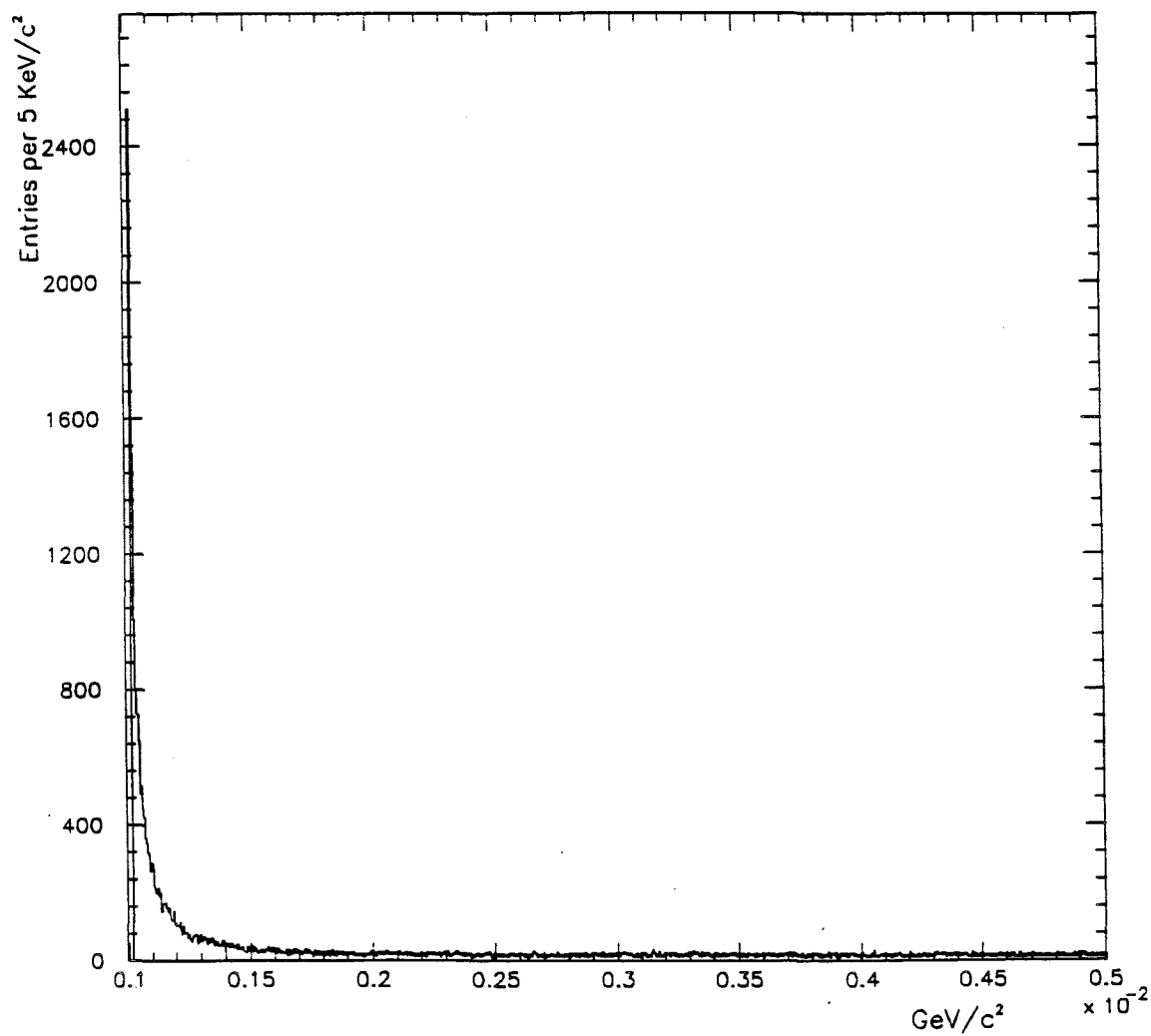


Figure 5.9 e^+e^- invariant mass distribution for double matched ZMP electrons after the cleaning cuts described in the text. Only tracking information was used to calculate the four momenta of these electrons.

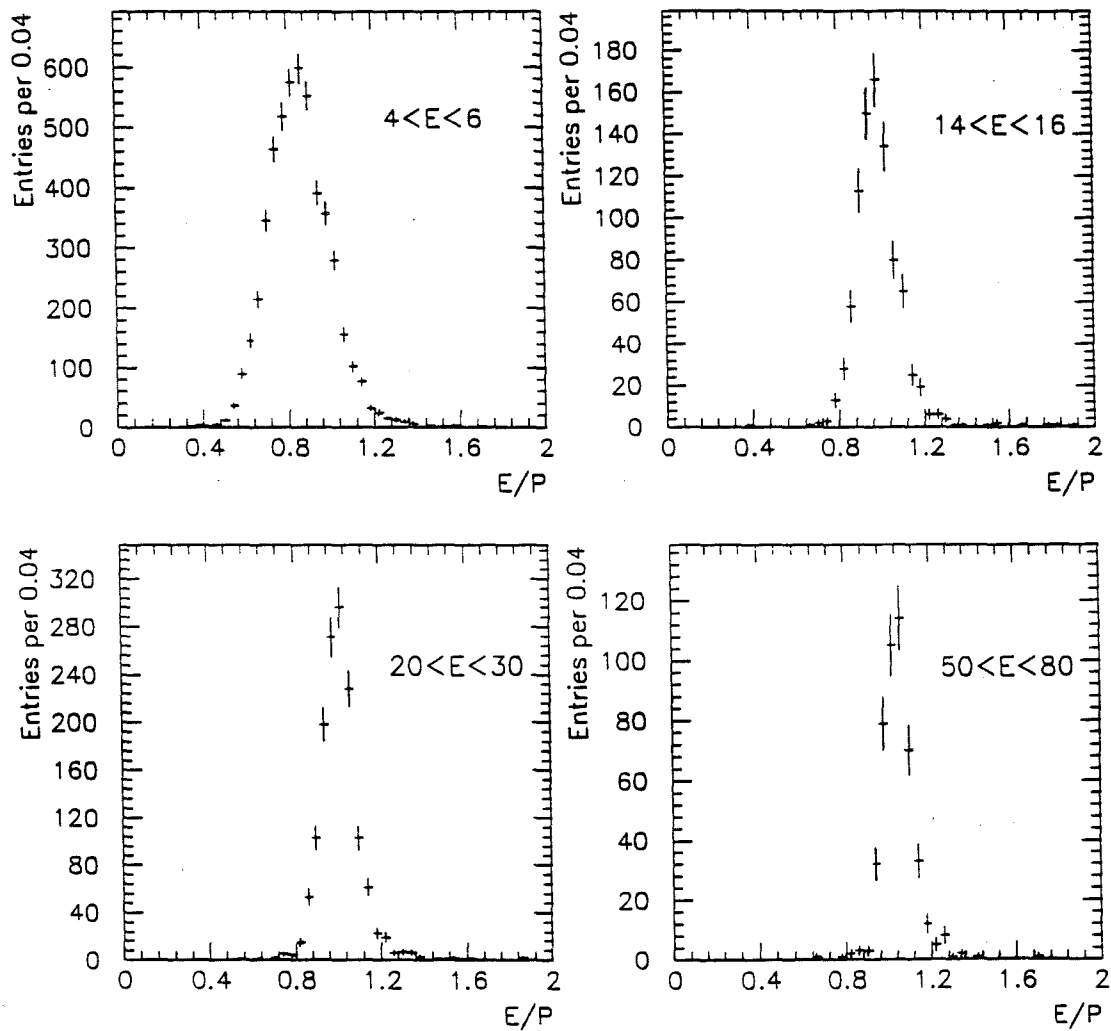


Figure 5.10 E/P distributions in several energy ranges for a high quality sample of ZMP electrons as described in the text.

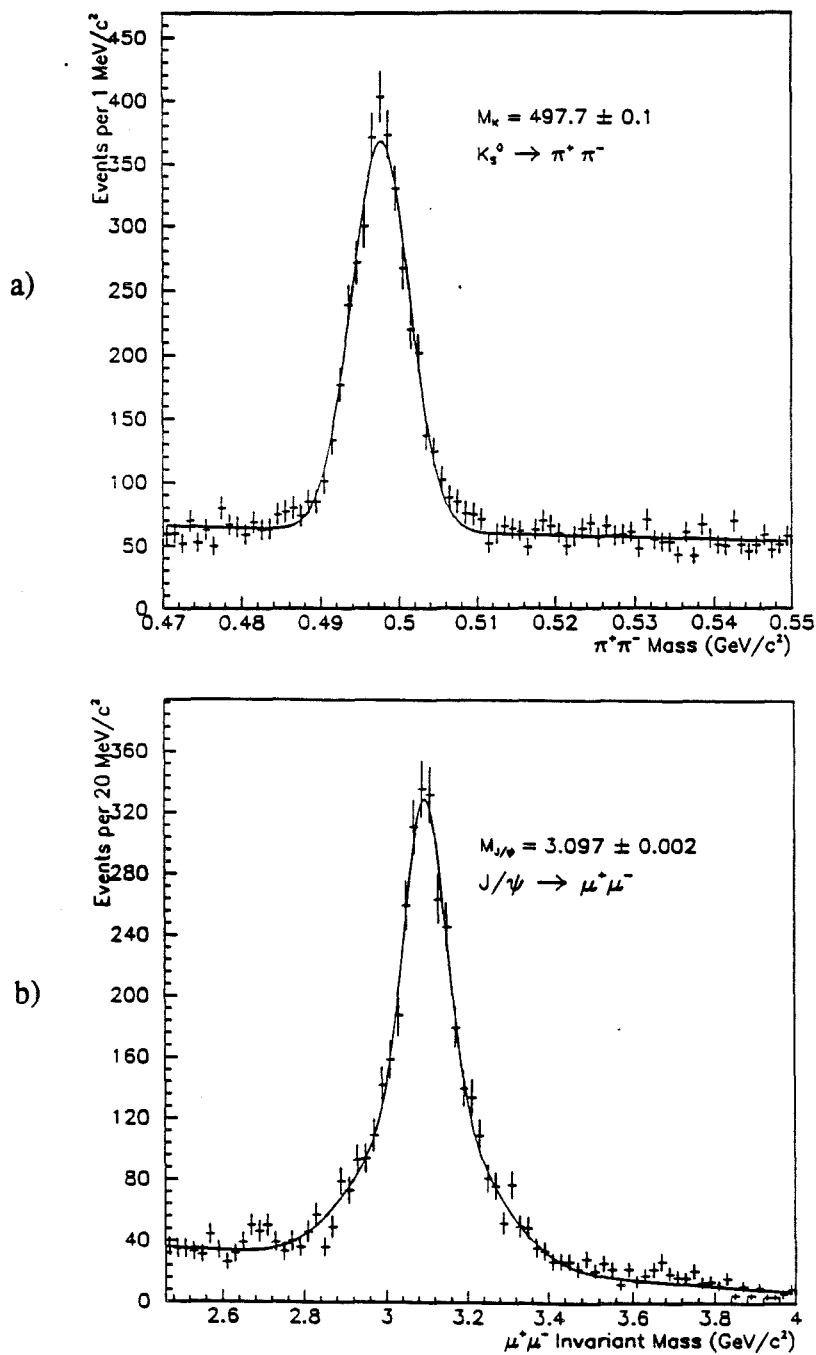


Figure 5.11 a) $\pi^+ \pi^-$ invariant mass in the K_S^0 mass region for secondary vertices upstream of the analysis magnet; b) $\mu^+ \mu^-$ invariant mass in the J/ψ region.

$\gamma\gamma$ Sample

Fig. 5.12 displays the $\gamma\gamma$ invariant mass spectrum for the two-photon pairs with $p_T > 3.5$ GeV/c that satisfy the following additional requirements:

- The event had a reconstructed vertex within the target area;
- Both photons were within the same octant;
- The three veto walls shadowing the EMLAC quadrant containing this photon pair did not contain evidence of an incident muon, where an incident muon was defined by a coincidence between a signal in the upstream veto wall quadrant and the logical OR of the signals from the two downstream veto walls;
- Both photons were within the fiducial region of the EMLAC;
- Both photons had χ^2 less than 5;
- Both photons had $E_{front}/E_{tot} > 0.2$.

The π^0 and η peaks are clearly visible. The solid line is the mass spectrum for all $\gamma\gamma$ pairs, while the dashed line represents only combinations which have an energy asymmetry of less than 0.5. The energy asymmetry is defined as:

$$A = \frac{|E_{\gamma 1} - E_{\gamma 2}|}{E_{\gamma 1} + E_{\gamma 2}} \quad (5.2)$$

where $E_{\gamma 1}$ and $E_{\gamma 2}$ represent the energies of the photons. This energy asymmetry cut was used to minimize the sensitivity of the reconstructed mass to possible uncertainties in energy scale as a result of two photons with large energy difference being close together.

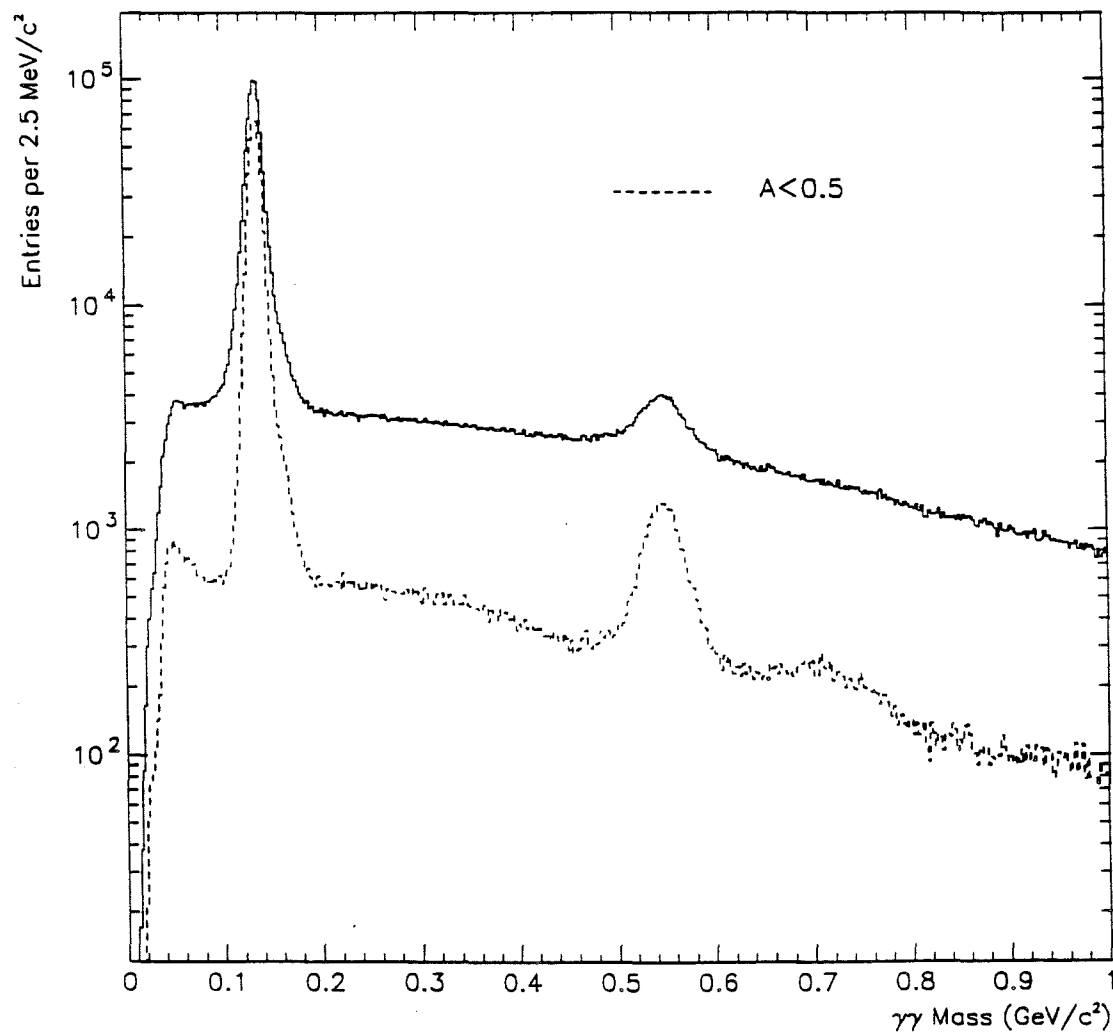


Figure 5.12 Two-photon invariant mass spectrum with $p_T > 3.5$ GeV/c. The π^0 and η peaks are clearly visible. The lower, dashed, line represents $\gamma\gamma$ pairs with energy asymmetry less than 0.5.

γe^+e^- Sample

Fig. 5.13 shows the three particle γe^+e^- invariant mass spectrum with total $p_T > 3$ GeV/c. Both π^0 and η signals are visible in this decay mode. The invariant mass was formed by the combination of the four momentum of the e^+e^- pair (using information only from the tracking system) with the four momenta of all other reconstructed showers in the event. Contributions to this plot are limited to those combinations for which both ZMP tracks matched with showers in the EMLAC and have $E_{front}/E_{tot} > 0.4$.

5.4 MONTE CARLO SIMULATION

The Monte Carlo simulation of the spectrometer used the GEANT software package developed at CERN.^[4] This package contains a data base of standard geometrical shapes and material properties which were used to model the E706 spectrometer. Each particle is tracked through the different parts of the spectrometer and allowed to interact. Each of the resulting daughter particles is then tracked in the same way and this process continued until the energies of the produced particles fall below a certain user defined limit. All the appropriate physics processes relevant in the development of electromagnetic showers are incorporated. This is a detailed method of event simulation and is referred to as the “full shower” method.

The LAC was modeled with special care inside GEANT.^[5] All geometrical dimensions and material specifications of the LAC components were carefully coded. Then this Monte Carlo was employed to generate a sample of ZMP electrons based

[4] R. Brun et al., GEANT3.15: CERN Data Handling Division, also in FNAL Computer Department publication PM0062 (1993).

[5] R. M. Roser, Eta Production at High Transverse Momenta by Negative 520 GeV/c Pions incident on Be and Cu Targets, Ph.D. Dissertation, University of Rochester (1994).

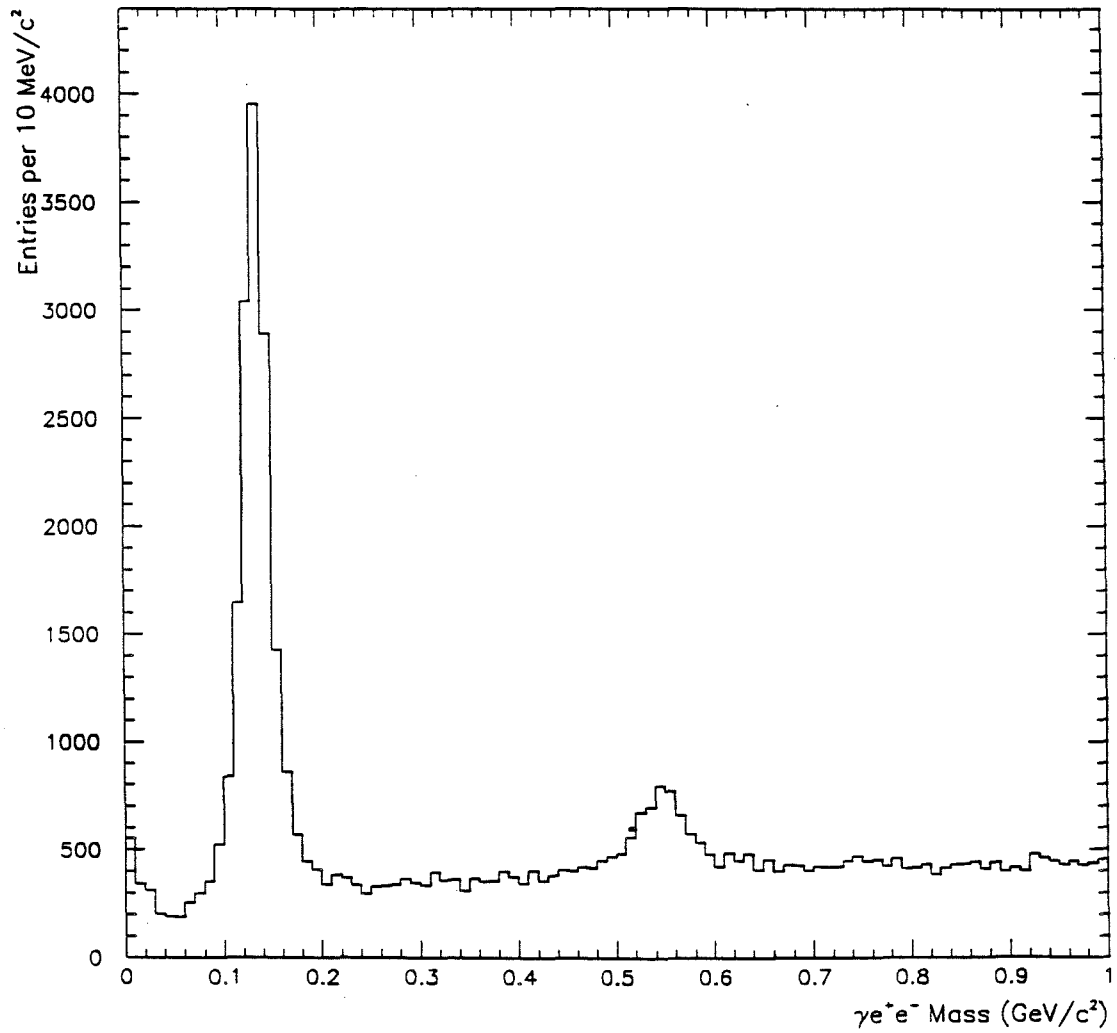


Figure 5.13 $\gamma e^+ e^-$ invariant mass spectrum with $p_T > 3$ GeV/c. The π^0 and η peaks are clearly visible.

on distributions taken from data. The results of this Monte Carlo simulation of the LAC were compared with various data distributions in order to fine tune the Monte Carlo performance. Due to the large CPU time required to generate complete electromagnetic showers, the threshold to which a particle was tracked through the LAC was tuned. For “full showers,” this threshold was set to 1 MeV and the electromagnetic showers produced with this cutoff were found to be in agreement with showers observed in data. However, in order to increase the Monte Carlo speed to an acceptable level, for general studies this threshold had to be raised to 10 MeV. The shower shape produced with this higher cutoff was adjusted by an empirical parametrization in order to match the shower shape observed in the data and reproduced by the “full shower” Monte Carlo. The details of this work are presented in Ref. [5].

Before the Monte Carlo generated events were reconstructed, they were preprocessed to simulate LAC related hardware effects, including electronic noise and gains fluctuations, dead channels, and the discrete energy spectrum due to the EWE resolution. The advantage of this “preprocessor” was that various detector effects could be tuned after the Monte Carlo event generation thus decoupling the electronics simulation from the shower generation which was the most CPU intensive part of the program.

The HERWIG event generator developed at CERN,^[6] was used as an input to GEANT to simulate the event multiplicities for high p_T events seen in the data. Comparisons with various data distributions relevant to the π^0 reconstruction efficiency calculation will be presented in Section 6.3. In this section, the Monte Carlo events will be used for the EMLAC energy scale studies.

[6] G. Marchesini et al., HERWIG V5.6: CERN Data Handling Division, also in FNAL Computer Department publication PU0124 (1993).

5.5 ENERGY CORRECTIONS FOR PHOTONS

The corrections to the reconstructed energy of photon initiated showers was determined in several steps. These steps are described in the next paragraphs in detail.

Octant-to-Octant Corrections

A first order octant-to-octant energy scale correction was implemented by rescaling the reconstructed shower energies in each octant by a factor determined from the observed π^0 mass for that octant. Octant-to-octant variations were $\approx 2\%$ (RMS) as shown in Fig. 5.14, where the ratio of the uncorrected π^0 mass to its accepted value is plotted as a function of octant number, for $p_T > 3.5$ GeV/c. Since the final determination of the overall octant scale was established after the application of other corrections discussed in the following paragraphs, fine tuning of the octant-to-octant variations was performed after all corrections were applied to the photon energies and was based on the observed η mass of each octant. The η signal was employed to minimize the sensitivity of the reconstructed mass value to the degree of overlap of the two photon showers, as photons originating from η decays have a separation which is about four times larger than that of photons coming from π^0 decays.

Inner/Outer ϕ Boundary Corrections

A correction to the ϕ GAMMA energies to account for reconstructed energy losses at the inner/outer ϕ boundary, was applied at the reconstruction level by EMREC (see Section 4.3). This correction was found to overcorrect the ϕ GAMMA

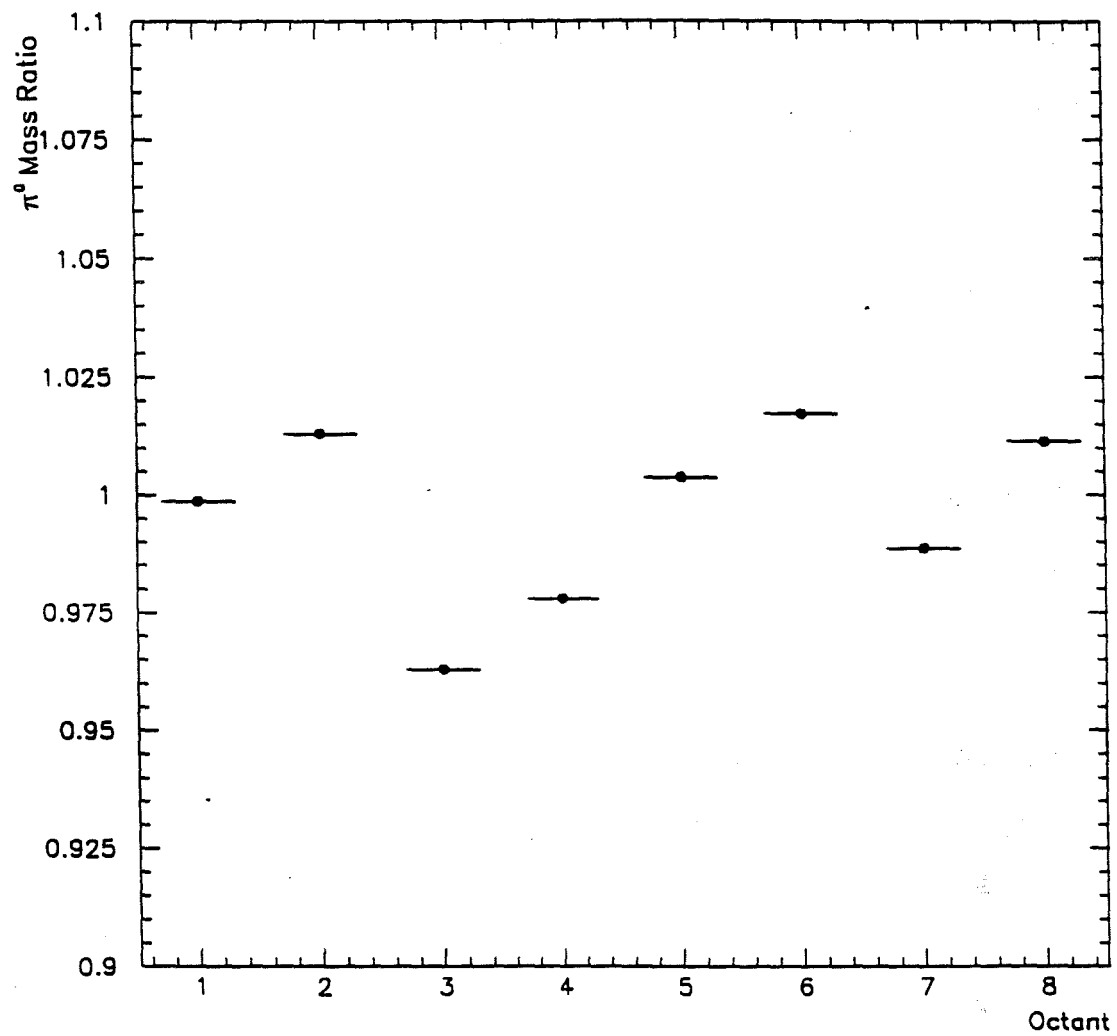


Figure 5.14 The ratio of the reconstructed π^0 mass to its accepted value as a function of octant number.

energies with respect to r GAMMA energies as indicated in Fig. 5.15, where the radial dependence of the reconstructed π^0 mass, with $p_T > 3.5$ GeV/c, relative to its nominal value is plotted using either twice the r view GAMMA energy as the photon energy (Fig. 5.15a) or twice the ϕ view GAMMA energy as the photon energy (Fig. 5.15b). Both octant-to-octant and E-loss (described below) corrections have been applied to the photons. To minimize the impact of sensitivity to the ϕ view complexity of the inner/outer ϕ boundary upon the photon's reconstructed energy, we elected to use as a total shower energy twice the r view GAMMA energy for showers reconstructed within ± 5 cm of this boundary.

E-loss Correction

The E-loss correction accounted for the energy lost due to showering in the material in front of the active region of the EMLAC. The Monte Carlo was used to determine this correction independently for photons and electrons. Fig. 5.16 shows the average energy lost for photon and electron initiated showers as a function of their reconstructed energy. The amount of energy lost for photons was about 40% less than the energy lost for electrons, which is attributed to the observation that photons start showering later than electrons.

Dependence of the Energy Scale on the Radial Position

The radial dependence of the reconstructed π^0 and η mass is shown in Fig. 5.17. The sample of π^0 events that contribute to Fig. 5.17 satisfied the $\gamma\gamma$ sample requirements and additionally the *TWO GAMMA* trigger requirement with $p_T > 2$ GeV/c, whereas the η events satisfied the *SINGLE LOCAL HI* trigger with $p_T > 3.5$ GeV/c. All of the already mentioned energy corrections have been applied

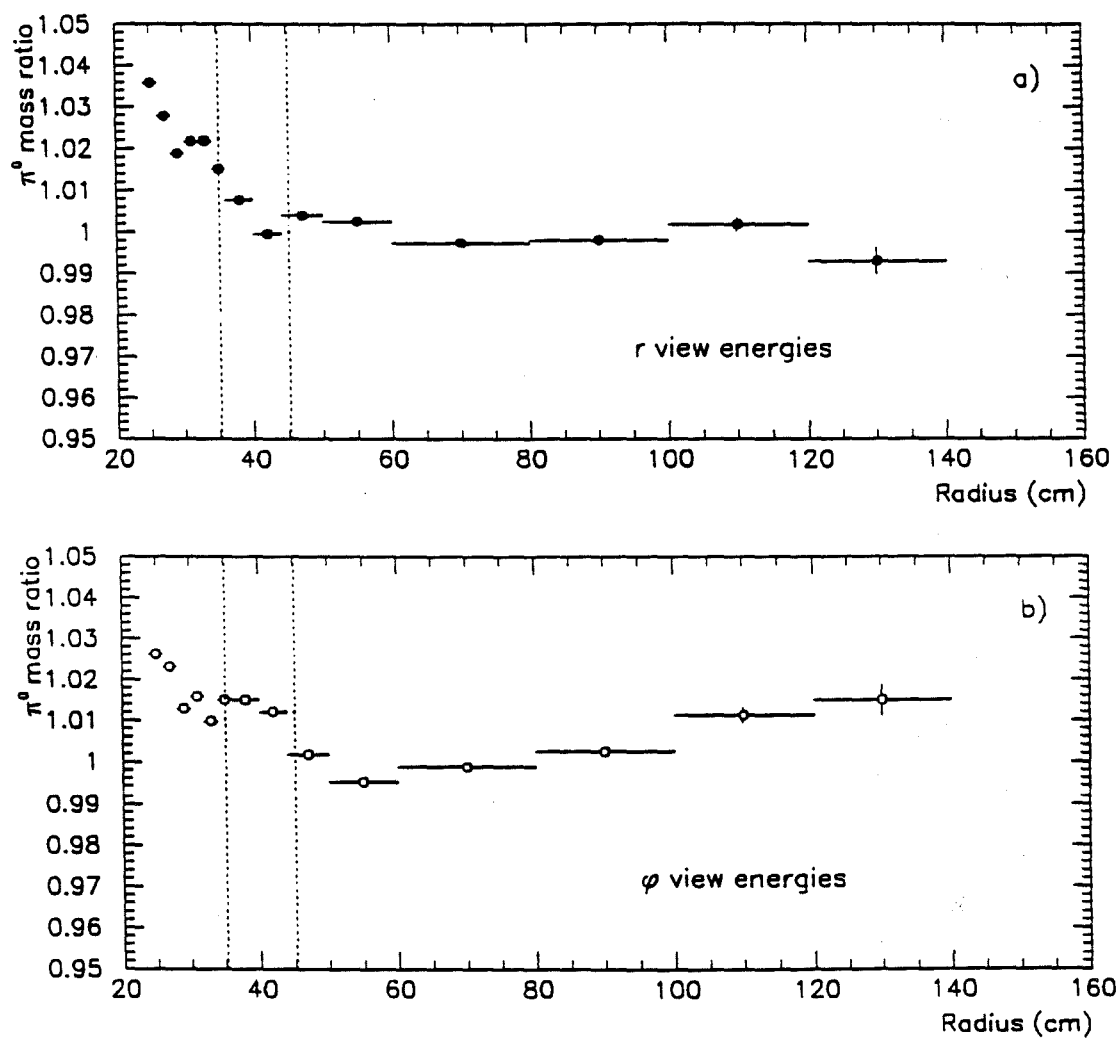


Figure 5.15 Radial dependence of the reconstructed π^0 mass relative to its accepted value using as photon energy a) twice the r view GAMMA energy or b) twice the ϕ view GAMMA energy. The dotted lines represent ± 5 cm from the inner/outer ϕ boundary.

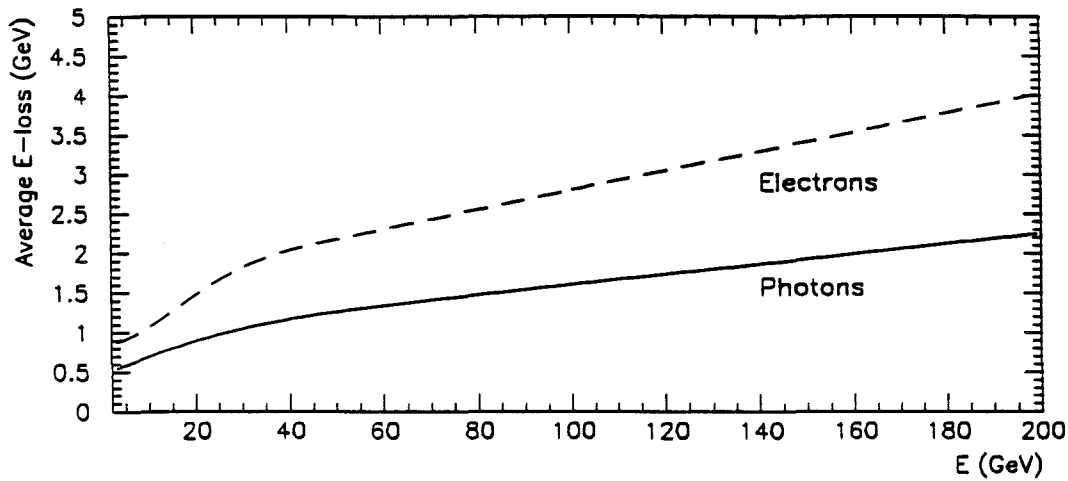


Figure 5.16 Average energy lost for photons (solid line) and electrons (dashed line) as a function of their reconstructed energy.

to the photons. From Fig. 5.17 we see that the measured π^0 and η masses are high in the inner r-region and decrease with radius. Since this sample of π^0 s and η s produce well separated photons, the observed radial dependence of the masses is attributed to residual radial dependence of the energy scale.

The radial dependence of η and low p_T π^0 masses is similar to the radial dependence of E/P for ZMP electrons of momentum $P \approx 20$ GeV/c, shown in Fig. 5.18. This also supports the hypothesis that the effect is related to the reconstructed energy, and that it is approximately independent of the shower energy and particle type[†].

[†] One hypothesis for the origin of the residual radial dependence of the reconstructed energy is that it is related to detector/capacitance effects on the signals produced in the EMLAC.

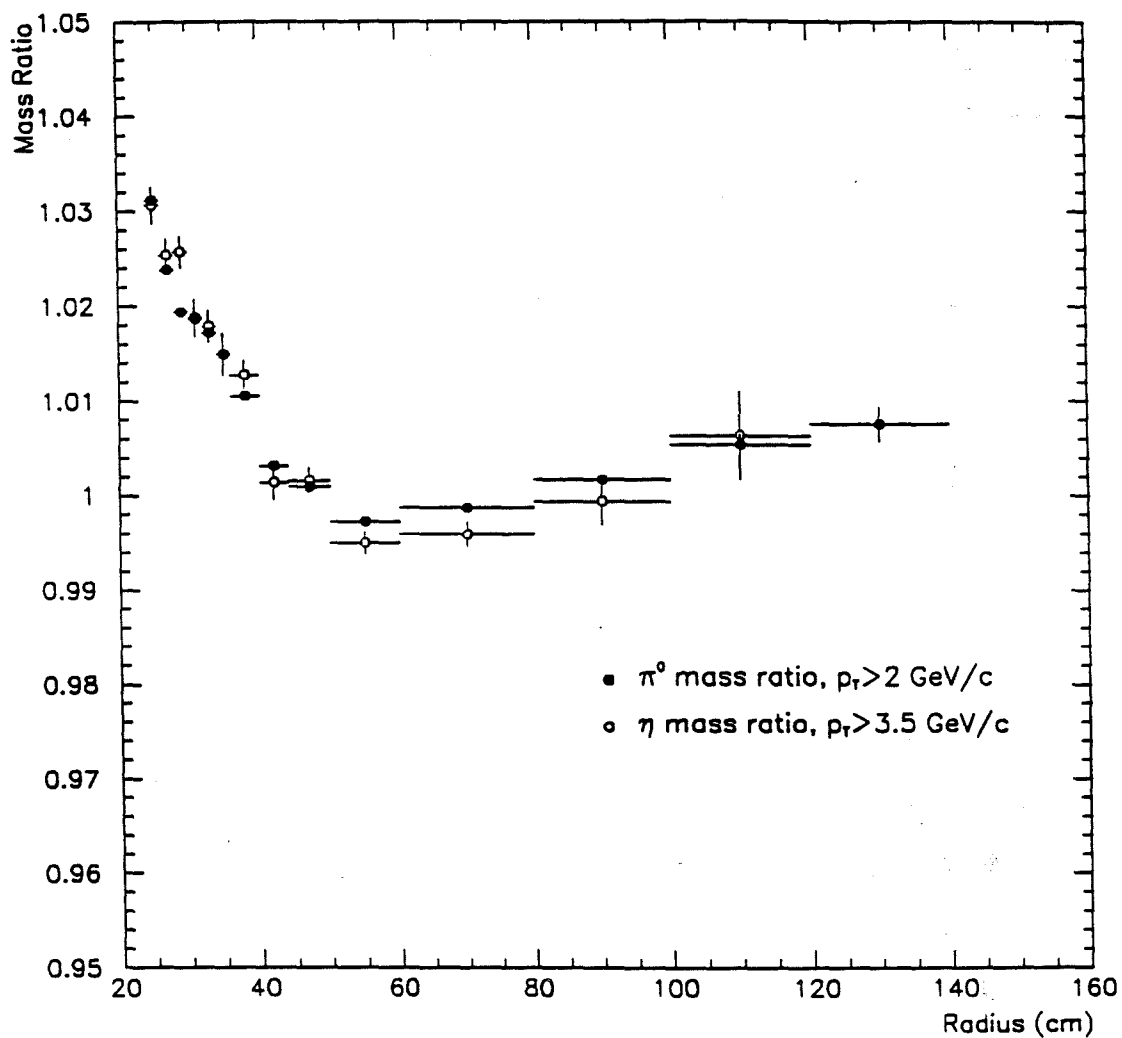


Figure 5.17 Radial dependence of the reconstructed π^0 and η masses relative to their accepted values. The π^0 events have $p_T > 2$ GeV/c whereas the η events have $p_T > 3.5$ GeV/c.

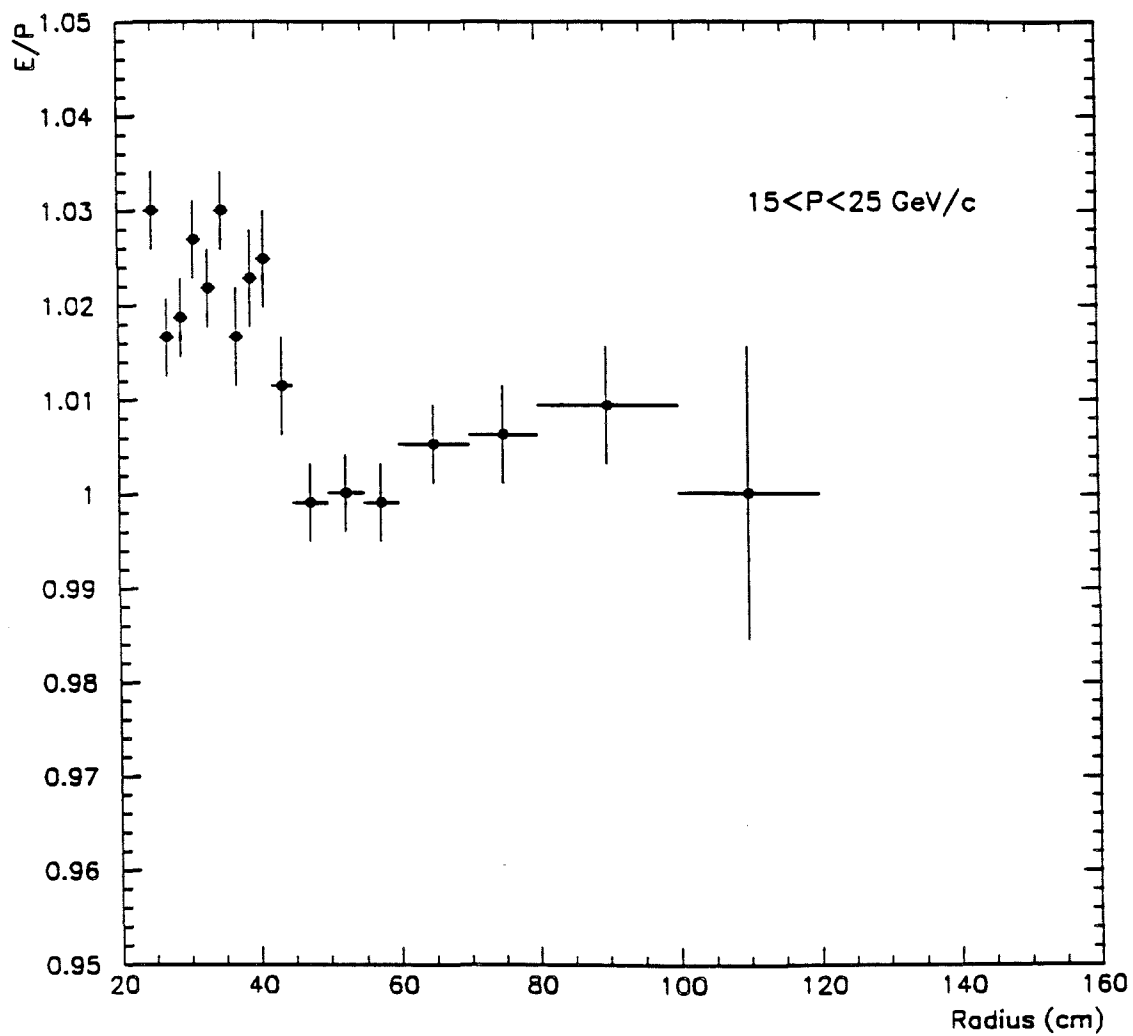


Figure 5.18 Radial dependence of the E/P ratio for ZMP electrons of momentum $P \approx 20$ GeV/c.

In addition, this effect is apparent in both r and ϕ view energies as illustrated in the Fig. 5.15. From Fig. 5.15 we also see that for radii greater than 60 cm, the ϕ view energies are increasing with radius relative to the r view energies. This difference in the energy scale between r and ϕ view energies is attributed to biases in the pedestal fitting algorithm FREDPED (see Section 4.3) for the outer ϕ view. Since the ϕ strip width is increasing with radius, more ϕ strips are eliminated from the pedestal fitting algorithm when a π^0 hits in the inner region of the outer ϕ view than when it hits in the outside part of the detector where the ϕ strips are wider.

In order to determine a correction to the shower energy as a function of the radial position of the shower in the LAC, the low p_T π^0 sample collected via the *TWO GAMMA* trigger was used. It was required that both π^0 photons had energies greater than 10 GeV in order to minimize the sensitivity of the reconstructed mass on any residual energy correction effects (i.e., not accounted by the E-loss correction). This radial correction was determined for each octant separately. The reason that this sample was chosen is twofold. First, it contained sufficient statistics to scan all octants in small radial bins. Second, the *TWO GAMMA* triggers had a lower p_T threshold than the *SINGLE LOCAL* triggers resulting in lower energy π^0 s which produce well-separated photons, and minimizing the sensitivity of the mass measurement on possible problems in reconstructing two overlapping photons.

Fig. 5.19 and 5.20 show the radial dependence of the relative π^0 mass for each octant. Based upon these distributions corrections were generated (by fitting the data points per octant) as an iterative procedure, and were based on the π^0 radial position. In these plots, the radial position of the π^0 was calculated as the energy weighted average of the radial positions of the two photons.

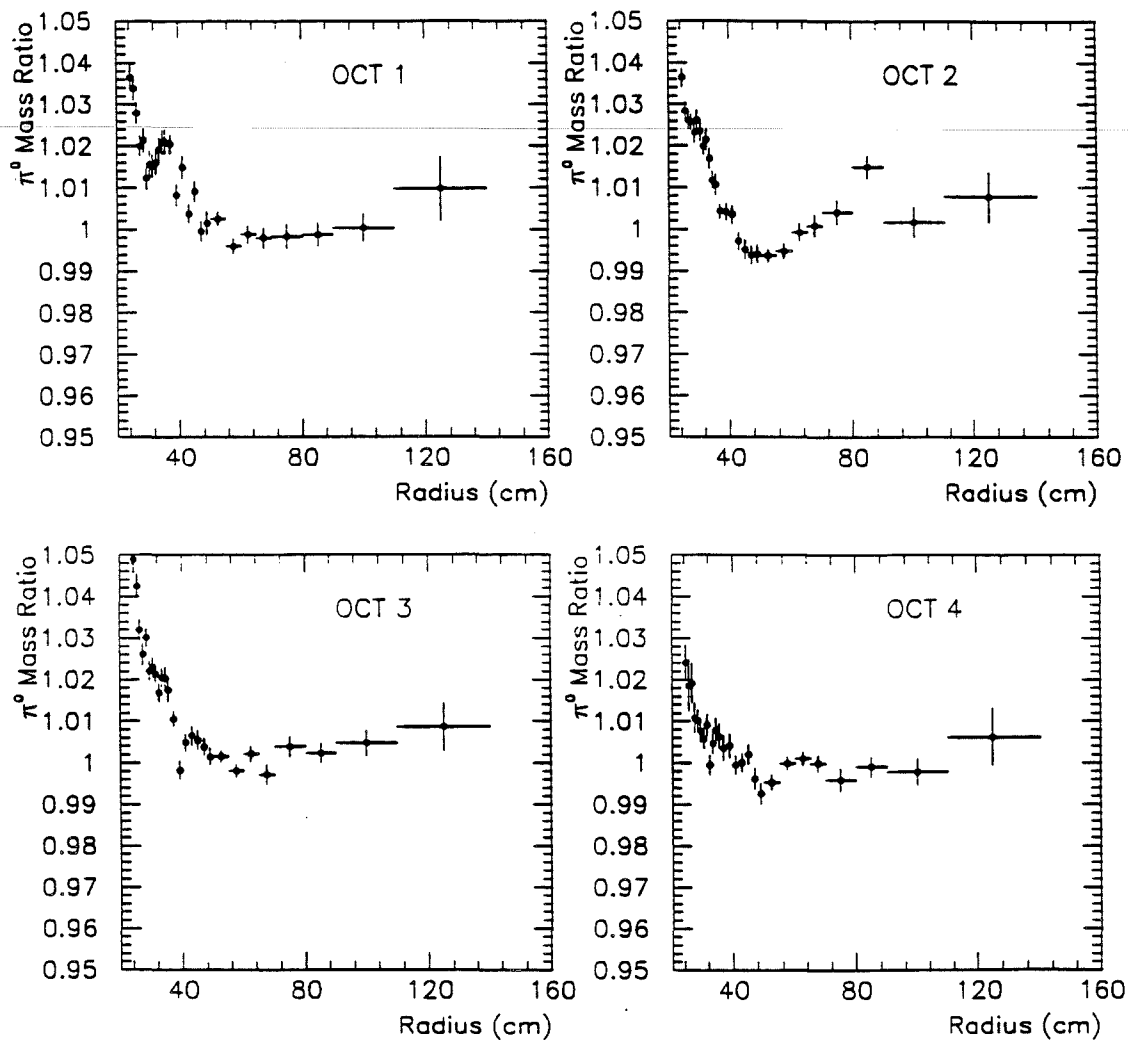


Figure 5.19 Radial dependence of the reconstructed π^0 mass with $p_T > 2$ GeV/c relative to its accepted value for octants 1 to 4.

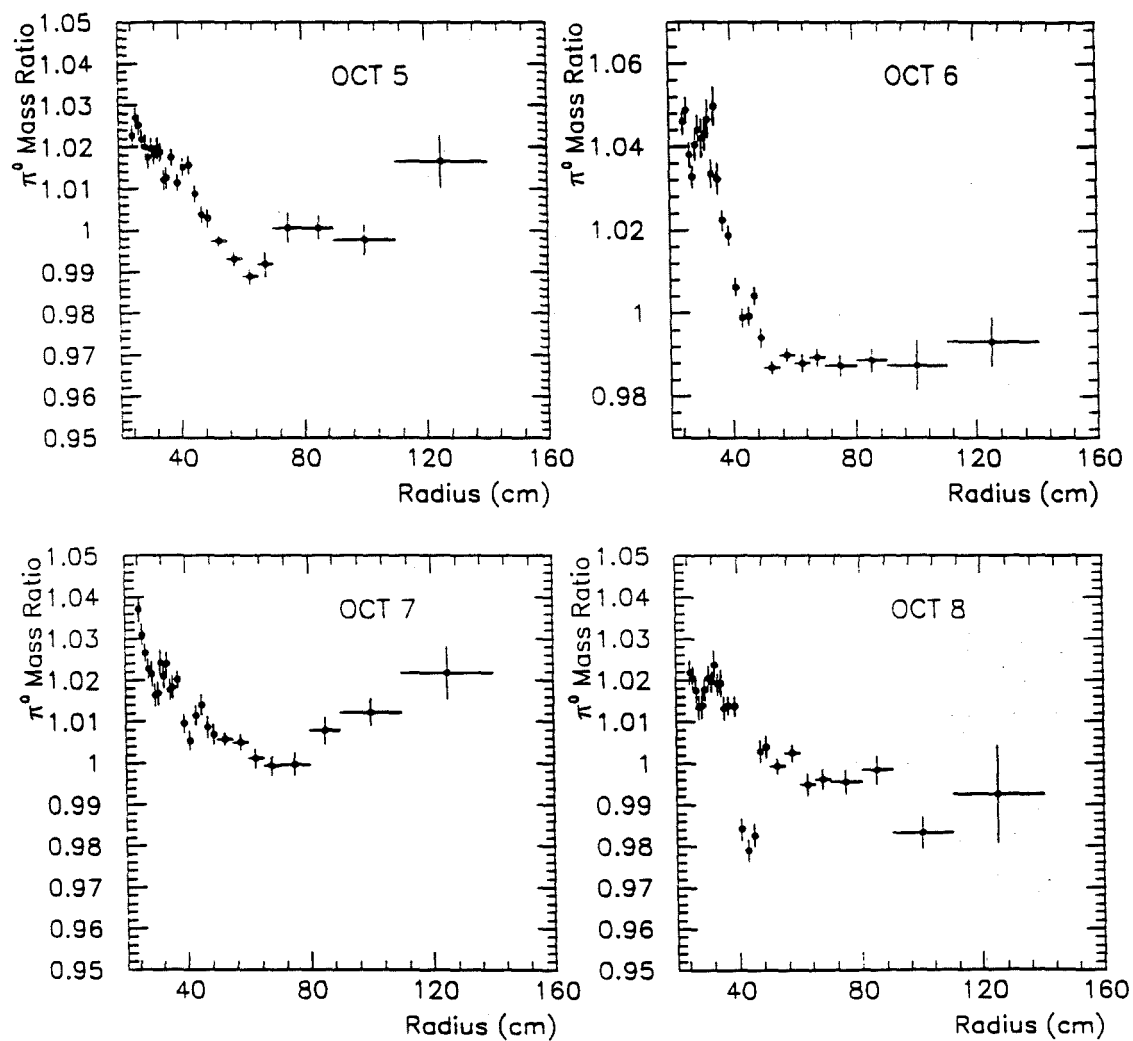


Figure 5.20 Radial dependence of the reconstructed π^0 mass with $p_T > 2$ GeV/c relative to its accepted value for octants 5 to 8.

The above radial corrections were valid for most of the running period. However, there was a period of approximately two weeks of running during which the BEFORE-AFTER gate was set to ≈ 400 ns (half of the standard value), and where the radial dependence of the energy scale was different. Fig. 5.21 shows the radial dependence of the relative π^0 mass with $p_T > 2$ GeV/c for these data. The effect is similar in magnitude, but opposite in sign to that shown in Fig. 5.17 (i.e., the energy scale increases with radius). The energy scale corrections applied to data from this running period were determined using the technique described above.

After all of the above corrections were applied to the photon energies, the final octant-to-octant scale was determined based on the measured η mass of each octant with $p_T > 4$ GeV/c.

Search for Residual Energy Corrections Using the $\gamma e^+ e^-$ Sample

With all energy scale corrections applied to photon energies and using the high quality sample of ZMP electrons, the resultant π^0 mass relative to its accepted value for the three particle $\gamma e^+ e^-$ system, with $p_T > 0.8$ GeV/c, is shown in Fig. 5.22a as a function of photon energy. No systematic variation in the mass as a function of the photon energy is apparent. This result suggests that the shower shape parametrization used to reconstruct the photon energies was very well tuned to match the observed photon shower shape, since there is no significant residual energy dependence that was not accounted for by the E-loss correction. However, the measured π^0 mass in the $\gamma e^+ e^-$ mode is about 1% lower than its accepted value. This is true for both π^0 and η masses evaluated via $\gamma e^+ e^-$ combinations with $p_T > 3$ GeV/c, as shown in Fig. 5.22b and c. The Monte Carlo reproduces this π^0 mass discrepancy between the two “decay” modes as illustrated in Fig. 5.23, and it is attributed to the electron’s

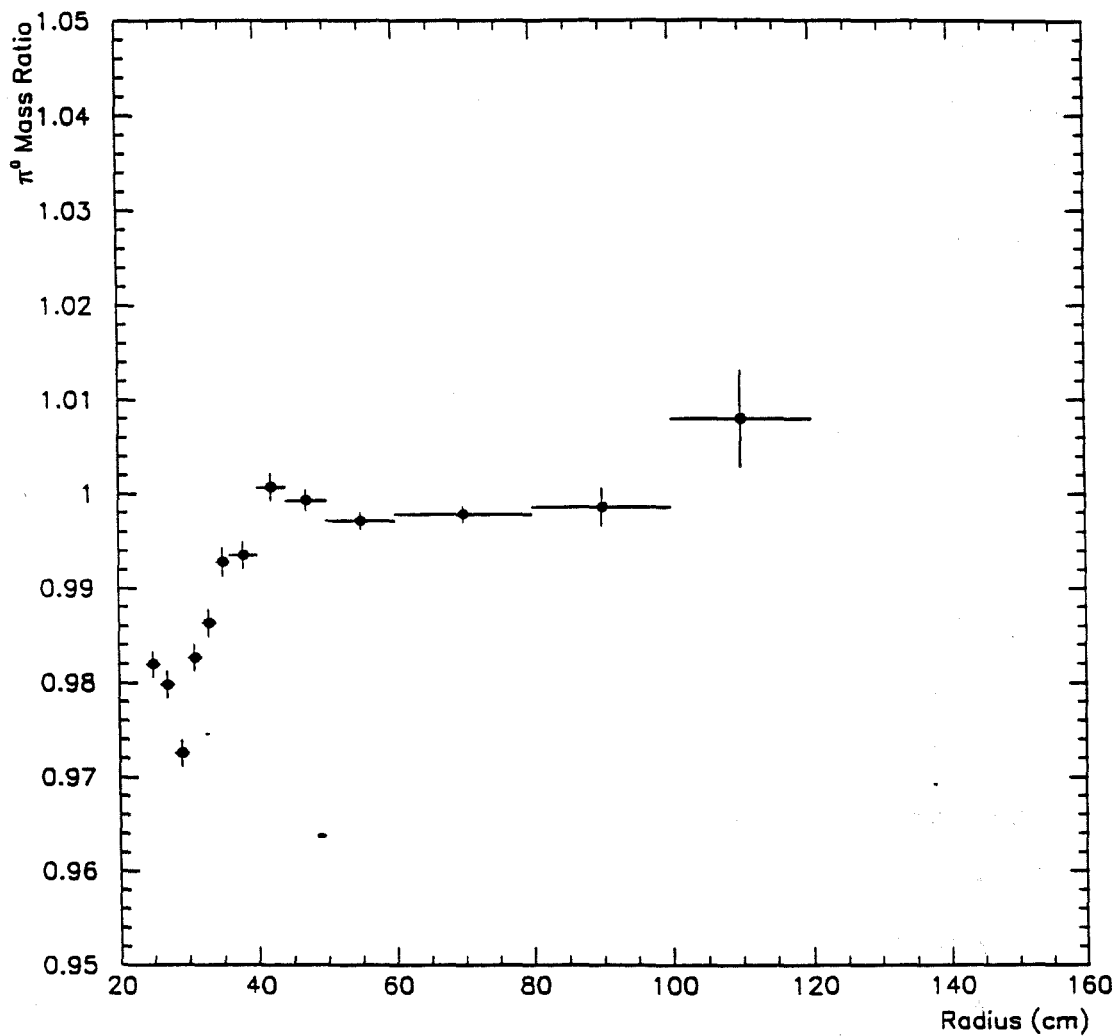


Figure 5.21 Radial dependence of the reconstructed π^0 mass relative to its accepted value for runs for which the BEFORE-AFTER gate was ≈ 400 ns, half of the standard value. The π^0 events have $p_T > 2$ GeV/c.

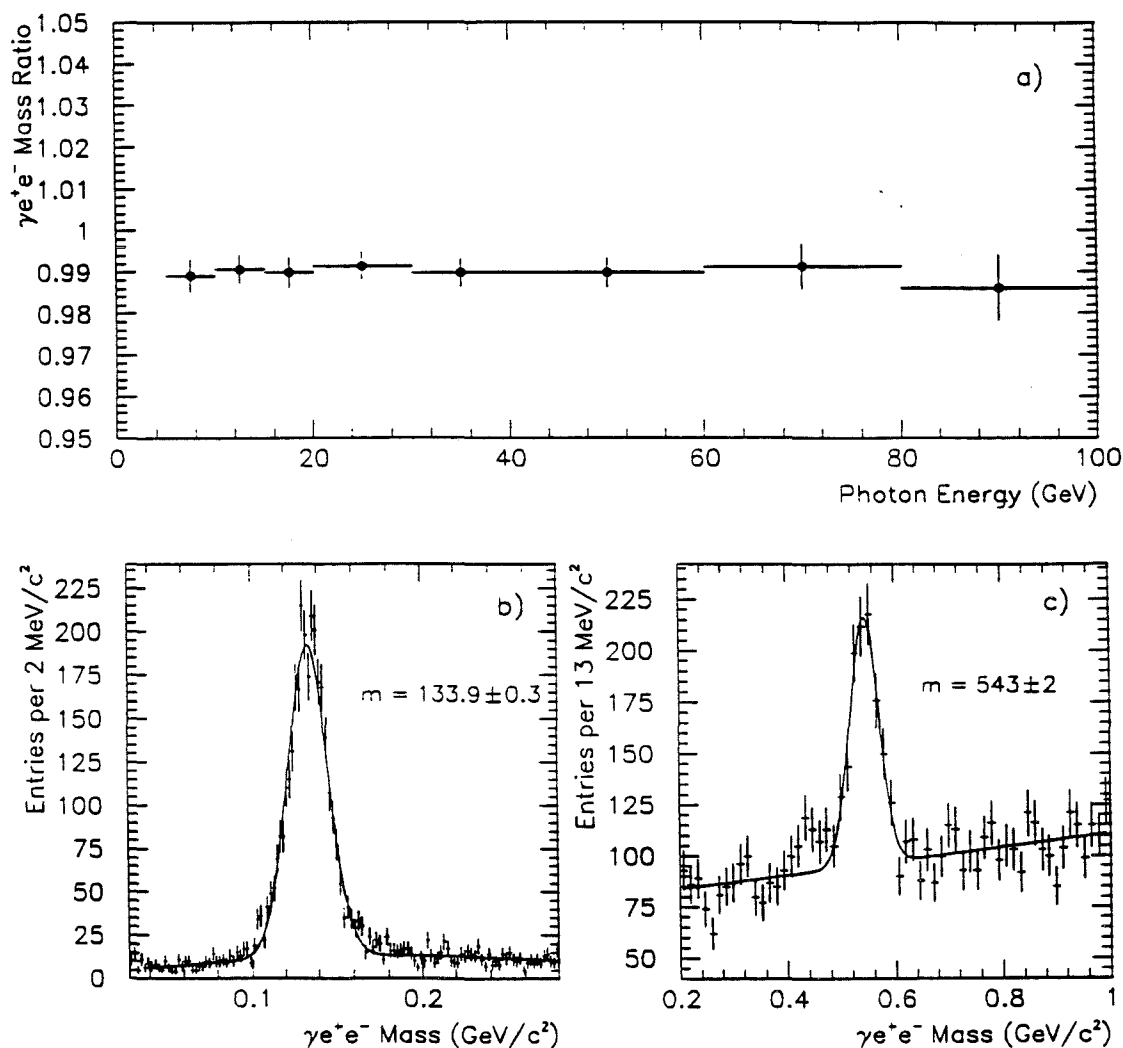


Figure 5.22

a) The ratio of the π^0 mass in the $\gamma e^+ e^-$ mode to its accepted value as a function of the photon energy. The $\gamma e^+ e^-$ events have $p_T > 0.8$ GeV/c. b) $\gamma e^+ e^-$ invariant mass distribution with $p_T > 3$ GeV/c in the π^0 mass region. c) $\gamma e^+ e^-$ invariant mass distribution with $p_T > 3$ GeV/c in the η mass region. For the above plots all energies are based on the final energy scale.

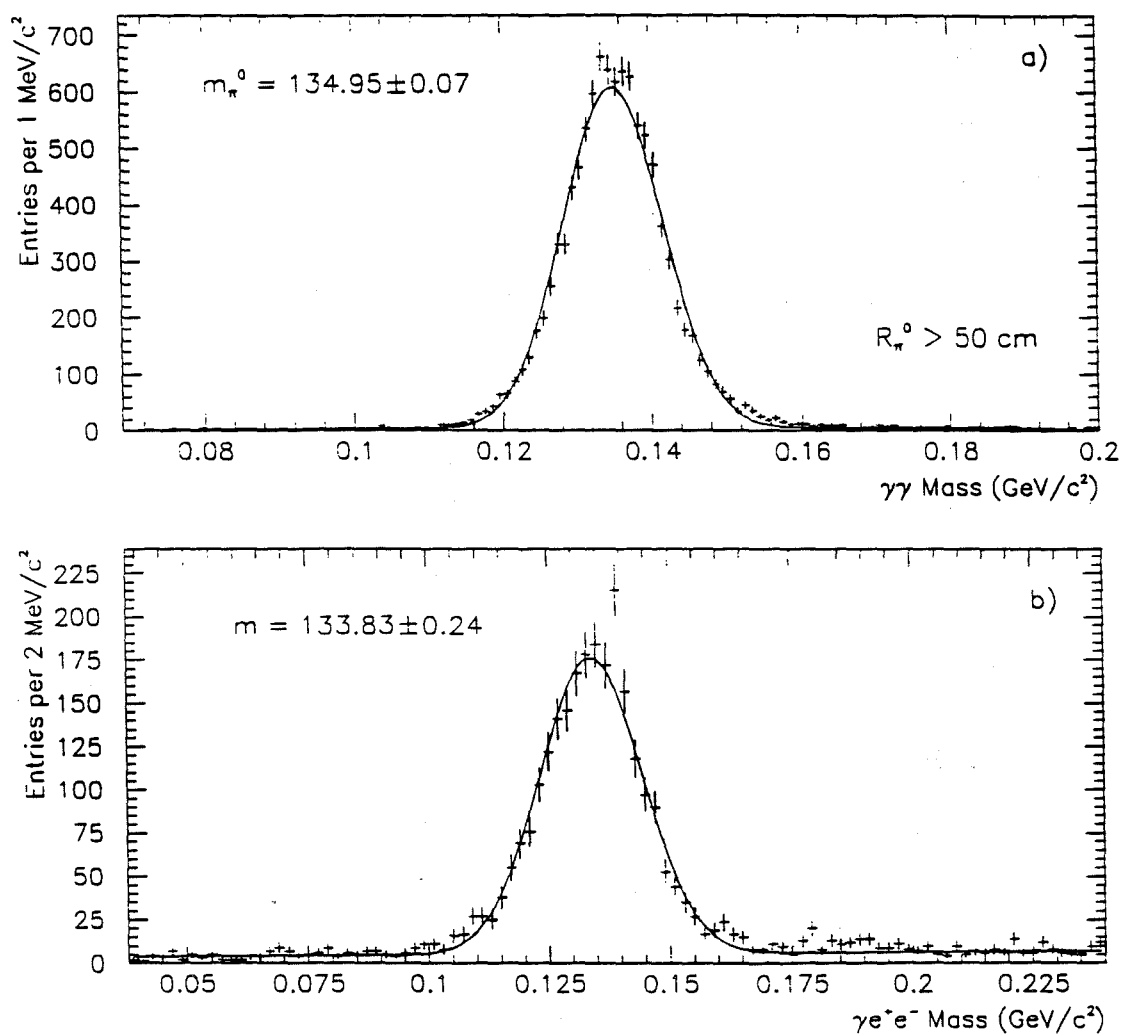


Figure 5.23

- a) Monte Carlo two-photon invariant mass distribution with $p_T > 4$ GeV/c and $A < 0.5$ in the π^0 mass region. The π^0 events have radii greater than 50 cm.
- b) Monte Carlo $\gamma e^+ e^-$ invariant mass distribution with $p_T > 3$ GeV/c in the π^0 mass region.

energy loss through the bremsstrahlung process when traveling through the target material and the SSD planes. Because of this energy loss, the reconstructed momenta of the electrons are on average reduced relative to their original values by the time they reach the analysis magnet. Fig. 5.24 shows the relative γe^+e^- mass for the π^0 as a function of the Z position of the reconstructed vertex. The dependence of the γe^+e^- mass with this variable is consistent with our hypothesis. The γe^+e^- mass corresponding to vertices in the most downstream Be piece is $\approx 0.3\%$ lower than the π^0 accepted value. Since electrons may continue losing energy when going through the SSD planes, agreement to this level is satisfactory.

The invariant mass spectrum for the four particle $e^+e^-e^+e^-$ system, for events with reconstructed primary vertices in the Be target, is shown in Fig. 5.25. The π^0 peak is clearly visible. Only tracking information was used to calculate the four momenta of these electrons. No track-shower matching was required for this sample and other quality tracking cuts were loosened for statistical purposes. The resultant π^0 mass for the $e^+e^-e^+e^-$ system is $\approx 2.5\%$ lower than the accepted value. This difference is consistent with the γe^+e^- sample since the effect due to bremsstrahlung energy losses is doubled in the $e^+e^-e^+e^-$ sample.

5.6 ENERGY CORRECTIONS FOR ELECTRONS

All energy scale corrections (except the E-loss correction) determined for photons were also applied to the reconstructed energy of electron initiated showers. The average E-loss correction for electrons, shown in Fig. 5.16, was determined using a Monte Carlo data driven sample of ZMP electrons. After all these corrections were applied, the residual variation of the mean of the E/P distribution versus the energy of the electron is illustrated in Fig. 5.26. The agreement between the

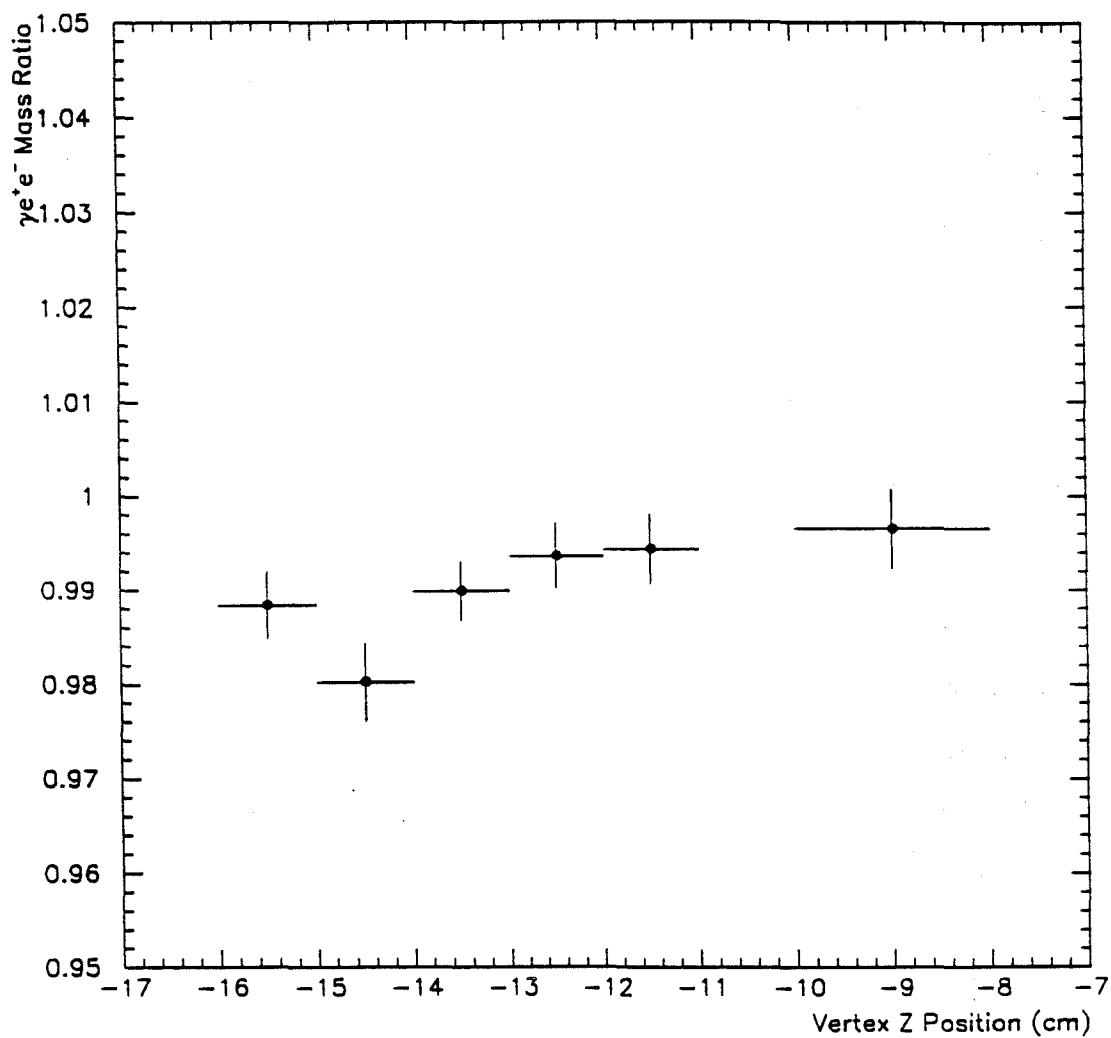


Figure 5.24 The ratio of the π^0 mass in the $\gamma e^+ e^-$ mode to its accepted value as a function of the Z position of the reconstructed vertex. All energies are based on the final energy scale.

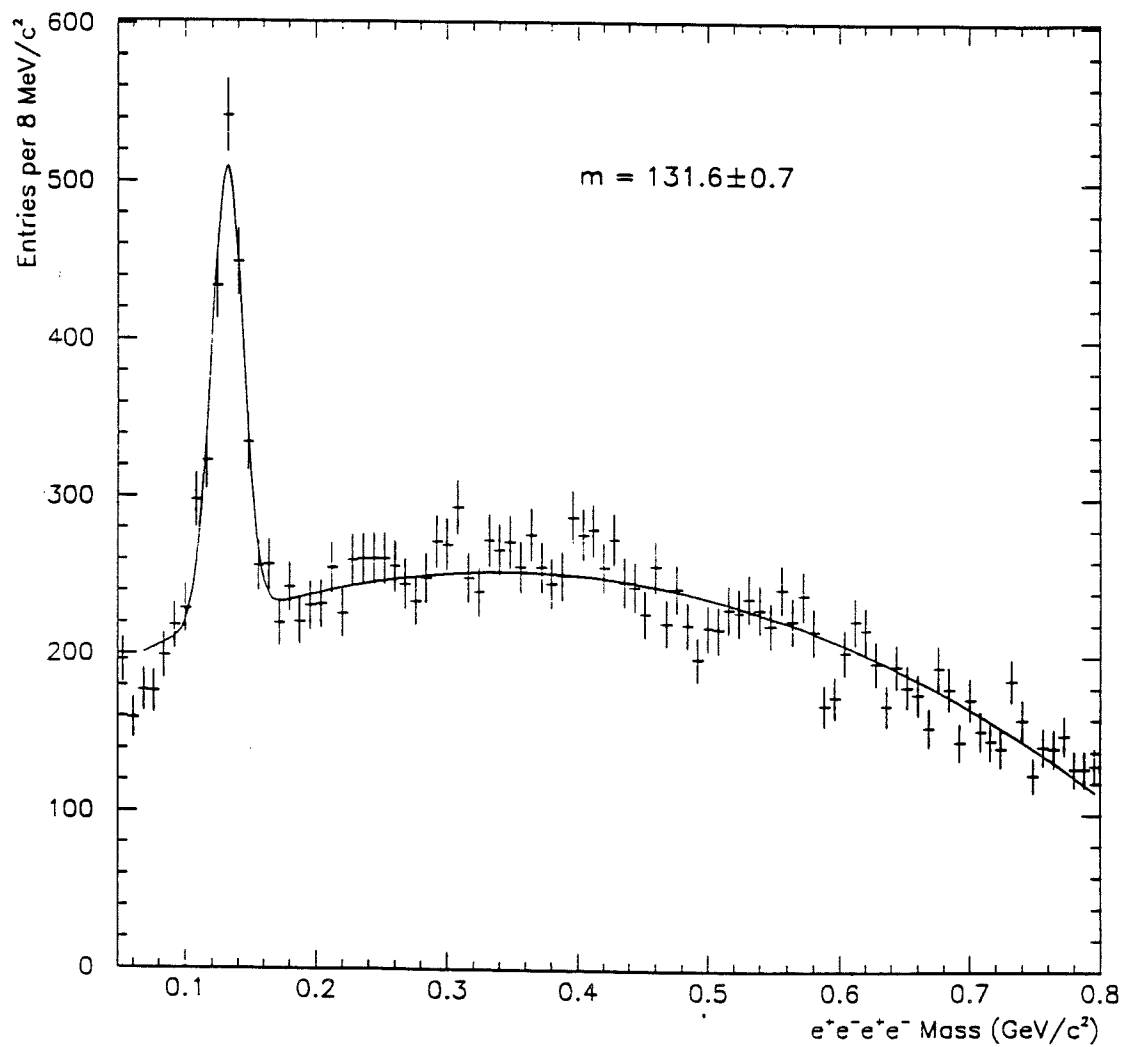


Figure 5.25 $e^+e^-e^+e^-$ invariant mass distribution for events with reconstructed primary vertices in the Be target. The π^0 peak is clearly visible. Only tracking information was used to calculate the four momenta of these electrons.

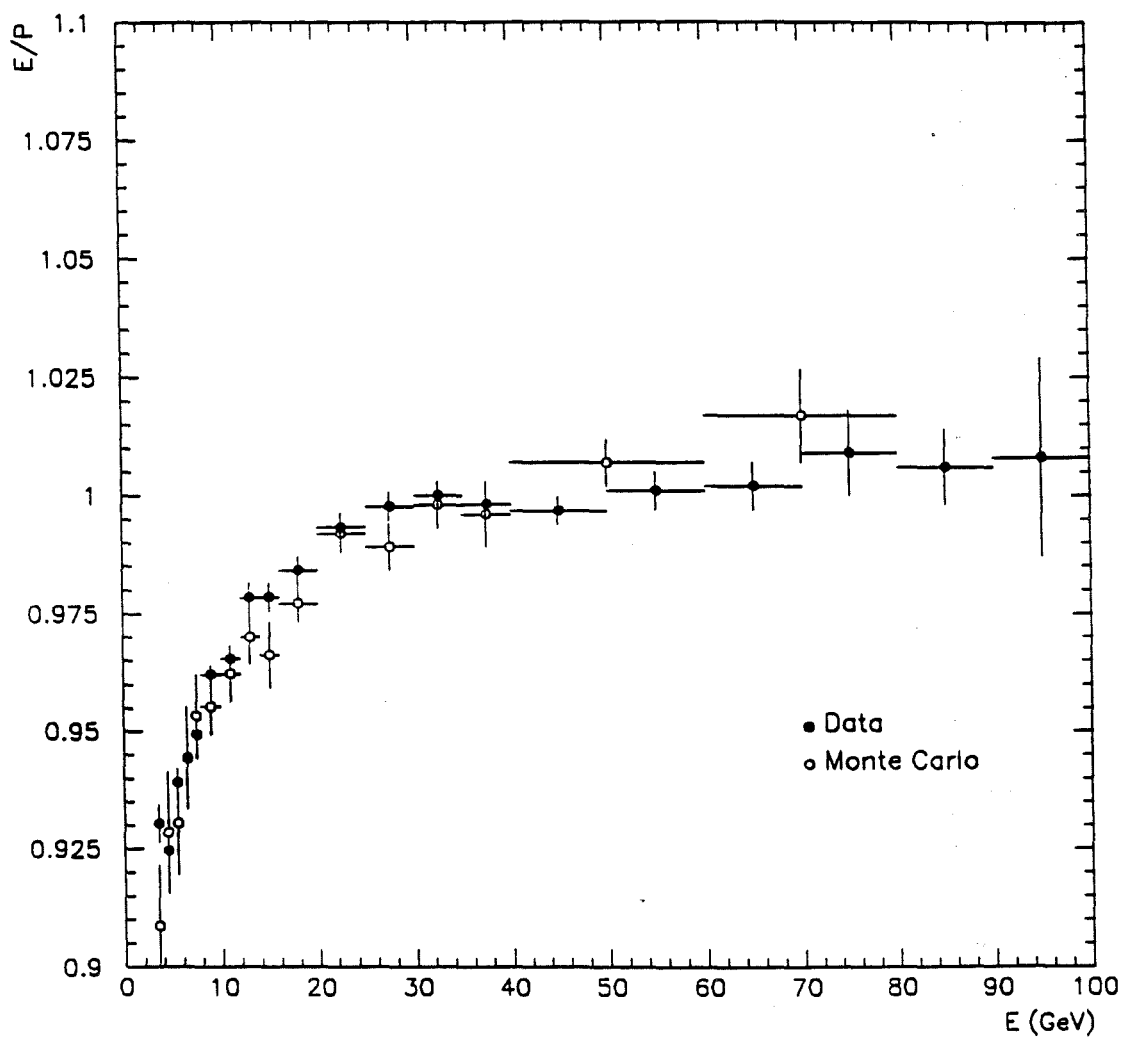


Figure 5.26 E/P ratio for ZMP electrons as a function of electron energy for data (dark circles) and Monte Carlo (open circles).

HERWIG/GEANT Monte Carlo sample of electrons and the data shown in this figure is very good. A fit to the data points was performed to calculate the residual correction to electron energies based upon the requirement that $E/P = 1.0$ for all energies[†].

The deviation of the mean of the E/P from 1.0 in the low-E region is attributed to differences in the shower shape between electrons and photons. As already mentioned the shower shape parametrization used in EMREC was tuned to match photon initiated showers which begin their shower development later than electrons and therefore had smaller “tails”. For high energy electrons the E/P approaches 1.0 which is consistent with the overall scale for photon showers as set based on the reconstructed η mass in each octant.

5.7 RESULTS AND SYSTEMATIC UNCERTAINTY

In this section, we will examine the stability of the energy scale corrections described above for photon and electrons in various data projections in order to assess the contribution to the systematic uncertainty in the π^0 cross section from residual uncertainties in the energy scale.

Fig. 5.27 and 5.28 display the $\gamma\gamma$ invariant mass in the π^0 and η mass range respectively, for *SINGLE LOCAL* triggers, with $p_T > 4$ GeV/c and $A < 0.5$. Fig. 5.27a shows the overall π^0 mass, whereas Fig. 5.27b shows the π^0 mass with the additional requirement that the π^0 radius be greater than 50 cm. Since the average π^0 energy decreases with radius for a given p_T bin, the radial cut results in a sample of

[†] The energy loss of the electrons due to the bremsstrahlung process in materials upstream of the magnet affects the reconstructed momentum and energy by approximately the same amount. When electrons brem downstream of the magnet, the momentum measurement will not be affected, but the EMLAC energy in principle would be reduced. However, this energy loss is accounted on the average by the Monte Carlo E-loss correction to the reconstructed energies.

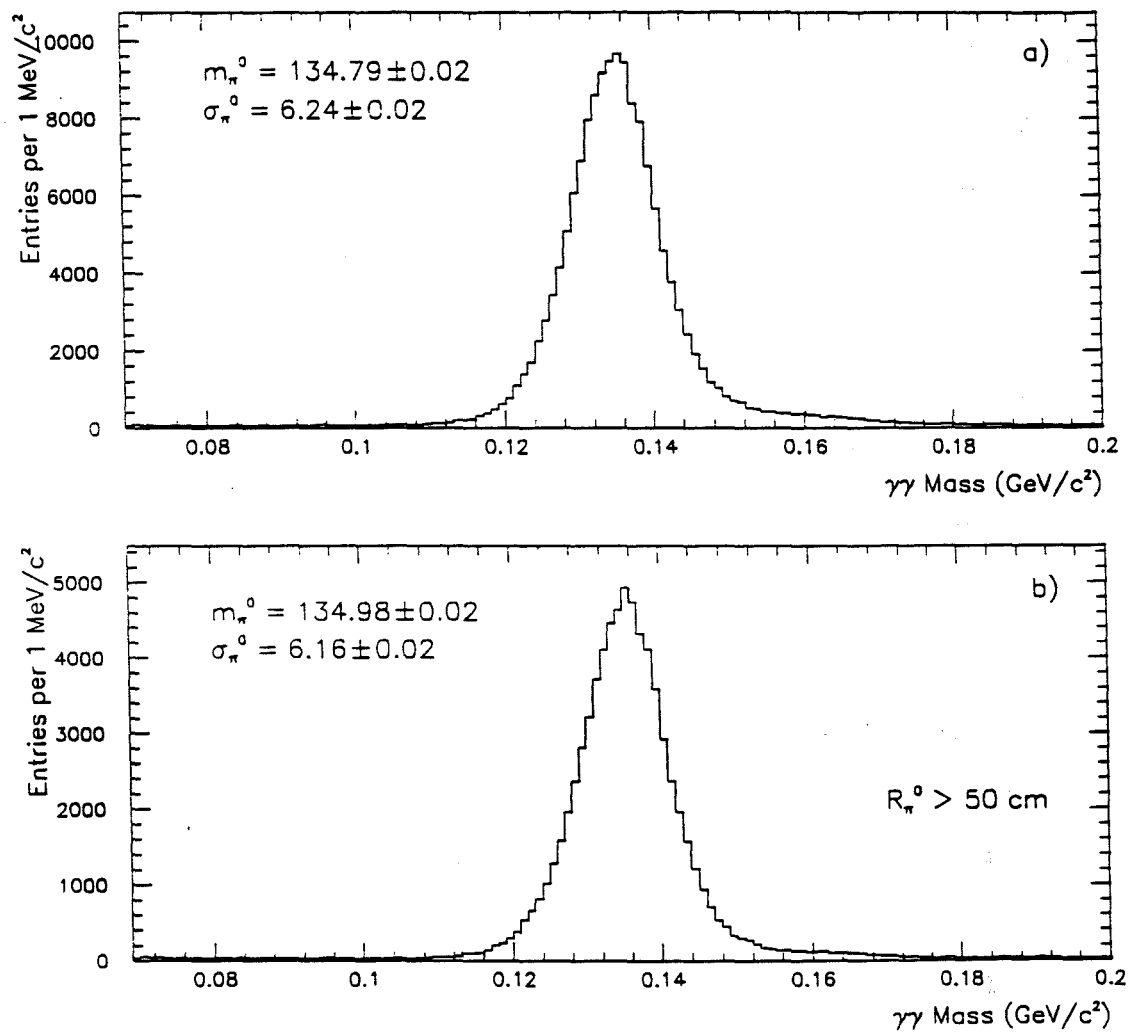


Figure 5.27 Two-photon invariant mass distribution with $p_T > 4$ GeV/c and $A < 0.5$ in the π^0 mass region after all energy scale corrections a) overall and b) for events with π^0 radius greater than 50 cm.

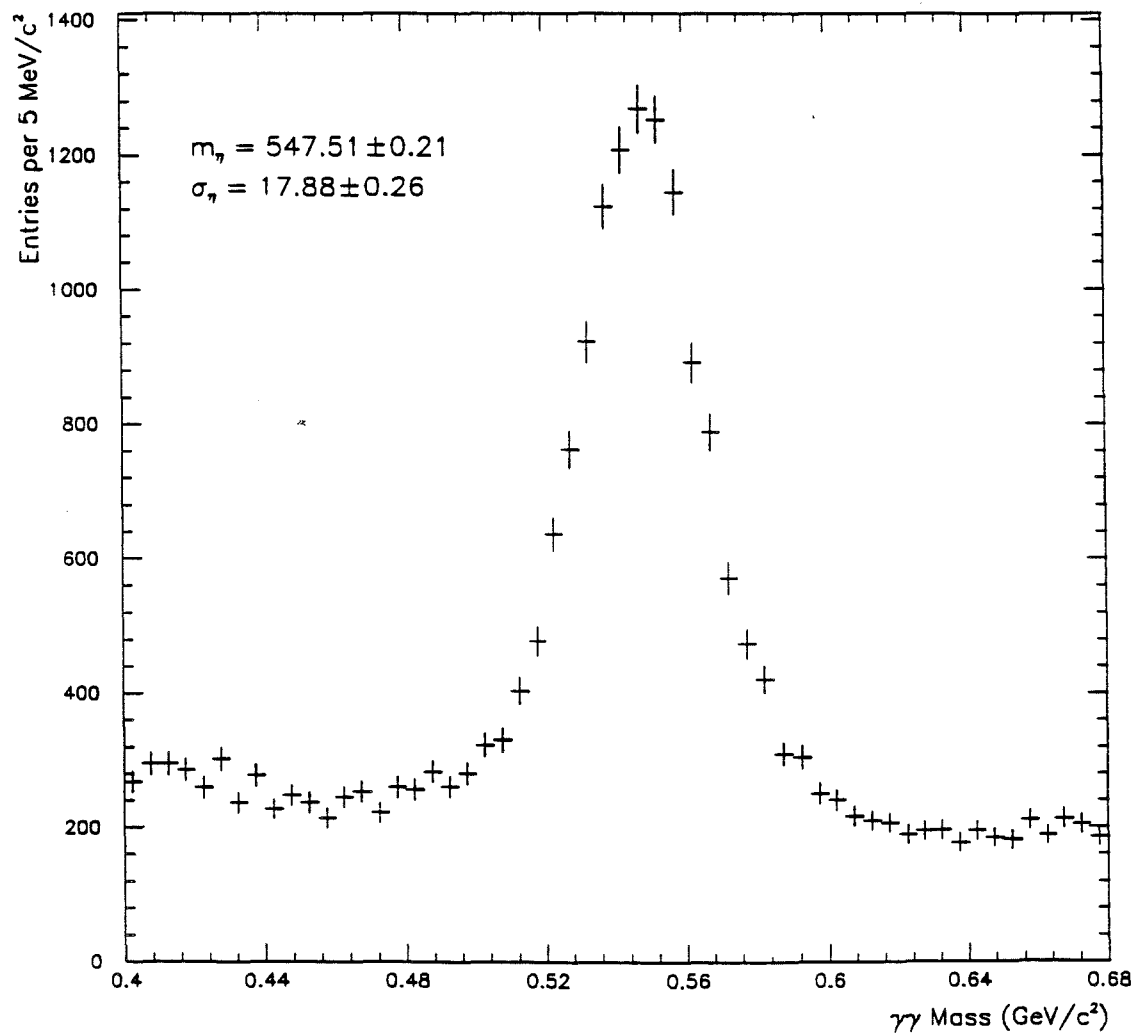


Figure 5.28 Two-photon invariant mass distribution with $p_T > 4 \text{ GeV}/c$ and $A < 0.5$ in the η mass region after all energy scale corrections.

lower energy π^0 s which decay into more widely separated photons^f and hence the sensitivity of the mass to the splitting of overlapping showers is reduced. Due to the larger η mass, the daughter photons are well separated at all radii. Both the π^0 and η masses are within 0.1% of their world average values.

Fig. 5.29 shows the invariant $\pi^0\gamma$ mass in the ω mass range (Ref. [3]), with $p_T > 3.5$ GeV/c, which provides an independent check on our energy scale between reconstructed π^0 and single-photons. The value 781.8 ± 1.8 MeV/c² for the ω signal confirms the establishment of a consistent energy scale.

Fig. 5.30a shows the π^0 (with $R > 50$ cm) and η masses relative to their accepted values as a function of octant number, for $p_T > 4$ GeV/c. The stability of the means of the two masses over all octants is better than 0.2%. The variation of the relative π^0 and η masses with respect to their p_T values is displayed in Fig. 5.30b. No dependence is apparent for the η mass, whereas the π^0 mass appears to decrease at high p_T s. This is due to the separation of the two photons, which decreases with p_T and at high p_T s, even with the radial cut, the effect upon the mass becomes apparent. Fig. 5.31 shows the relative η mass as a function of the energy asymmetry for $p_T > 3.5$ GeV/c. Within the limits of uncertainties no variation is observed, except at the highest asymmetries where the signal to background ratio is significantly reduced.

^f In π^0 decay, the separation δ between the two photons is given by:

$$\delta = \Theta d = \frac{2m}{p_T} \frac{R}{\sqrt{1-A^2}}$$

where Θ is the opening angle between the two photons, d is the distance from the target to the LAC, and R is the π^0 radial distance from the center of the LAC. For example, consider a π^0 with energy asymmetry $A = 0.25$ and $p_T = 4$ GeV/c. At radius $R = 30$ cm, the photon separation is $\delta \approx 2$ cm, whereas at $R = 80$ cm the separation is $\delta \approx 5$ cm.

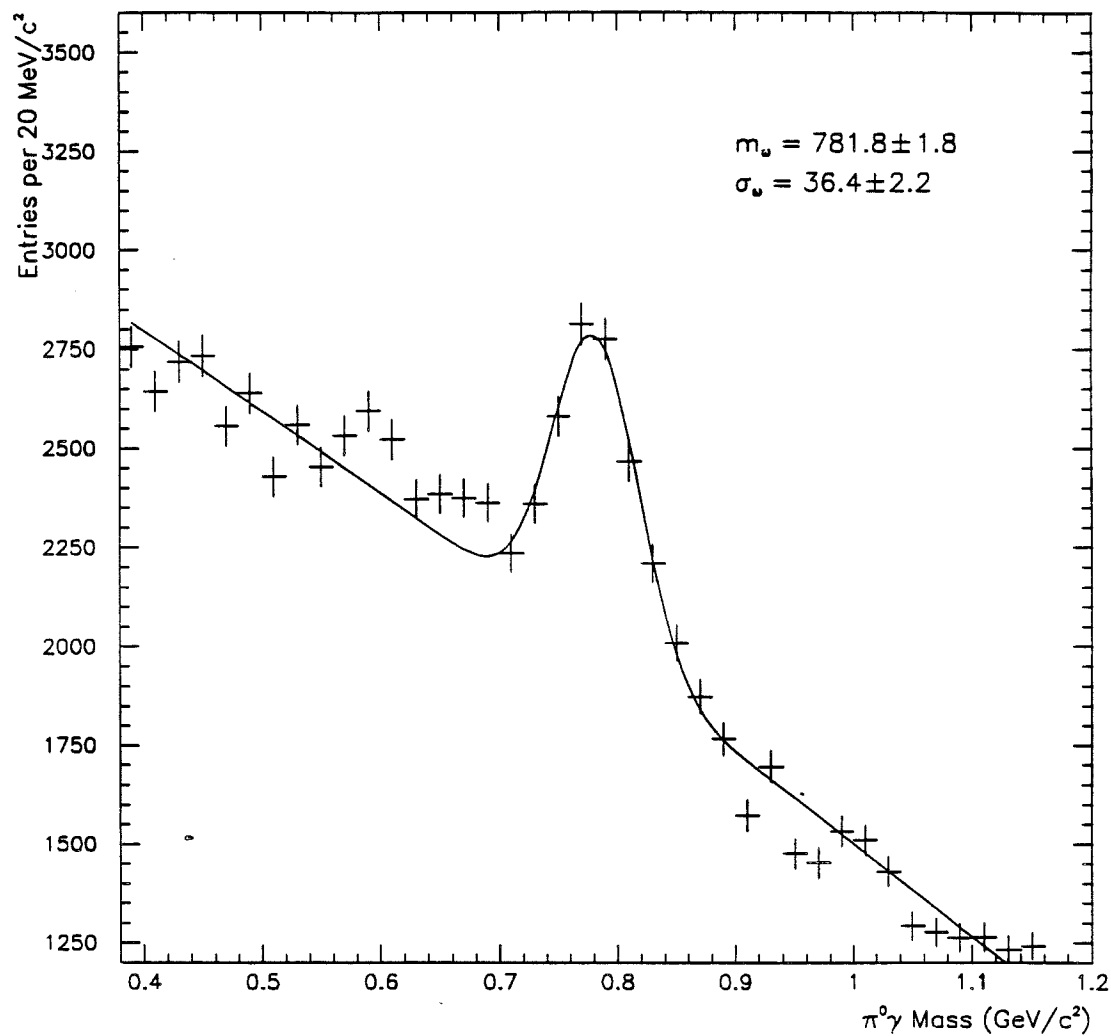


Figure 5.29 $\pi^0\gamma$ invariant mass in the ω mass range, with $p_T > 3.5$ GeV/c. All energies are based on the final energy scale.

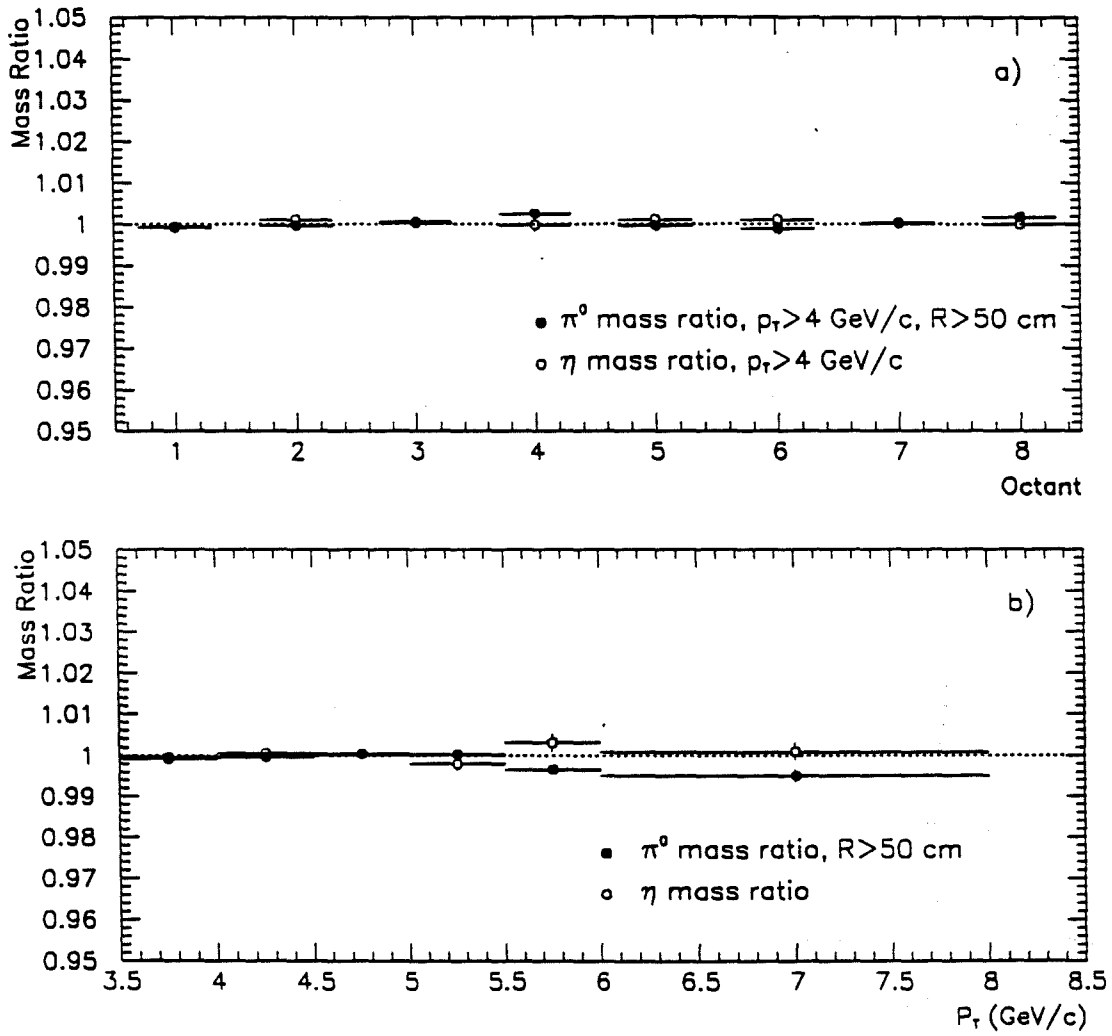


Figure 5.30 The ratio of the π^0 and η masses relative to their accepted values a) as a function of octant number and b) as a function of p_T . All energies are based on the final energy scale.

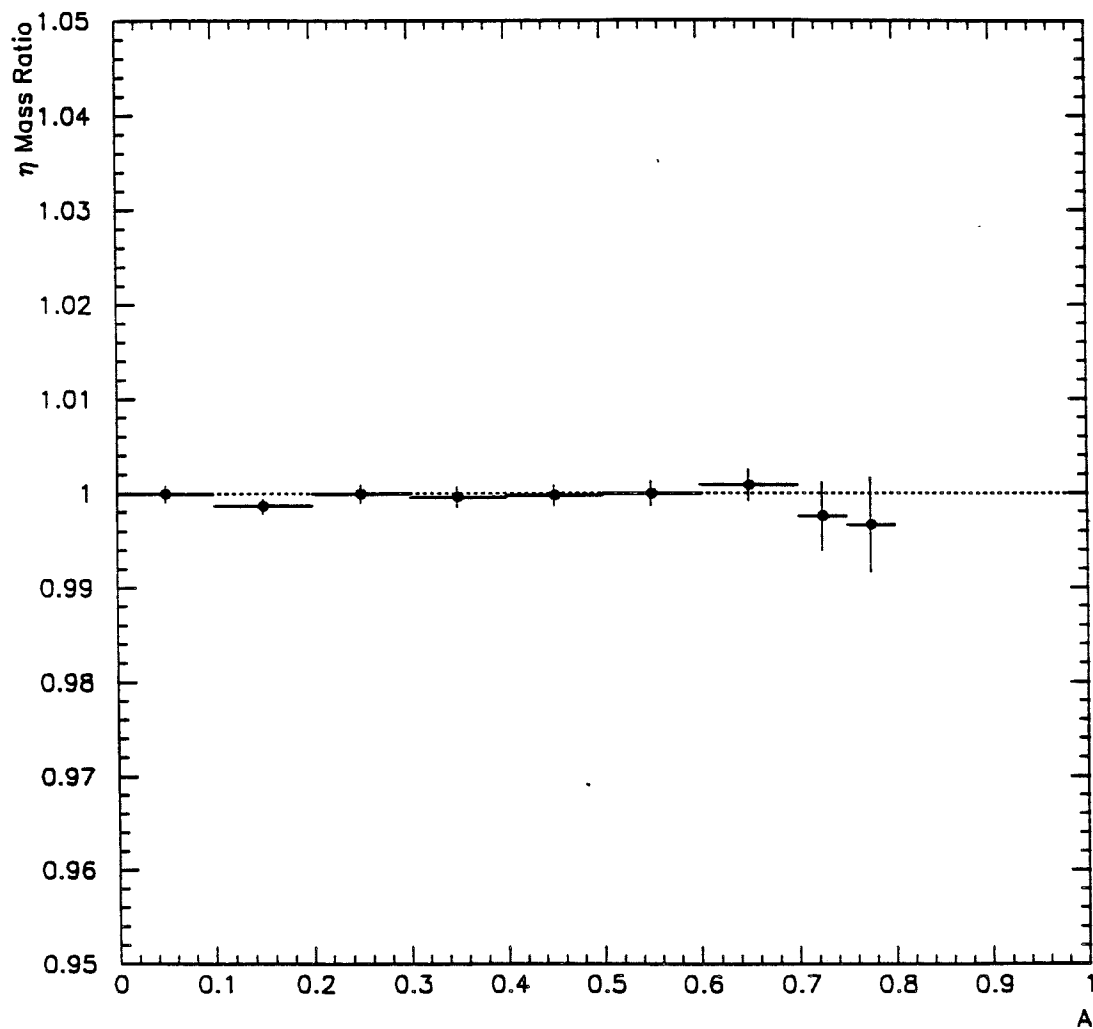


Figure 5.31 The ratio of the η mass to its accepted value as a function of energy asymmetry for $p_T > 3.5$ GeV/c. All energies are based on the final energy scale.

The radial dependencies of the relative π^0 and η masses for *SINGLE LOCAL HI* triggers are shown in Fig. 5.32. Fig. 5.32a shows that the π^0 mass with $p_T > 3.5$ GeV/c decreases slightly in the inner r-region, a result which is reproduced by the Monte Carlo π^0 s, and is attributed to problems in position reconstruction of highly overlapping showers. This plot also illustrates the reason (already mentioned) that this high p_T sample of π^0 s was not used to determine the radial correction of the energy scale. Fig. 5.32b shows the relative η mass as a function of radius with $p_T > 3.5$ GeV/c and $p_T > 5$ GeV/c. The variation of the η mass with radius is within 0.3% of its accepted value (i.e., consistent with the low p_T π^0 sample used to determine the radial correction).

Fig. 5.33 illustrates the stability of the relative π^0 mass as a function of run number. The run range shown in this plot represents the data set used in this thesis and it covers 45 days of running period. The variation of the π^0 mass observed is about 0.4%.

Fig. 5.34a shows the mean E/P as a function of radius for ZMP electrons with $E > 15$ GeV. The variation observed is of the order of 0.5%. Since this sample of ZMPs was not used to determine the radial dependence correction, agreement to this level is a consistency check. Fig. 5.34b displays the mean E/P as a function of the electron energy. No systematic deviation from 1.0 is observed over the entire range of energies. The resultant E/P distribution for electrons with $E > 10$ GeV is shown in Fig. 5.35. The mean value is 0.999 ± 0.001 -- i.e., consistent with the photon overall energy scale.

Another important result already illustrated earlier is that the π^0 mass in the $\gamma e^+ e^-$ mode does not vary as a function of the photon energy. In addition, the

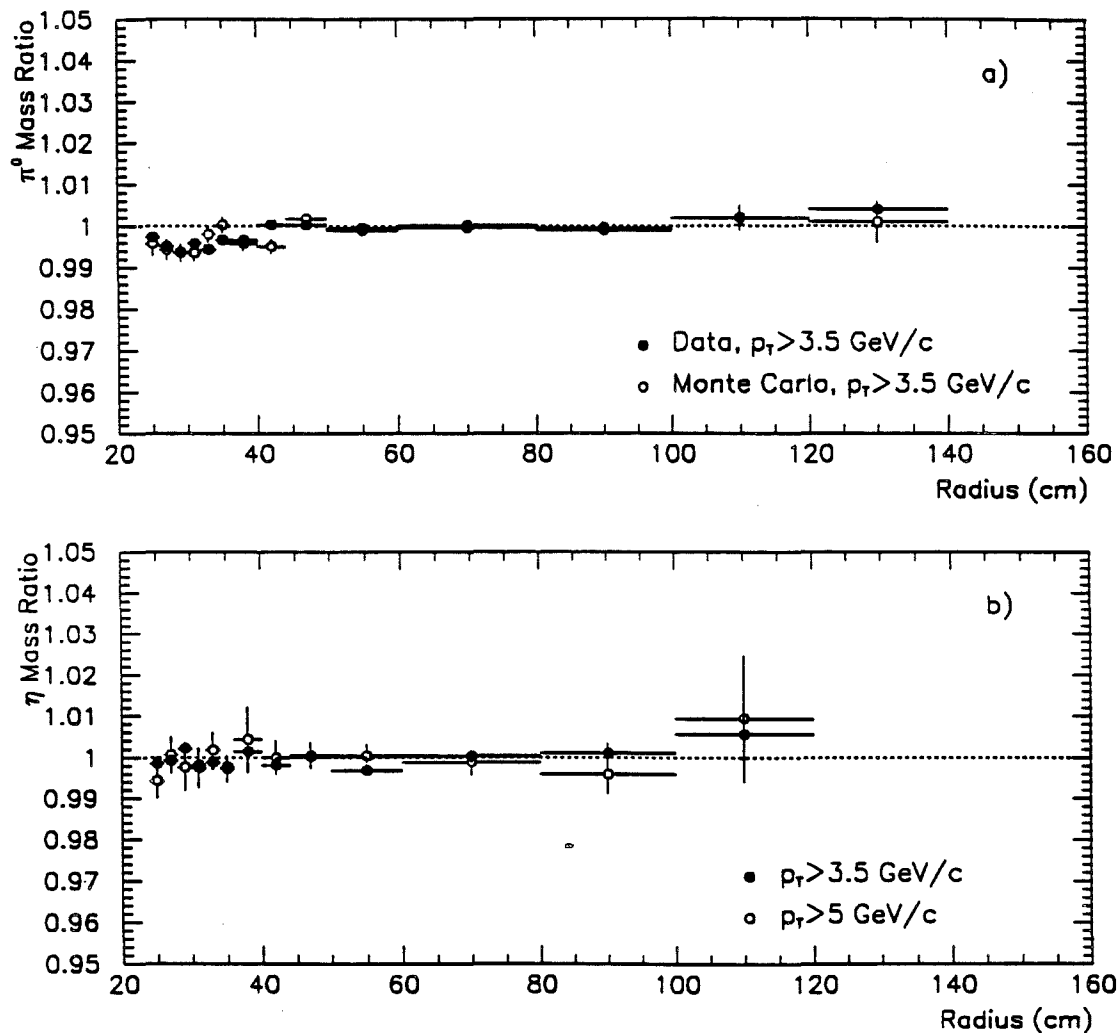


Figure 5.32 a) Radial dependence of the π^0 mass relative to its accepted value for data (dark circles) and Monte Carlo (open circles). b) Radial dependence of the η mass relative to its accepted value for events with $p_T > 3.5$ GeV/c (dark circles) and for events with $p_T > 5$ GeV/c (open circles). All energies are based on the final energy scale.

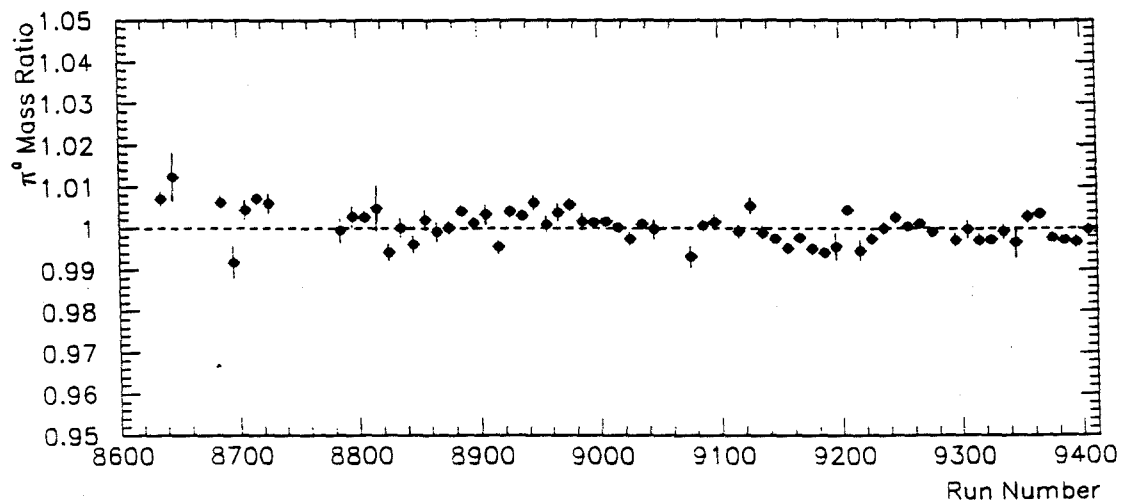


Figure 5.33 The ratio of the π^0 mass to its accepted value as a function of run number after all energy scale corrections.

discrepancy between the π^0 mass in the $\gamma\gamma$ and γe^+e^- modes is reproduced by the Monte Carlo simulation.

From the above projections, the residual uncertainty in the overall energy scale is estimated to be no larger than $\approx 0.5\%$, which contributes $\approx 6\%$ uncertainty to the absolute π^0 cross section at p_T of 4 GeV/c (see Section 7.2).

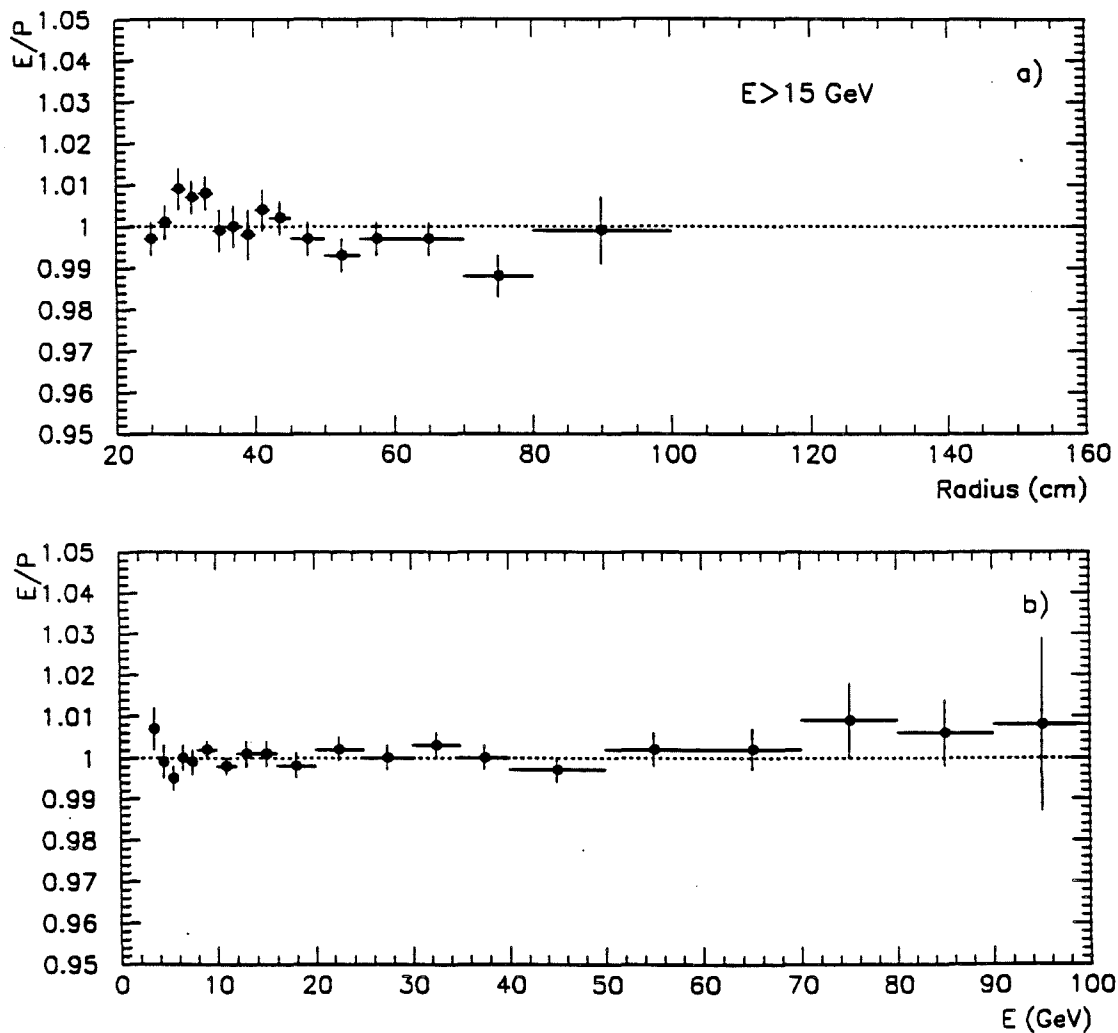


Figure 5.34 a) Radial dependence of the E/P ratio for ZMP electrons with $E > 15$ GeV. b) E/P ratio as a function of electron energy. All energies are based on the final energy scale.

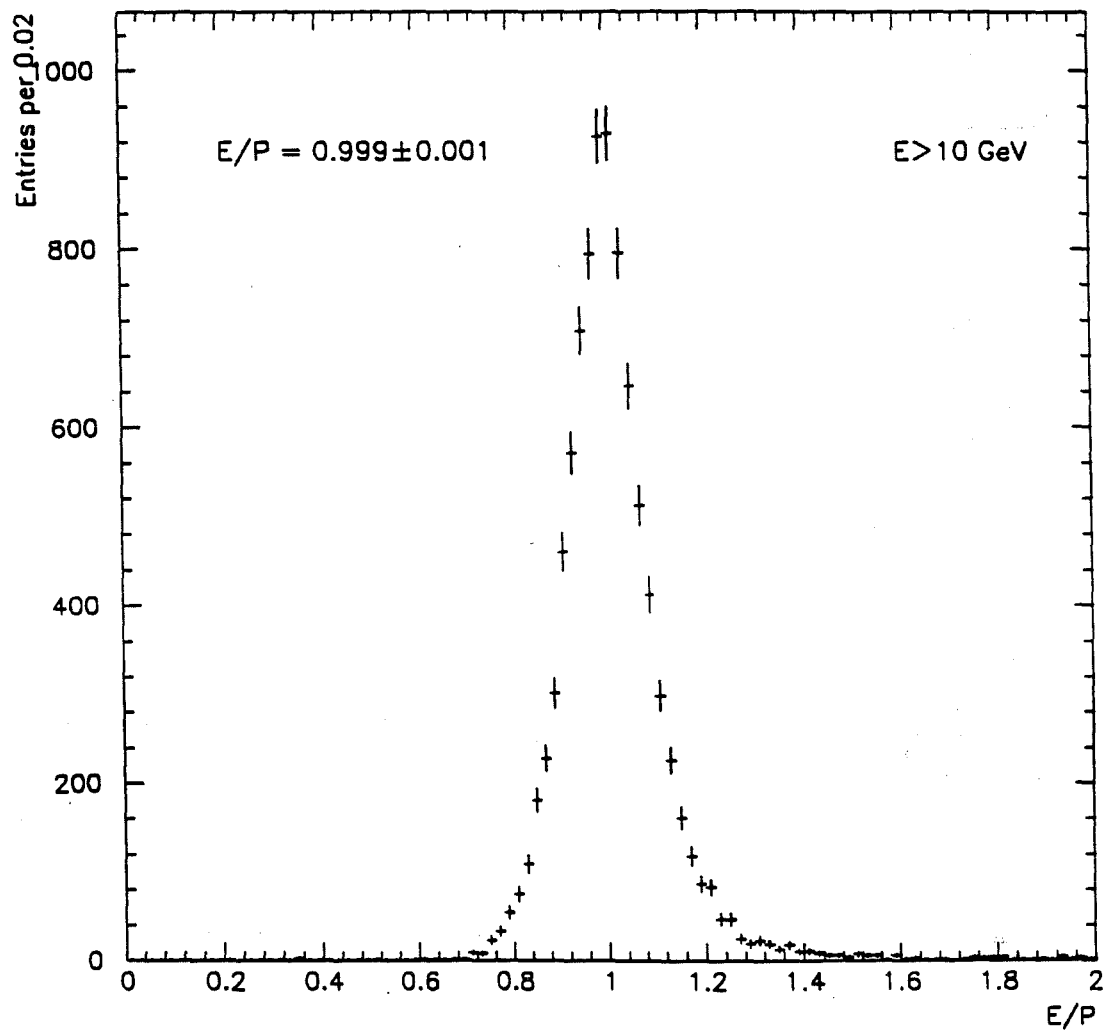


Figure 5.35 E/P distribution for ZMP electrons with $E > 10$ GeV and after all energy scale corrections.

6. DATA ANALYSIS

6.1 DATA SELECTION

The data used for this analysis were acquired during the 1990 Fermilab fixed target run. They were taken with 520 GeV/c π^- beam incident on beryllium and copper targets. Table 6.1 summarizes the total 1990 data sample of E706 triggered events that were reconstructed and written out in DST format. The different data sets represent run segments where the trigger conditions (i.e., trigger thresholds, hardware performance, etc.) are expected to be constant.

Set	Run Number Range	Number of Events Processed
1	9181 - 9434	5,904,433
2	8989 - 9180	4,051,049
3	8629 - 8988	5,839,137
4	8240 - 8628	3,931,743
5	8055 - 8239	2,864,491
6	7594 - 8054	4,966,478

Table 6.1 Data sets from 1990 running period.

For this analysis two kind of triggers were used; the *SINGLE LOCAL HI* for $p_T > 4$ GeV/c and the *SINGLE LOCAL LOW* for $3.5 < p_T < 4$ GeV/c. Since the

SINGLE LOCAL LOW trigger existed only for data set 1, these data were used to cover the lower end of the p_T range. For *SINGLE LOCAL HI* triggers only data sets 1, 2, and 3 were used for this analysis.

To insure the quality of the data, a number of cuts were imposed on the events selected for this analysis. The following paragraphs discuss the cuts applied to the data in some detail.

Vertex Cut

Each event was required to have a reconstructed vertex within the target area. Fig. 6.1 shows the reconstructed Z position of the primary vertex for events that have a π^0 with $p_T > 3.5$ GeV/c. The two Cu and Be targets, as well as the SSD planes nearest to the target are clearly visible.

Fig. 6.2 shows the X and Y positions of the reconstructed vertices in the two Be (Fig. 6.2a) or two Cu pieces (Fig. 6.2b). In these plots the target areas are also shown along with the area (square) covered by the beam hodoscope which was used to define incident beam particles. From these projections, we see that the beam was well centered on the beam hodoscope but not on the targets. Consequently, there were beam particles, counted by the beam hodoscope, that were not hitting the targets. In order to ensure that the same amount of beam was hitting both targets, a transverse target fiducial region was defined with the following constraints:

- $\sqrt{(V_X + 1.12)^2 + (V_Y - 0.07)^2} < 0.96$ cm;
- The reconstructed vertex was inside the area covered by the hodoscope.

To determine a correction to the beam count, the vertices reconstructed in the two SSD planes upstream of the Cu target were used. The ratio of vertices reconstructed

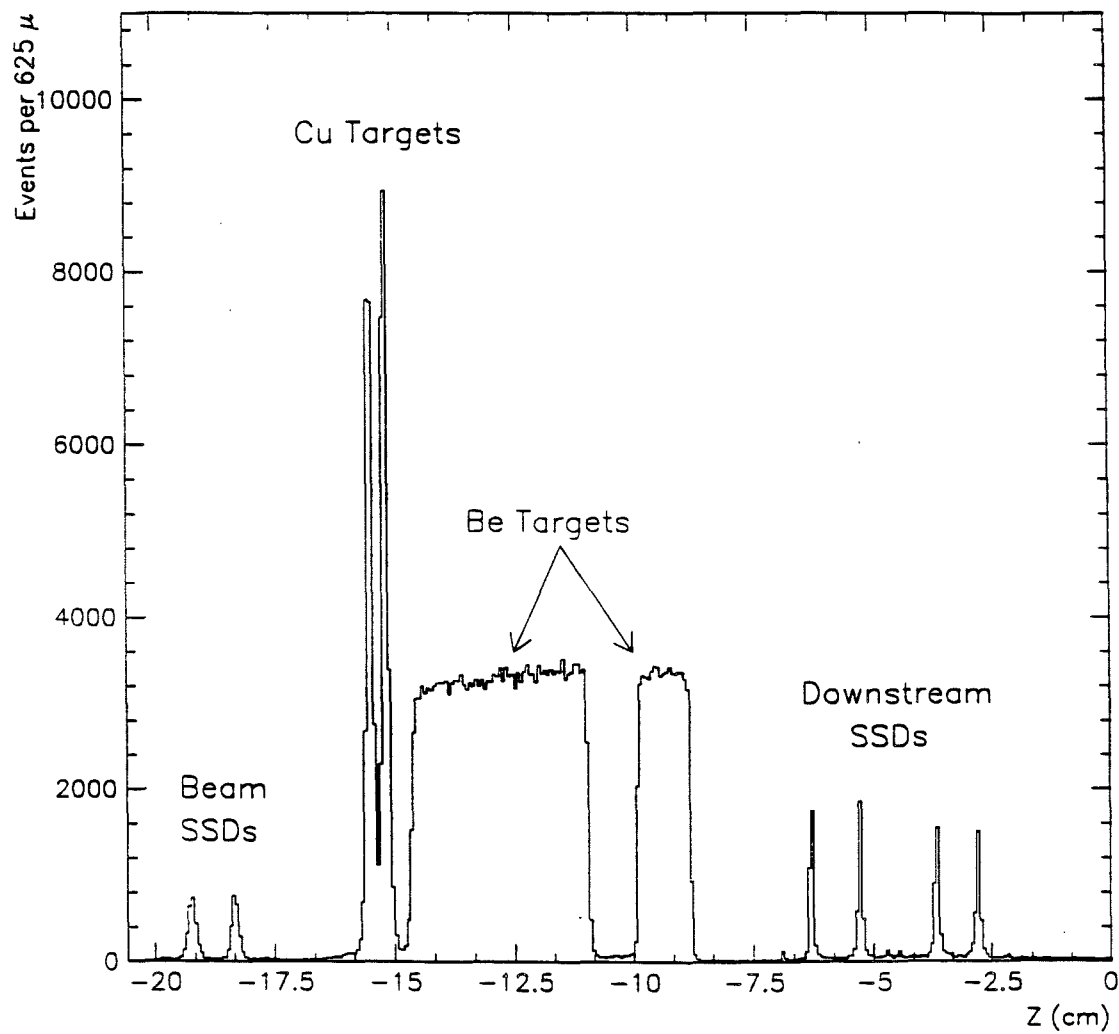


Figure 6.1 Distribution of reconstructed primary vertices for high p_T π^0 events. The two Be and Cu targets as well as the SSD planes nearest to the target are clearly visible.

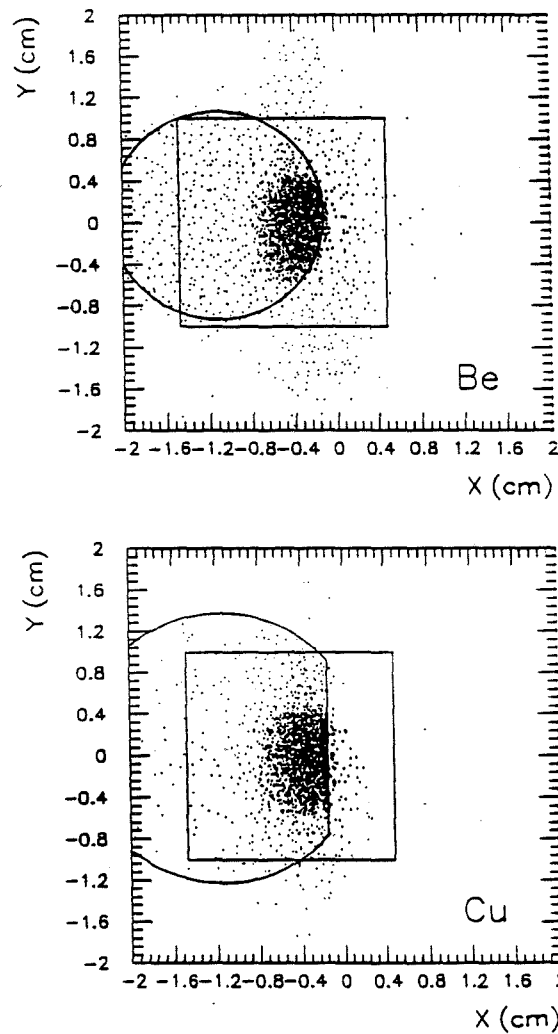


Figure 6.2

X and Y positions of reconstructed vertices for high p_T π^0 events which interacted a) in the two Be targets or b) in the two Cu targets. The square corresponds to the sensitive area of the beam hodoscope, the circle (a) shows the physical location of the Be targets, and the truncated circle (b) shows the shape of the Cu targets.

within the above fiducial region in these SSD planes, over all vertices found in the SSD region shadowed by the beam hodoscope was calculated. The correction was determined to be 35% with a systematic uncertainty of order 2%.

Fiducial Cut

A fiducial cut was imposed to define the active region of the EMLAC. Since the detection efficiency for π^0 s was significantly lower around the edges of the calorimeter, showers were rejected if the reconstructed R position did not fall within the region $22.7 < R < 149.5$ cm, or if the ϕ position was less than two ϕ strips away from a quadrant or octant boundary. The correction for this cut, referred to as the “geometric acceptance,” will be discussed later.

E_{front}/E_{tot} Cut

In order to eliminate hadron initiated showers detected in the EMLAC, only showers with $E_{front}/E_{tot} > 0.2$ were included in the analysis (see also Section 5.2). This cut also eliminated some fraction of the muons, since muons tend to generate showers having a much larger fraction of energy in the back section of the EMLAC, which had twice the amount of material as the front section. A correction for losses of real photon showers due to this cut was incorporated in the calculation of the π^0 reconstruction efficiency using the Monte Carlo event sample.

Muon Rejection

A major source of background to the very high p_T π^0 signal is muon triggered events. These events were generated by muons in the beam halo, traveling nearly parallel to the beam line, but displaced several feet away from it. A fraction of these muons interacted in the calorimeter and produced a photon via the bremsstrahlung

process,^[1] thereby mimicking high p_T showers in the EMLAC. As already mentioned, during data acquisition information from the three veto walls was used to reject many of the events generated by muons. The trigger logic rejected an event when the upstream veto wall recorded a signal in coincidence with the logical OR of the signals from the two downstream veto walls for the quadrant covering the triggering octant within ± 75 ns of the interaction time. However, due to inefficiencies in the veto walls, gaps between the scintillation counters in the veto wall geometry, and the limited duration of the on-line veto wall window, some muons escaped on-line detection.

The effect of muons on the high p_T $\gamma\gamma$ mass plot is illustrated in Fig. 6.3, where the π^0 mass region is shown for $\gamma\gamma$ combinations with $7 < p_T < 10$ GeV/c for positive and negative rapidities. For this sample, the E_{front}/E_{tot} cut was applied to both photons. In Fig. 6.3b, we note that the π^0 signal is hardly visible for negative rapidities (which corresponds to the outside part of the detector). The large low mass peak is a result of muon generated showers which EMREC split into two very close photons (the focusing of the LAC results in asymmetric shower shapes for particles incident parallel to the beam axis). This effect is more pronounced at large radii where the shower shape asymmetry is enhanced and the muon flux is higher. To reject these remaining muons, three cuts were employed; an off-line veto wall cut, a directionality cut, and a balanced p_T cut.

The logical software veto wall signal (VWS) for the veto wall quadrant shadowing the triggering octant was defined via a coincidence between the signal in the upstream veto wall quadrant and the logical OR of the signals from the two downstream veto walls within a ± 20 ns time window (as recorded by the Minnesota

[1] J. P. Mansour, E706 Internal Note 195 (1992).

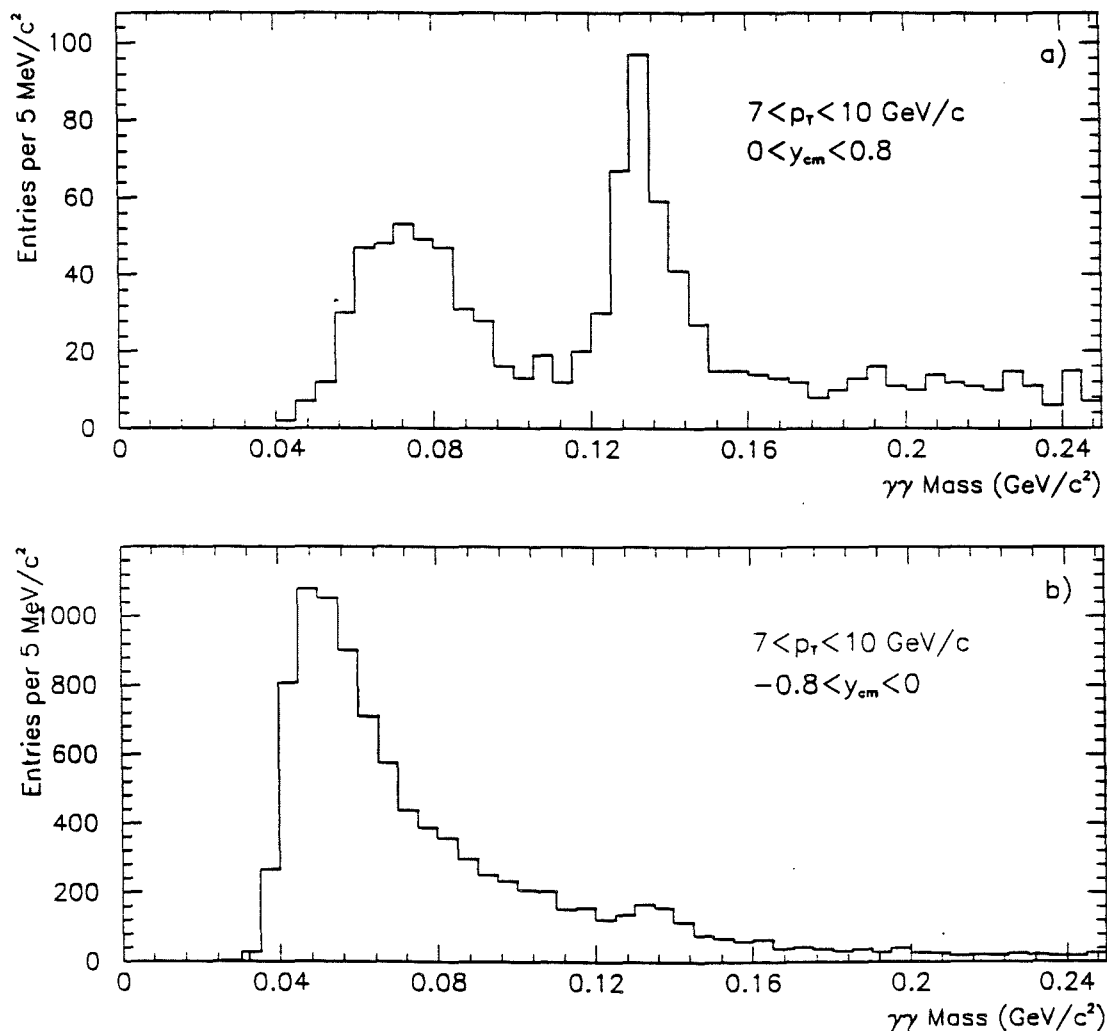


Figure 6.3 Two-photon mass distribution in the π^0 mass region with $7 < p_T < 10 \text{ GeV/c}$ a) for $0 < y_{cm} < 0.8$ and b) for $-0.8 < y_{cm} < 0$. For this sample, only the E_{front}/E_{tot} cut was applied to both showers.

Latches[†]). To construct this signal the latched veto walls were searched in a 300 ns wide window centered around the interaction. The triggering octant was removed from consideration when a VWS coincidence was encountered. This cut was applied unconditionally to all events. Although the VWS condition eliminated a good fraction of the muons, as illustrated in Fig. 6.4, it did not entirely eliminate the muon background in the very high p_T π^0 sample. Thus, the directionality and the balanced p_T cuts were also applied to the π^0 sample with $p_T > 5.5$ GeV/c.

The directionality (δ_R) parameter associated with a shower is a measurement of the particle trajectory inside the EMLAC and is defined as:

$$\delta_R = R_f - \frac{Z_f^{LAC}}{Z_b^{LAC}} R_b \quad (6.1)$$

where R_f and R_b are the reconstructed front and back radial positions of the shower, and Z_f^{LAC} and Z_b^{LAC} are the longitudinal distances of the front and back sections of the EMLAC from the target. The concept of directionality is shown in Fig. 6.5. Showers originating in the target have directionality close to zero, while showers produced from muons traveling nearly parallel to the beam line have large positive directionalities.

The directionality cut for the high p_T $\gamma\gamma$ sample was applied only to the higher energy photon of the pair that had radius greater than 40 cm (the inner/outer ϕ boundary). The radius requirement was invoked since the directionality measurement improves with radius and the need for the directionality cut also increases with radius since the muon fraction increases. Fig. 6.6 shows the directionality distribution of the

[†] The "Minnesota Latches" were latches used during data acquisition to store time profiles (up to 15 consecutive beam buckets) for several counters, including beam hodoscope, interaction counters, and veto walls.

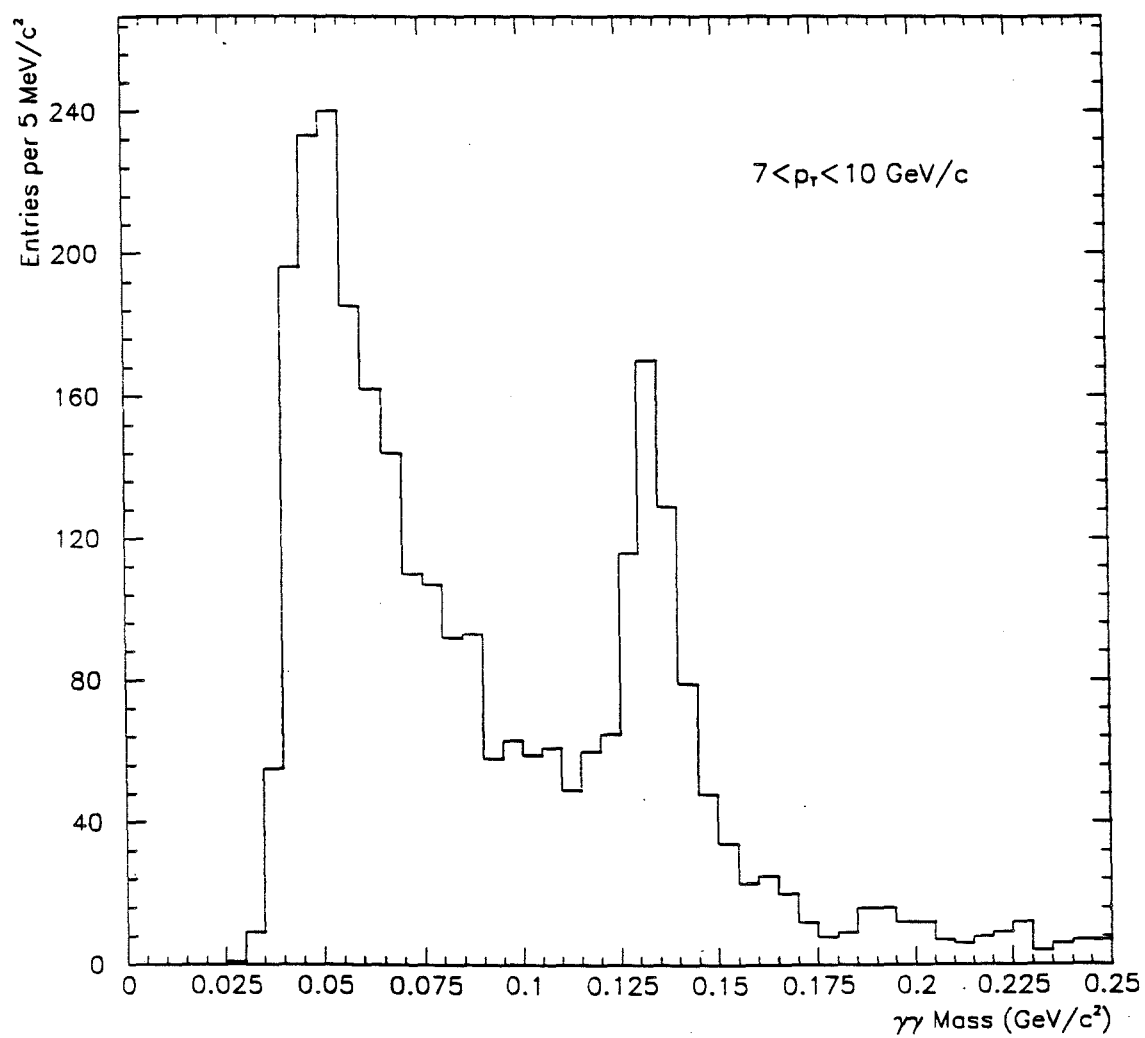


Figure 6.4 Two-photon mass distribution in the π^0 mass region with $7 < p_T < 10 \text{ GeV/c}$ after the veto wall cut.

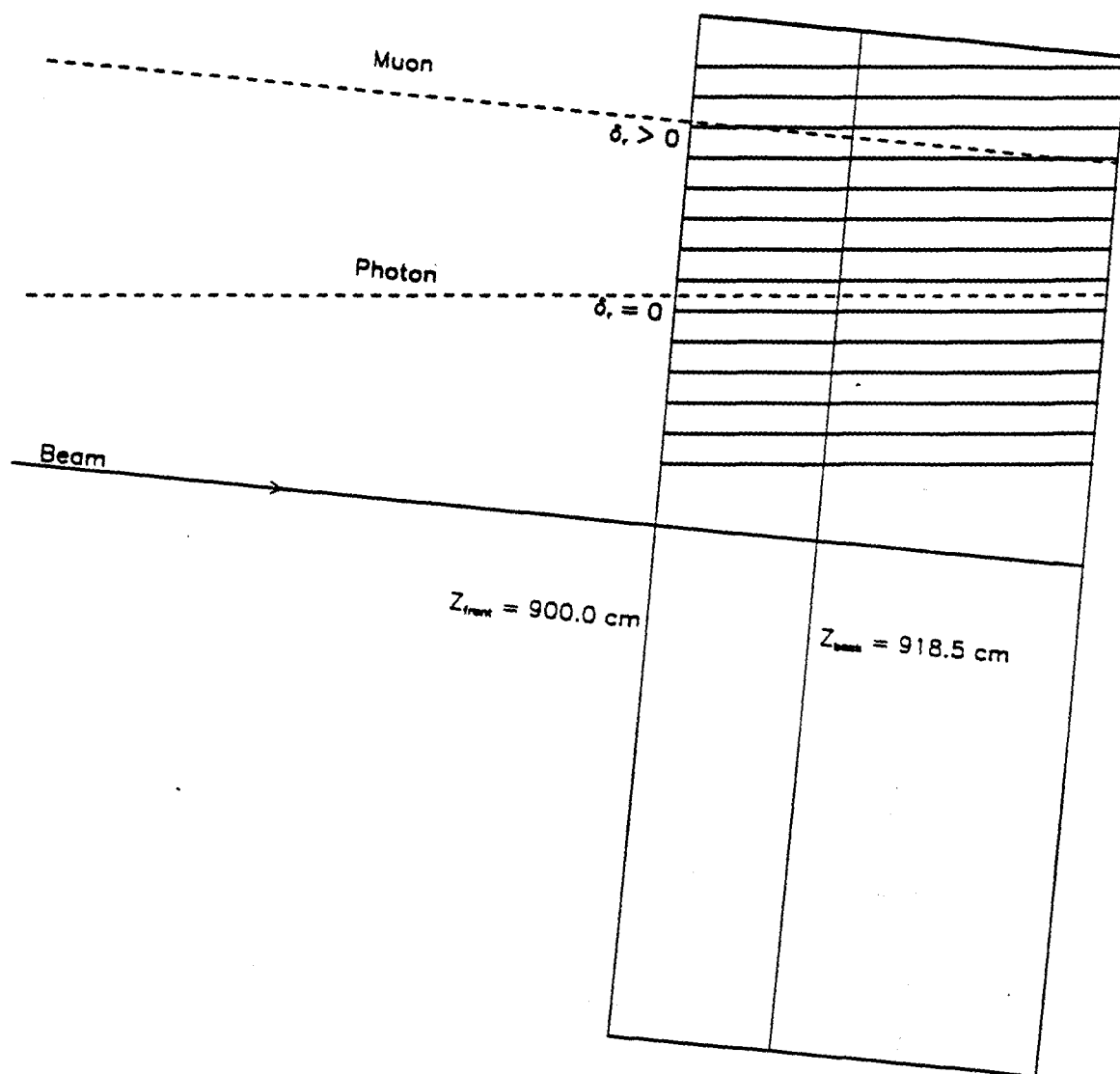


Figure 6.5

Illustration of the concept of photon directionality. Showers generated by particles from the target have directionalities close to zero. Showers produced by particles incident parallel to the beamline have large positive directionalities.

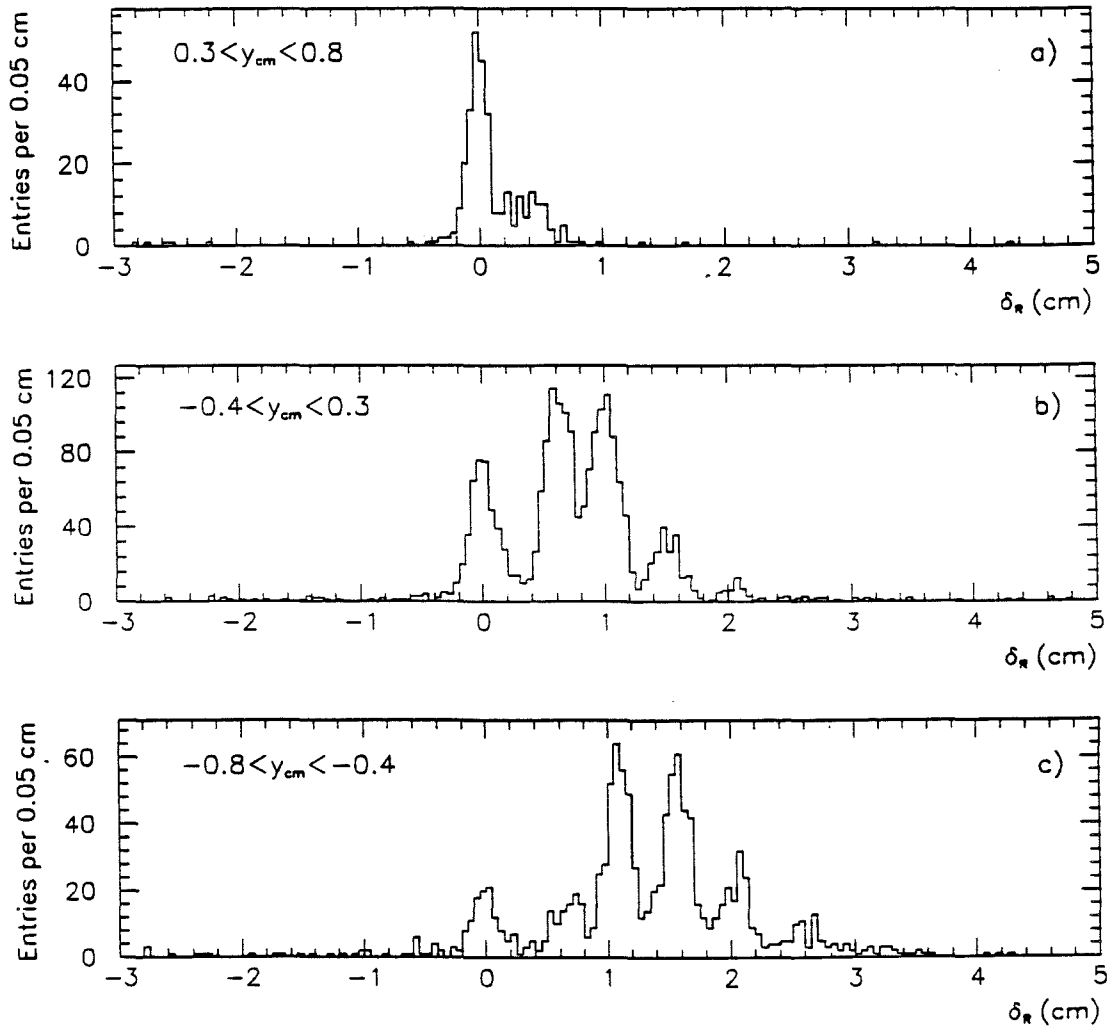


Figure 6.6 Directionality distribution for the higher energy photon of the $\gamma\gamma$ pair with $5.5 < p_T < 10$ GeV/c and mass in the π^0 region for events when the VWS signal indicated a potential muon candidate; a) for $0.3 < y_{cm} < 0.8$, b) $-0.4 < y_{cm} < 0.3$, and c) $-0.8 < y_{cm} < -0.4$.

higher energy photon of the $\gamma\gamma$ pair with $5.5 < p_T < 10$ GeV/c and mass in the π^0 region, for some rapidity intervals when VWS signal indicated a potential muon candidate. From these distributions, muon-induced peaks with large positive directionalities are clearly visible. Note that there are also some photon candidates that have directionalities around zero that will be eliminated by this software veto wall cut. A correction for these losses therefore needs to be applied. The directionality distributions for events that did not have a VWS signal are shown in Fig. 6.7. It is clear from these distributions that the directionality cut is more effective when applied to photons in the outer part of the detector.

Since the directionality resolution increases with energy, the cut imposed on directionality was a function of the radius. The $\gamma\gamma$ pair was eliminated when the directionality of the higher energy photon (with radius $R > 40$ cm) was greater than $0.3456 + 0.00156 \times R$.

To further reduce the muon contribution to the high p_T π^0 background the balanced p_T cut was also employed. This cut was based on the hypothesis that muon triggered events should generally have larger p_T imbalances than high p_T hard scattering events, since muon induced showers are uncorrelated with interactions in the target, which typically produce low p_T particles. Fig. 6.8 and 6.9 show the distribution of the ratio of the total away side transverse momentum to the p_T of the π^0 candidate with $5.5 < p_T < 10$ GeV/c for some selected rapidity regions and for candidate muon induced triggers and non-muon induced triggers, respectively.

The away side p_T was defined as the sum of the p_T s for particles detected in the tracking system and the EMLAC whose angle in the transverse plane was between 120° and 240° relative to the direction of the π^0 candidate. Only good quality tracks with $p_T > 0.3$ GeV/c and momenta less than 250 GeV/c, and photon showers with

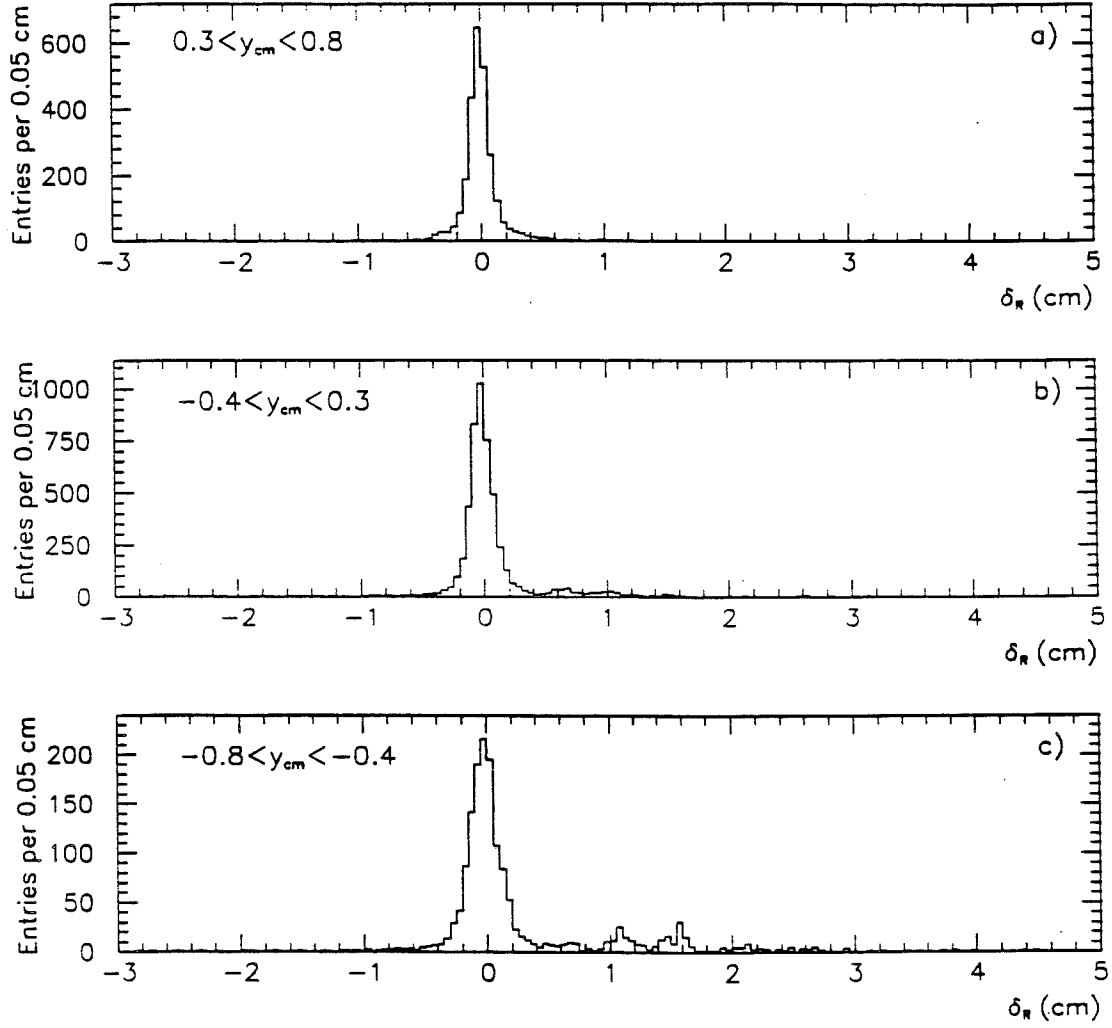


Figure 6.7

Directionality distribution for the higher energy photon of the $\gamma\gamma$ pair with $5.5 < p_T < 10$ GeV/c and mass in the π^0 region after the veto wall cut; a) for $0.3 < y_{cm} < 0.8$, b) $-0.4 < y_{cm} < 0.3$, and c) $-0.8 < y_{cm} < -0.4$.

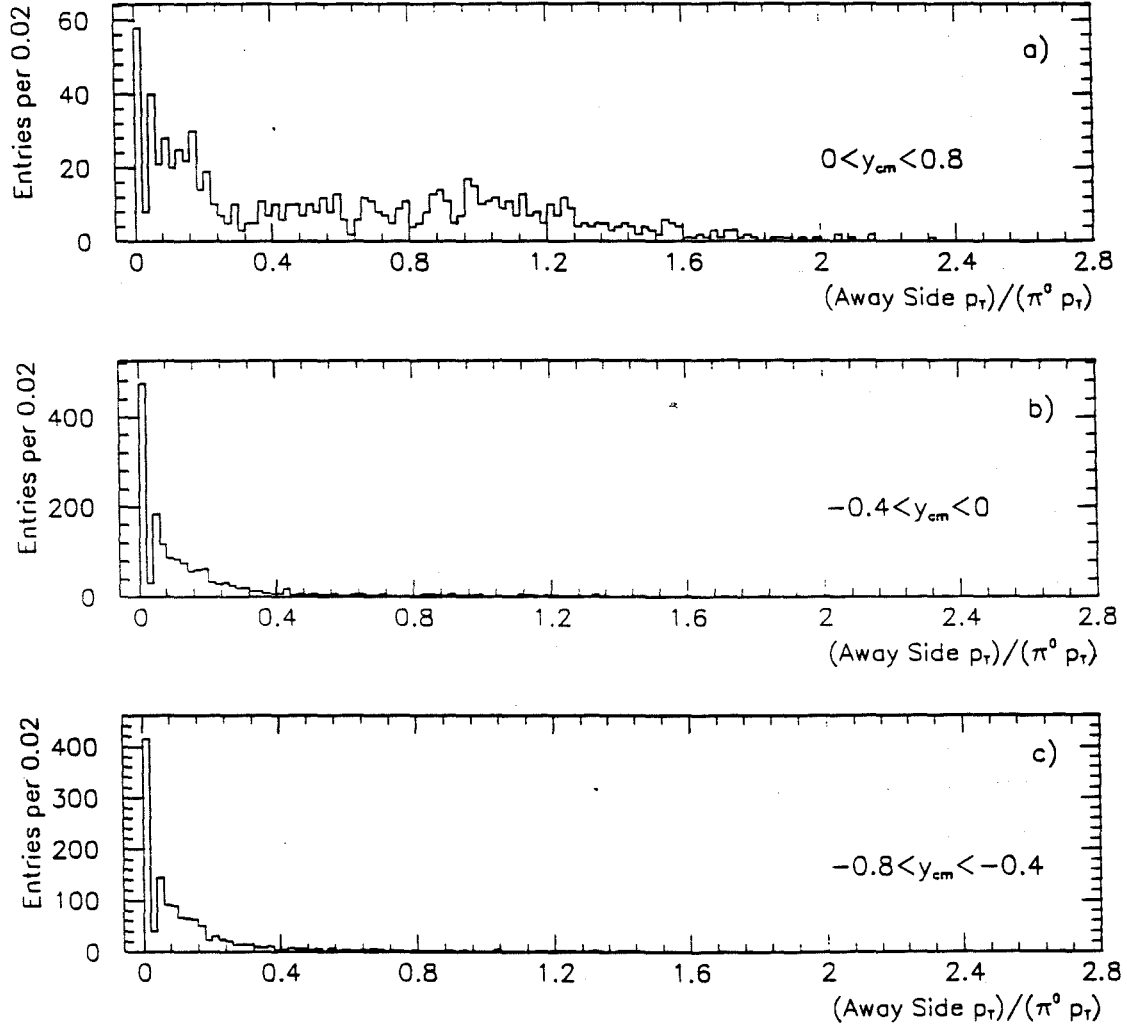


Figure 6.8 Ratio of the total away side p_T to the p_T of the π^0 candidate with $5.5 < p_T < 10$ GeV/c for events when the VWS signal indicated a potential muon candidate; a) for $0 < y_{cm} < 0.8$, b) $-0.4 < y_{cm} < 0$, and c) $-0.8 < y_{cm} < -0.4$.

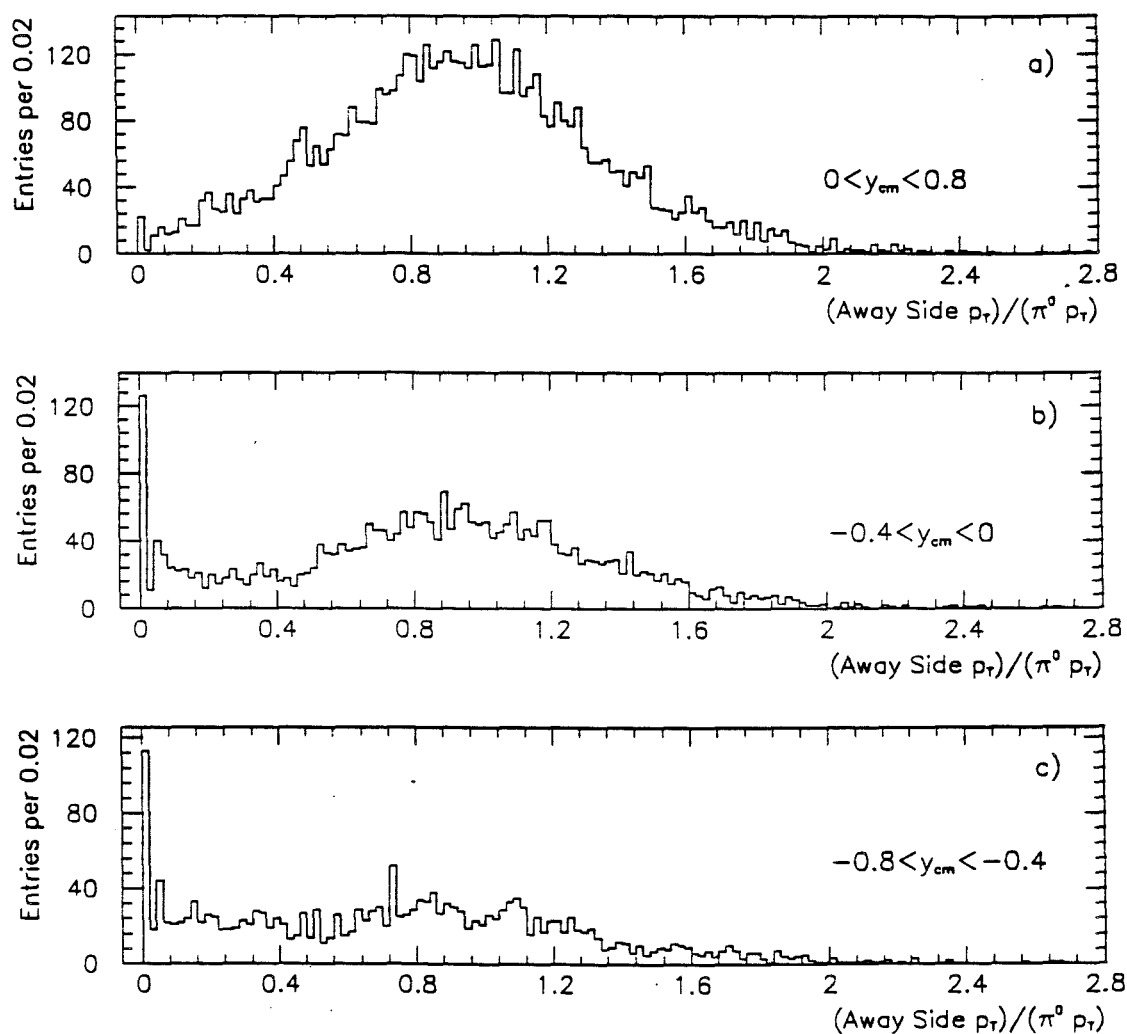


Figure 6.9 Ratio of the total away side p_T to the p_T of the π^0 candidate with $5.5 < p_T < 10$ GeV/c after the veto wall cut; a) for $0 < y_{cm} < 0.8$, b) $-0.4 < y_{cm} < 0$, and c) $-0.8 < y_{cm} < -0.4$.

$p_T > 0.3$ GeV/c were included in the definition of the away side p_T . Combinations with away side p_T less than 30% of the π^0 p_T were rejected.

The effectiveness of the three muon cuts is illustrated in Fig. 6.10, where the π^0 mass region is shown for several p_T intervals. The π^0 signal is reasonably clean, even at the highest p_T values.

Although the three cuts described above were very effective in eliminating muons, they also rejected some good events for which we must apply a correction. Losses from random coincidence of the software veto wall cut with good events were corrected by determining the number of good π^0 events with $4 < p_T < 5$ GeV/c that were eliminated by the application of the VWS criterion. This correction was found to be approximately independent of rapidity and p_T , and averaged 8.4% with an uncertainty of 1%.

Corrections for the directionality and balanced p_T cut were determined simultaneously in order to eliminate any correlation effects. The correction was determined by counting the number of π^0 s left after both cuts were applied to the uncut π^0 sample with $5 < p_T < 6$ GeV/c. In both samples, the software veto wall cut was applied. The correction was found to be approximately rapidity and p_T independent and averaged 4.5% with an uncertainty of about 1%.

6.2 π^0 SIGNAL DEFINITION

Fig. 6.11 displays the $\gamma\gamma$ invariant mass in the π^0 mass range for *SINGLE LOCAL* triggers, requiring a p_T of at least 3.5 GeV/c and energy asymmetry $A < 0.75$ for the two-photon pairs. The asymmetry cut of 0.75 was applied to the data in order to improve the signal to background ratio. Because the asymmetry distribution is isotropic (see following paragraph), such a cut does not introduce any

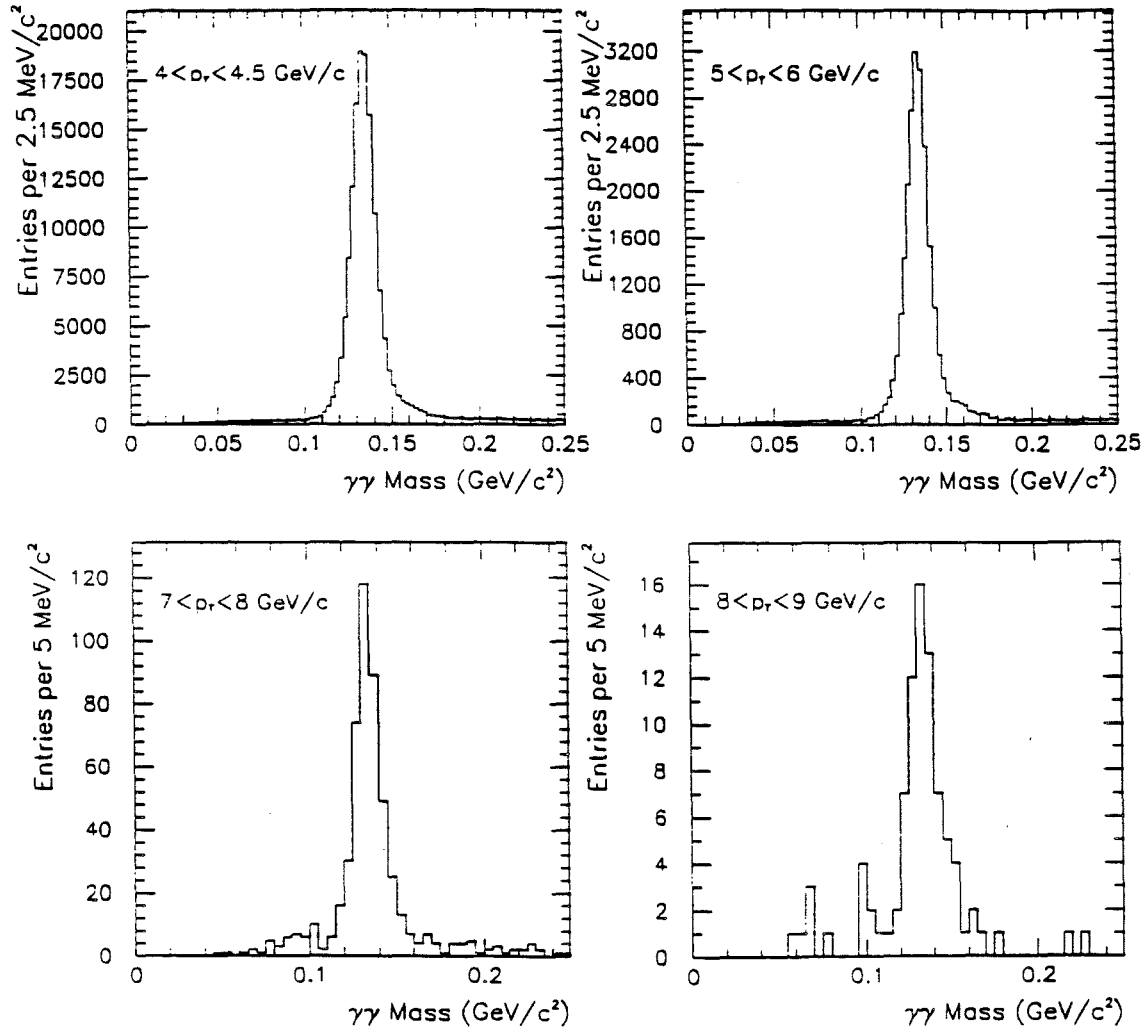


Figure 6.10 Two-photon mass distribution in the π^0 mass region for some selected p_T intervals after the muon rejection cuts.

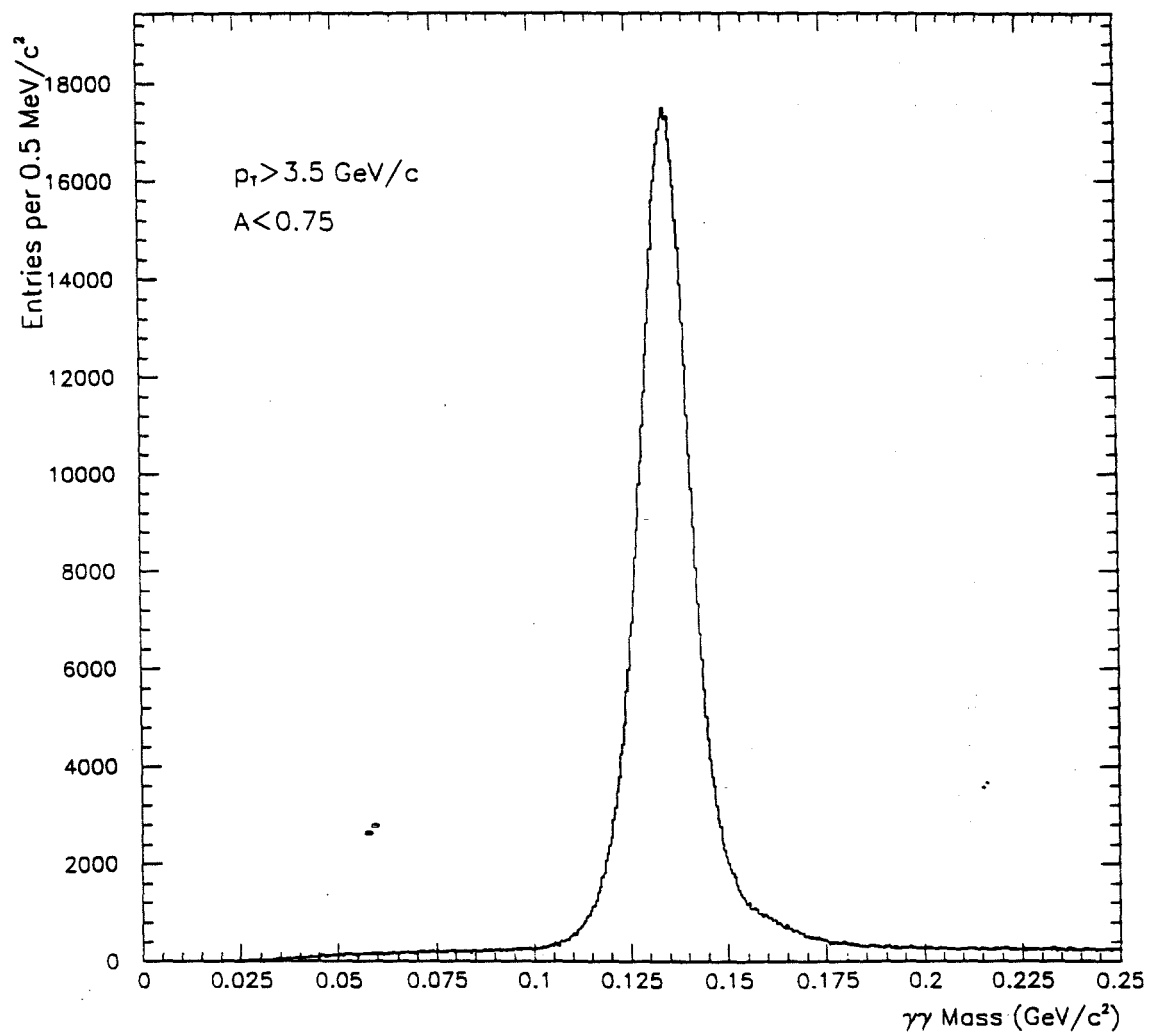


Figure 6.11 Two-photon mass distribution in the π^0 mass region for $p_T > 3.5$ GeV/c and $A < 0.75$.

bias into the π^0 sample. In order to study π^0 production, the $\gamma\gamma$ mass range $100 \text{ MeV}/c^2 < M_{\gamma\gamma} < 180 \text{ MeV}/c^2$ was defined as the π^0 mass band. To account for combinatorial background under the π^0 signal, sidebands were selected which covered half of the mass range of the π^0 peak. For $p_T < 7 \text{ GeV}/c$, the half sideband region was defined as the ranges $80 - 100 \text{ MeV}/c^2$ and $190 - 210 \text{ MeV}/c^2$, while for $p_T > 7 \text{ GeV}/c$, the half sidebands were $90 - 100 \text{ MeV}/c^2$ and $190 - 220 \text{ MeV}/c^2$. This adjustment in the definition of sidebands was done to minimize the sensitivity to any residual muon contribution to the low mass background. The π^0 signal was defined as the number of $\gamma\gamma$ pairs found in the π^0 mass band region minus twice the number of $\gamma\gamma$ pairs counted in the half sideband regions.

The energy asymmetry distribution for π^0 s with $p_T > 4 \text{ GeV}/c$ is shown in Fig. 6.12. Fig. 6.12a and b show the asymmetry distributions for the π^0 mass region and half sideband regions respectively. Fig. 6.12c displays the sideband subtracted asymmetry distribution. Since the π^0 is a spin zero particle, it decays isotropically in its rest frame, and thus it is expected that the energy asymmetry distribution (which corresponds to $\beta |\cos\vartheta^*|$ in its rest frame, where ϑ^* is the photon decay angle, and $\beta \approx 1$ at high energies) will be flat from zero to one. The fall-off at large asymmetries is attributed to losses of low energy photons. In addition, the small decrease in the number of π^0 s with asymmetries around zero is attributed to miscorrelations in reconstructing the energies of the photons with approximately equal energies.

6.3 COMPARISON OF DATA AND MONTE CARLO

As mentioned in Section 5.4, we used the GEANT software package and the HERWIG event generator for our Monte Carlo simulation of the spectrometer. The

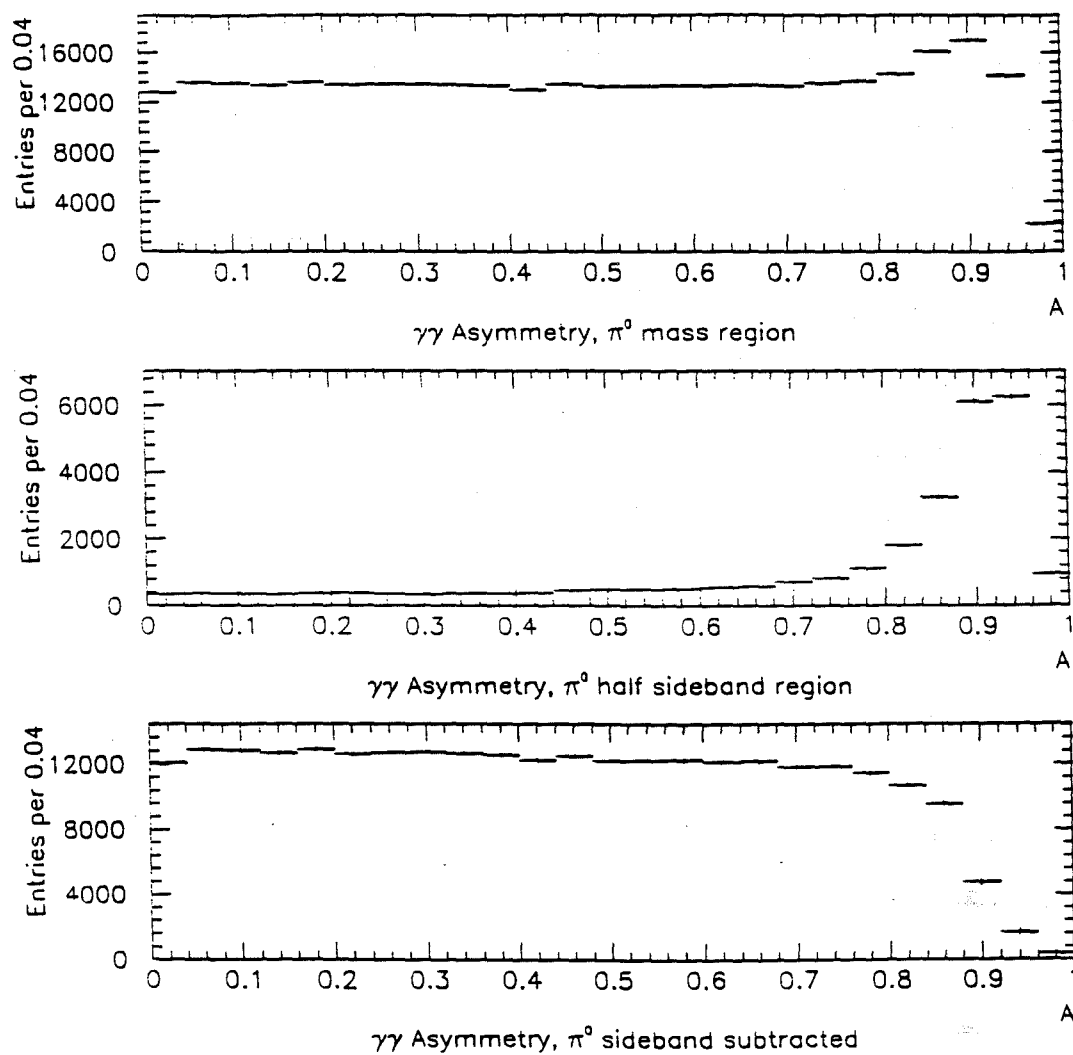


Figure 6.12 Two-photon energy asymmetry distribution for the π^0 mass region, half sideband regions, and sideband subtracted for $p_T > 4$ GeV/c.

Monte Carlo was used to estimate the π^0 reconstruction efficiency as a function of p_T and rapidity. In the Chapter 5 discussion of the energy scale study, we demonstrated that the Monte Carlo simulation agrees with various data projections remarkably well. In this section, we will present some additional comparisons between Monte Carlo and data.

Partially reconstructed or misidentified π^0 s account for the major source of background to the direct-photon signal. Fig. 6.13a shows the background subtracted π^0 energy asymmetry distribution for both data and Monte Carlo. In this plot the Monte Carlo events were normalized relative to the data in the flat region. The agreement between data and Monte Carlo is quite good which implies that the π^0 reconstruction efficiency will adequately account for any residual π^0 losses with $A < 0.75$.

Fig. 6.13b shows the π^0 mass distribution for both data and Monte Carlo, with $p_T > 4$ GeV/c and $A < 0.75$. These distributions are also in quite good agreement. The small difference observed in the tails of the π^0 peak is attributed to non-Gaussian effects in the data that were not fully simulated in the Monte Carlo. Due to these non-Gaussian tails we had to increase the π^0 mass range definition (discussed earlier) in order to account for these π^0 s.

Another important comparison involved the E_{front}/E_{tot} distribution. Fig. 6.14 shows the E_{front}/E_{tot} distribution for data and Monte Carlo in different photon energy ranges. The agreement is very good. This indicates that the Monte Carlo reproduces the photon shower development very well and can thus be used to account for the π^0 losses due to the photon E_{front}/E_{tot} cut applied to the data.

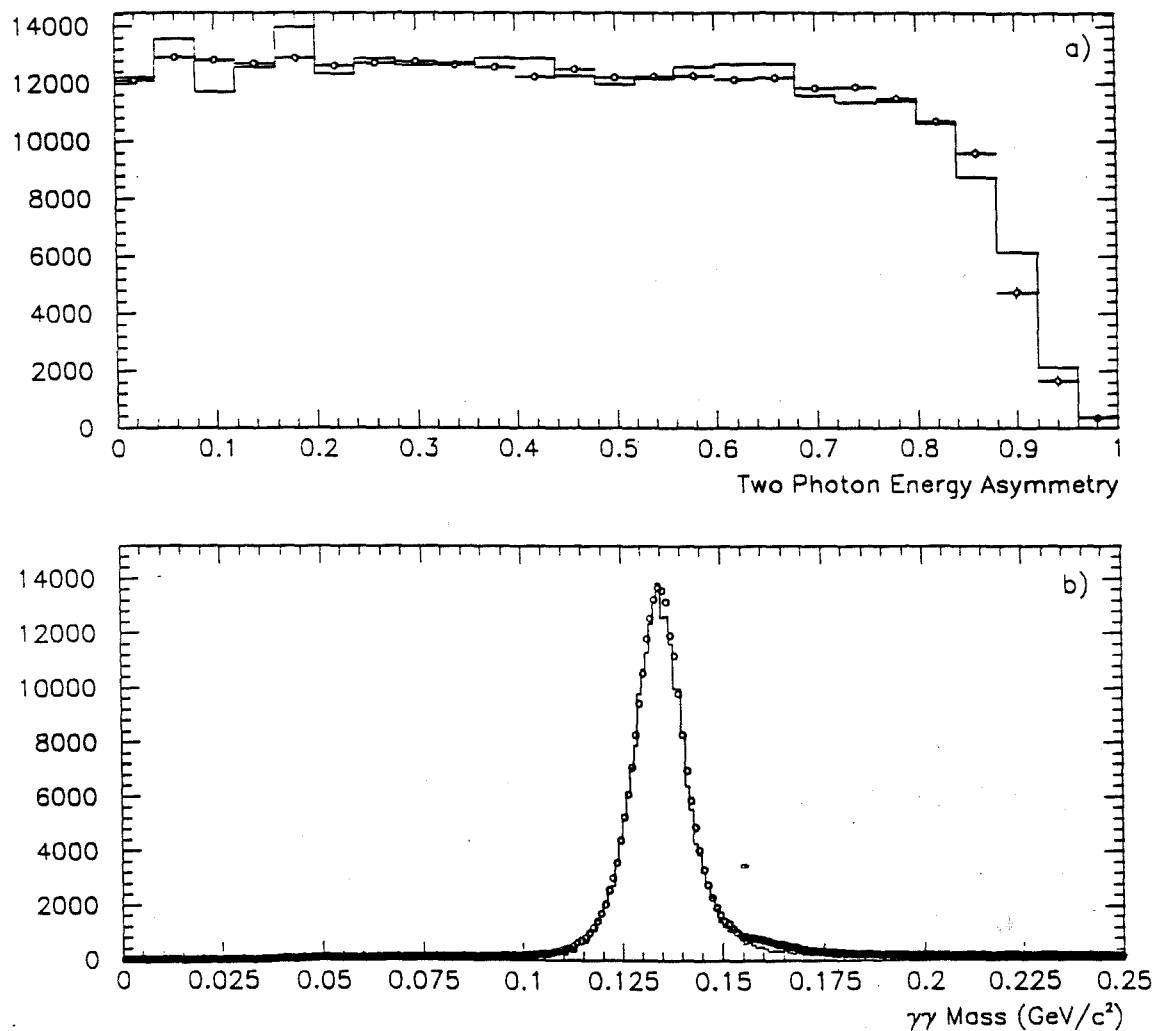


Figure 6.13 a) The sideband subtracted two-photon energy asymmetry distribution for photon pairs in the π^0 mass range for $p_T > 4$ GeV/c. The Monte Carlo distribution is shown as the histogram and the data with the circles. b) Two-photon mass distribution in the π^0 mass region with $p_T > 4$ GeV/c for data (circles) and Monte Carlo (histogram).

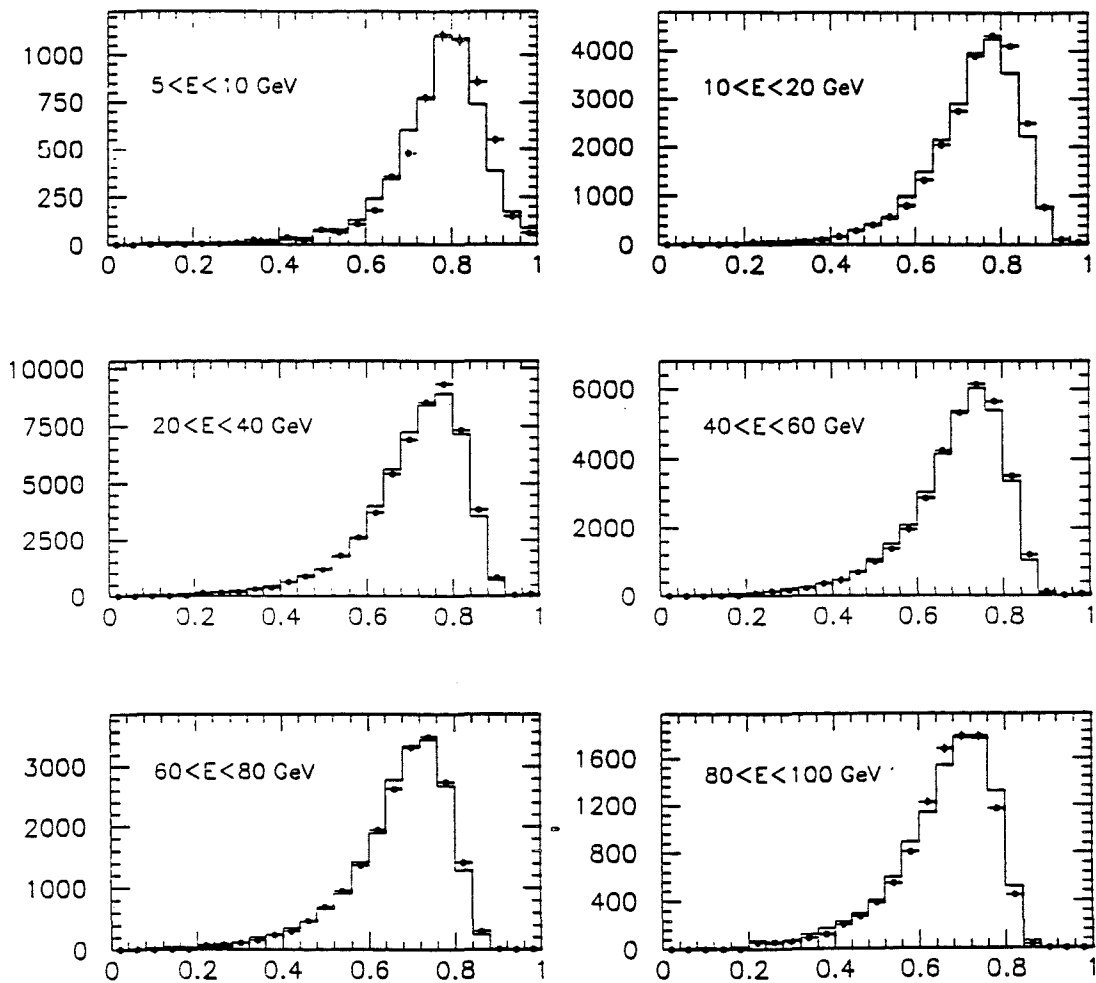


Figure 6.14 E_{front}/E_{tot} distribution for data (points) and Monte Carlo (histogram) in different photon energy ranges.

6.4 π^0 CROSS SECTION CALCULATION

The invariant π^0 cross section per nucleon can be written in the form:

$$E \frac{d^3\sigma}{dp^3} = \frac{1}{2\pi p_T \Delta p_T \Delta y_{cm}} \frac{1}{\rho l N_a} \frac{N^{corr}(p_T, y_{cm})}{(LTB)} (ABS) \quad (6.2)$$

where

$$N^{corr}(p_T, y_{cm}) = \sum_{i=1}^{N^{obs}} W_i \quad (6.3)$$

is the corrected number of π^0 s per p_T and rapidity (y_{cm}) interval, and W_i is the event weight given by:

$$W_i = C W_{trig} W_{conv} W_{vrtx} W_{accpt} W_{rec} \quad (6.4)$$

The meaning of the variables in the above expressions are:

ρ is the density of the target material;

l is the length of the target;

N_a is Avogadro's number;

ABS is the correction due to beam absorption ($ABS = e^{z/\lambda}$, λ is the absorption length for the material, calculated using π^- absorption cross section measurements^[2]);

LTB is the live triggerable beam;

C is a correction factor for the cuts applied;

N^{obs} is the observed number of π^0 s in the selected p_T and y_{cm} interval;

W_{trig} is the octant based trigger weight calculated event by event;

W_{conv} is the correction for π^0 losses due to photon conversions;

[2] A. S. Carroll et al., *Phys. Lett.* B80 (1979), 319.

W_{vrtx} is the vertex reconstruction efficiency correction;

W_{acpt} is the weight employed to account for the π^0 geometric acceptance;

W_{rec} is the π^0 reconstruction efficiency correction.

Geometric Acceptance

The geometric acceptance accounted for the π^0 losses when at least one of the photons fell outside of the fiducial region in the EMLAC. To study this acceptance a “simple” Monte Carlo program was developed. This Monte Carlo generated single π^0 s in the target area which decayed uniformly in asymmetry with $A < 0.75$, and the resulting photons were projected to the face of the EMLAC. The π^0 geometric acceptance was determined as the ratio of the number of π^0 s for which both decay photons fell within the fiducial volume to the total number of generated π^0 s. The acceptance was tabulated as a function of p_T , the pseudorapidity in the *lab* system[†] y_{lab} , the V_Z vertex position and the radial distance from the vertex to the axis of the EMLAC. Events were generated in a four-dimensional grid in p_T , y_{lab} , V_Z and R_T , with 20 bins in p_T from 2.5 to 12 GeV/c, 34 bins in y_{lab} from 2.51 to 4.335, 11 bins in V_Z from 0 to -40 cm, and 11 bins in R_T from 0 to 2 cm. To calculate the acceptance twenty thousand π^0 s were generated at each $(p_T, y_{\text{lab}}, V_Z, R_T)$ point on this grid; at other points a quadratic interpolation was performed. Fig. 6.15 displays the π^0 acceptance as a function of y_{cm} for some selected p_T regions, averaged in V_Z

[†] The reason for choosing the pseudorapidity in the lab reference system was that the acceptance tables would thereby be independent of beam momentum. The relation between y_{cm} and y_{lab} is $y_{\text{cm}} = y_{\text{lab}} - y_{\text{cm/lab}}$, where $y_{\text{cm/lab}} = 3.2$ for 520 GeV/c incident beam particles.

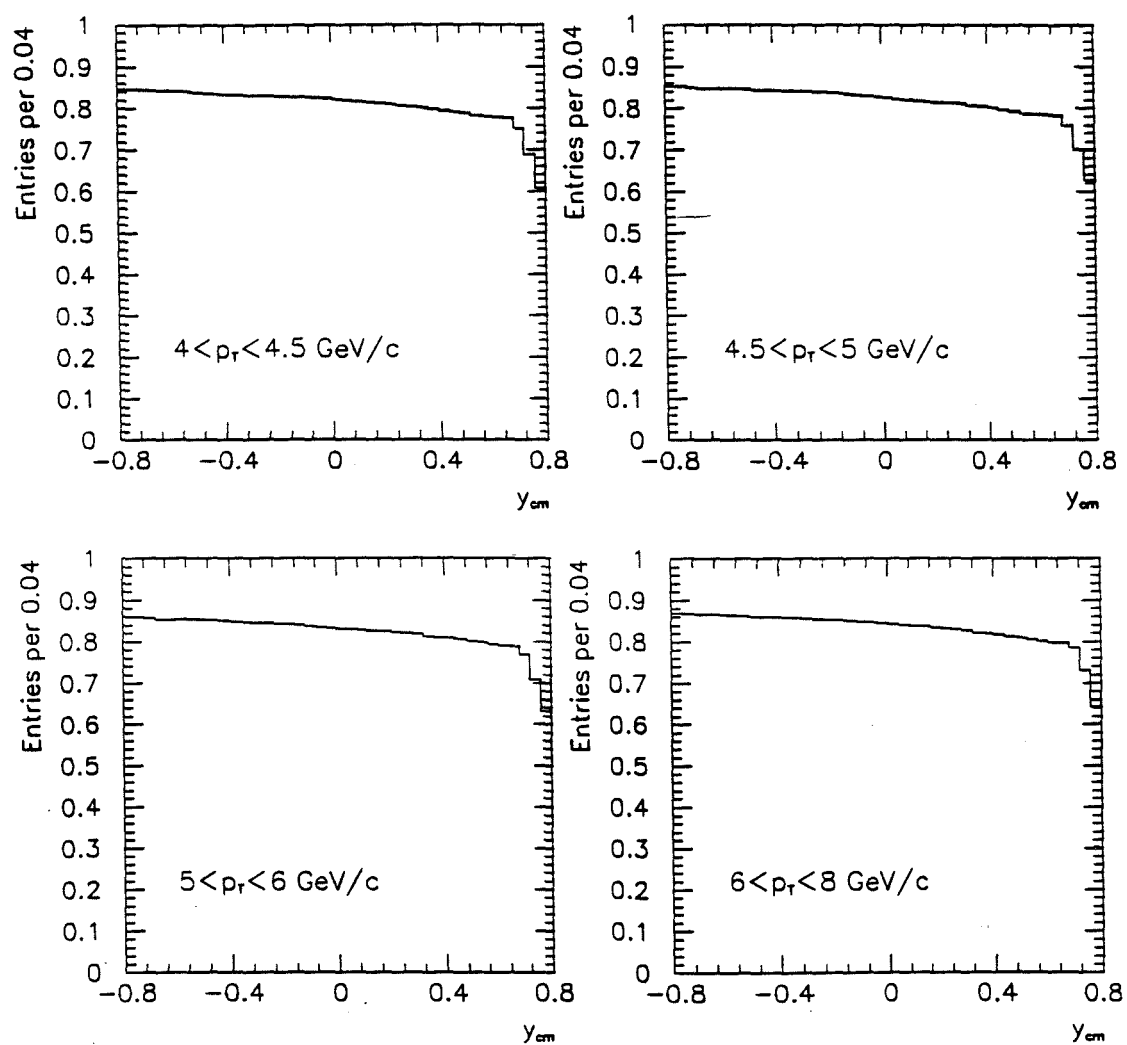


Figure 6.15 π^0 geometric acceptance as a function of y_{cm} for selected p_T intervals.

and R_T from the data sample used in this analysis. The inverse of this acceptance was used to weight π^0 s in the data.

π^0 Reconstruction Efficiency

To study the reconstruction efficiency, the GEANT/HERWIG π^0 Monte Carlo sample was used. These Monte Carlo events were processed using the same reconstruction code used for the data. Only generated π^0 s that produced photons that were within the fiducial region and did not convert to an e^+e^- pair upstream of the downstream interaction counters were considered. The ratio of the number of reconstructed π^0 s to the number of unconverted π^0 s generated within the fiducial region was determined as a function of p_T and y_{cm} . An asymmetry cut of 0.75 was applied. In addition, $E_{front}/E_{tot} > 0.2$ was required for all reconstructed showers.

This method for determining π^0 reconstruction efficiency also accounted for the energy resolution of the EMLAC. Since the cross section has a steep p_T dependence, the effect of the p_T resolution is to shift the observed cross section from low to higher values in p_T .

Fig. 6.15 shows the π^0 reconstruction efficiency, based on a two dimensional fit to the Monte Carlo results, as a function of p_T and y_{cm} . The inverse of this function was used to weight the observed number of π^0 s in the data. From Fig. 6.16 we see that for large p_T values and forward rapidities the reconstruction losses are quite large. This is attributed to the inability of the reconstruction algorithm to identify highly overlapping showers as two independent photons. The decrease in efficiency at low p_T s and backward rapidities was due to reconstruction losses of low energy photons.

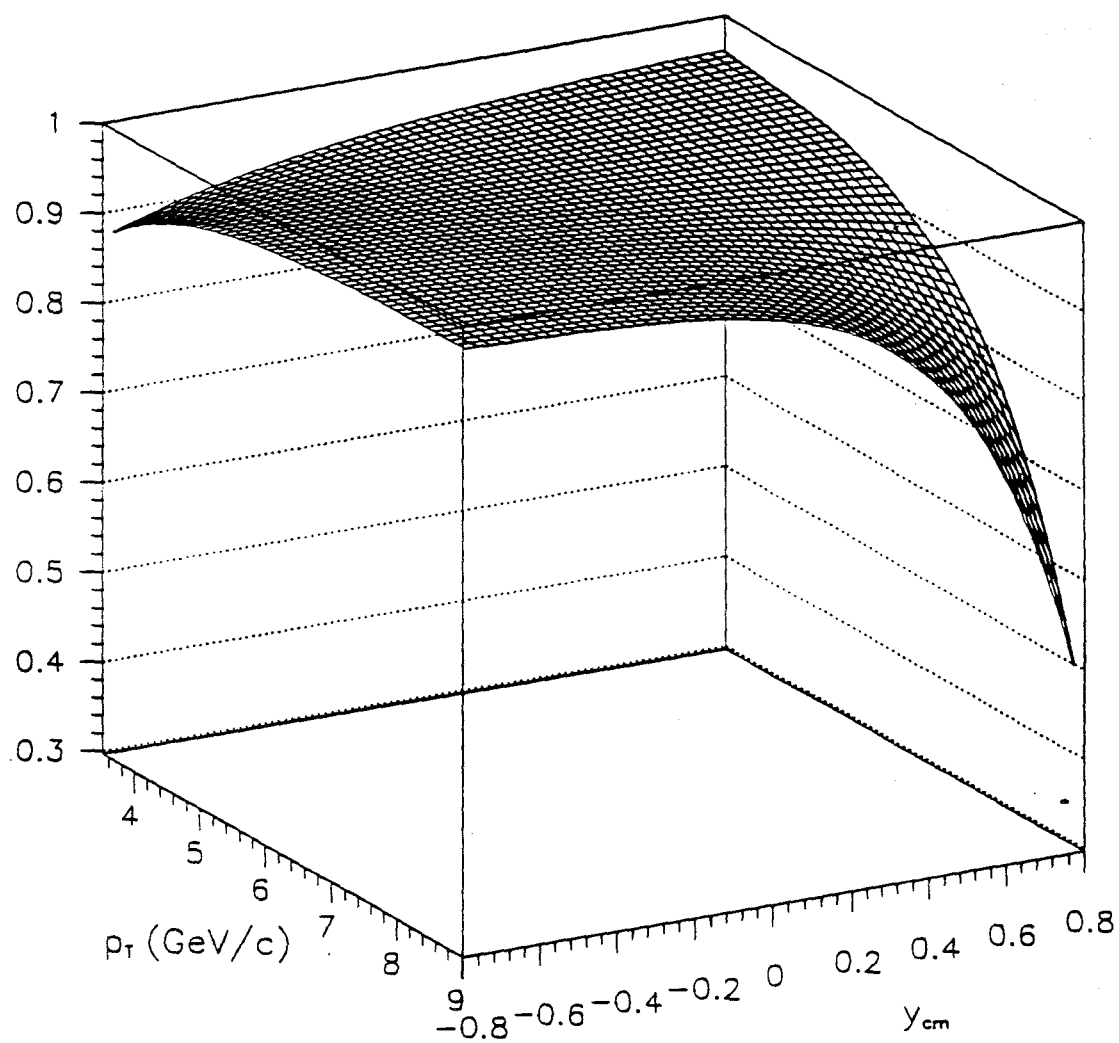


Figure 6.16 π^0 reconstruction efficiency as a function of p_T and y_{cm} .

The uncertainty of the π^0 reconstruction efficiency is estimated to be $\approx 5\%$ for $p_T < 6$ GeV/c and $\approx 8\%$ for $p_T > 6$ GeV/c.

Trigger Corrections

This analysis used events selected by the *SINGLE LOCAL HI* trigger for π^0 s with $p_T > 4$ GeV/c and the *SINGLE LOCAL LOW* trigger for $3.5 < p_T < 4$ GeV/c. The prescaled (by a factor of 40) *SINGLE LOCAL LOW* trigger data were employed for the lower p_T data so that average trigger efficiencies would be greater than 50%. Corrections for the trigger efficiencies were evaluated on an event by event basis using the measured octant based trigger efficiency of the EMLAC.

The weights to account for the trigger “turn on” were evaluated on an event by event basis. When reconstructing an event, the strip energies were also used to simulate of the trigger as follows: The r view was divided into 31 sections of sixteen contiguous r-strips overlapping by eight strips. These sections corresponded to the on-line trigger regions of this octant. The summed energy in these strips was weighted by the same weights used in the formation of the on-line trigger to determine the p_T for each region. In order to properly simulate the on-line trigger, none of the energy scale corrections discussed in Chapter 5 were applied to the strip energies.

To eliminate possible biases all octants except the triggering octant in an event were used for this study. The number of successes over the number of trials in each region potentially satisfying the trigger was determined as a function of the region’s p_T . A fit to the “turn-on” distribution of each region of each octant was performed to determine the probability that this region could have fired the trigger. Then by

combining all 31-region probabilities an octant probability was generated. The inverse of this octant probability was used as the trigger weight for that octant.

Fig 6.17 shows the “turn-on” distribution of four regions of a typical octant for *SINGLE LOCAL HI* triggers. Similar “turn-on” distributions for *SINGLE LOCAL LOW* triggers are shown in Fig. 6.18.^[3] Recall that the p_T shown in these plots corresponds to the trigger- p_T and not to the p_T of the π^0 .

Note that these trigger weights do not account for an inefficiency of the LAC *PRETRIGGER*. The “turn-on” distributions for the *PRETRIGGER* inner and outer regions as a function of trigger- p_T and π^0 p_T are shown in Fig. 6.19 and 6.20 respectively (Ref. [3.21]). These distributions imply that for the p_T range of interest the *PRETRIGGER* was essentially fully efficient. Thus no explicit *PRETRIGGER* correction was necessary.

In addition, due to trigger inefficiencies or hardware malfunctions, certain regions of some octants were eliminated from the cross section calculation. These acceptance losses were accounted for based upon results from corresponding regions in other octants.

Live Beam Count

The total number of incident beam particles during the time that the experiment was ready to accept a trigger is called *live triggerable beam (LTB)*. To determine the *LTB* information from various experimental scalers was used. These scalers were read out by the DA system at the end of each spill. Using the terminology of Section 3.8, the *LTB* can be expressed in the form:

[3] P. Chang, private communication.

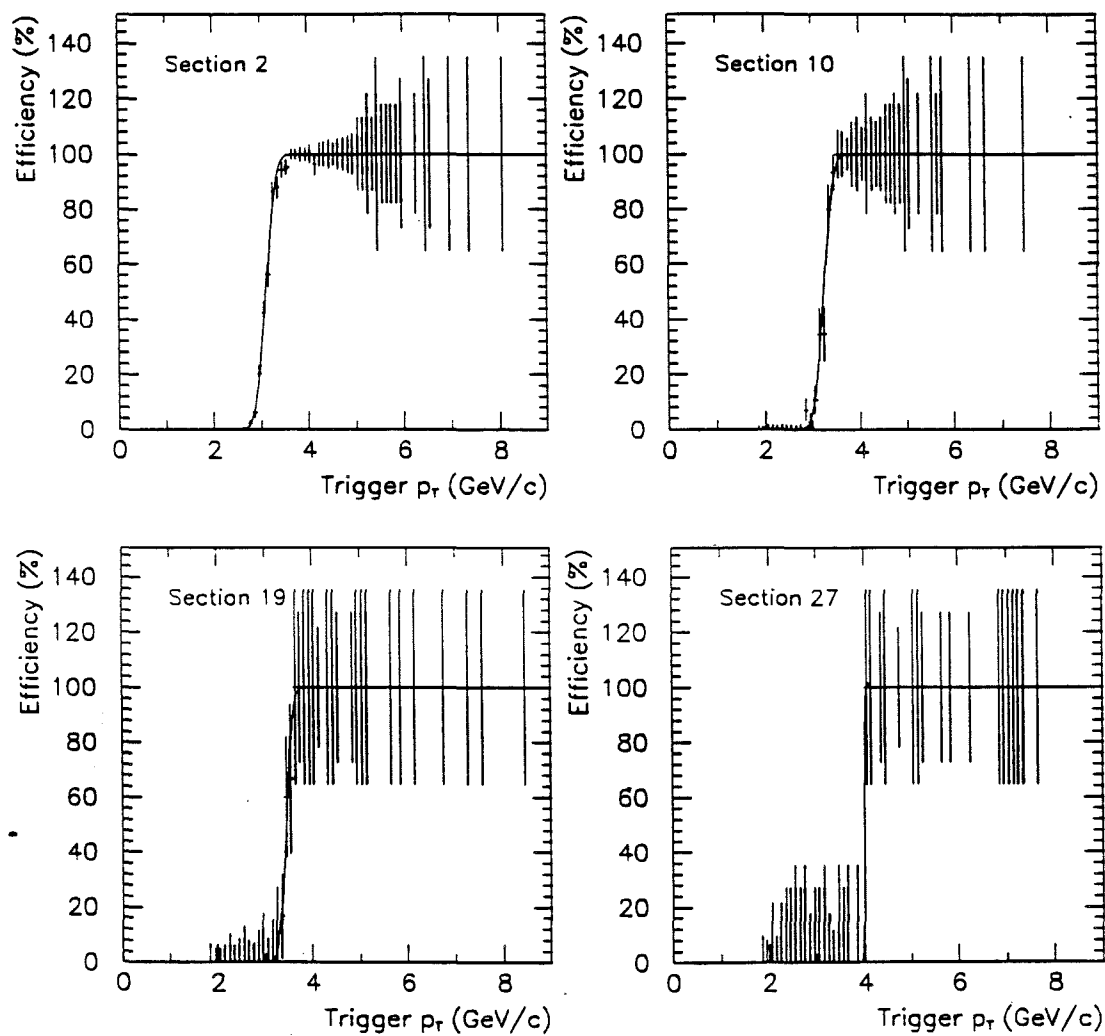


Figure 6.17 Efficiency distribution for four sections of an octant for *SINGLE LOCAL HI* triggers as a function of trigger p_T .

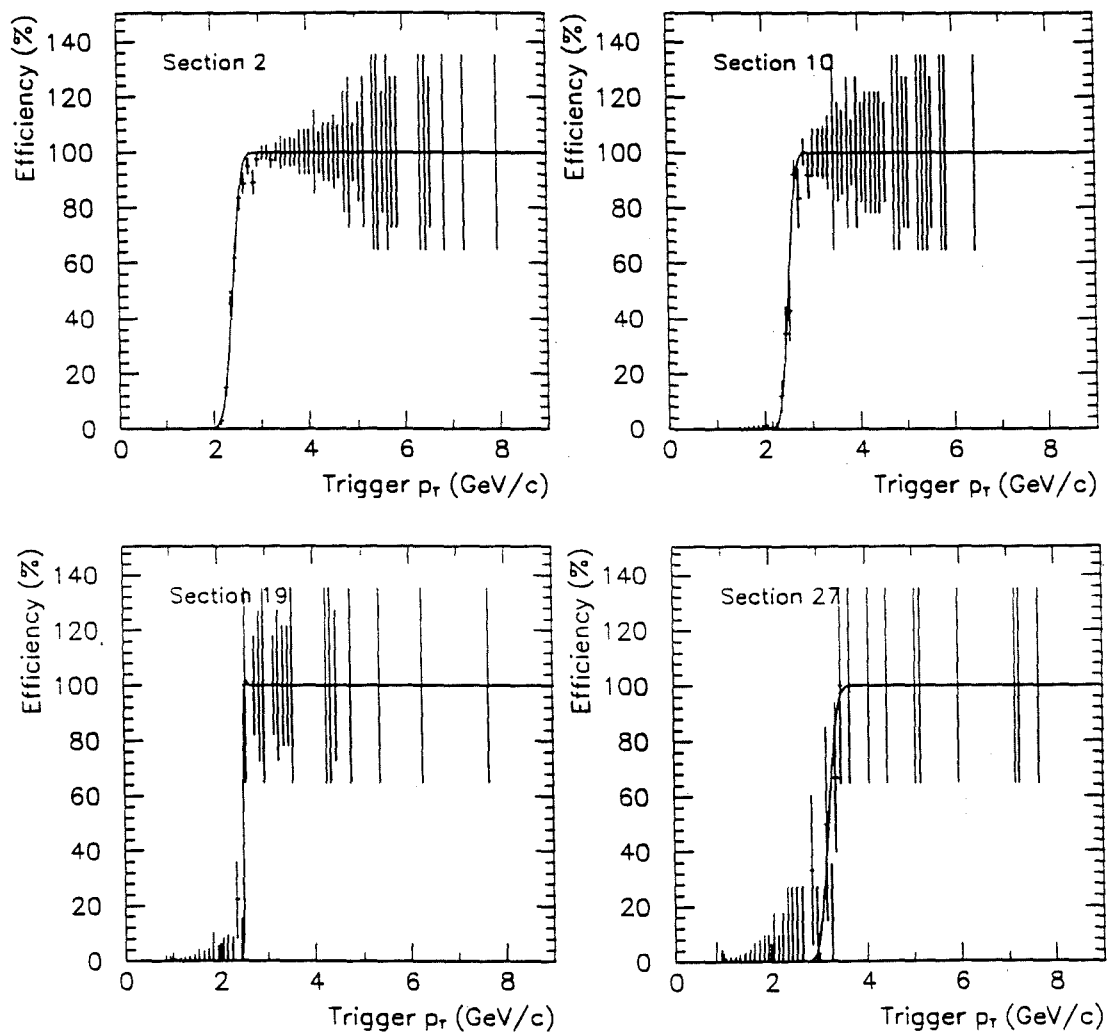


Figure 6.18 Efficiency distribution for four sections of an octant for *SINGLE LOCAL LOW* triggers as a function of trigger p_T .

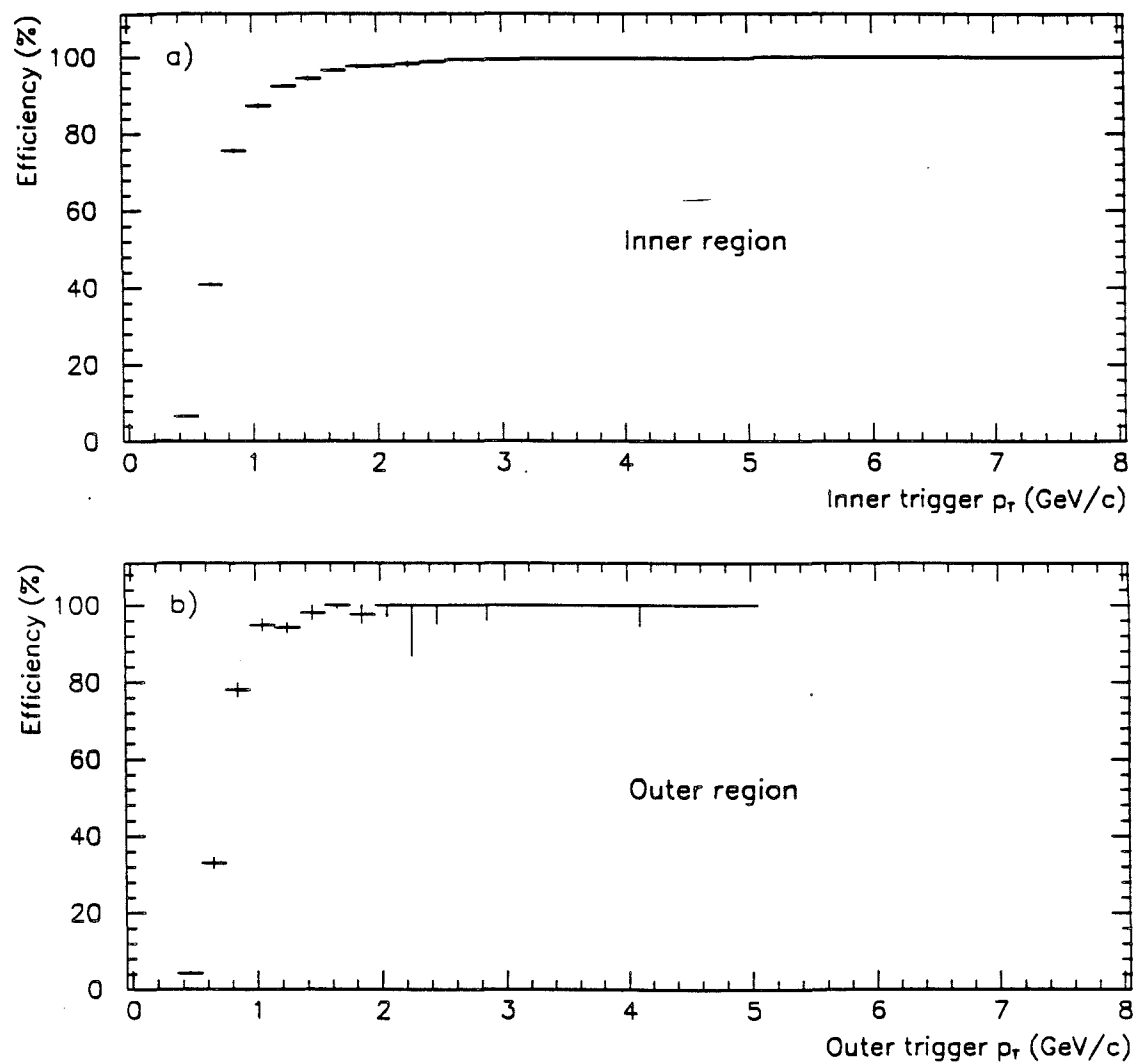


Figure 6.19 *PRETRIGGER* efficiency distribution as a function of trigger p_T a) for the inner region and b) for the outer region.

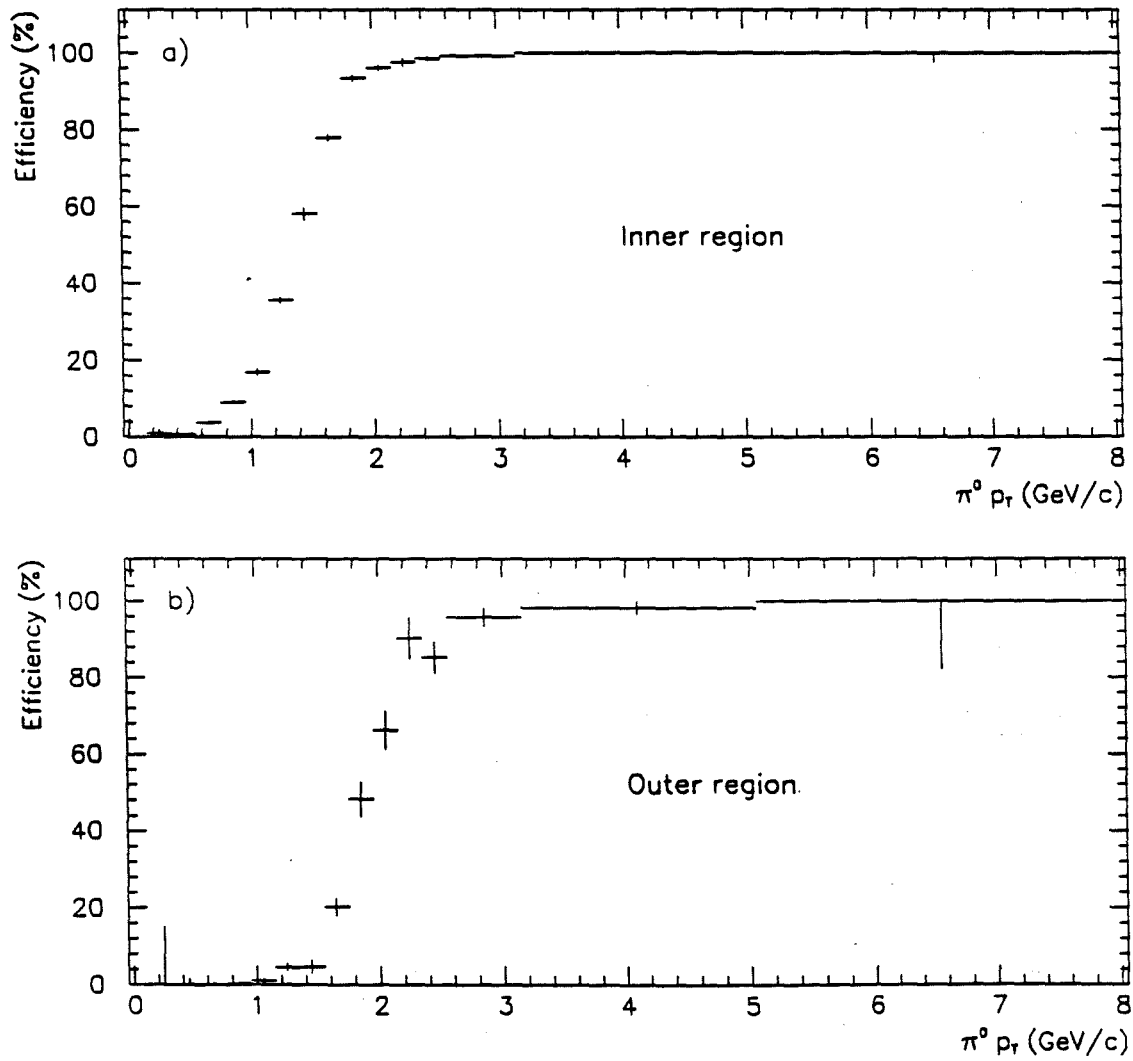


Figure 6.20 *PRETRIGGER* efficiency distribution as a function of $\pi^0 p_T$ a) for the inner region and b) for the outer region.

$$LTB = BEAM1 \otimes \overline{BH} \otimes (Live\ Fraction) \quad (6.5)$$

where

$$(Live\ Fraction) = (DA\ Live\ Fraction) \otimes \left(\frac{CLEAN_INT}{INT} \right) \otimes (PRETRIGGER\ Live\ Fraction) \otimes ("Trigger"\ Live\ Fraction) \quad (6.6)$$

The *CLEAN_INT* fraction accounted for the “dead” time due to the requirement that there was no other interaction within ± 60 ns of the interactions of interest. The “*TRIGGER*” live fraction accounted for various trigger related “dead” times, including the on-line veto wall requirement, *SCRKILL*, and early p_T vetoing.

Since the live fraction calculation was octant dependent, the *LTB* used for the cross section normalization was determined separately for each octant. The *LTB* also depended upon the p_T range, since for $3.5 < p_T < 4$ GeV/c only set 1 runs contributed to that cross section measurement.

Other Corrections to the Cross Section

In addition to the corrections discussed in the previous paragraphs, the measured π^0 cross section also included corrections for the following effects:

- **Asymmetry cut:** To define the π^0 signal an energy asymmetry cut of 0.75 was applied for the two-photon pairs. Since the asymmetry distribution for a spin zero particle is expected to be uniform, a correction of $1/0.75$ was applied to correct for this cut.
- **Photon conversions (W_{conv}):** As we have already discussed in Section 5.2, some photons convert to e^+e^- pairs as they pass through materials in the spectrometer. These photon conversions result in losses of π^0 s as observed in the two photon mode. A correction for these losses was determined using the π^0 s found and was based on the position of the reconstructed vertex and the

number of radiation lengths of material each of the reconstructed photons traversed. The average correction used to weight the π^0 s in data was $\approx 38\%$ for interactions in Cu and $\approx 17\%$ for interactions in Be.

- **Beam absorption (*ABS*):** This correction accounted for the loss of beam particles due to interactions in the material between the beam counters and the interaction point in the target. The correction depended upon the Z position of the vertex and averaged (including the *ABS* due to beam SSD planes) around 0.7% for Cu and around 5.4% for Be.
- **Vertex reconstruction efficiency (W_{vtx}):** This correction was determined from Monte Carlo events and was found to be of order of 0.4%.
- **Beam muon contamination:** A correction accounted for the muon content of the beam was determined from measurements performed during the 1991 running period using the FCAL.^[4] These results suggested that the muon fraction in the beam was around 0.5%.

Table 6.2 summarizes the corrections used in determining the π^0 cross section.

^[4] G. B. Osborne, E706 Internal Note 197 (1992).

Corrections	$\pi^- + \text{Be}$	$\pi^- + \text{Cu}$
Geometric acceptance	Function of p_T , y_{lab} , V_Z , and R_T	
Reconstruction efficiency	Function of p_T and y_{cm}	
Trigger corrections	Function of run, p_T and y_{cm}	
Target fiducial cut	1.347	
Vertex reconstruction	1.004	
Beam muon contamination	1.005	
π^0 Branching ratio to $\gamma\gamma$ decay	1.012	
Asymmetry cut	1.333	
Veto wall cut	1.084	
Balance p_T and δ_R cut	1.045	
Photon conversions	1.175	1.380
Beam absorption	1.054	1.007
Target density (g/cm^3)	1.848	8.96
Target atomic weight	9.012	63.546
Absorption length (cm)	57.953	19.289

Table 6.2 Listing of average values of corrections applied to the data.

7. RESULTS AND CONCLUSIONS

7.1 CROSS SECTIONS

The inclusive invariant cross sections per nucleon for π^0 production in 520 GeV/c π^- Be interactions, averaged over p_T and rapidity intervals are presented in Table B.1. These results are also displayed in Figs. 7.1 through 7.3. There is no significant variation in the shape of the cross section for the different rapidity regions shown. The data presented in the p_T range 3.5 to 4 GeV/c were accumulated with the *SINGLE LOCAL LOW* trigger.

Fig. 7.4 shows the cross section as a function of rapidity for some selected p_T intervals. The shape of the cross section has similar behavior as a function of rapidity for the p_T regions shown. The maximum of the π^0 cross section occurs for $y_{cm} > 0$ which can be attributed to partons in the π^- beam carrying on the average a higher fraction of the hadron momentum than partons in the nucleon since nucleons have one more valence quark than mesons. Therefore parton-parton rest system tends to move forward with respect to the hadron-hadron center of mass system.

Tables B.2 and B.3 present the invariant cross sections per nucleon for $\pi^- + \text{Be} \rightarrow \pi^0 + X$ and $\pi^- + \text{Cu} \rightarrow \pi^0 + X$, respectively, averaged over the rapidity range $-0.75 < y_{cm} < 0.75$, as a function of p_T . Figs. 7.5 and 7.6 display these results along with next-to-leading-log QCD calculations of Aversa et al. (Ref. [1.37]). The calculated cross sections have been scaled by the factor $A^{\alpha-1}$, where A is the appropriate atomic weight and $\alpha = 1.083 \pm 0.003$ is the average value measured for all p_T s (see Section 7.3), in order to take into account nuclear dependence effects.

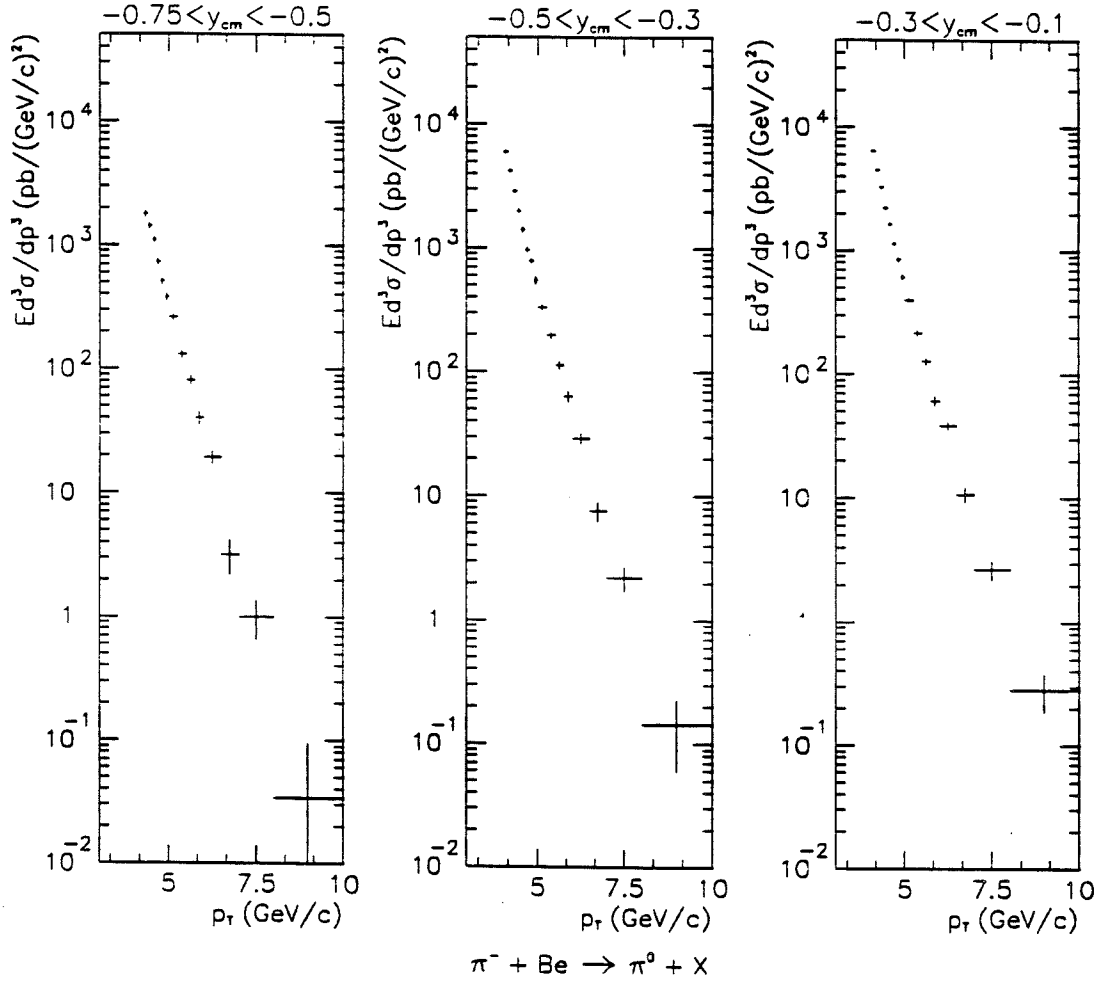


Figure 7.1

Inclusive invariant cross sections per nucleon for π^0 production in 520 GeV/c π^- Be interactions, as a function of p_T averaged over the rapidity intervals: $-0.75 < y_{cm} < -0.5$, $-0.5 < y_{cm} < -0.3$, and $-0.3 < y_{cm} < -0.1$.

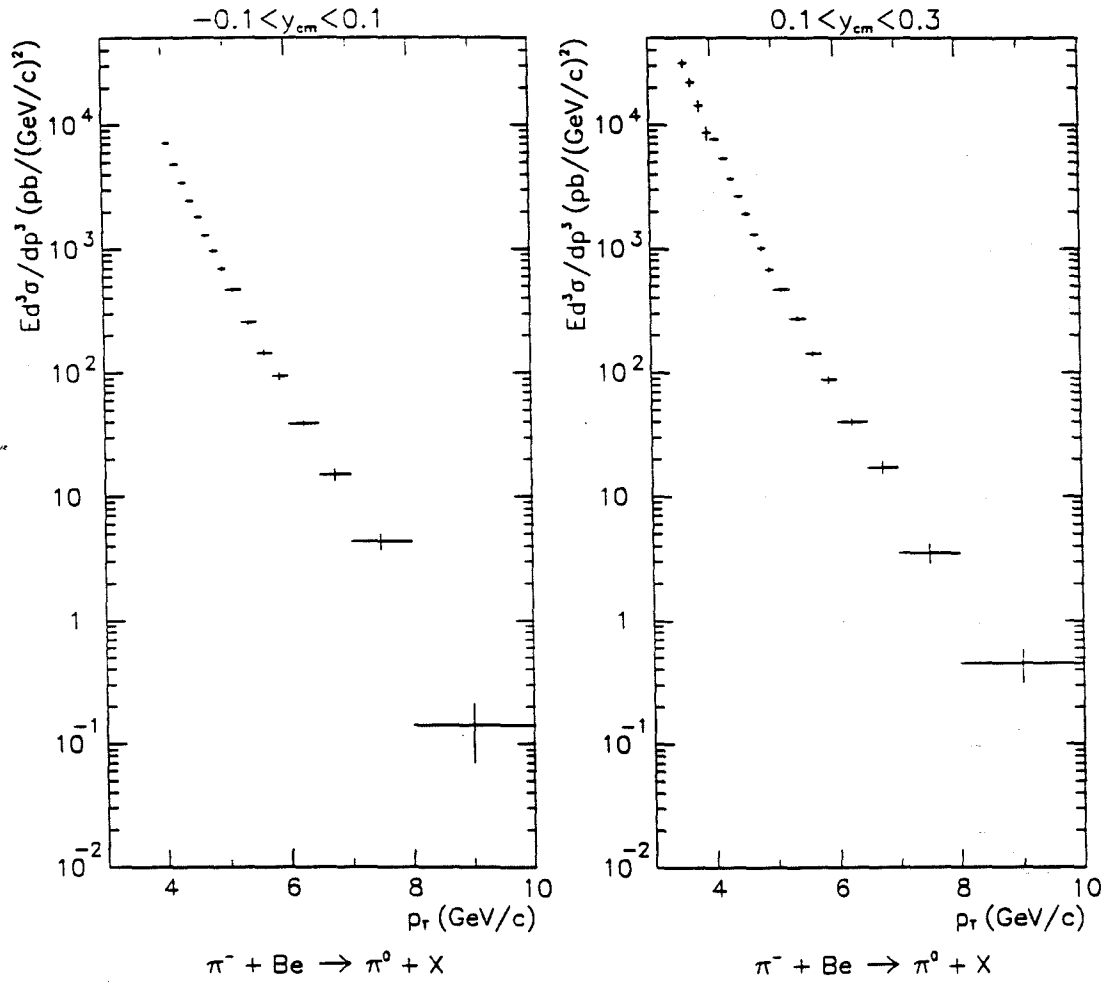


Figure 7.2

Inclusive invariant cross sections per nucleon for π^0 production in $520 \text{ GeV}/c$ π^- -Be interactions, as a function of p_T averaged over the rapidity intervals: $-0.1 < y_{cm} < 0.1$ and $0.1 < y_{cm} < 0.3$.

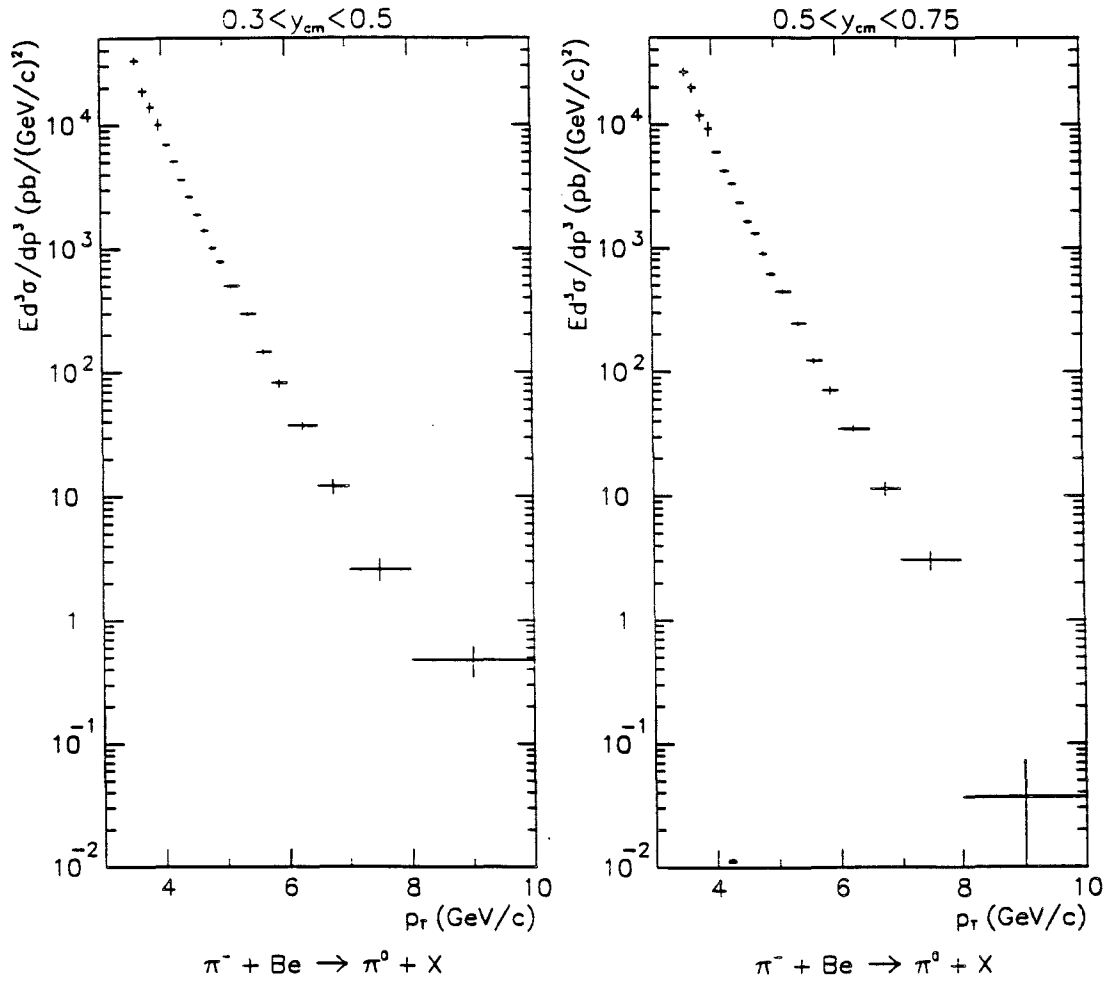


Figure 7.3 Inclusive invariant cross sections per nucleon for π^0 production in 520 GeV/c $\pi^- \text{Be}$ interactions, as a function of p_T averaged over the rapidity intervals: $0.3 < y_{cm} < 0.5$ and $0.5 < y_{cm} < 0.75$.

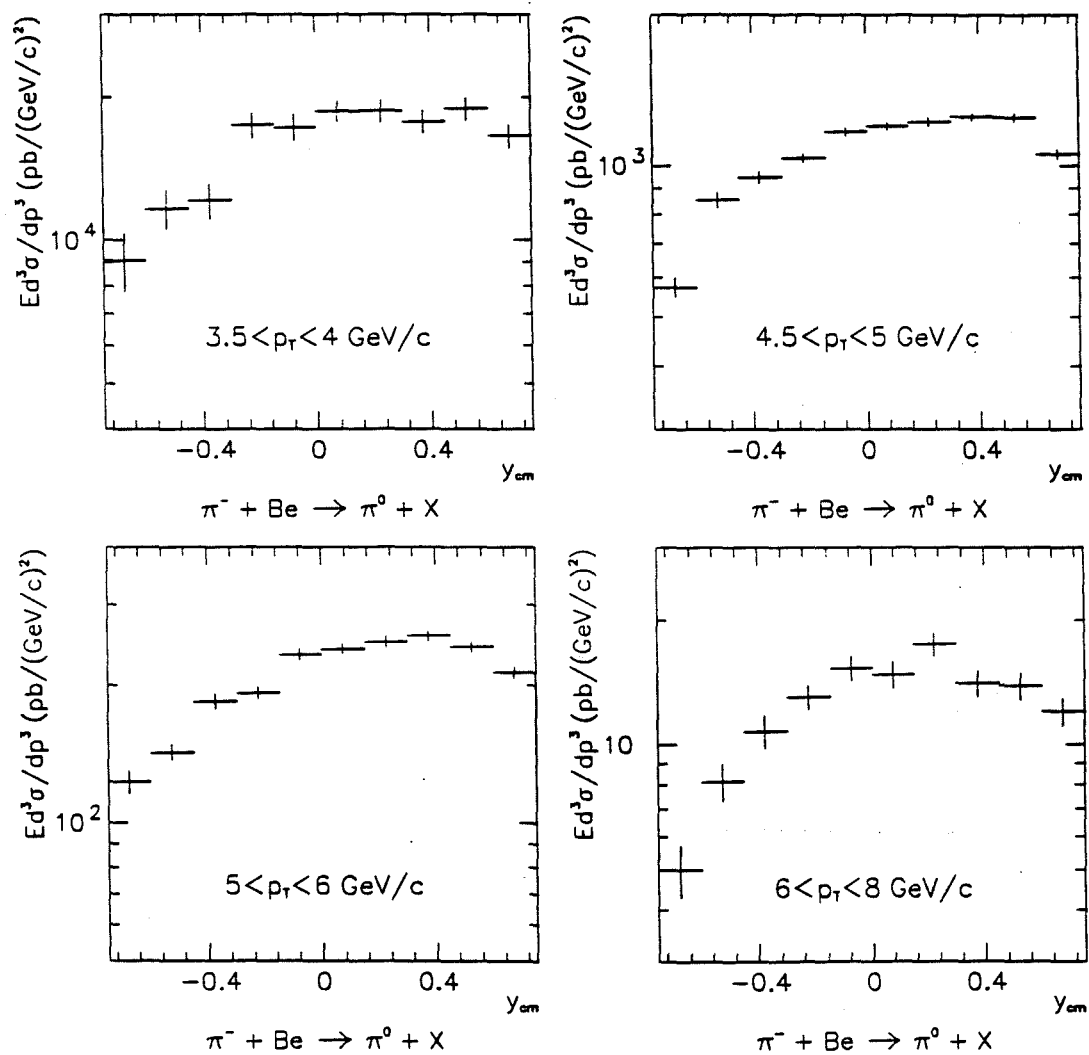


Figure 7.4

Inclusive invariant cross sections per nucleon for π^0 production in 520 GeV/c π^- Be interactions, as a function of rapidity averaged over different p_T intervals.

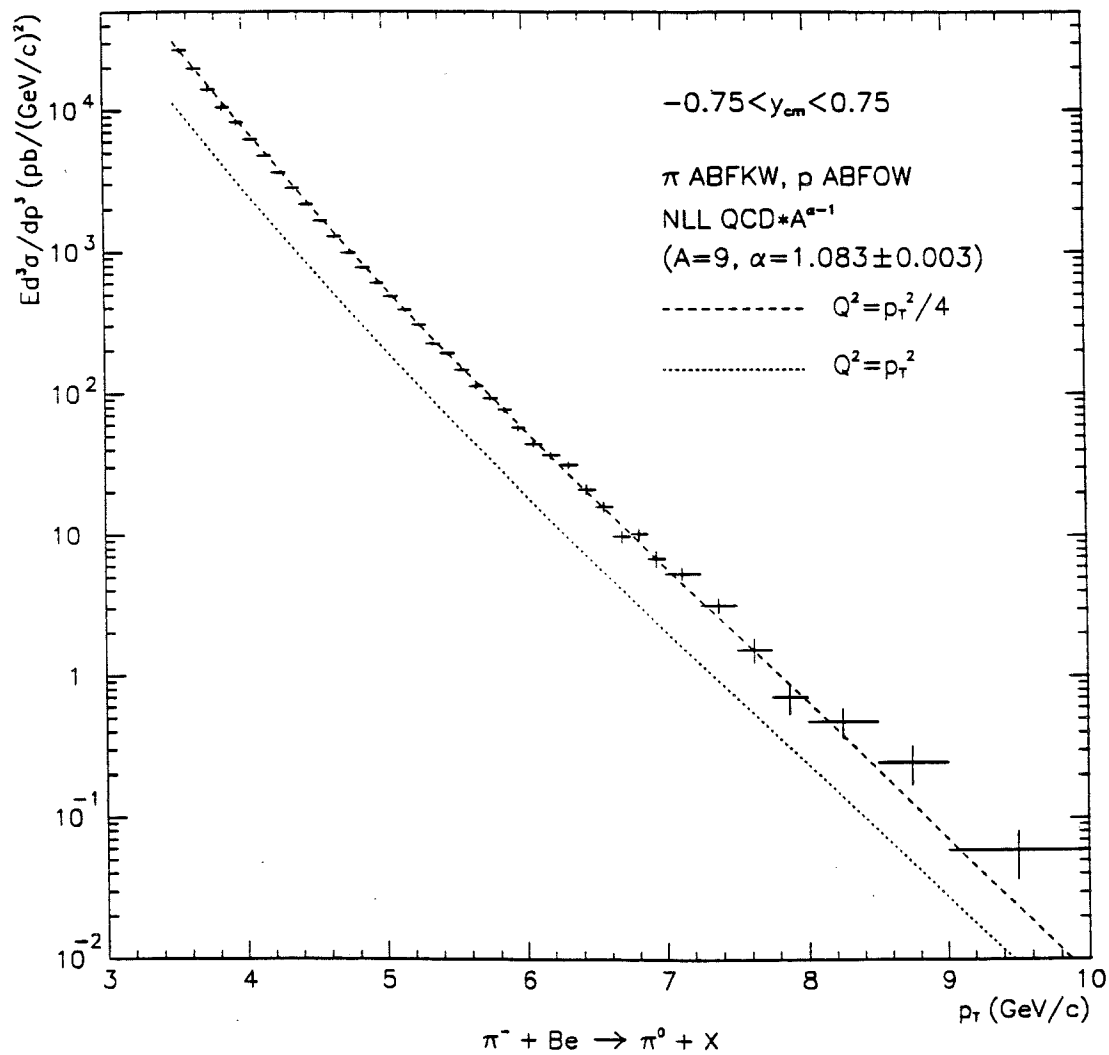


Figure 7.5 Inclusive invariant cross section per nucleon for π^0 production in 520 GeV/c π^- Be interactions, as a function of p_T averaged over the full rapidity range, $-0.75 < y_{cm} < 0.75$. The curves represent QCD calculations as described in the text.

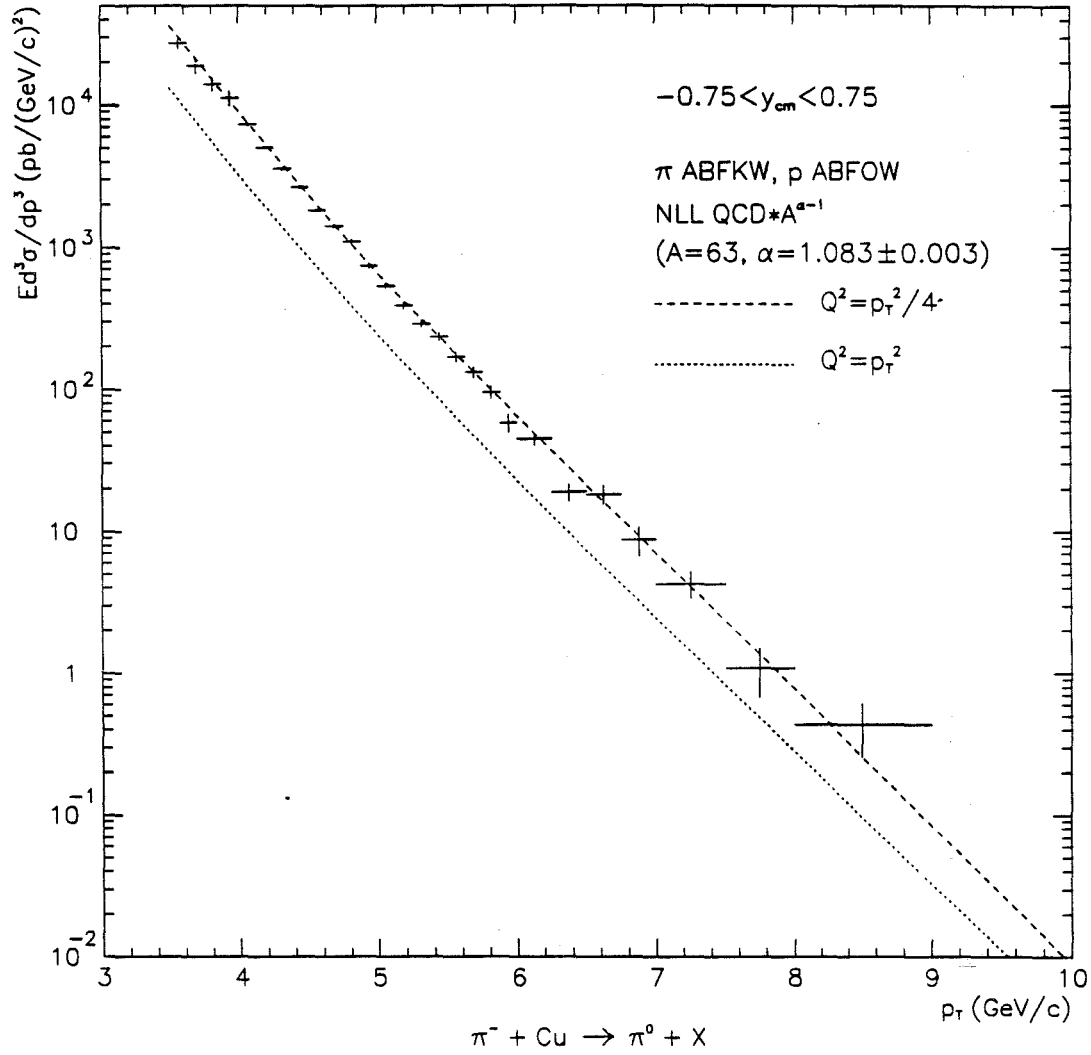


Figure 7.6 Inclusive invariant cross section per nucleon for π^0 production in 520 GeV/c π^- Cu interactions, as a function of p_T averaged over the full rapidity range, $-0.75 < y_{cm} < 0.75$. The curves represent QCD calculations as described in the text.

We have used the ABFKW^[1] set of parton distribution functions for the pion, the ABFOW^[2] set of parton distribution functions for the nucleon, and the next-to-leading-log π^0 fragmentation functions from Chiappetta et al. (Ref. [1.38]). The theoretical calculations were evaluated using two choices of the scale Q^2 (p_T^2 and $p_T^2/4$). With the smaller choice of scale the agreement between data and theory is remarkably good over the entire p_T range. However, the large dependence of the calculations on the choice of scale (about a factor of 3 for the scales shown) indicates that even the next-to-leading-log QCD description may be not fully adequate.

7.2 SUMMARY OF SYSTEMATIC UNCERTAINTIES

The uncertainties quoted in the cross sections presented in the previous section are statistical only. In this section, we will discuss the primary sources contributing to the systematic uncertainty associated with our measurements.

As already mentioned in Section 5.7, the uncertainty in the overall energy scale is estimated to be $\approx 0.5\%$. The energy scale uncertainty results in an uncertainty on the p_T measurement. To estimate the uncertainty in the inclusive π^0 cross section due to an uncertainty on the p_T measurement, we parametrize the cross section with a function of the form (see Section 1.1):

$$E \frac{d^3\sigma}{dp^3} \approx C \frac{(1-x_T)^m}{p_T^n} \quad (7.1)$$

The relative error in the cross section then can be written as:

[1] P. Aurenche et al., *Phys. Lett.* B233 (1989), 517.

[2] P. Aurenche et al., *Phys. Rev.* D39 (1989), 3275.

$$\left| \frac{\Delta \left(E \frac{d^3\sigma}{dp^3} \right)}{E \frac{d^3\sigma}{dp^3}} \right| = \left[x_T \left(\frac{n}{x_T} + \frac{m}{(1-x_T)} \right) \right] \frac{\Delta p_T}{p_T} \quad (7.2)$$

To estimate the cross section uncertainty due to the 0.5% relative uncertainty in the p_T scale, the data for Be averaged over the full rapidity range were fitted with Eq. (7.1). The results of the fit are: $m = 5.49 \pm 0.09$, $n = 9.47 \pm 0.05$, and $C = 18.6 \pm 0.9$ mb/(GeV/c)²/nucleon (Fig. 7.7). For $p_T = 4$ GeV/c and in our center-of-mass energy $\sqrt{s} = 31.2$ GeV, we estimate that the relative uncertainty on the cross section is about 11.4 times the relative uncertainty on the p_T measurement, i.e., $\approx 6\%$. For $p_T = 8$ GeV/c the relative uncertainty on the cross section is $\approx 7.6\%$.

Another source of uncertainty in the cross section originates from the π^0 reconstruction efficiency as calculated using Monte Carlo generated events. This uncertainty is estimated to be $\approx 5\%$ for $p_T < 6$ GeV/c and $\approx 8\%$ for $p_T > 6$ GeV/c. In addition, the uncertainty on the Monte Carlo energy scale is estimated to be $\approx 0.3\%$ which contributes a $\approx 3.4\%$ uncertainty on the π^0 reconstruction efficiency at p_T of 4 GeV/c.

The systematic uncertainties in the magnitude of the trigger corrections were estimated by comparing the cross sections as determined using data from triggers with different thresholds (i.e., *SINGLE LOCAL HI* and *SINGLE LOCAL LOW*). From this method, the overall trigger correction uncertainty was estimated to be $\approx 5\%$ at p_T of 4 GeV/c diminishing to $\approx 1\%$ at p_T of 6 GeV/c. For backward rapidities the uncertainties in the trigger corrections are expected to be larger due to statistical difficulties of calculating the efficiencies of these regions.

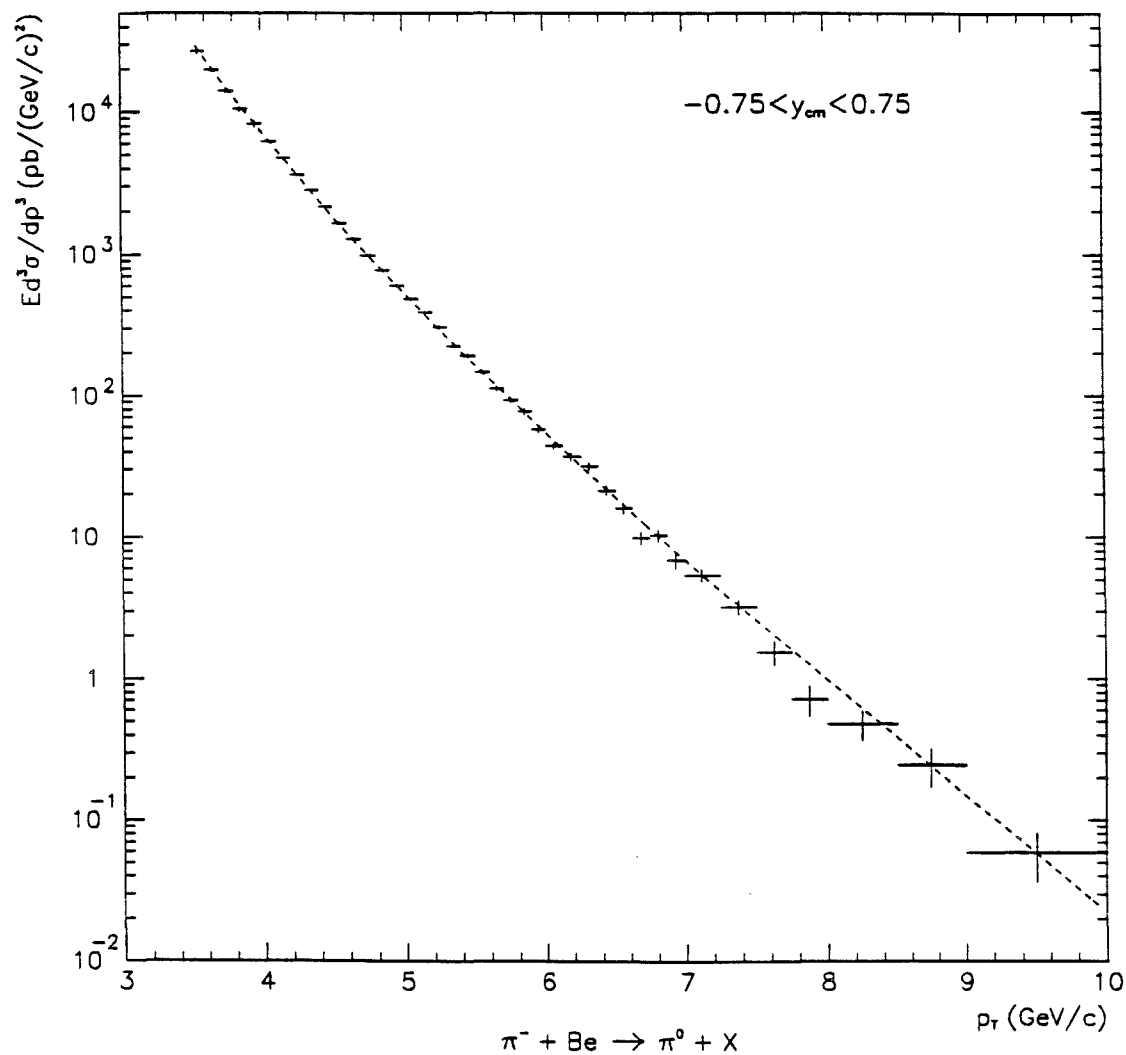


Figure 7.7 Inclusive invariant cross section per nucleon for π^0 production in 520 GeV/c π^- Be interactions, as a function of p_T averaged over the full rapidity range, $-0.75 < y_{cm} < 0.75$. The curve represents a fit of Eq. (7.1) to the data points.

Some other sources of systematic uncertainties in the π^0 cross section include the following:

- Target transverse fiducial correction: The uncertainty associated with this correction was estimated by comparing the correction derived using the vertices found in the two upstream SSD planes from the target to the correction evaluated using the two downstream SSD planes. The systematic uncertainty in the cross section from this source was estimated to be $\approx 2\%$.
- Muon rejection corrections: An uncertainty of $\approx 1\%$ was estimated for the software veto wall cut and $\approx 1\%$ for the directionality and balanced p_T cuts applied for π^0 s with $p_T > 5.5$ GeV/c.
- π^0 mass and sideband definitions: By varying the π^0 mass band and sideband regions a systematic uncertainty of $\approx 0.5\%$ was estimated to the cross section from this source.
- Overall normalization: An uncertainty of $\approx 10\%$ was estimated for the overall cross section normalization. The primary contributions to this uncertainty arise from the following sources: uncertainties in the experimental scalers used in determining the *LTB* count, event losses due to data acquisition failures, events caused by upstream interactions, failures during event reconstruction, and uncertainties in the vertex reconstruction efficiency and photon conversions corrections.

Combining all the systematic uncertainties mention above in quadrature yields a total uncertainty in the π^0 cross section of $\approx 14\%$ at p_T of 4 GeV/c and $\approx 16\%$ at p_T of 8 GeV/c.

The central value of the beam momentum was uncertain to $\approx 3\%$. This introduces an uncertainty into the theoretical calculations of $\approx 3.5\%$ at p_T of 4 GeV/c up to $\approx 18\%$ at p_T of 10 GeV/c.

7.3 NUCLEAR DEPENDENCE OF CROSS SECTIONS

By measuring the π^0 production from Be and Cu targets we can extract the A -dependence of the cross sections. As mentioned in Section 1.4, the form A^α is used to parametrize the cross section per nucleus. Since we report our results as cross sections per nucleon, we calculate the parameter α from the ratio:

$$\frac{\sigma_{\text{Cu}}}{\sigma_{\text{Be}}} = \left(\frac{A_{\text{Cu}}}{A_{\text{Be}}} \right)^{\alpha-1} \quad (7.3)$$

implying

$$\alpha = 1 + \frac{\ln(\sigma_{\text{Cu}}/\sigma_{\text{Be}})}{\ln(A_{\text{Cu}}/A_{\text{Be}})} \quad (7.4)$$

where σ_{Cu} and σ_{Be} are the measured cross sections per nucleon in the specified target[†].

Fig. 7.8 shows the variation of α as a function of p_T using the cross sections integrated over the full rapidity range. These values of α for these p_T intervals are also listed in Table B.4. The value of α is clearly larger than one in our p_T range. Our data are consistent with measurements of the A -dependence of charged pion production by experiment E258 (Ref. [1.43]) for similar regions of p_T (also shown in Fig. 7.8), as well as E706 measurements based on the 1988 data sample (Ref. [1.44]).

[†] Since the parameter α depends on the ratio of the two cross sections, trigger corrections applied to these cross sections cancel out and therefore to increase our statistics we used the *SINGLE LOCAL HI* triggers for the entire p_T range.

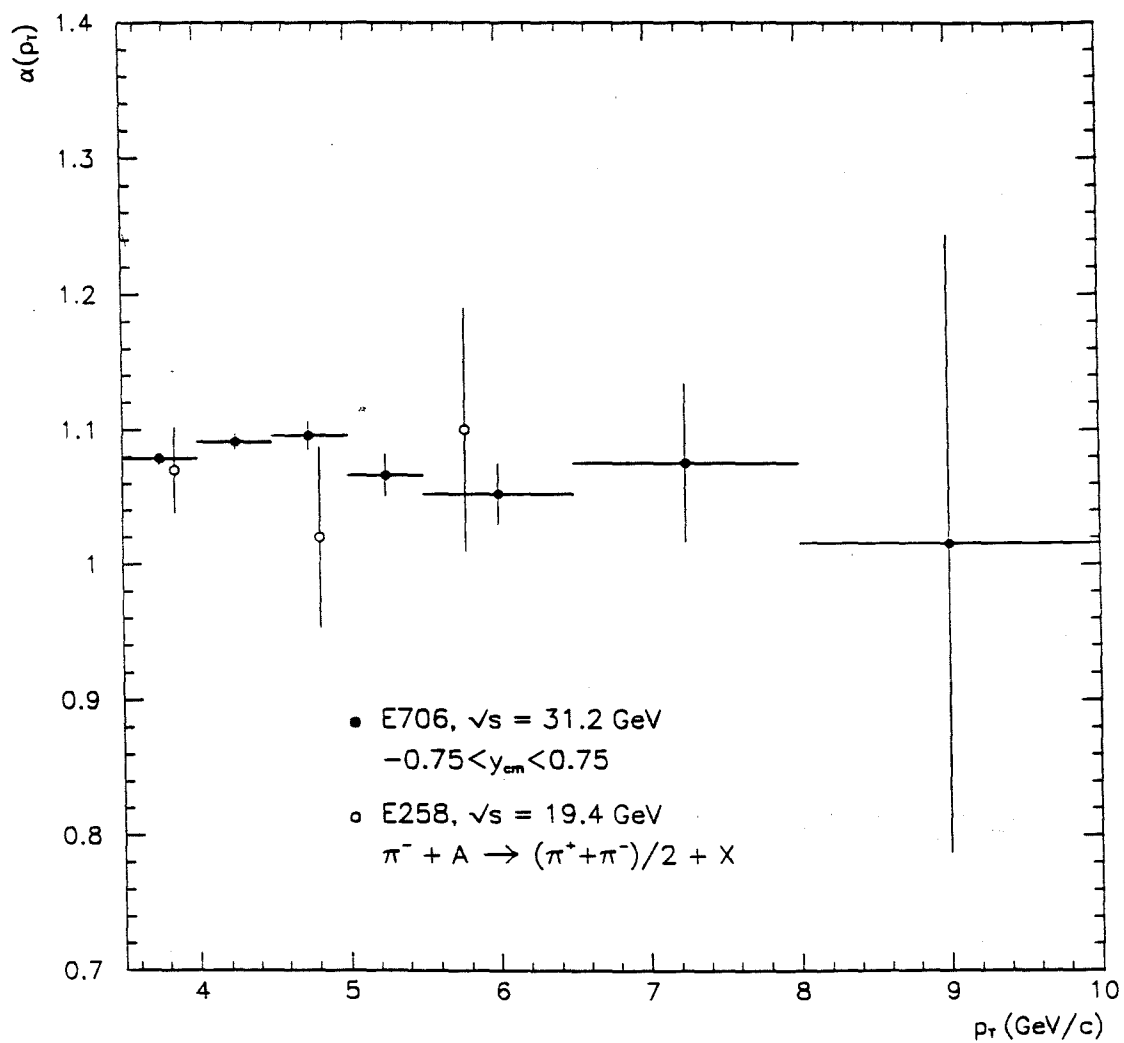


Figure 7.8 The value of α as a function of p_T (dark circles), as determined from the ratio of π^0 cross sections from 520 GeV/c π^- interactions on Cu and Be targets. The measurements of the value of α by experiment E258 for similar regions of p_T are also shown (open circles).

The dependence of α on rapidity is illustrated in Fig. 7.9 for some selected p_T intervals. For $p_T > 4$ GeV/c, the value of α is essentially independent of π^0 rapidity in the range of our measurement. However, in the p_T range 3.5 to 4 GeV/c a dependence of the value of α upon rapidity is not excluded by our data.

7.4 COMPARISON TO OTHER EXPERIMENTS

The π^0 cross sections measured by previous experiments using π^- beams in this general energy range is plotted in Fig. 7.10 along with our measurement on Be target. For experiments E706 and NA3 we have scaled the cross sections by the A -dependence factor using our average measurement of α (1.083 ± 0.003). As can be seen, our data cover a wide range of p_T values in very small bins. As expected, due to our higher center of mass energy, our cross sections lie above the previous measurements.

Fig. 7.11 compares our current higher statistics measurement of π^0 production (integrated over the rapidity range $-0.7 < y_{cm} < 0.7$) with the cross section reported by E706 based upon the 1988 data sample. The 1990 cross section is systematically larger than the 1988 measurements. Fig. 7.12 shows the ratio between the π^0 cross sections for the two data samples. The dashed line represents the theoretical calculation for the cross section ratio for the increase of the π^- beam momentum from 500 to 520 GeV/c between the two runs. Although the data points are still higher than the line, taking into account the systematic uncertainties for the 1990 (as discussed in Section 7.2) and the 1988 (Ref. [1.44]) measurements, the two data samples are consistent with each other.

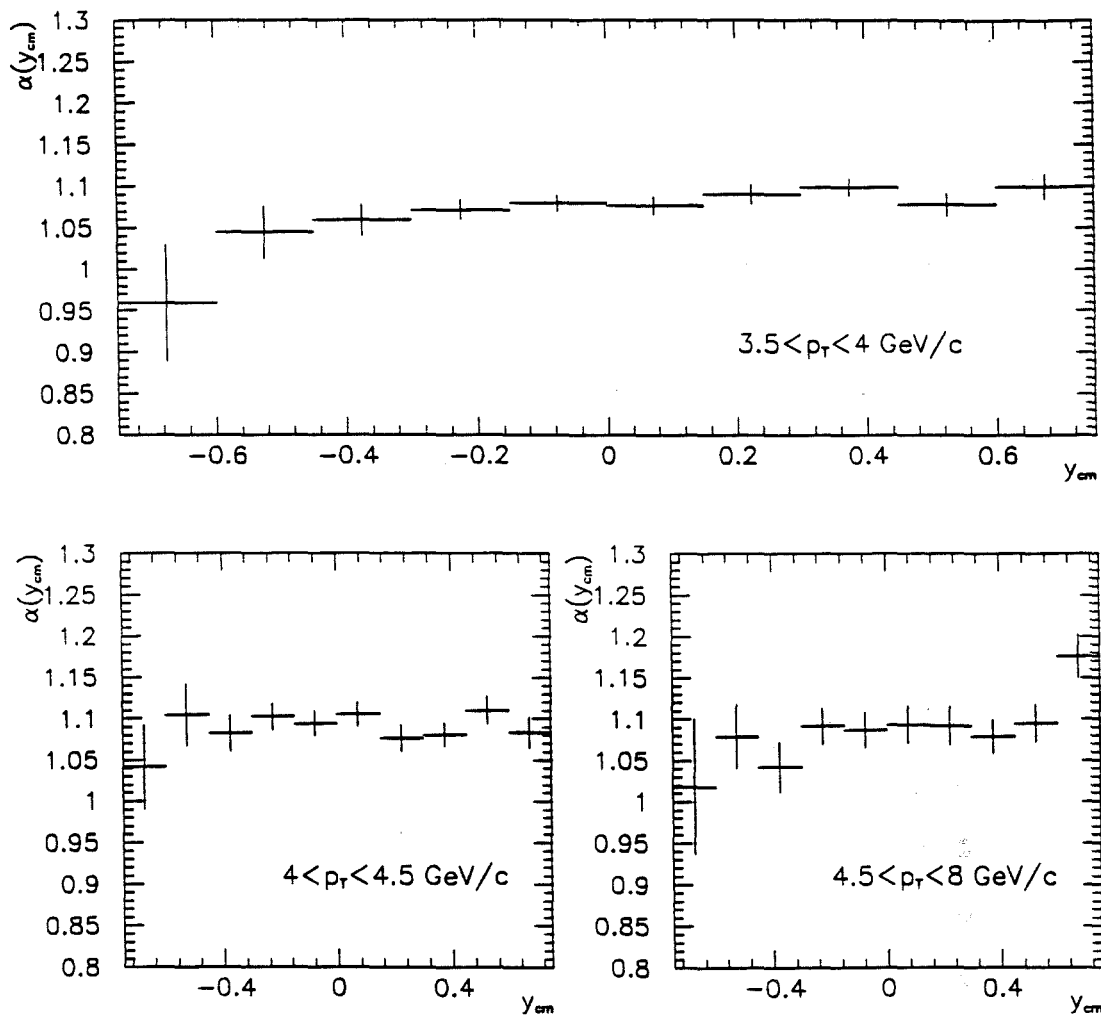


Figure 7.9

The value of α as a function of rapidity for three p_T regions, as determined from the ratio of π^0 cross sections from 520 GeV/c π^- interactions on Cu and Be targets.

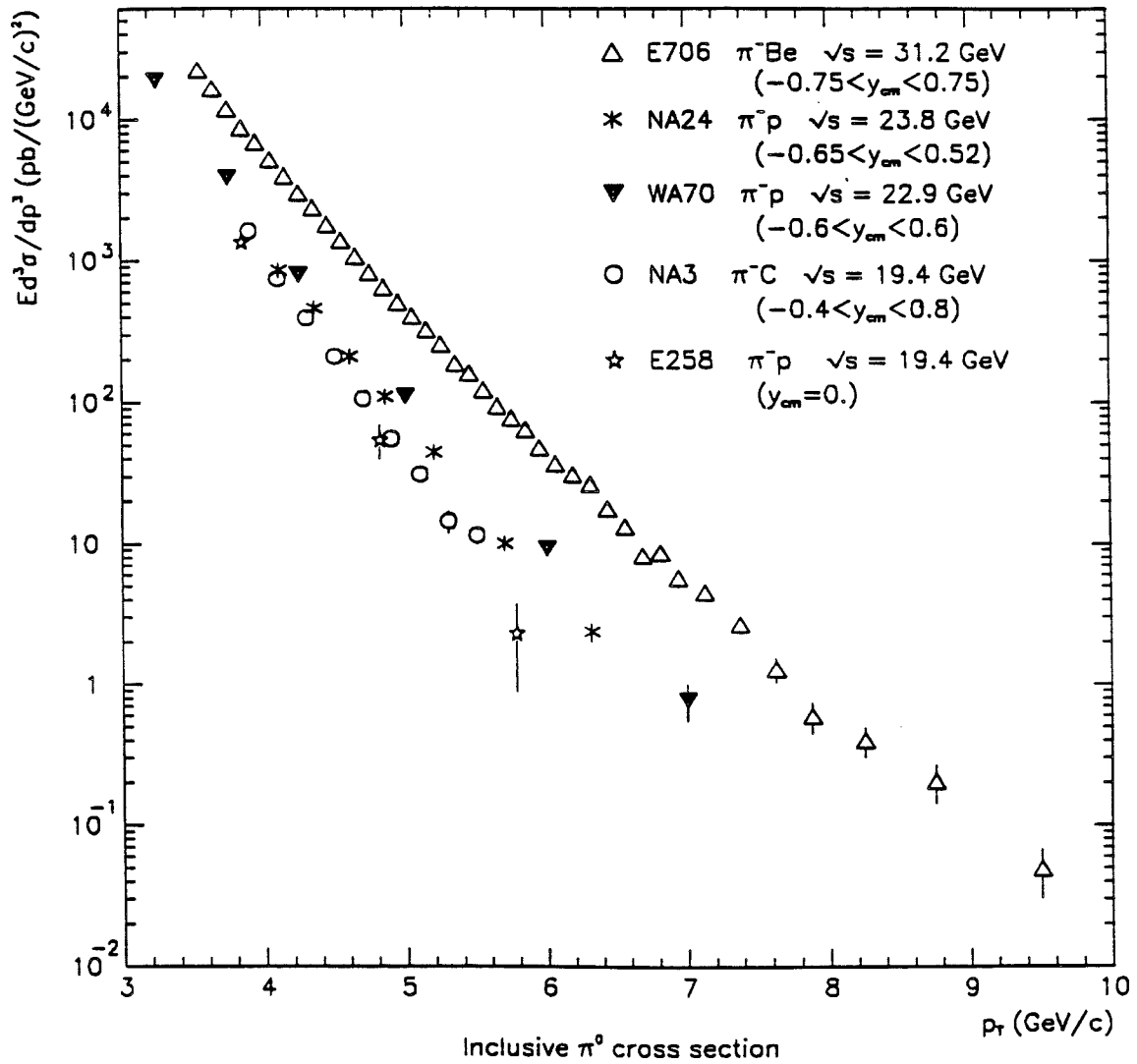


Figure 7.10 π^0 cross sections per nucleon in π^- induced collisions as a function of p_T , from several experiments. For experiments E706 and NA3 we have scaled the cross sections by the A -dependence factor using our average measurement of α .

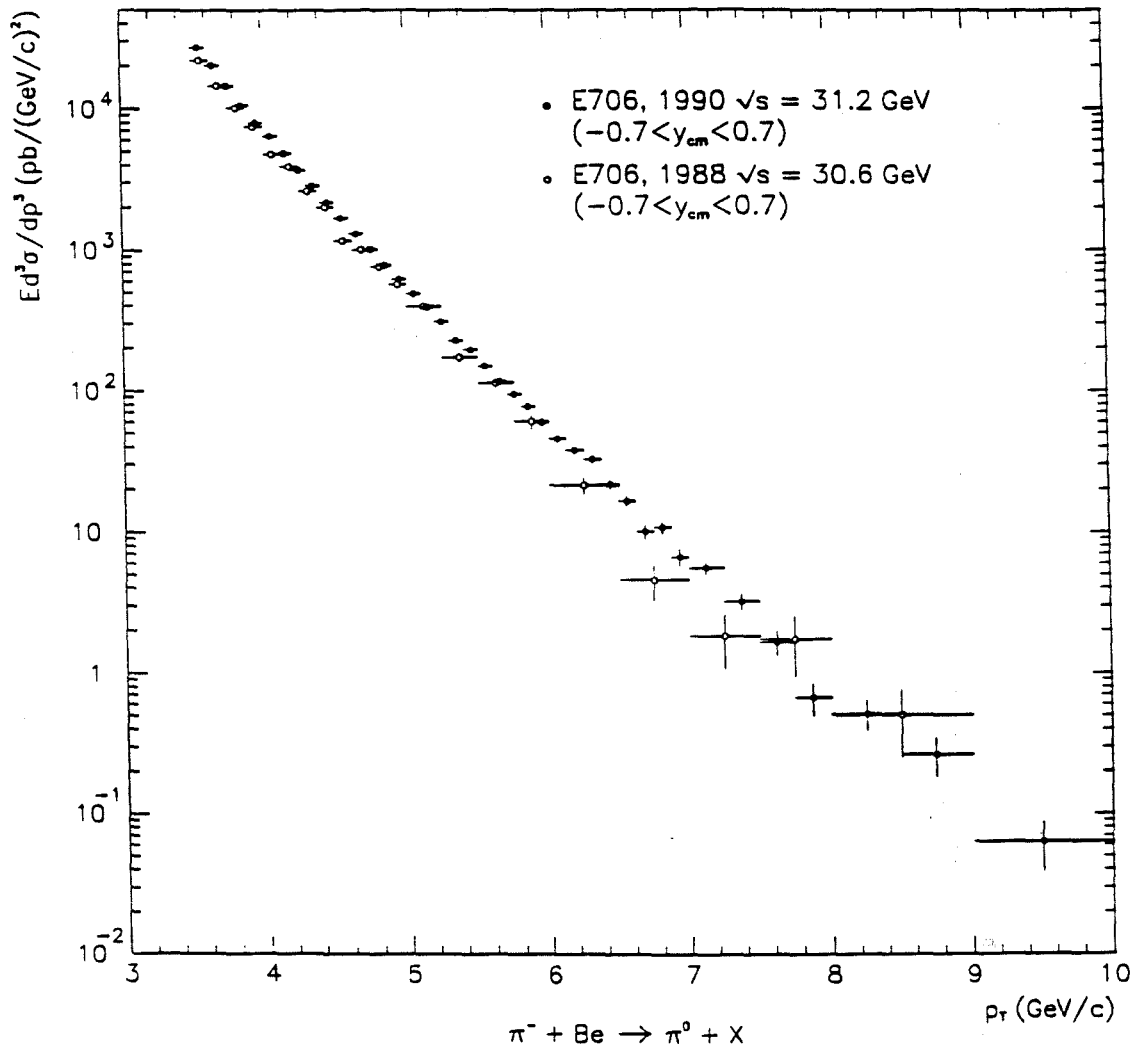


Figure 7.11 Inclusive invariant cross section per nucleon for π^0 production in 520 GeV/c π^- Be interactions, as a function of p_T averaged over the rapidity range $-0.7 < y_{cm} < 0.7$ (dark circles). The π^0 cross section in 500 GeV/c π^- Be interactions reported by E706 based upon the 1988 data sample is shown with the open circles.

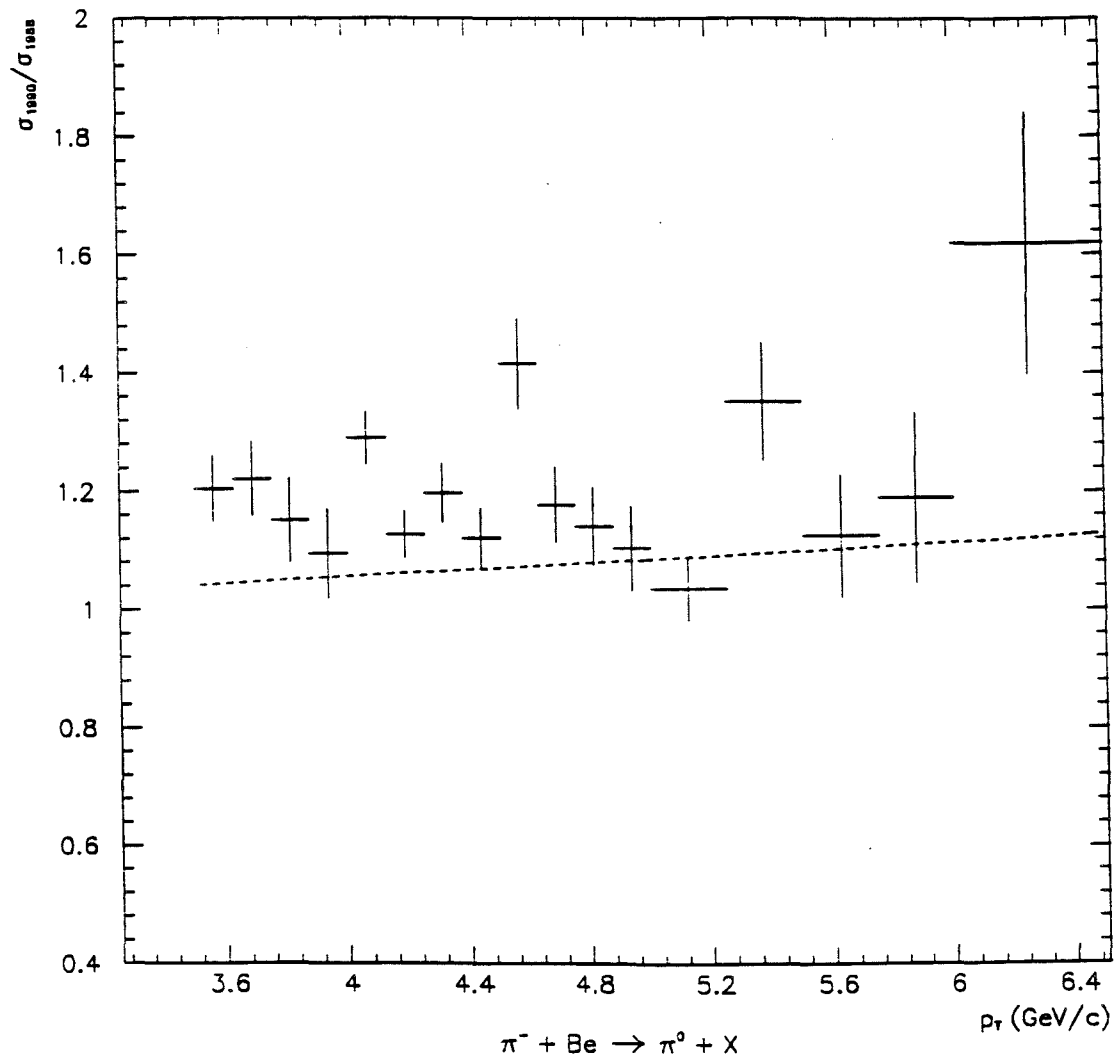


Figure 7.12 The ratio between the π^0 cross sections based on measurements using the 1990 and 1988 data samples, as a function p_T averaged over the rapidity range $-0.7 < y_{cm} < 0.7$. The dashed line represents the theoretical calculation for the cross section ratio for the increase of the π^- beam momentum from 500 to 520 GeV/c between the two runs.

7.5 CONCLUSIONS

In this thesis π^0 production was studied using ≈ 5.2 events/pb of π^- Be data and ≈ 0.84 events/pb of π^- Cu data collected during the 1990 run of the Fermilab experiment E706. This data sample represents about an order of magnitude increase in statistics over the data sample collected during the experiment's 1988 run, and is the highest energy measurement of π^0 production in π^- induced collisions. We measured the inclusive π^0 cross section in 520 GeV/c π^- Be and π^- Cu interactions covering the kinematic regions of transverse momentum between 3.5 and 4 GeV/c and rapidity between -0.75 and 0.75 . No significant dependence in the shape of the cross section as a function of rapidity for different p_T regions was observed.

From the cross sections measured for the two nuclear targets, we extracted the nuclear dependence of π^0 production parametrized as A^α . The average value of α in our kinematic range is 1.083 ± 0.003 , which is consistent with previous measurements reported by E706 and E258. No significant dependence of the value α upon the π^0 rapidity was observed.

The reported cross sections were found to be higher than previous experiments, consistent with our higher center of mass energy. Present measurement is also systematically higher than our previous result using the 1988 data sample, consistent with the increase of the π^- beam momentum from 500 to 520 GeV/c.

Finally, our measured π^0 cross sections integrated over the full rapidity range has been compared with next-to-leading-log expectations from QCD for two choices of the Q^2 scale. The agreement between the data and the theoretical calculation is very satisfactory over the entire p_T range, when Q^2 is chosen to be $p_T^2/4$.

REFERENCES

- [1.1] M. Gell-Man, *Phys. Lett.* 8 (1964), 214.
- [1.2] G. Zweig, CERN report 8182/Th. 401 (1964).
- [1.3] For a broader historical perspective, see: R. N. Cahn and G. Goldhaber, *The Experimental Foundations of Particle Physics*, Cambridge Univ. Press, 1989.
- [1.4] J. D. Bjorken and E. A. Paschos, *Phys. Rev.* 185 (1969), 1975.
- [1.5] R. P. Feynman, *Phys. Rev. Lett.* 23 (1969), 1415.
- [1.6] M. Gell-Mann, *Acta Phys. Austriaca Suppl.* 9 (1972), 733.
- [1.7] M. R. Pennington, *Rep. Prog. Phys.* 46 (1983), 393.
- [1.8] T. Muta, *Foundations of Quantum Chromodynamics*, World Scientific Publishing Co. 1987.
- [1.9] H. Fritzsch et al., *Phys. Lett.* 47B (1973), 365.
- [1.10] D. J. Gross and F. Wilczek, *Phys. Rev. Lett.* 30 (1973), 1343.
- [1.11] H. D. Politzer, *Phys. Rev. Lett.* 30 (1973), 1346.
- [1.12] CTEQ Collaboration, *Handbook of Perturbative QCD*, Version 1.0 (1993), FERMILAB-PUB-93/094.
- [1.13] R. D. Field, *Applications of Perturbative QCD*, Addison-Wesley Publishing Co. 1989.
- [1.14] A. J. Buras, *Rev. Mod. Phys.* 52 (1980), 199.
- [1.15] G. Sterman, *An Introduction to Quantum Field Theory*, Cambridge University Press 1993.
- [1.16] R. D. Field and R. P. Feynman, *Phys. Rev.* D15 (1977), 2590.
- [1.17] S. D. Ellis and M. B. Kislinger, *Phys. Rev.* D9 (1974), 2027.
- [1.18] R. Cutler and D. Sivers, *Phys. Rev.* D17 (1978), 196.
- [1.19] J. F. Owens, *Rev. Mod. Phys.* 59 (1987), 465.

- [1.20] B. L. Combridge, et al., *Phys. Lett.* 70B (1977), 234.
- [1.21] G. Altarelli and G. Parisi, *Nucl. Phys.* B126 (1977), 298.
- [1.22] J. F. Owens, *Phys. Rev. Lett.* B76 (1978), 85.
- [1.23] T. Ferbel and W. R. Molzon, *Rev. Mod. Phys.* 56 (1984), 181.
- [1.24] L. Camilleri, CERN-EP/88-125 (1988).
- [1.25] A. P. Contogouris et al., *Phys. Rev.* D32 (1985), 1134.
- [1.26] L. Cormell and J. F. Owens, *Phys. Rev.* D22 (1980), 1609.
- [1.27] F. Halzen and D. M. Scott, *Phys. Rev.* D18 (1978), 3378.
- [1.28] R. Ruckl et al., *Phys. Rev.* D18 (1978), 2469.
- [1.29] R. P. Feynman et al., *Phys. Rev.* D18 (1978), 3320.
- [1.30] A. P. Contogouris et al., *Phys. Rev.* D17 (1978), 2314.
- [1.31] P. Aurenche et al., *Phys. Lett.* 140B (1984), 87.
- [1.32] P. Aurenche et al., *Nucl. Phys.* B297 (1988), 661.
- [1.33] H. Baer et al., *Phys. Rev.* D42 (1990), 61.
- [1.34] P. M. Stevenson, *Phys. Rev.* D23 (1981), 2916.
- [1.35] H. D. Politzer, *Nucl. Phys.* B194 (1982), 493.
- [1.36] W. M. Geist et al., *Phys. Rep.* 197 (1990), 263.
- [1.37] F. Aversa et al., *Nucl. Phys.* B327 (1989), 105.
- [1.38] P. Chiappetta et al., preprint CPT-92/PE.2841 (1992).
- [1.39] J. W. Cronin et al., *Phys. Rev.* D11 (1975), 3105.
- [1.40] D. Antreasyan et al., *Phys. Rev.* D19 (1979), 764.
- [1.41] K. Kastella et al., *Phys. Rev.* D39 (1989), 2586.
- [1.42] G. Donaldson et al., *Phys. Rev. Lett.* 36 (1976), 1110.
- [1.43] H. J. Frisch et al., *Phys. Rev.* D27 (1983), 1001.
- [1.44] G. Alverson et al., *Phys. Rev.* D48 (1993), 5.
- [1.45] J. Badier et al., *Z. Phys.* C30 (1986), 45.

- [1.46] C. De Marzo et al., *Phys. Rev. D* 36 (1987), 16.
- [1.47] M. Bonesini et al., *Z. Phys.* C37 (1987), 39.
- [2.1] I. Kourbanis, The A Dependence of Leading Particle Production by 800 GeV/c Protons, Ph.D. Dissertation, Northeastern University (1989).
- [2.2] C. Bromberg et al., *Nucl. Instr. and Meth.* 200 (1982), 245.
- [2.3] E. Engels et al., *Nucl. Instr. and Meth.* A279 (1989), 272.
- [2.4] K. Hartman, Hadronic Production of π^0 Pairs and Associated Event Structure, Ph.D. Dissertation, Pennsylvania State University (1990).
- [2.5] C. Bromberg et al., *Nucl. Instr. and Meth.* A307 (1991), 292.
- [2.6] W. E. DeSoi, Construction and Performance of a Liquid Argon Calorimeter for Use in Experiment E-706 at the Fermi National Accelerator Laboratory, Ph.D. Dissertation, University of Rochester (1990).
- [2.7] F. Lobkowicz et al., *Nucl. Instr. and Meth.* A235 (1985), 332.
- [2.8] C. B. Lirakis, A Study of High Transverse Momentum η Production in 530 GeV/c Hadronic Interactions, Ph.D. Dissertation, Northeastern University (1990).
- [2.9] J. Engler et al., *Nucl. Instr. and Meth.* 120 (1974), 157.
- [2.10] L. S. Miller et al., *Phys. Rev.* 166 (1968), 871.
- [2.11] T. Doke, *Portugal Phys.* 12 (1981), 9, also in *Experimental Techniques in High Energy Physics*, Addison-Wesley Publishing Company 1987, T. Ferbel, ed.
- [2.12] W. J. Willis and V. Radeka, *Nucl. Instr. Meth.* 120 (1974), 221, also in *Experimental Techniques in High Energy Physics*, Addison-Wesley Publishing Company 1987, T. Ferbel, ed.
- [2.13] J. Engler et al., *Nucl. Instr. and Meth.* 133 (1976), 521.
- [2.14] E. Prebys and F. Lobkowicz, E706 Internal Note 163 (1988).

- [2.15] A. Lanaro, π^0 Production with K^- and π^+ Beams at 530 GeV/c, Ph.D. Dissertation, University of Rochester (1989).
- [2.16] R. Benson, Characteristics of Forward Energy Production in Proton-Nucleus and Pion-Nucleus Collisions at $\sqrt{s} = 31.5$ GeV, Ph.D. Dissertation, University of Minnesota (1990).
- [3.1] IEEE Standard FASTBUS Modular High-Speed Data Acquisition and Control System, IEEE 1986, ISBN 471-84472-1.
- [3.2] D.D. Skow, A Study of High Transverse Momentum Eta Meson Production, Ph.D. Dissertation, University of Rochester (1990).
- [3.3] CAMAC Instrumentation and Interface Standards, IEEE 1982, ISBN 0-471-89737.
- [3.4] VAXONLINE System, FNAL Computer Department publication PN-252.
- [3.5] G. Drake, *Nucl. Instr. and Meth.* A269 (1988), 68-81.
- [3.6] C. R. Benson, Next Generation Digital Readout Electronics for the E706 Liquid Argon Calorimeter, M.S. Dissertation, University of Rochester (1989).
- [3.7] C. Lirakis, E706 Data Acquisition System, in Proceedings of the First Annual Conference on Electronics for Future Colliders, edited by George Blonar, LeCroy Corporation (1991), 37-50.
- [3.8] DSP56000/DSP56001 Digital Signal Processor User's Manual, available as DSP56000UM/AD from Motorola Literature Distribution, P.O. Box 20912, Phoenix, Arizona 85036.
- [3.9] GPM Manual, STR500, Dr. B. Struck.
- [3.10] pSOS-68K User's Manual, available as PK68K-MAN V4.1 from Software Components Group Inc., Santa Clara, California.
- [3.11] 1821 SM/I Manual, LeCroy Corporation.

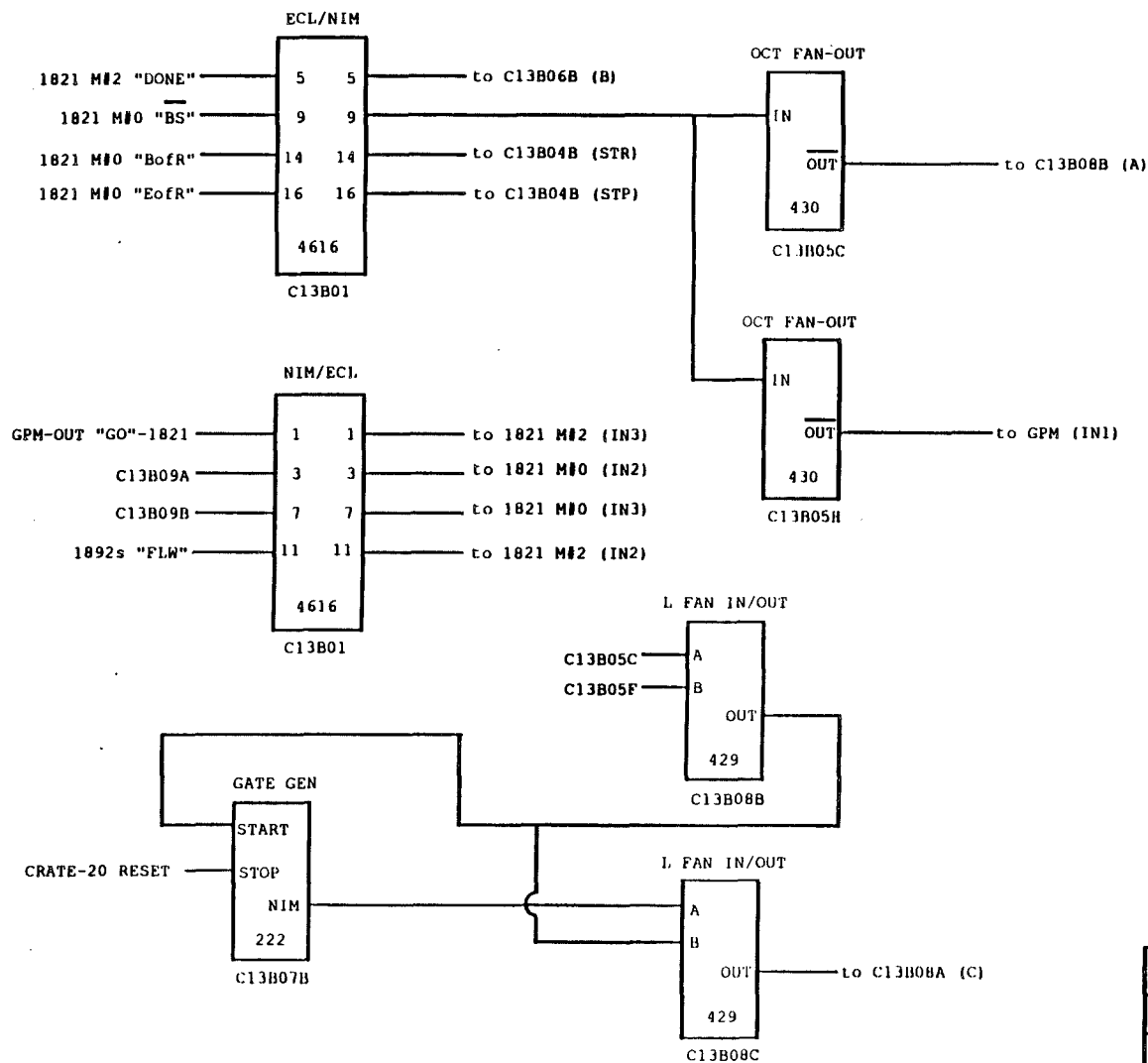
- [3.12] LeCroy 1821 Microcode Tools, FNAL Computer Department publication IN-128.
- [3.13] 1821/DEC Manual, LeCroy Corporation.
- [3.14] 1821/ECL Manual, LeCroy Corporation.
- [3.15] 1892 Manual, LeCroy Corporation.
- [3.16] Guide to Status Manager Database and Routines, FNAL Computer Department publication PN-304.
- [3.17] Low Level Routines for the LeCroy 1821, FNAL Computer Department publication FBN-039.
- [3.18] Interactive List Generation Program FLMENU, FNAL Computer Department publication FBN-047.
- [3.19] LeCroy 1821 SM/I Diagnostic Tool (LDT), FNAL Computer Department publication FBN-041.
- [3.20] C. M. Yosef, Production of High Transverse Momentum π^0 Mesons in Interactions of 530 GeV/c Proton and π^- Beams on Beryllium and Copper Targets, Ph.D. Dissertation, Northeastern University (1990).
- [3.21] L. Sorrell, private communication.
- [4.1] G. O. Alverson and E. L. Pothier, E706 Internal Note 139 (1985).
- [4.2] H. J. Klein and J. Zoll, PATCHY reference manual, CERN Computer Center program library (1983).
- [4.3] R. Brun et al., ZEBRA User's Guide, CERN Computer Center program library, DD/EE/85-6, Q100, or FNAL Software note PU-0046.
- [4.4] A. P. Sinanidis, Particles Produced in Association with High Transverse Momentum Single Photon and π^0 in Hadronic Collisions, Ph.D. Dissertation, Northeastern University (1989).

- [4.5] S. Easo, Structure of Events Containing a Direct Photon or Neutral Pion in Hadronic Interactions, Ph.D. Dissertation, Pennsylvania State University (1989).
- [4.6] S. Blusk, private communication.
- [4.7] J. P. Mansour, High Transverse Momentum π^0 Production from π^- and p Beams at 530 GeV/c on Be and Cu, Ph.D. Dissertation, University of Rochester (1989).
- [4.8] W. Dlugosz, private communication.
- [4.9] M. Zielinski, private communication.
- [4.10] L. Apanasevich, private communication.
- [4.11] R. Roser, E706 Internal Note 193 (1991).
- [5.1] K. Kleinknecht, Detectors for Particle Radiation, Cambridge University Press 1986.
- [5.2] J. W. Motz et al., *Rev. Mod. Phys.* 41 (1969), 581.
- [5.3] L. de Barbaro, private communication.
- [5.4] R. Brun et al., GEANT3.15: CERN Data Handling Division, also in FNAL Computer Department publication PM0062 (1993).
- [5.5] R. M. Roser, Eta Production at High Transverse Momenta by Negative 520 GeV/c Pions incident on Be and Cu Targets, Ph.D. Dissertation, University of Rochester (1994).
- [5.6] G. Marchesini et al., HERWIG V5.6: CERN Data Handling Division, also in FNAL Computer Department publication PU0124 (1993).
- [6.1] J. P. Mansour, E706 Internal Note 195 (1992).
- [6.2] A. S. Carroll et al., *Phys. Lett. B* 80 (1979), 319.
- [6.3] P. Chang, private communication.
- [6.4] G. B. Osborne, E706 Internal Note 197 (1992).

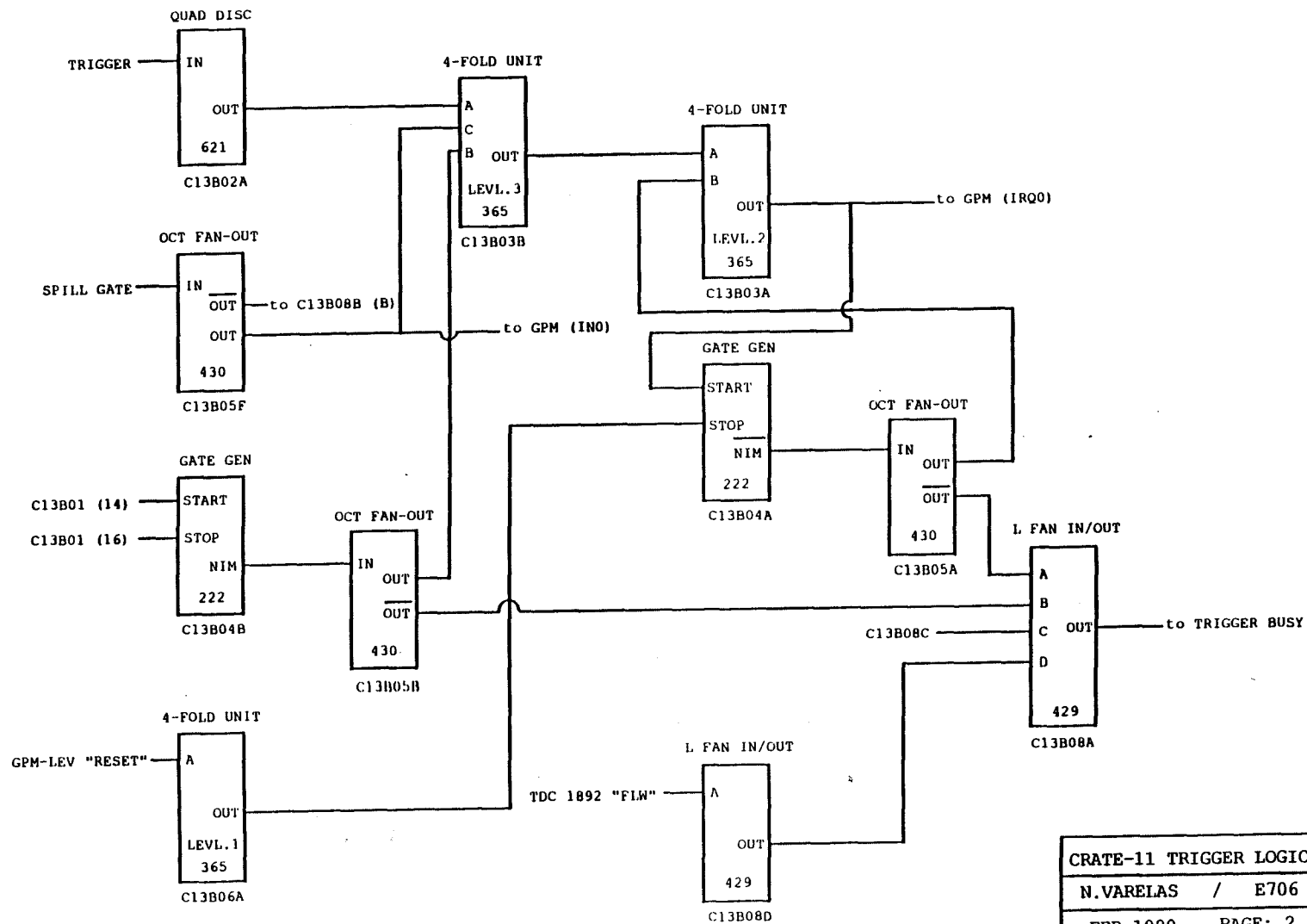
- [7.1] P. Aurenche et al., *Phys. Lett.* B233 (1989), 517.
- [7.2] P. Aurenche et al., *Phys. Rev.* D39 (1989), 3275.

APPENDIX A

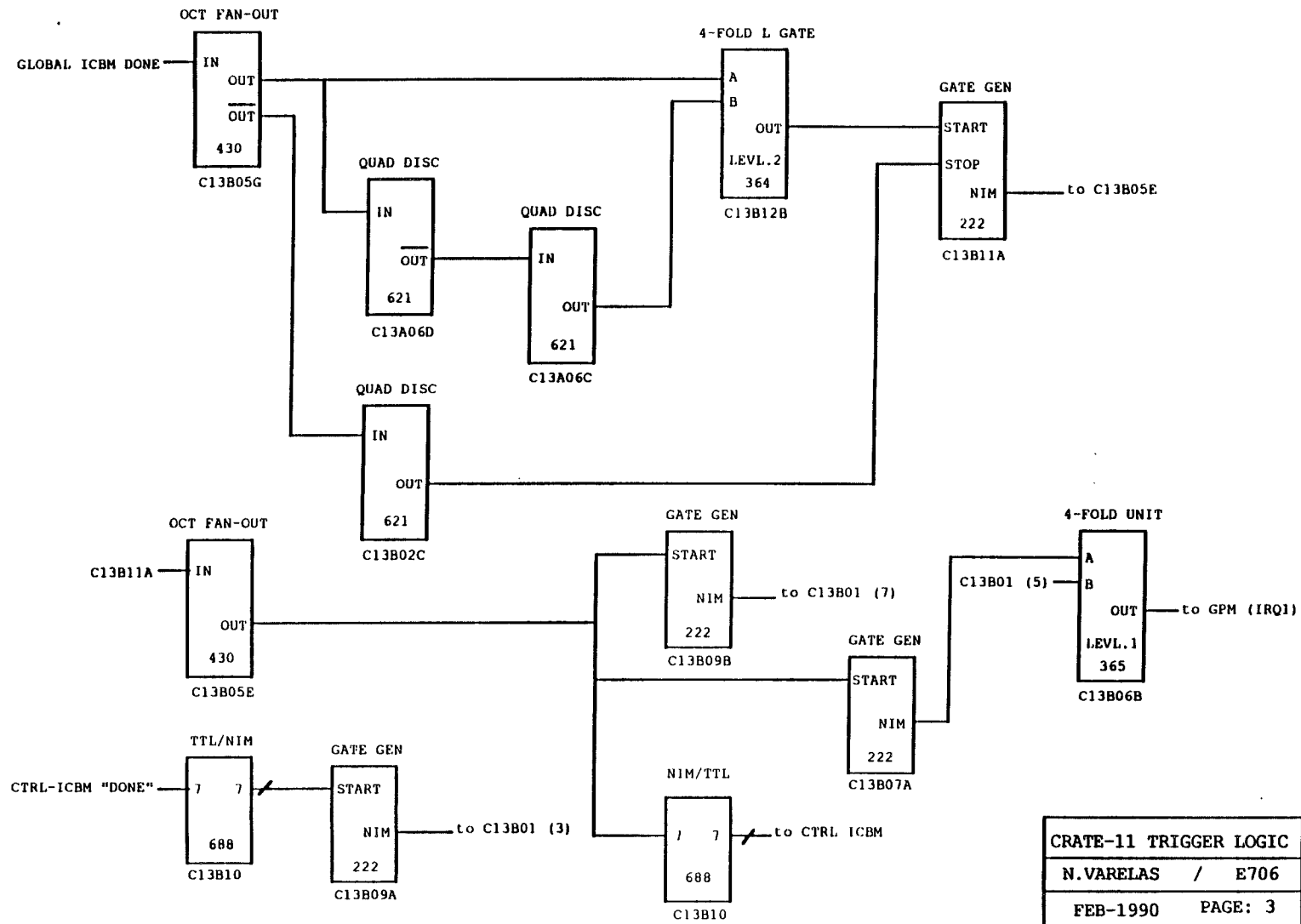
This appendix contains the block diagram for the LAC DA trigger busy logic described in Chapter 3.



CRATE-11 TRIGGER LOGIC	
N.VARELAS	/ E706
FEB-1990	PAGE: 1



CRATE-11 TRIGGER LOGIC	
N.VARELAS	/ E706
FEB-1990	PAGE: 2



CRATE-11 TRIGGER LOGIC	
N.VARELAS	/ E706
FEB-1990	PAGE: 3

APPENDIX B

This appendix presents the tables for the inclusive invariant cross sections for π^0 production in 520 GeV/c π^- Be and π^- Cu interactions.

p_T (GeV/c)	$-0.75 < y_{cm} < -0.5$	$-0.5 < y_{cm} < -0.3$	$-0.3 < y_{cm} < -0.1$
3.500 - 3.625	-	-	-
3.625 - 3.750	-	-	-
3.750 - 3.875	-	-	-
3.875 - 4.000	-	-	-
4.000 - 4.125	-	6010 ± 170	6450 ± 120
4.125 - 4.250	-	4200 ± 140	4510 ± 90
4.250 - 4.375	1790 ± 100	2880 ± 100	3260 ± 70
4.375 - 4.500	1420 ± 80	2000 ± 80	2230 ± 60
4.500 - 4.625	1100 ± 60	1410 ± 60	1640 ± 50
4.625 - 4.750	733 ± 44	971 ± 46	1150 ± 40
4.750 - 4.875	507 ± 32	787 ± 37	855 ± 33
4.875 - 5.000	380 ± 28	550 ± 36	611 ± 26
5.000 - 5.250	262 ± 17	332 ± 18	398 ± 14
5.250 - 5.500	130 ± 10	197 ± 12	218 ± 11
5.500 - 5.750	80.4 ± 7.3	114 ± 9	128 ± 8
5.750 - 6.000	40.3 ± 4.9	63.6 ± 6.2	61.1 ± 5.6
6.000 - 6.500	19.3 ± 2.2	29.1 ± 2.9	38.5 ± 3.0
6.500 - 7.000	3.18 ± 0.97	7.57 ± 1.35	10.8 ± 1.4
7.000 - 8.000	1.00 ± 0.35	2.20 ± 0.48	2.67 ± 0.45
8.000 - 10.000	0.03 ± 0.06	0.14 ± 0.08	0.28 ± 0.09

Table B.1 Invariant differential cross section per nucleon in units $\text{pb}/(\text{GeV}/c)^2$ for the inclusive π^0 production in 520 GeV/c π^- Be interactions. The cross sections are averaged over the specified p_T and y_{cm} intervals.

p_T (GeV/c)	$-0.1 < y_{cm} < 0.1$	$0.1 < y_{cm} < 0.3$	$0.3 < y_{cm} < 0.5$
3.500 - 3.625	-	31350 ± 2220	32960 ± 2300
3.625 - 3.750	-	21920 ± 1820	18720 ± 1650
3.750 - 3.875	-	14160 ± 1510	13910 ± 1450
3.875 - 4.000	-	8630 ± 1100	10050 ± 1220
4.000 - 4.125	7130 ± 110	7720 ± 120	6920 ± 110
4.125 - 4.250	4840 ± 90	5310 ± 90	5060 ± 90
4.250 - 4.375	3420 ± 70	3660 ± 70	3590 ± 70
4.375 - 4.500	2460 ± 60	2640 ± 60	2610 ± 60
4.500 - 4.625	1810 ± 50	1900 ± 50	1880 ± 50
4.625 - 4.750	1280 ± 40	1300 ± 40	1400 ± 40
4.750 - 4.875	961 ± 37	1010 ± 40	1010 ± 30
4.875 - 5.000	691 ± 28	680 ± 28	786 ± 28
5.000 - 5.250	468 ± 17	468 ± 16	497 ± 16
5.250 - 5.500	255 ± 12	273 ± 12	297 ± 12
5.500 - 5.750	145 ± 9	143 ± 9	146 ± 8
5.750 - 6.000	93.4 ± 7.5	88.6 ± 6.6	81.6 ± 6.4
6.000 - 6.500	39.1 ± 2.9	40.2 ± 3.0	37.0 ± 2.9
6.500 - 7.000	14.9 ± 1.8	17.3 ± 1.9	12.0 ± 1.7
7.000 - 8.000	4.33 ± 0.60	3.52 ± 0.62	2.58 ± 0.54
8.000 - 10.000	0.14 ± 0.07	0.45 ± 0.14	0.48 ± 0.13

Table B.1 Continued.

p_T (GeV/c)	$0.5 < y_{cm} < 0.75$
3.500 - 3.625	26460 ± 1880
3.625 - 3.750	19840 ± 1570
3.750 - 3.875	11940 ± 1220
3.875 - 4.000	9250 ± 1180
4.000 - 4.125	6020 ± 110
4.125 - 4.250	4220 ± 80
4.250 - 4.375	3320 ± 70
4.375 - 4.500	2350 ± 50
4.500 - 4.625	1640 ± 50
4.625 - 4.750	1310 ± 40
4.750 - 4.875	907 ± 32
4.875 - 5.000	620 ± 26
5.000 - 5.250	448 ± 14
5.250 - 5.500	246 ± 10
5.500 - 5.750	124 ± 7
5.750 - 6.000	71.1 ± 5.5
6.000 - 6.500	35.0 ± 2.5
6.500 - 7.000	11.4 ± 1.4
7.000 - 8.000	3.07 ± 0.54
8.000 - 10.000	0.04 ± 0.04

Table B.1 Continued.

p_T (GeV/c)	$\pi^- + \text{Be} \rightarrow \pi^0 + X$ $-0.75 < y_{cm} < 0.75$
3.500 - 3.600	26660 ± 1070
3.600 - 3.700	19800 ± 780
3.700 - 3.800	14130 ± 710
3.800 - 3.900	10440 ± 590
3.900 - 4.000	8200 ± 510
4.000 - 4.100	6220 ± 60
4.100 - 4.200	4760 ± 50
4.200 - 4.300	3600 ± 40
4.300 - 4.400	2820 ± 30
4.400 - 4.500	2150 ± 30
4.500 - 4.600	1660 ± 20
4.600 - 4.700	1270 ± 20
4.700 - 4.800	981 ± 16
4.800 - 4.900	771 ± 14
4.900 - 5.000	601 ± 12
5.000 - 5.100	480 ± 11
5.100 - 5.200	387 ± 9
5.200 - 5.300	304 ± 8
5.300 - 5.400	224 ± 7
5.400 - 5.500	191 ± 6
5.500 - 5.600	146 ± 5
5.600 - 5.700	112 ± 5
5.700 - 5.800	92.6 ± 4.1

Table B.2 Invariant differential cross section per nucleon in units $\text{pb}/(\text{GeV}/c)^2$ for the inclusive π^0 production in 520 GeV/c π^- Be interactions. The cross sections are averaged over the full rapidity range, $-0.75 < y_{cm} < 0.75$.

p_T (GeV/c)	$\pi^- + \text{Be} \rightarrow \pi^0 + X$ $-0.75 < y_{cm} < 0.75$
5.800 - 5.900	77.1 ± 3.8
5.900 - 6.000	57.4 ± 3.3
6.000 - 6.125	44.3 ± 2.4
6.125 - 6.250	36.9 ± 2.2
6.250 - 6.375	31.7 ± 1.9
6.375 - 6.500	21.3 ± 1.7
6.500 - 6.625	16.0 ± 1.4
6.625 - 6.750	9.9 ± 1.1
6.750 - 6.875	10.4 ± 1.0
6.875 - 7.000	6.87 ± 0.91
7.000 - 7.250	5.41 ± 0.55
7.250 - 7.500	3.20 ± 0.40
7.500 - 7.750	1.55 ± 0.30
7.750 - 8.000	0.72 ± 0.18
8.000 - 8.500	0.48 ± 0.11
8.500 - 9.000	0.25 ± 0.08
9.000 - 10.000	0.06 ± 0.02

Table B.2 Continued.

p_T (GeV/c)	$\pi^- + \text{Cu} \rightarrow \pi^0 + X$ $-0.75 < y_{cm} < 0.75$
3.500 - 3.625	27210 ± 2280
3.625 - 3.750	18880 ± 2120
3.750 - 3.875	14060 ± 1620
3.875 - 4.000	11190 ± 1330
4.000 - 4.125	7430 ± 140
4.125 - 4.250	5030 ± 110
4.250 - 4.375	3560 ± 90
4.375 - 4.500	2650 ± 70
4.500 - 4.625	1840 ± 60
4.625 - 4.750	1420 ± 50
4.750 - 4.875	1100 ± 40
4.875 - 5.000	736 ± 33
5.000 - 5.125	535 ± 24
5.125 - 5.250	387 ± 20
5.250 - 5.375	290 ± 19
5.375 - 5.500	234 ± 16
5.500 - 5.625	168 ± 13
5.625 - 5.750	131 ± 11
5.750 - 5.875	95.2 ± 9.6
5.875 - 6.000	57.7 ± 8.2
6.000 - 6.250	44.7 ± 4.5
6.250 - 6.500	19.0 ± 2.7
6.500 - 6.750	18.2 ± 2.8

Table B.3 Invariant differential cross section per nucleon in units $\text{pb}/(\text{GeV}/c)^2$ for the inclusive π^0 production in 520 GeV/c π^- Cu interactions. The cross sections are averaged over the full rapidity range, $-0.75 < y_{cm} < 0.75$.

p_T (GeV/c)	$\pi^- + \text{Cu} \rightarrow \pi^0 + X$ $-0.75 < y_{cm} < 0.75$
6.750 - 7.000	8.69 ± 2.03
7.000 - 7.500	4.28 ± 0.94
7.500 - 8.000	1.08 ± 0.41
8.000 - 9.000	0.44 ± 0.18

Table B.3 Continued.

p_T (GeV/c)	α
3.5 - 4.0	1.079 ± 0.004
4.0 - 4.5	1.091 ± 0.006
4.5 - 5.0	1.096 ± 0.010
5.0 - 5.5	1.066 ± 0.016
5.5 - 6.5	1.052 ± 0.020
6.5 - 8.0	1.075 ± 0.060
8.0 - 10.0	1.016 ± 0.230

Table B.4 Values of α averaged over the full rapidity range $-0.75 < y_{cm} < 0.75$ for π^- induced collisions. The parameter α was determined assuming an A^α dependence for the cross sections on Be and Cu.

